Experimental and Numerical Investigation of Turbulent Flow and Transfer in Staggered Tube Bundles

Meyer, Knud Erik; Larsen, Poul Scheel; Kristensen, Hans Saustrup

Publication date:
1994

Document Version
Publisher's PDF, also known as Version of record

Link back to DTU Orbit

Citation (APA):
Meyer, K. E., Larsen, P. S., & Kristensen, H. S. (1994). Experimental and Numerical Investigation of Turbulent Flow and Transfer in Staggered Tube Bundles. Kgs. Lyngby, Denmark: Technical University of Denmark (DTU). (MEK; No. 94-03).

AFM - 94-03 Januar 1994
ISSN 0590-8809

Experimental and Numerical Investigation of Turbulent Flow and Heat Transfer in Staggered Tube Bundles

Knud Erik Meyer

**DEPARTMENT
OF
FLUID MECHANICS**

TECHNICAL UNIVERSITY OF DENMARK

Printed 1994
Department of Fluid Mechanics,
Building 404,
Technical University of Denmark
DK-2800 Lyngby

Preface

This thesis is submitted as a partial fulfilment of the requirements for the Ph.D. degree at the Technical University of Denmark. The thesis is based on experimental and theoretical work carried out during the period February 1st 1991 to January 31st 1994 at the Department of Fluid Mechanics, Technical University of Denmark and under the guidance of Professor Poul Scheel Larsen, Ph.D. and Lektor Hans Saustrup Kristensen, Ph.D.

I would like to thank everybody at the Department for fruitful discussions and kind assistance. I will just mention a few: Mr. K. B. Jensen for his careful work with the construction of the measuring tube, Lektor Jørgen Christiansen for his assistance with measuring instruments and Lektor Hans Saustrup Kristensen, Ph.D. for his guidance concerning the design of experiments. A special thank goes to my main supervisor Professor Poul Scheel Larsen, Ph.D. for his continuous support and interest which has been essential for my study.

Finally I would like to thank Anne Mette for her patience with me during my study.

January 1994
Knud Erik Meyer

Abstract

The two-dimensional mean velocity and Reynolds stress fields have been measured using laser Doppler anemometry (LDA) in the middle of a staggered tube bundle in cross flow of water. The tube bundle had transverse to longitudinal pitches of 2 × 2 and the Reynolds number for the flow was $Re = 32\,000$. The measurements did not cover the region close to the tube walls. A recirculation zone extended one diameter behind the axis of each tube. Visualizations illustrates this zone further.

Two tube bundles with transverse to longitudinal pitches and Reynolds numbers: 2 × 2, $Re = 34\,000$–$92\,000$ and 2.07 × 1.04, $Re = 40\,000$, were placed in cross flow in a wind tunnel. Here, the local heat tranfer was measured in steps of 1.8° around the perimeter of one tube that was electrically heated with a constant heat flux generated in a thin gold coating.

The commercial code FLOW3D from Harwell Laboratories, UK was used for calculations with the k-ϵ model and the Reynolds stress and flux models and with wall laws as boundary conditions. Calculations of the local heat transfer for an abrupt pipe expansion gave satisfactory results when a more accurate handling of the wall boundary was implemented in the code. However, the test case of an impinging jet showed that the same wall laws could not predict the correct heat transfer near the impingement zone.

Compared to the experimental results, the k-ϵ model was able to find reasonable levels of heat transfer and turbulent kinetic energy, but was unable to find the local variations. Surprisingly, the Reynolds stress model predicted much too low levels of turbulent kinetic energy and heat transfer although it, contrary to the k-ϵ model, predicted velocity distributions close to those of the experimental data. The reason for this has not been established, but it is likely that this problem is related to the inadequacy of wall functions.

Abstrakt (in danish)

De to-dimensionale tidsmidlede hastigheds- og Reynoldsspændingsfelter er blevet målt med laser Doppler anemometri (LDA) i midten af et forskudt rørbundt tværstrømt med vand. De relative afstande mellem rørene er 2 × 2 i henholdsvis den transversale og den longitudinale retning og Reynolds tallet for stømningen er 32 000. Målingerne dækkede ikke området tæt ved rørvæggene. En recirkulerende zone udstrækker sig til en diameter efter hverts rørs akse. Visualiseringer illustrerer denne zone yderligere.

To rørbundter med de relative transversale og longitudinale afstande, samt Reynolds tal: 2 × 2, $Re = 34\,000$–$92\,000$ og 2.07 × 1.04, $Re = 40\,000$, blev placeret i tværstrøm i en vindkanal. Her blev den lokale varmeoverføringskoefficient målt i spring på 1.8° omkring perimeteren af et rør, som blev elektriskt opvarmet med en konstant varmeflux genereret i en tynd guld belægning.

Det kommercielle program FLOW3D fra Harwell Laboratories i England blev brugt til beregninger med k-ϵ modellen og med Reynolds stress og flux modellerne. Væglove blev brugt som vægrandbetingelser. Beregninger af den lokale varmeoverføring for en pludselig rørudvidelse gav tilfredstillende resultater, når en mere nøjagtig behandling af vægrandbetingelsen var blevet implementeret i programmet. Et test tilfælde med en jet stømmende mod en væg viste imidlertid, at den samme vægrandbetingelse for dette tilfælde ikke kunne forudsige varmeoverføringen.

Sammenlignet med de experimentelle resultater, giver k-ϵ modellen fornuftige niveauer for varmeoverføring og turbulent kinetisk energi, mens denne model ikke var i stand til at finde de lokale variationer. Det er overraskende, at Reynolds stress modellen forudsiger et alt for lavt niveau for den turbulente kinetiske energi og for varmeoverføringen, selv om den finder en hastighedsfordeling, som er tæt på de experimentelle data. Grunden til dette er ikke fundet, men det er sandsynligt, at problemet er relateret til utilstrækkeligheder ved vægrandbetingelserne.

Contents

Chapter 1

Introduction

Most industrial flow are turbulent and many of these flows involve complex geometries. The flows often have complicated structures like recirculating regions, impinging zones etc. Examples are burners, chemical reactors, cyclones and heat exchangers. Typical parameters of interest are the pressure drop and global transfer rates for heat and mass. In some cases local values of e.g. heat transfer are important. Local flow characteristics like the position and size of a recirculating region can also be of interest.

Traditionally, the design of industrial flows are based on experience and correlations that have been determined by experiments. In the literature, correlations based on numerous experiments are found. These correlation are valuable tools in the design process, but they have their limitations. They are often limited to quite general geometries, fluids and flows and if many parameters are taken into account in a correlation, it is often not very accurate. In cases with special geometries and flow conditions, or in cases where a high degree of optimization is needed, the design process often has to be done through expensive experimental work. There is therefore a great interest in numerical models for flow and heat transfer prediction. These models can be used for numerical experiments that have lower costs and that usually makes it very easy to vary the geometry and other parameters. Numerical models can also give information that is impossible or at least very difficult to find experimentally.

With the rapid development of computers and their calculation capacity, the numerical calculations of flows are now a tool that it is realistic to use in the design of industrial processes. But at the same time no computer today is able of giving a full simulation of a turbulent flow at Reynolds numbers typical for industrial processes. In most cases only the time averaged values of the different parameters like velocities, pressure and heat transfer are of interest. The common way of overcoming the problems with a full simulation of the flow is to use a model that describes the effect of the turbulence on the time averaged values of velocities, temperature etc. Several turbulence models have been proposed over the last decades, but it is only within the recent years that it has been possible to make calculations with these models for more complex flows.

Two different models have been tested in the present study. The k-ϵ models are a kind of 'industrial standard', because these models are used for many practical problems today. They model the effect of the turbulence through an effective viscosity and through other effective diffusion coefficients that usually are found as a scaling of the effective viscosity. They have been tested for numerous types of flows and give fair results for many of the simple types. For more complex flows the k-ϵ models have severe weaknesses and there is therefore an interest for more sophisticated models like the Reynolds stress and flux models. These models are more complicated and requires a significantly larger computational effort, but they also have the potential of modelling various aspects of the turbulence more accurately. They are still in a stage of research and are not used much for practical design purposes yet. It is therefore interesting to test these models against some of the more complicated flows that are found in industrial processes.

To represent industrial flows it has been chosen to study different test cases with local heat transfer on a wall. This will be done by comparing the results of calculations with different turbulence models with available experimental data. Experiments have been performed in this study to supply data that can be used for verification of the models. Even though many flows have been investigated thoroughly through experiments, there is still a need for data that are well suited for verification of turbulence models. Such data should consist of measurements of both local turbulent flow parameters, like mean velocities and the Reynolds stresses, and of local heat transfer data. Furthermore, it is very important that the experiment is designed so that the boundary conditions can be reproduced in the numerical models.

A tube bundle in cross flow has been chosen as a test case. The tube bundle is one of the most used designs for heat exchangers. It has both a quite complex geometry and a complex flow with features that are found in many industrial flows. The flow and heat transfer in the middle of a tube bundle is only affected little by the in- and outlet conditions for the hole tube bundle. During the present study it has been attempted to establish a set of experimental data that can be used for verification of calculations with turbulence models. Other more simple test cases will be used in the calculations to test some of the flow features that is found in the tube bundle flow.

The commercial computer program FLOW3D for computational fluid dynamics (CFD) is used for the calculations. This has two purposes: It saves the effort of making a new program (perhaps by modifying another program) and it gives an opportunity of testing how well a commercial program performs for more complicated flows relevant for the industry. FLOW3D has been chosen because it is one of the very few commercial available programs that has the more complicated Reynolds stress and flux turbulence models implemented and because it was possible to obtain the parts of the source code that was necessary for the study.

In the following chapters, this report will describe: An overview of the physical aspects of the flow in a tube bundle followed by descriptions of LDA-measurements, visualizations and heat transfer experiments for a tube bundle. Then follows reviews of the turbulence models and the computational method used in this study and finally the results of calculations made on an abrupt pipe expansion, on an impinging jet and on two tube bundles will be presented.

Chapter 2

Measurements in a tube bundle

2.1 Introduction

This chapter will describe the experimental work done in the present study with the purpose of determining local velocities, turbulence parameters and the local Nusselt number in a staggered tube bundle.

Cylinders in crossflow are used in many applications in the industry. It is probably the most common way to make heat exchangers. There has been extensive investigations of the flow and heat transfer around a single circular cylinder in crossflow. The tube bundle has also been subject to many investigations, but the majority of the experiments only measure global parameters like the mean Nusselt number and the pressure drop over the tube bundle, since these are the parameters used in the design of applications.

There are many parameters, both geometric and physical, that determine the flow and heat transfer in a tube bundle. It is therefore difficult and laborious to make good correlations that take all the parameters into account. The known correlations may vary considerably from each other. For special or complicated geometries none of the available correlations might be applicable. In some applications, the local conditions have interest, e.g. when the maximum surface temperature should be kept under a certain level. There is therefore a great interest in models that can be used for detailed calculation of the flow and the heat transfer.

There are only few reported measurements of local variables. They are usually more complicated to measure and are less important in the design process. However, they are of great importance for the understanding and for the modelling of the flow and heat transfer. A main purpose with the measurements described in this chapter is therefore to establish a set of experimental data that can be used to verify different computational models for turbulent heat transfer.

The next section will describe general definitions and characteristics of flow in tube bundles. Then follows sections describing LDA measurements, visualizations and heat transfer measurements.

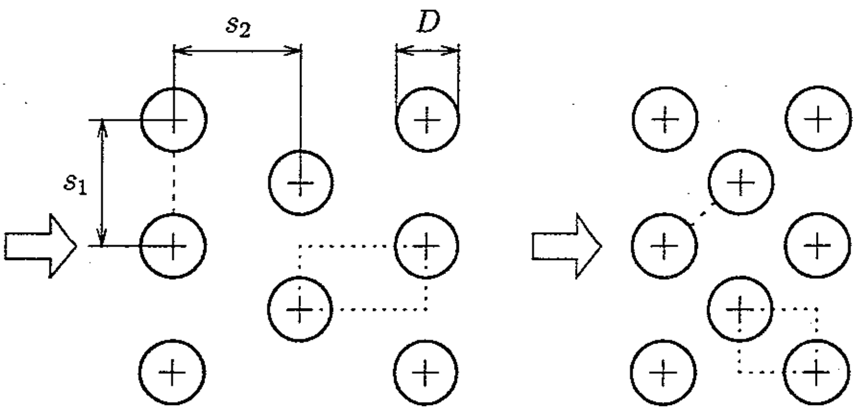

Figure 2.1: Characteristic lengths in staggered tube bundles — minimum flow section is shown with dashed line and "unit-cell" is shown with dotted box.

2.1.1 Definitions related to the tube bundle

In the literature several different ways of describing the geometry of a tube bundle are used. The tubes in a tube bundle are usually arranged in either in-line or staggered arrangements. Only staggered tube bundles will be used in the present study. The definitions used by Žukauskas and coworkers [1] will be adopted. The staggered tube bundle is characterized by the relative transverse ($a = s_1/D$) and longitudinal ($b = s_2/D$) distances (pitches) between the axes of the tubes, see figure 2.1. This report will use the term row for tubes on the same transverse line. Only smooth circular tubes are considered.

According to [1], several authors have found that is is convenient to generalize the results using a Reynolds number, $Re = (U_m D)/\nu$, based the diameter of the tubes D, the kinematic viscosity ν and the mean velocity U_m in the minimum flow section between the tubes. The minimum flow section is the cross section between the tubes where the mean velocity is largest. As it is illustrated in figure 2.1, the position of the minimum flow section depends on the geometry.

The heat transfer will be described by the Nusselt number, $Nu = hD/\lambda$, where h is the heat transfer coefficient, D the diameter of the tubes and λ is the thermal conductivity of the fluid. Both ν and λ are evaluated at the free stream temperature. In a tube bundle where all tubes are heated the free stream temperature is assumed to be the mean fluid temperature just upstream of the local tube. The local Nusselt number is evaluated using the local heat transfer coefficient based on the local wall heat flux, the local wall temperature and the fluid mean temperature upstream of the local tube. The angle ϕ from the front stagnation point is used to characterize the position on the surface of tube, see figure 2.2.

The mean Nusselt number $\overline{Nu}$ could be defined as the mean value of the local Nusselt numbers. However, most experiments only use global parameters like the average heat flux from a tube and the mean temperature of the tube

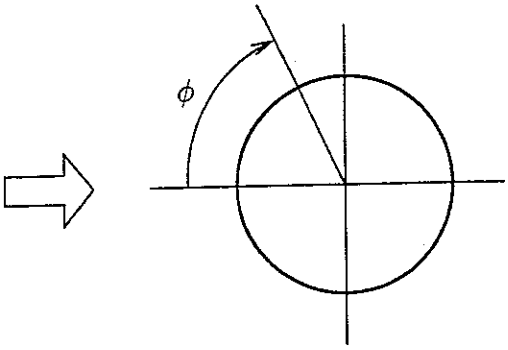

Figure 2.2: The angle ϕ from the front stagnation point on a tube.

wall. Therefore, in order to be able to compare the results with these experiments the mean Nusselt number is evaluated using a heat transfer coefficient based on the average heat flux and the mean wall temperature for the tube. In case of a constant wall temperature this $\overline{Nu}$ would be equal to a $\overline{Nu}$ calculated as the mean value of the local Nusselt numbers.

2.1.2 Characteristics for flow and heat transfer in a tube bundle

The flow around a tube in the middle of a staggered tube bundle is similar to the flow around a single cylinder. Žukauskas and coworkers [1-3] have reported extensive reviews on both flows. Following these, the flow around a single cylinder can be divided into different domains depending on the Reynolds number *Re*.

In the front of the cylinder, a laminar boundary layer is formed and its thickness increases downstream. For $Re < 1$ the inertial forces are negligibly small and the boundary layer separates from the surface at the rear stagnation point. For $Re > 5$ a pair of symmetrical vortices are formed at the rear part of the cylinder forming a recirculating region and for $Re > 40$ these vortices become unstable; they are periodically shed from the rear of the tube and the *von Karman* vortex street is formed. When $Re > 150$ small irregular vortices are formed together with the large vortices.

The range from $Re \approx 1000$ and up to the critical Reynolds number $Re \approx 2 \cdot 10^5$ is called the subcritical flow regime. Here the flow is a combination of a laminar flow in the front and a turbulent wake with regular vortices. The vortex shedding is very regular with the dimensionless frequency, the Strouhal number ($Sr \equiv fD/U$ where f is the frequency), being almost constant, $Sr = 0.2$. The separation point for the laminar boundary layer is at $\phi \approx 80°$.

The mechanism behind the separation found must be found in the balance between the pressure gradient at the wall and the viscous forces. The pressure gradient is favourable ($dP/dx < 0$) at the front part of the cylinder and increasing to become adverse ($dP/dx > 0$) at the rear part. The viscous forces are largest at the wall. At the point where the decreasing force from the pressure gradient have the same order of magnitude as the viscous forces, separation occurs. Further down the cylinder wall, fluid particles will start moving in the opposite direction of the main flow and the fluid begin to curl. This forms the vortices that sheds from the tube.

At the critical Reynolds number the laminar boundary layer gradually becomes turbulent and the separation point shifts downstream to approximately $\phi \approx 140°$. There are not full agreement on the mechanisms for the laminar-turbulent transition. Žukauskas [2] suggest the laminar boundary layer still separates at the front part of the cylinder, forms a separation bubble that reattaches to the surface and then again separates at $\phi \approx 140°$. The change of this effective separation point gives a large decrease of the drag coefficient and the size of the wake. It also gives large changes of the Strouhal number Sr.

Heat exchangers with tube bundles are typically made in one of two configurations: The in-line and the staggered tube bundle. In the in-line tube bundle all tubes are located on a rectangular grid while in the staggered tube bundle the rows are staggered as illustrated on figure 2.1. Compared to the in-line tube bundle, the staggered tube bundle is characterized by a larger heat transfer, but also a larger pressure drop. The staggered tube bundle in the subcritical flow domain is probably the most widely used configuration in industrial application and it will be used as the test case for the present study.

The flow around the first row of tubes in a tube bundle is quite similar to the flow around a single cylinder. For the following tubes, the flow is still similar to that of the single cylinder the difference being that the velocity profile upstream of the tube is non-uniform and highly turbulent. The flow is usually considered to be fully developed from the 3rd–5th row depending on the geometry. In the fully developed region all the characteristics of the flow are usually found in a "unit-cell" containing a part of two different tubes, see figure 2.1. It is usually only just upstream of the last row in a tube bundle that the flow at the outlet of the tube bundle differs from the flow in an inner unit cell.

This pattern where the flow is organized in unit-cells can, especially for in-line configurations, be disturbed by two mechanisms. The flow can in some cases go criss-cross through the bundle instead of just in the streamwise directions. This happens when some passages in other directions have a smaller flow resistance that the streamwise direction. The other mechanism is periodic oscillations down through the tube bundle. Vortex shedding can occurs from the first row, but usually not for rows further down. For an in-line tube bundle Ziada and Oengören [4] found that the vortex shedding from the first row could excitate a resonance phenomenon in the flow. It is probably less likely that this phenomenon will appear in a staggered tube bundle. However, for both types of tube bundles vortex shedding from the first row can excite mechanical resonances of the tubes. Vibrating tubes are an important problem in the design of real heat exchangers.

A typical distribution of the local heat transfer for the same Reynolds number around a single tube and around a tube in a tube bundle is shown in figure 2.3. The mean Nusselt number for a single cylinder in the subcritical

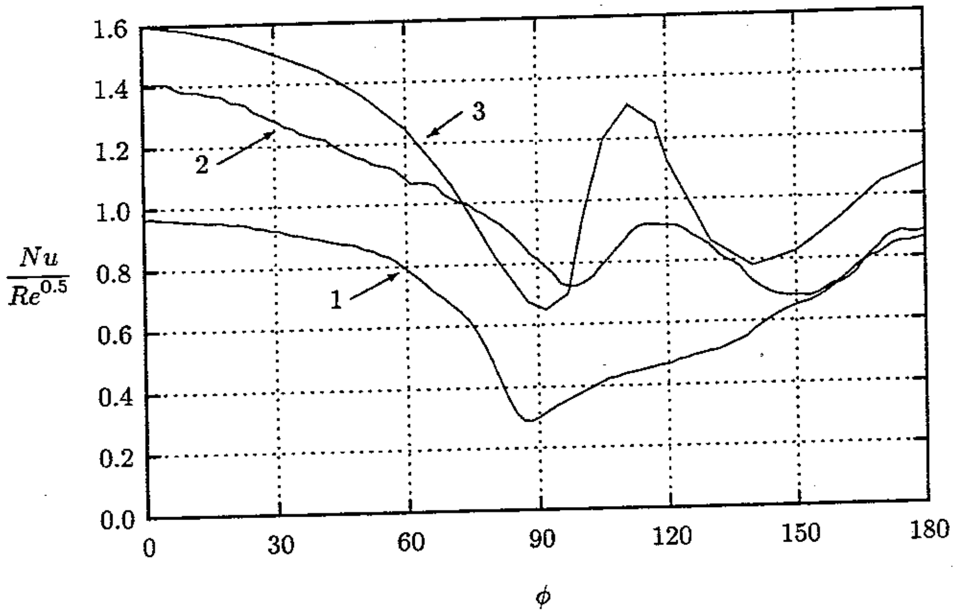

Figure 2.3: Local heat transfer on cylinder: (1) single cylinder, $Re = 38\,350$, $Tu = 0.4\%$ [5]; (2) tube bundle, $Re = 41\,500$, 4. row, $a \times b = 2 \times 2$, present study; (3) single cylinder, $Re = 39\,000$, $Tu = 11.5\%$, adapted from [2]

domain usually correlates with $Re^{0.5}$. In figure 2.3 the local heat transfer has therefore been plotted as $Nu/Re^{0.5}$ so that measurements with different Reynolds numbers easily can be compared. For a single cylinder in a flow of low turbulence the local Nusselt number has a maximum at the front stagnation point. It decreases towards the separation point and then increases again until the rear stagnation point where it reaches approximately the same value as at the front stagnation point.

Two factors are important for the local heat transfer on a single cylinder: The blockage factor and the turbulence intensity. Normally it is assumed that the flow around the cylinder is not affected by boundaries such as walls. However, if a cylinder is located in e.g. a channel, the effect of the walls can often be described by the blockage factor k_q: The blockage area of the cylinder as a fraction of the cross section area of the empty channel. The effect of the blockage factor is significant for blockage factors larger than $k_q \approx 0.2$; according to [3] an increasing blockage factor will result in larger velocities near the surface of the cylinder and therefore also in higher heat transfer coefficients. Furthermore, the separation point and the minimum for the local heat transfer will move downstream.

The turbulence intensity Tu is the RMS value of the velocity fluctuations as a fraction of the time averaged velocity. With increasing turbulence intensity in the main flow, the heat transfer also increases. A higher turbulence intensity will also cause the transition to a turbulent flow in the boundary layer to occur at a lower Reynolds number. Žukauskas [2] estimates that the critical flow regime is established for $Re \cdot Tu > 150\,000$ where Tu is expressed as a percentage.

According to this criterion, the measurement performed with $Tu = 11.5\%$ in figure 2.3 is in the turbulent regime and this changes the distribution of the local Nusselt number significantly. It still has a maximum at the front stagnation point and is then decreasing until about $\phi = 90°$. Here it is assumed that there is a separation of the laminar boundary layer and then a transition to a turbulent boundary layer that reattaches. This gives a sharp rise in Nu over a distance of $\Delta\phi \approx 10°$. After the transition Nu again decreases toward the separation of the turbulent boundary layer at $\phi \approx 140°$ where there is a second minimum for Nu.

The distribution of the local Nusselt number for the 4. row in a tube bundle is plotted in figure 2.3. The result is quite similar to the distribution of Nu for the single cylinder in a turbulent flow. The difference between the local minima and maxima for the tube bundle is smaller than for the single cylinder and the minima are all placed about 10° closer to the rear stagnation point. The mechanisms forming Nu is therefore probably the same and the main difference is probably due to the high blockage factor and the non-uniform upstream flow condition for a tube in a tube bundle.

In the highly turbulent flow in a tube bundle the effective diffusivity of heat is high throughout the flow. The main heat resistance is found in the laminar sublayer at the walls. The local Nusselt number is mainly determined by the thickness of the laminar sublayer and therefore by the flow conditions. Because of this, there is little difference between measurements where all tubes in a tube bundle are heated and measurements where just one tube is heated; most authors therefore use only one heated tube in their experiments in turbulent flows [1].

2.2 LDA-measurements

This section reports measurements of local velocity and Reynolds stresses in a tube bundle. The measurements are performed using laser Doppler anemometry (LDA). The results are used in section 5.4 for comparison with calculations.

2.2.1 Review of literature

Although the global heat transfer of tube bundles have been extensively investigated, only few measurements of local velocities and turbulence quantities have been carried out for a turbulent flow in a tube bundle. Such measurements are complicated because the flow is highly turbulent and because the tubes make it difficult to reach the inner part of a tube bundle.

A few measurements have been performed using hot-wires etc. Neal and Hitchcock [6] performed measurements with a hot-wire anemometer and Simoneau and VanFossen [7] performed similar measurements with a hot-film anemometer probe. In both cases the experiments have been performed in rather narrow test sections with only 2–3 tubes in each row. The hot-wire and hot-film techniques can only be used in the limited parts of the flow where the turbulence intensities are not too high and where the flow direction is known.

In particular it is therefore not possible to get reliable measurements in the recirculation zone.

The laser Doppler anemometer is a more generally applicable technique because it is able to deal with the highly turbulent flows. However, a limiting factor for a traditional measurement with LDA is that the probe volume is produced by two intersecting beams. If the optical axis is aligned with the axis of the tubes, the angle of the beams therefore gives a limit on how close the probe volume can come to the tube wall. There is therefore a conflict between the desire for measuring far away from the side wall of the tube bundle to avoid three-dimensional effects of the side walls and the desire for measuring close the tube wall.

More complicated LDA-techniques can be used to overcome this problem. A fluid with a refractive index matched to the tube material could be used to give full freedom in the positioning of the probe volume. However, this technique demands a complicated flow system with a very accurate temperature control. To the author's knowledge this technique has so far only been applied to laminar flows in tube bundles [8]. Another possibility is to give the optical axis an angle with the tube axis. This will probably require a more complicated optical system for most test channels. It is also possible to complement the measurements with measurements of the velocity component that is locally tangential to the tube wall. This can be done with a two beam configuration either aligned with the tube axis or looking out through a window in the tube wall. To the author's knowledge none of these techniques have been used so far.

Measurements with the optical axis aligned with the tube axis have been performed by Halim and Turner [9] and Simonin and Bacouda [10]. Both studies are comparable to the present study, but in all cases the geometries are different.

2.2.2 Experimental set-up

The present measurements have been performed with the set-up shown in figure 2.4. The isothermal test section contains 9 rows in a staggered arrangement with 3–4 tubes in each row. Acrylic rods with a diameter $D = 10\,\mathrm{mm}$ are used as 'tubes'. The transversal and longitudinal pitches are $a \times b = 2.0 \times 2.0$ and the length of each tube is 6 diameters. The sides of the test section consist of 10 mm transparent acryl of good optical quality. The inlet to the test section contains a flow straightener that consist of closely packed plastic tubes with thin walls. They have a length of 50 mm, a diameter of 5 mm and are fixed in the flow by a fine grid.

The flow system is shown in figure 2.4. From a reservoir, tap water is circulated by a centrifugal pump. The mean flow rate is measured with an orifice plate and can be regulated with a valve. The orifice plate is constructed according to DIN 1952 [11] and is placed in a 2 inch tube with 40 diameters of tube upstream and 10 diameters of tube downstream. The temperature of the water is regulated to $25.3° \pm 0.3°\mathrm{C}$ by cooling water and a thermostatic controlled electrical heater. The mean flow rate, regulated by a throttle valve,

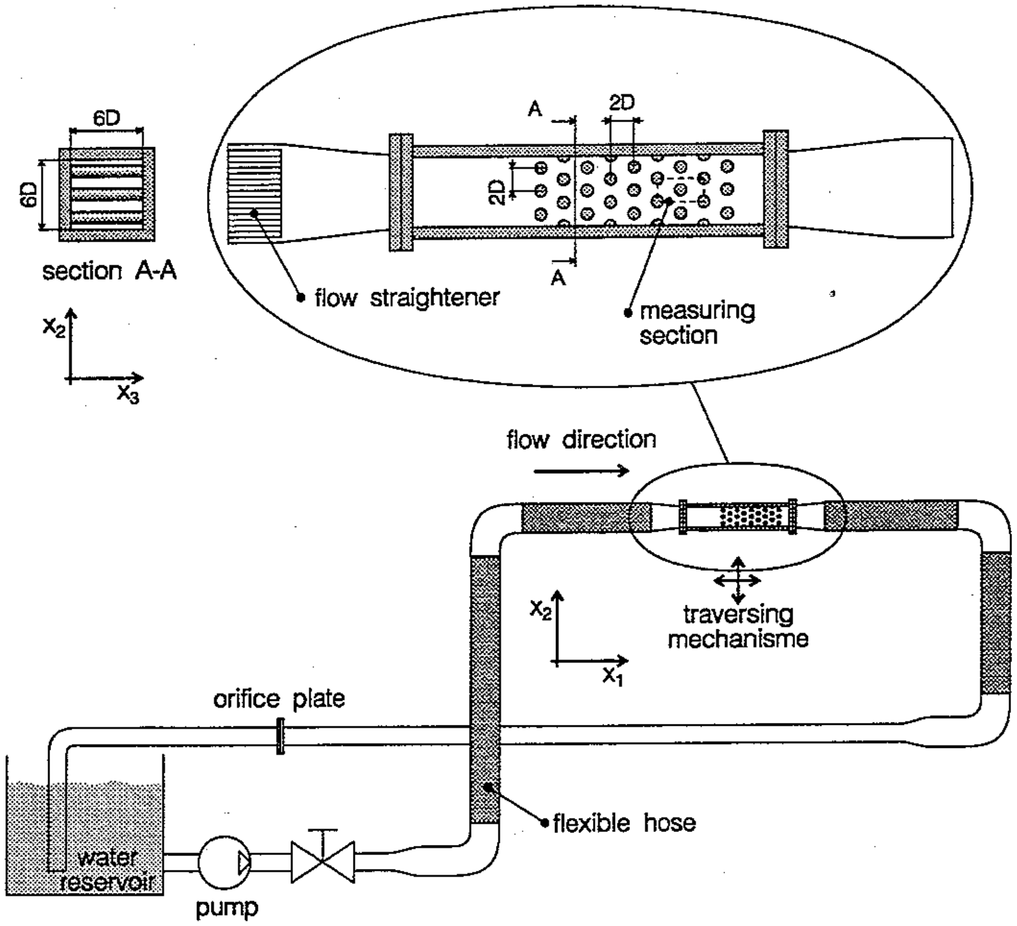

Figure 2.4: The experimental set-up for LDA measurements

is believed to be steady within ±1%. The measurements were performed at a Reynolds number $Re = 30\,000$ based on the tube diameter D, the mean velocity U_m between two tubes in a row estimated from the flow rate measured by the orifice plate and the kinematic viscosity at the temperature 25.3 °C, $\nu = 0.890 \cdot 10^{-6}\,\mathrm{m}^2/\mathrm{s}$.

The test section is connected to the flow system with flexible 3 inch hoses which enables the transversing mechanism to move the test section relative to the optics. The resolution of the transversing mechanism is better than 0.01 mm. However, the error on the positioning is believed to be within ±0.15 mm. Larger errors occurred while moving several tube diameters in the flowwize direction. These errors are believed to be due to the loading of the flexible hoses connected to the test section and they were corrected assuming a linear variance of this error.

The laser-Doppler anemometer consists of a 1.5 W Spectra Physics Argon laser, a 4 beam, two-component optical unit and two photomultipliers in forward scatter mode. The laser light contains a blue and a green line. In the Dantec optical unit (55X) the laser beam is split into two beams and one of the beams passes a Bragg cell shifting the frequency 40 Mhz. The beams are split into four beams, two of each colour, and then expanded in a beam expander with an expansion ratio of 1.94 to a diameter of 2.43 mm.

The beams are focused using a front lens with a focal length of 160 mm. The intersection angles between for the two sets of beams have been measured and the relevant data for the two data channels are listed in table 2.1. The probe volume is estimated to have a length of 0.50 mm and a diameter of 0.04 mm.

		x_1-direction	x_2-direction
colour		green	blue
beam intersection angle		12.8°	13.4°
wavelength	[nm]	514.5	488.0
fringe spacing	[μm]	2.300	2.085
frequency shift	[kHz]	2000	3000
high pass filter	[kHz]	64	256
low pass filter	[kHz]	4000	8000

Table 2.1: Parameters for the two data channels

The signals from the photomultipliers are coupled to a Dantec frequency shifter (55N15), where the 40 Mhz signal from the Bragg cell is subtracted except for a shifting frequency. The setting of frequency shifting and hi- and low-pass filters ensured for both channels and for all measuring positions that all data points lying within 5 standard deviations of the mean value were treated correctly.

The signals are then passed to two Dantec LDA counter processors (55L96) equipped with a coincidence filter in order to ensure the simultaneity of the signals. The maximal time difference between the two signals was chosen to 50 μs. Each signal is filtered with a high and a low pass filter. Typical data rates were between 10 and 50 Hz. These data rates give an average time between samples that is significantly larger that correlation time for the flow. The data from the counters are collected and processed to the final results with a program running on a personal computer [12].

The flow in the tube bundle is highly turbulent. It is therefore important to avoid velocity bias errors. Following [13], the residence time is therefore used as weighting factor in the computation of statistical quantities.

The direction of the axis of coordinate system used in the measurements are shown in figures 2.4–2.5. The origo of the coordinate system is located in the middle of the measuring section, i.e. at the center of the middle tube in the 7th row. In the x_3-direction (along the tubes) the origo is located at the wall closest to the front lens of the optical unit.

2.2.3 Measurements and results

The purpose of the measurements is to estimate velocities and Reynolds stresses in a plane in the middle of a tube bundle. This will be done in the measuring

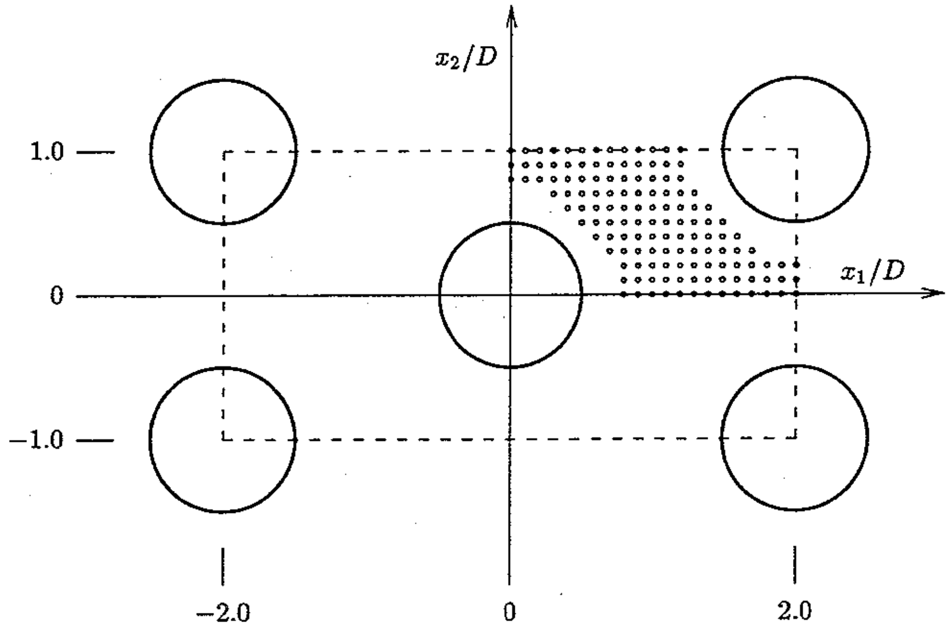

Figure 2.5: Measuring section (dashed line) and coordinate system used for the measurements. Both are centred around the tube in the middle of the 7th row (see figure 2.4). The measurements are transformed to the upper right unit cell and here the position for each transformed measurement is indicated with a small ring.

section shown in figure 2.5. To determine whether this measuring section can be used to give a reasonable estimate of the flow in the middle of a tube bundle, different investigations have been carried out.

To find an indication of the influence of the number of samples, series of measurements where performed at a single point. The number of samples in each measurement was changed in steps from 100 to 6000 samples. The measuring point had the approximate coordinates $(x_1, x_2, x_3) = (0.85\,D,\ 0,\ 0)$ and the results of these measurements are shown in appendix B.1. Similar measurements have been performed at other points with the same qualitative results.

The measurements indicate that increasing the number of samples from 100 to 1000 leads to a significant decrease of the variance of the statistical quantities. Increasing the number of samples to 6000, indicates in most cases a further but not so significant decrease of the variance. At 6000 samples there is still a visible variance. It was chosen to use 5000 samples at each point for the further measurements although even larger samples could be justified.

It is expected that the actual mean velocity in the minimum flow section for the measuring section will be higher that the mean velocity estimated by the orifice plate measurement. This is due to wall effects in the test channel and due to the inaccuracy of the orifice plate measurement. The actual mean velocity has been estimated by LDA-measurements of the U_1 velocity compo-

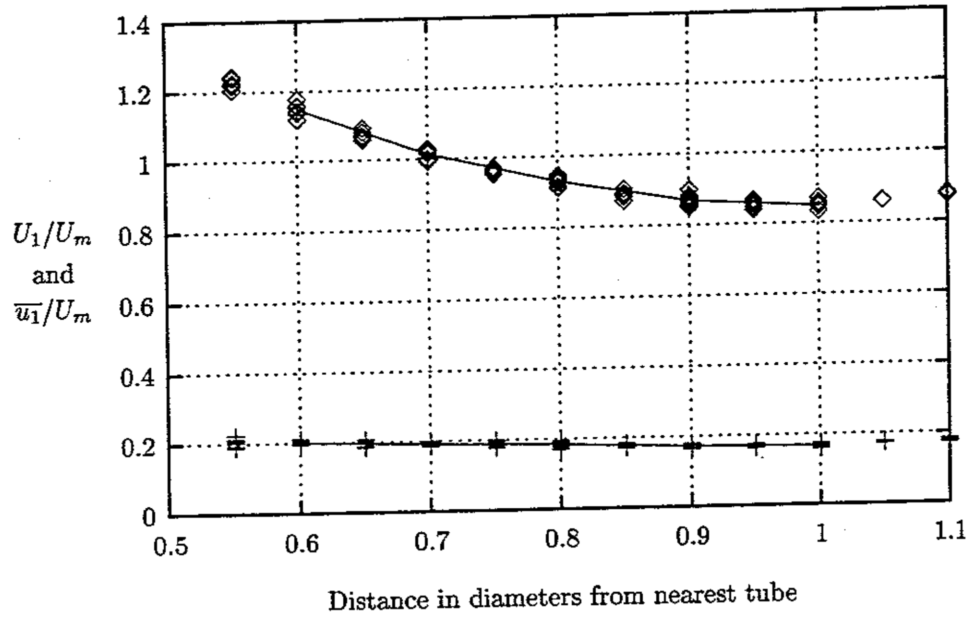

Figure 2.6: Velocity component in x_1-direction and is rms value at the minimum cross-sections of the measuring section: ◇ : U_1, + : $\overline{u_1}$, ——— : average values.

nent in the smallest cross-sections of the measuring section ($x_1/D = -2, 0, 2$ and $-1.1 < (x_2/D) < 1.1$). These measurements are shown on figure 2.6. The mean velocity in the minimum flow section is found to be $U_m = 2.85\,\mathrm{m/s}$ by numerical integration of all the measurements. This is 6.7% higher than that estimated from the orifice plate measurement assuming identical conditions between all tubes, and the actual Reynolds number is therefore $Re = 32000$. In the presentation of the measurements the velocity and the Reynolds stress components have been made dimensionless with $U_m = 2.85\,\mathrm{m/s}$.

The flow in the middle of a large tube bundle is assumed to be two-dimensional. To determine how large three-dimensional effects are in the test channel, profiles have been taken in the x_3-direction at various points in the measuring section. In a two-dimensional flow these profiles would show constant values of the measured varables. No three-dimensional effects were found in the middle of the flow and the wall effects were generally small. The measuring volume was not able to resolve the laminar sublayer at the walls. The largest effects were found in the wakes just behind the tubes.

Figure 2.7 shows an example of the U_1-velocity component measured in the recirculating region behind a tube, approximately at $(x_1, x_2) = (0.85D, 0.0)$. Figure 2.7 shows 3 different sets of measurements at the same point. While there can be seen only a small effect of the wall on the fluctuating velocity components $\overline{u_1}$, there is a significant effect of the wall on the mean velocity component U_1 which is decreasing until about 1 diameter from the wall and then increasing slightly. This effect is probably due to a flow pattern similar to the horseshoe vortex observed for a cylinder at a wall. The slight increase

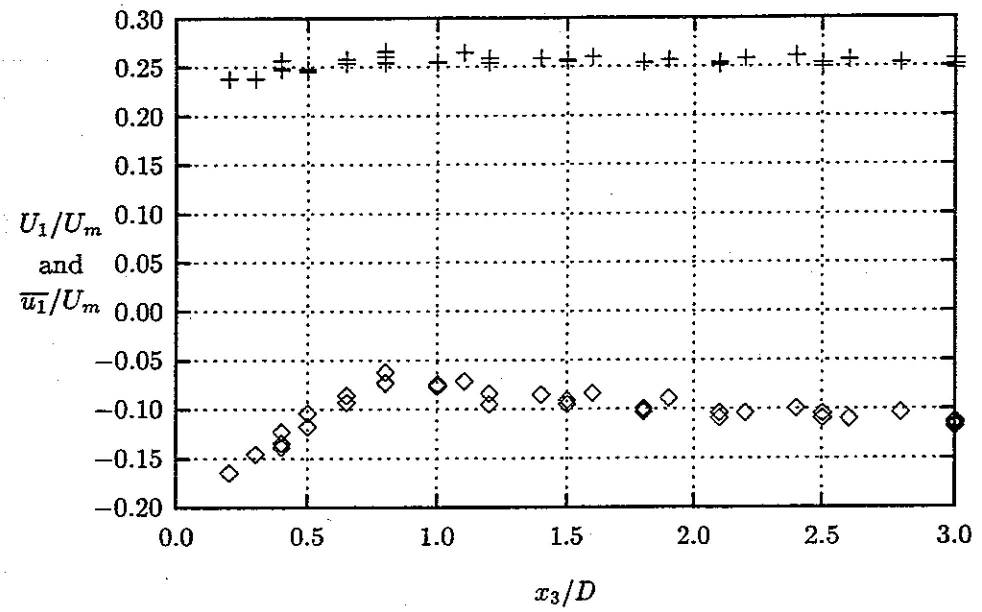

Figure 2.7: Variation of U_1 (key: ◇) and $\overline{u_1}$ (key: +) in the x_3-direction approximately in the point $(x_1, x_2) = (8.5D, 0.0)$; wall at $x_3/D = 0$, centerline at $x_3/D = 3$.

of the velocity from about 1.5 diameter from the wall is probably due to the fact that the x_3-axis of the traversing mechanism makes a small angle (about 1°) to the optical axis.

The final measurements have been performed in the middle of the test channel, i.e. at $x_3 = 3D$. In this position the beam angles did not permit measurements closer than 0.3 diameter from the surfaces of the tubes. The measurements have been performed on a grid with a spacing of 0.1 diameter and covering the measuring section shown in figures 2.4–2.5. A few measurements were also taken just outside the measuring section. All the measurements are plotted on graphs in appendix B.2. The measuring section covers 4 unit cells and the results have been transformed and plotted on the upper right unit cell together with a curve showing the average of the transformed values. The positions of the measurements transformed to the upper right unit cell are shown in figure 2.5.

During the experiments a small velocity bias error was found on the U_2 velocity component. This error is only significant in the wake behind the tubes and here it is seen as a systematic difference between the transformed measurements from different unit cells. This difference is seen for the velocity component in the x_2-direction and for the Reynolds stresses that contain a component in the x_2-direction. In the wake the fluctuating component of the velocity has the same order of magnitude as the mean component and it is therefore expectable to find the largest velocity bias errors here. The error was found consistently at many different positions in the flow and it is therefore believed that the bias error does not arise from the flow but from the measuring system. However, it has not been possible to ascertain whether the bias error arises from the optical system or from the processing of the signals. The velocity bias error is found in appendix B.2 in the wake for U_2, $\overline{u_2u_2}$ and $\overline{u_1u_2}$. The error is reduced by the averaging of all measurements. This is confirmed by the fact that averaged values of U_2 and $\overline{u_1u_2}$ are quite close to zero for $x_2 = 0.0$. The average values of the measurements are therefore believed to give a fair estimate of the mean values of velocity and Reynolds stresses.

An impression of the error of the measurements is given in appendix B by the standard deviation of repeated measurements with the same number of samples (see table B.1) and by the scattering of the single measurements compared to the mean values plotted in section B.2. Besides the uncertainty due to the limited number of samples in each measurement, the most important error is probably introduced in the determination of U_m. It has been found by a series of measurements and is estimated to have an uncertainty of about 1 %. Other errors arising from the measuring system are assumed to be less important. It is therefore estimated that the error on the mean velocities is less than 2 % of U_m and the error on the Reynolds stresses is less than 5 % of their local levels. The errors on U_2, $\overline{u_2u_2}$ and $\overline{u_1u_2}$ might be a little higher due to the mentioned velocity bias error.

Besides the velocity bias error, the measurements from the four unit cells in the measuring section are all close to the averaged values. This indicates that a periodic boundary condition can be assumed for up- and downstream boundaries. Along the sides of the unit cells ($x_2 = 0.0$ and $x_2 = \pm D$) the gradient of U_1, $\overline{u_1u_1}$ and $\overline{u_2u_2}$ and the values of U_2 and $\overline{u_1u_2}$ are approximately zero. Together with the fact that most of the measured values are close to the mean values this indicates that a symmetric boundary condition at the sides of a unit cell can be assumed. These conclusions support the numerical model used in chapter 5.4.

The measurements show a recirculating zone behind the cylinder, but only the last part of this zone is captured. The zone extends to about $x_1/D = 1.0$, i.e. 0.5 diameter downstream of the tube.

2.2.4 Conclusions

The LDA data seem to give reasonable estimates of the mean velocity and the Reynolds stresses in the middle of a tube bundle at the 7th row where the flow appears to be fully developed. It has been found reasonable to assume that the flow is two-dimensional and that all the characteristics of the flow can be found in a unit cell with asymmetric periodic boundary conditions upstream and downstream, and symmetric boundary conditions on the sides. A limitation with the measurement is the lack of data near the tube walls.

Although the accuracy of the measured data is satisfactory for the verification of turbulence models, the accuracy could be improved in several ways. The use of 5000 samples in each measurements have been found reasonable, but it could be justified to use significantly more samples; particularly if moments of higher order than two are sought. The problems with the velocity bias error could purhaps be solved by a very careful examination of the optical system and the data processing system. Other improvements could be a more accurate transversing mechanism and a more stable flow system.

It has been shown that three-dimensional effects exist, but only close to the side walls of the test channel. These measurements indicate that it would be possible to make measurements closer to the side walls without distortions due to wall effects. This would allow access closer to the tube walls. An interesting supplement would be measurements of the velocity component tangentially to the tube wall using a 2 beam LDA set-up that is rotated to follow the wall.

Furthermore it would be interesting to investigate the flow near the boundaries of the tube bundle, i.e. inlet, outlet and sides and to investigate the flow development through the first rows.

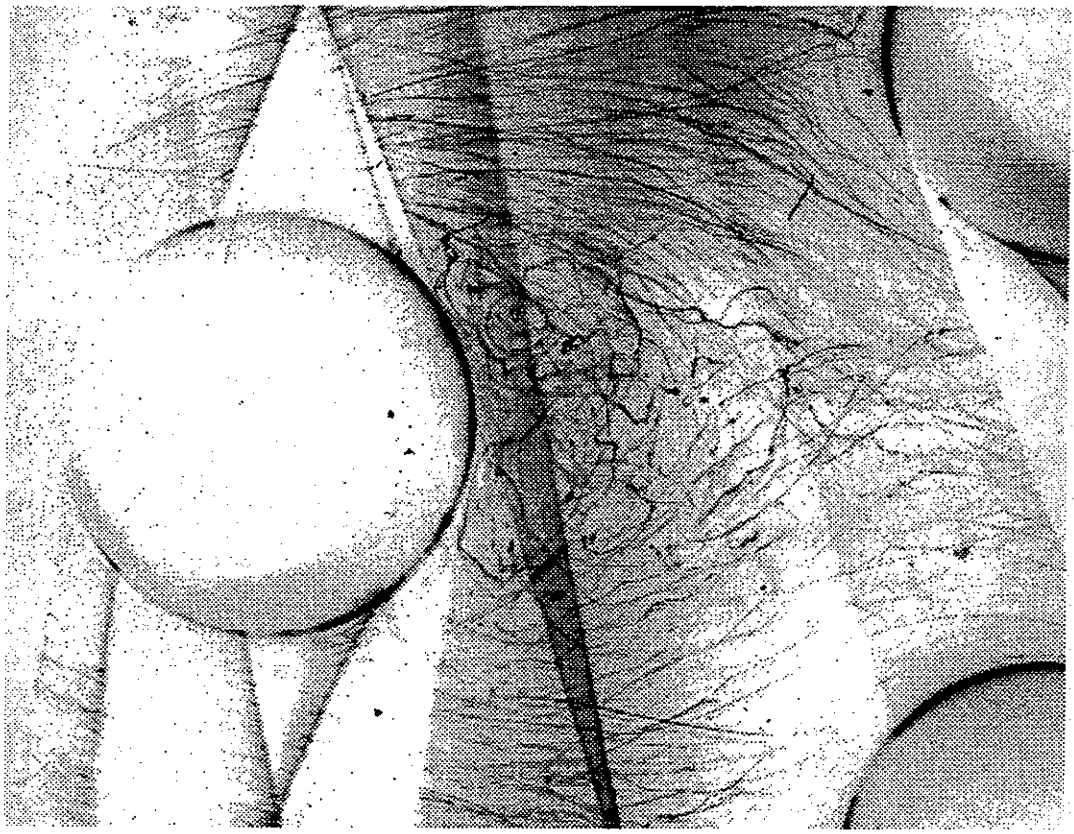

Figure 2.8: Picture of the flow with exposure time 1/30 second. Flow from left to right.

2.3 Visualization of the flow

To give a qualitative impression of the flow in a tube bundle visualizations have been performed in the test channel described in the previous section, see figure 2.4. The test section was rotated 90° around the x_1-axis. The two green beams from the LDA-optics were send through two cylinder lenses to produce

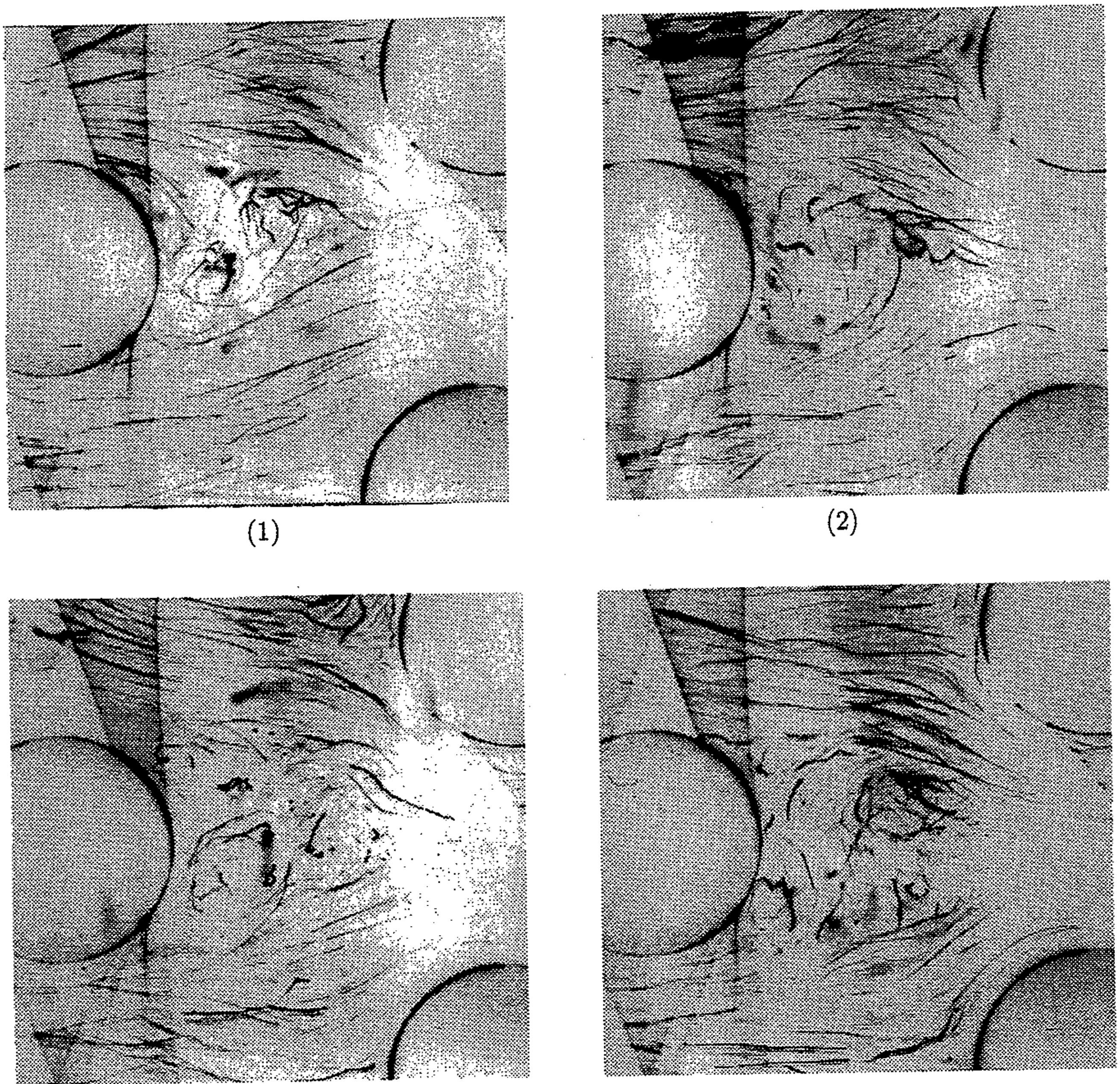

(1) (2) (3) (4)

Figure 2.9: Picture series of the flow (part 1) – exposure time 1/500 second. Flow from left to right.

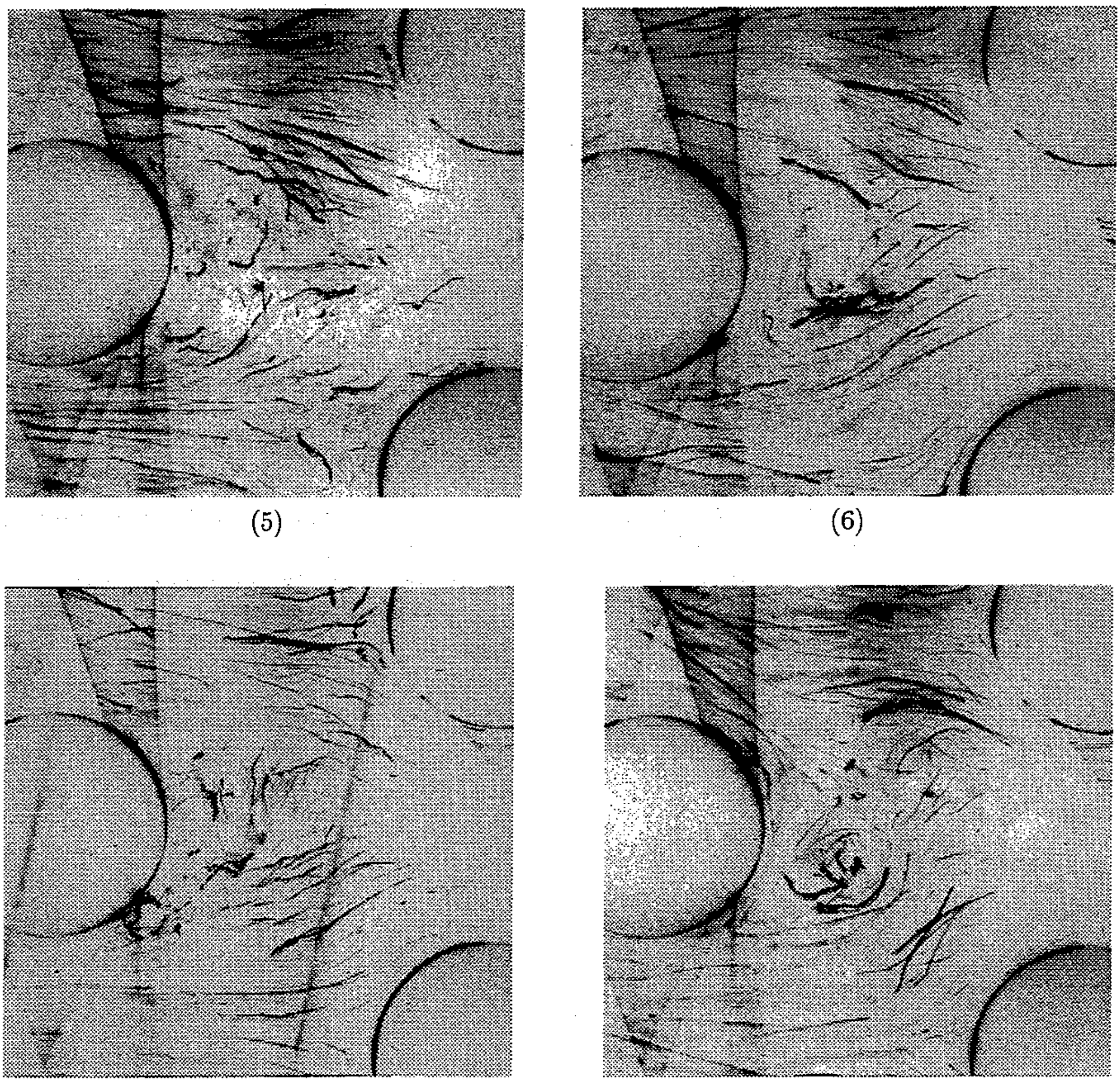

(5) (6)

(7) (8)

Figure 2.10: Picture series of the flow (part 2) – exposure time 1/500 second. Flow from left to right.

two sheets of laser light. The lenses were carefully arranged together with mirrors at the opposite side of the channel in order to cover as much of the inner flow as possible. The resulting laser sheet was located behind the middle tube in the 7th row and between the two side walls ($x_3 = 3\,D$). The thickness of the laser sheet was approximately 1 mm.

Photographs were taken with a traditional SLR camera (Nikon F90) fitted with a 105 mm lens. This gave a magnification with a ratio of approximately 1 : 1. The film was a black-and-white, 36×24 mm film (Ilford HP5, 400 ASA). The magnified pictures are shown as negatives and show a flow from left to right. They contain areas with different degree of shading. These areas are due to reflections and lens effects from the acrylic rods that were used as 'tubes'.

The flow was visualized by adding air bubbles to the water. Air was injected in the straight tube before the orifice plate. The air bubbles flow together with the water into the water reservoir. Here only minor bubbles manage to reach the inlet to the pump. In the pump the bigger bubbles are split into smaller bubbles and at the inlet to the test section the water is therefore seeded with quite small bubbles. It is estimated that most of the bubbles have diameters smaller than 0.1 mm. They are not expected to follow the flow completely, but it is assumed that they give a fair impression of the large scale motions in the flow.

The visualizations have been performed at approximately the same flow conditions as the LDA-measurements. Using the correction of the orifice plate measurement found in section 2.2.3 the velocity in the minimum flow section is $U_m \approx 3.0\,\mathrm{m/s}$ corresponding the a Reynolds number of $Re \approx 35000$.

Figure 2.8 shows a picture taken with an exposure time of 1/30 second. During the exposure time the main flow has moved approximately 7 diameters. The picture therefore gives an impression of the mean flow. The flow seems to be divided into two regions: The region behind the cylinder with large vortices and the rest of the flow where no vortices can be seem. However, in the latter region, the tracks of the bubbles cross each other indicating that there is a high degree of turbulence in this region also. In the region behind the cylinder the existence of large vortices indicates that flow reversal occurs.

A series of pictures taken with an exposure time of 1/500 second is shown in figures 2.9 and 2.10. In this case the exposure time has been obtained by placing a shutting mechanism from another camera in the laser beam and using this to make a short flash of laser light. During the exposure time the main flow has moved approximately 0.6 diameters. These pictures can therefore be interpreted as snapshots of the flow. They are taken as a series within approximately one minute.

The snapshots show the same two regions found in figure 2.8. The region with flow reversal contains many vortices, both of large and small scales. There is a clear interaction between the large vortices behind the tube and the direction of the main flow. The first vortices appear at $\phi \approx 120°$. This is perhaps most evident in picture (7), where a relatively large vortex is seen at the lower part of the tube just after $\phi = 120°$. Unfortunately these vortices can not be seen in figure 2.8 because this part of the flow is poorly illuminated.

These vortices indicate that separation occurs before $\phi = 140°$ which will be in contradiction with the theory of Žukauskas [2] referred in section 2.1.2. It is not possible to make any further quantitative conclusions based on the present visualizations, but the observations show that it would be desirable to make a more detailed investigation of the flow close to the walls of the tubes.

2.4 Measurements of local heat transfer

This section will describe measurements of the local heat transfer for a cylinder in a tube bundle in crossflow with a constant heat flux.

2.4.1 Review of literature

There have been performed several measurements of the local heat transfer for a tube in a staggered tube bundle in the subcritical flow range. Some of these studies are reported in references [14-19]. Most of the measurements use different geometries. General measurement of the heat transfer in tube bundles together with a review of the literature can be found in the work of Žukauskas and Ulinskas [1]. Some of the measurements are combined with measurements of the local velocities and turbulence. However, no reports of measurements of good quality that combines heat transfer and velocity/turbulence have been found.

Different boundary conditions for the heat transfer have been used in the cited measurements. For measurements made with concern to test numerical simulations, a boundary condition with either constant temperature or constant heat flux are of special interest because these boundary conditions are simple to implement. However, in some experiment both the temperature and the heat flux vary along the perimeter of the tube and special concerns are often needed to keep one of them constant.

Several techniques can be used for heat transfer measurements. One technique is to use the analogy between heat and mass transfer, e.g. to use sublimation of naphthalene to estimate the Nusselt number [14]. However, the two most used techniques are probably to either heat the tube with an electrical current in a thin electrical layer on the surface or to heat (or cool) the inside of a tube to yield a constant surface temperature by e.g. water or stream.

A constant heat flux produced by electrical heating of a plastic foil with a thin gold coating is used in the present study. Baughn *et al* [20] have reported thorough investigations of this technique and used it for measurements similar to the present [19]. A general difficulty using electrical heating of a surface is that materials that are electrical conductive usually also have high heat conductivities. This results in tangential heat conduction that disturbs the uniformity of the constant heat flux generated by the electrical heating. In the case of the gold coated plastic foil the gold coating is very thin and tangential heat conduction is therefore reduced to conduction in the plastic foil and the support material.

As it is discussed in section 2.1.2 only the single measuring tube will be heated in the experiment.

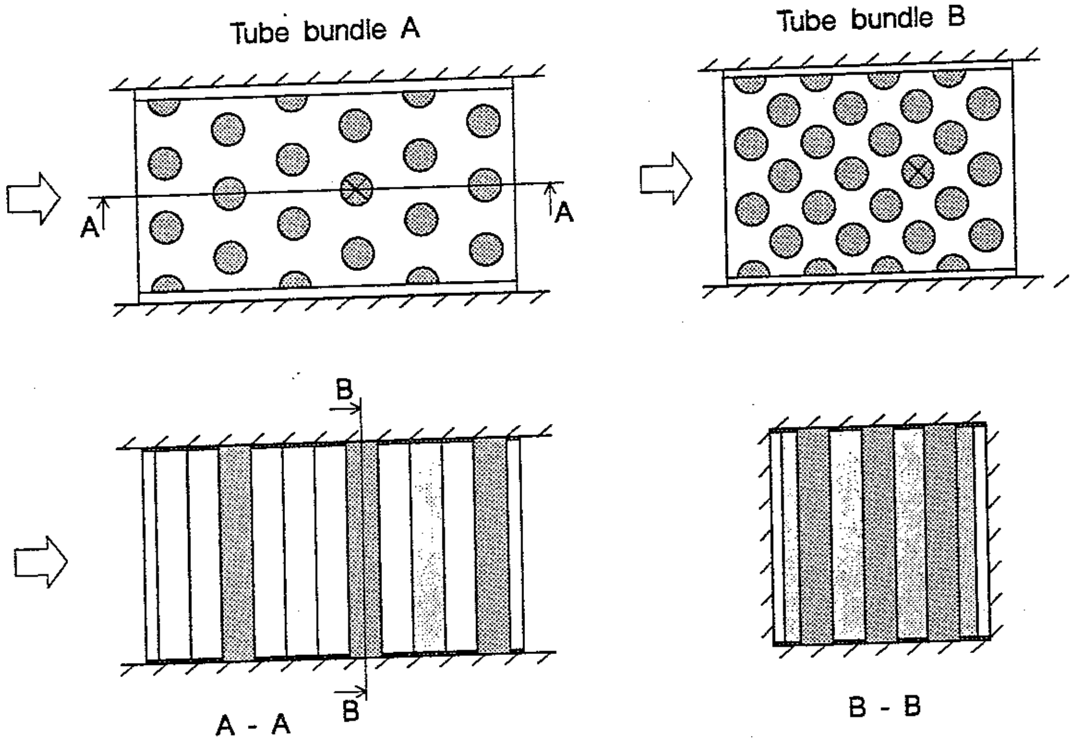

Figure 2.11: The tube bundle sections for the wind tunnel. The position of the measuring tube is shown with a ×.

2.4.2 Experimental equipment

The experiments have been carried out in air in a wind tunnel with a closed loop. The air is cooled to maintain a constant temperature at $20.0 \pm 0.1\,^{\circ}\mathrm{C}$. The test section of the wind tunnel has a length of 1.8 m and a nominal square cross section of $0.3\,\mathrm{m} \times 0.3\,\mathrm{m}$ at the inlet. The test section is slightly divergent to compensate for the growth of the boundary layer at the walls of the empty test section. Upstream of the inlet of the test section the air is accelerated through a contraction with an areal reduction of 12.94 : 1. The pressure drop over the contraction and the pressure difference between the inlet and the surroundings are measured with a Schiltknecht water micro manometer (estimated resolution of $0.02\,\mathrm{mm\,H_2O}$). These pressure differences are used to determine the mean velocity at the inlet, see appendix C.1. The mean velocity at the inlet is regulated by setting the velocity of rotation of the blower. Some minor fluctuations with a typical time scale of 10 seconds were observed for the mean velocity. When this is considered together with the uncertainty in the measurement of the pressure difference over the contraction, it is estimated that the mean velocity can be determined with an accuracy of 2 %.

The two tube bundle sections shown in figure 2.11 can be inserted into the test section of the wind tunnel. The longitudinal and transversal pitches are for tube bundle A: $a \times b = 2.00 \times 2.00$, and for tube bundle B: $a \times b = 2.07 \times 1.04$. In both cases the tube bundle is constructed in an open ended box. Commercial 45 mm steel tubes are mounted between two 5 mm acrylic plates. The sides of the box consist of 1 mm steel plates. Half tubes are mounted on the sides and there is a gap of a few milimeters between the steel plates and the sides of the

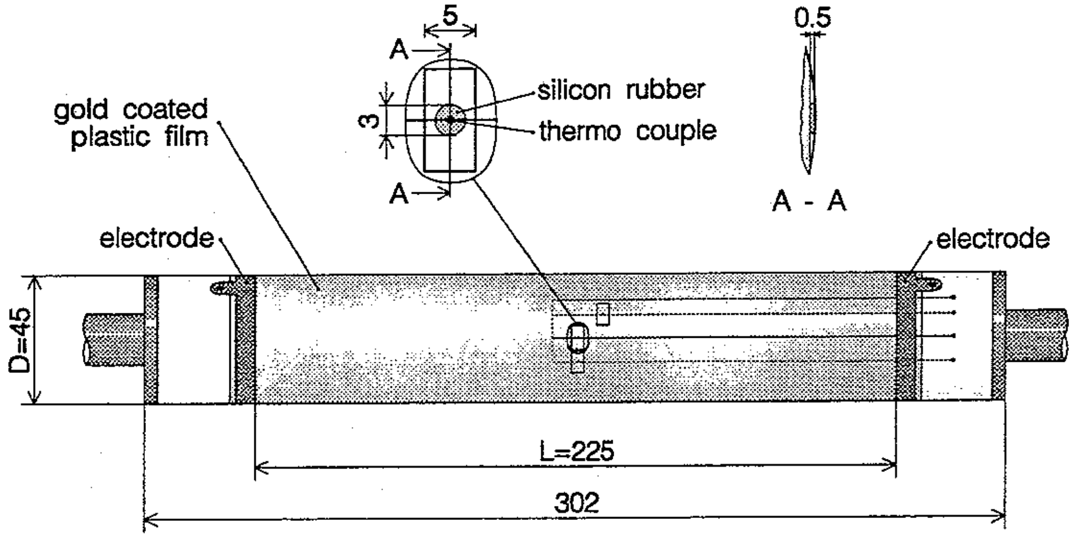

Figure 2.12: Measuring tube.

wind tunnels test section.

The tube bundles are prepared for measurements with a single hot-wire in the space between two tubes in the same row. For further details about these measurements, see appendix C.3.

The measuring tube is shown in figure 2.12. It consists of a gold coated plastic film mounted on a tube made of cast acryl and with a wall thickness of 5 mm. The plastic film is manufactured by Courtaulds Performance Films [21]. It has a thickness of 0.17 mm and is made of transparent PET (thermoplastic polyester). The gold coating has been sputter deposited in a continuous process onto the PET film and the film is supplied in a 330 mm wide roll. It has a nominal surface resistance of 25 Ω and the gold coating is thin enough to be somewhat transparent. It is estimated that the tangential heat conduction in the gold coating is less that 1 % of the tangential heat conduction in the PET film and the heat conduction in the gold coating is therefore ignored.

The uniformity of the surface resistance has been tested by measurements of several 20 mm by 20 mm pieces of the film. The variations in the central parts of the film were found to be within ±3% from the mean value. Near edges of the film the resistance is somewhat higher and therefore a piece from the central 40 % of the roll was used for the measuring tube. This piece were mounted by applying glue near two of the sides and then wrapping it around the tube. Plastic foil was then wrapped around the film and a rubber rod was used to apply pressure on the glued section of the film while the glue hardened. This insured that the film was fixed tight and smooth around the acryl tube. The outer diameter for the complete tube is $D = 45\,\text{mm} \pm 0.1\,\text{mm}$.

The electrical connections on the measuring tube are shown on figure 2.13. Two electrodes made of copper foil is glued to the ends of the gold coating using

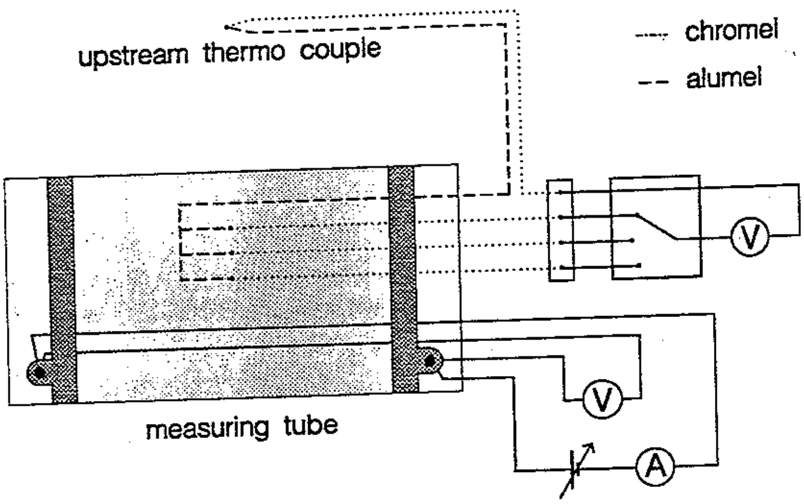

Figure 2.13: Diagram over the electrical connections for the measuring tube

a silver loaded paint to ensure good electrical contact. The length between the edges of the silver paint were $L = 225\,\mathrm{mm} \pm 0.5\,\mathrm{mm}$. A four-wire connection was used for the electrodes so that the current supply and the measuring of the voltage applied to the gold coating used separate wires. DC voltages up to 30 V were used.

Three thermocouples were glued to the back side of the PET film. The wires consist of respectively chromel and alumel and has a thickness of 75 μm. Small track were made in the acryl tube to give space for the wires. Inside the tube the wires are connected to thicker wires of the same material. The cold junction of the thermocouples is used as a sensor of the upstream temperature. In this way the voltage from the thermocouples are directly related to the temperature difference between the wall and the upstream air. The thermocouple wires are connected to copper wires using special connectors designed for thermocouples. Furthermore, all the connectors are in the same insulated volume in order to minimize local temperature differences. During preliminary measurements the three thermocouples gave almost the same results and the middle thermocouple was chosen for the final measurements reported here.

A manual switch box especially designed for small voltages makes it possible to connect each of the thermocouples to a voltmeter. The voltmeter (Solartron 7151 computing multimeter) has a resolution of 0.1 μV corresponding to 0.0025°C. A stepping motor is via a gear able to rotate the measuring tube in steps of 0.36°. All movements were ended with a rotation in the positive direction in order to avoid slack. The tube could be positioned with an accuracy better than 1°. Both the voltmeter and the controller of the stepmotor were controlled by a personal computer.

2.4.3 Data reduction

Although the measuring tube has been designed to give a constant heat flux from the surface, small variations occur and they will therefore be modelled in order to achieve the correct Nusselt number. The heat flux q''_{el} produced by the electrical heating of the gold coating is absorbed by three processes: Convection q''_{conv} to the air, conduction q''_{cond} from the gold coating into the measuring tube and radiation q''_{rad} from the surface to the surroundings. It is q''_{conv} that is used to determine the Nusselt number. The heat balance can be written

$$q''_{conv} = q''_{el} - q''_{cond} - q''_{rad}. \tag{2.1}$$

If the tube bundle is assumed to be a large, blackbody surface with the same temperature as the upstream air then the radiation can be expressed as $q''_{rad} = \epsilon_g \sigma (T_w^4 - T_0^4)$ where ϵ_g is the emissivity of the gold coated film and σ is Stefan-Boltzmann's constant. The conduction q''_{cond} can be found from a finite difference analysis. This is shown in appendix C.4.

If the electrical resistance of the gold coating were constant, q''_{el} could be found from the voltage V_{el} between the electrodes and the surface resistance. However, two effects will be taken into account:

- Nonuniformities in the gold coating causes a nonuniform surface resistance.
- The resistance depends on the temperature.

It is assumed that the local surface resistance can be found as $R'' = R''_\beta(1 + \beta(T - T_\beta))$ where β is the temperature coefficient of resistance and R''_β is the local surface resistance at T_β. Both R''_β and β can be found by calibration. The local electrically produced heat flux can then be assumed to be described with the equation

$$q''_{el} = \frac{(V_{el}/L)^2}{R''_\beta(1 + \beta(T - T_\beta))}. \tag{2.2}$$

The local heat transfer coefficient can now be found as $h = q''_{conv}/(\Delta T)$. Following [19] the temperature difference ΔT is the difference between the wall temperatures for respectively the heated tube and the unheated tube under the same flow conditions. In all the measurements these two temperatures were measured in two separate runs. Since the measured wall temperature represents an adiabatic wall temperature, it will differ slightly from the upstream temperature. During the measurements this difference did not exceed 0.15 °C at any position.

2.4.4 Measurements and results

Some simple measurements of the local mean velocities have been performed with a single hot-wire. They are described in appendix C.3. The purpose is to test whether the flow is in reasonable agreement with flow found by LDA measurements. The flow is highly turbulent and the results therefore not very accurate. The measurements indicate that the mean flow is quite similar to the flow found by LDA-measurements. The measurements of the local turbulence intensity are quite uncertain and no conclusions about this could be drawn.

All the calibrations have been performed with the measuring tube in the empty wind tunnel. First the thermocouples and the temperature coefficient of resistance were calibrated using different temperatures of the air in the wind tunnel. It is estimated that the uncertainty in the measurement of the temperatures is less than ±0.1 K. Then the local surface resistance was found by measurements of the heat transfer at the front stagnation point. This surface resistance differs less than 1 % of the value found from a measurement of the total resistance of the gold coating. The details of the calibrations are found in appendix C.2. Here it is also shown that the emissivity of the gold coating is quite low and therefore q''_{rad} is neglected in the determination of the Nusselt number.

Before each measurement the measuring tube was kept at constant heating and flow conditions for more than 30 minutes to ensure that the tube had reached a stable temperature. The measurement was started with the thermocouple at $\phi = 0°$ and then moved in steps of 1.8° until $\phi = 180°$. At each position at least 5 single measurements of the thermocouple voltage V_t were performed with intervals of 12 seconds. The voltmeter was constructed to return a voltage that was a result of an average of samples taken over approximately 9 seconds.

At each position the last 4 or in some cases the last 10 single measurements of V_t were used to estimate whether stable conditions were reached. This was done by calculating the difference between the average values of the first half and the last half of these measurements. If the difference was less than a temperature change corresponding to 0.025 K/minute, then the average value of the last half was assumed to be the wall temperature. It should be noted that after steady conditions were reached the fluctuations of the single measurements of V_t were significantly larger on the rear part of the cylinder compared to the front part.

Figure 2.14 shows two separate measurements of the wall temperature taken for the same row, the same tube bundle and the same heating and flow condition. The solid line is measurements taken with steps for ϕ going from 0° to 180° and the dashed line is measurements taken with steps going from 180° to 360°, but plotted so that the angle from the front stagnation point is in the interval 0°–180°. The figure shows that these temperature curves are quite close to each other, and that the Nusselt number therefore is symmetrical around the stagnation points. The figure also shows that there is no significant difference between measurements taken with steps that approached or moved away from the front stagnation point, respectively. This indicates that the check for steady conditions described in the previous paragraph is successful.

The final measurements consist of four measurements in tube bundle A and one measurement in tube bundle B. An overview of the measurements is shown in table 2.2. This table also shows the mean Nusselt number $\overline{Nu}$ (found as described in section 2.1.1) compared with the mean Nusselt number found

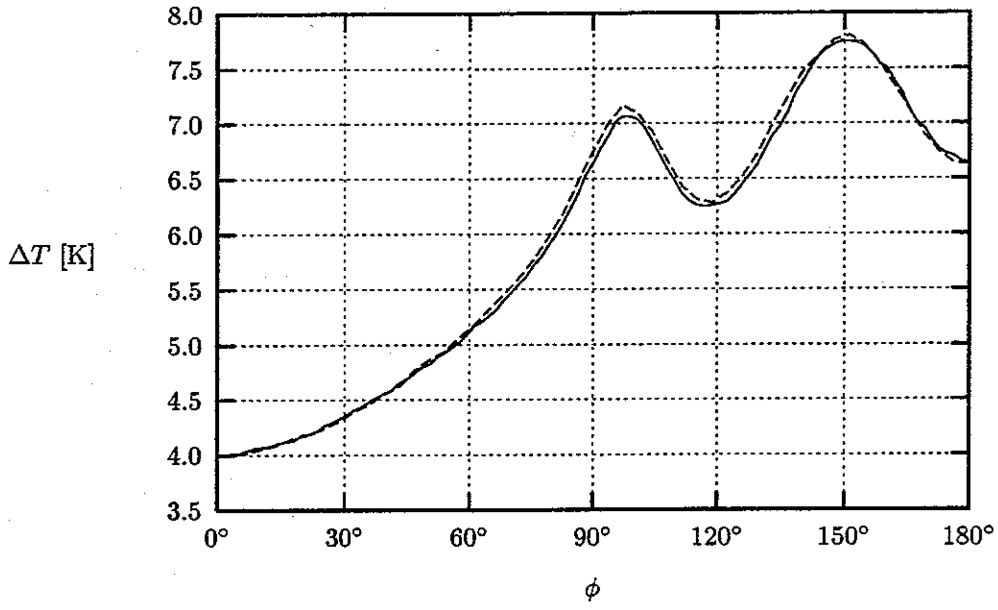

Figure 2.14: Local wall temperature (shown as ΔT) on 4. row in tube bundle A with $Re = 41\,500$. Solid line shows positive angles and dashed line negative angles, measured from the front stagnation point.

from the correlation [1]:

$$\overline{Nu} = 0.35 \left(\frac{a}{b}\right)^{0.2} Re^{0.60} Pr_{\infty}^{0.36} \left(\frac{Pr_{\infty}}{Pr_w}\right)^{0.25} . \tag{2.3}$$

This equation is supposed to be valid in the subcritical flow domain and for $(a/b) < 2$. It has been evaluated using data from table C.1 and assuming that the Prandtl number at the wall Pr_w is equal to the upstream Prandtl number Pr_{∞}. The difference between the measured $\overline{Nu}$ and $\overline{Nu}$ from (2.3) in percent of the latter is also shown in table 2.2. The difference is about 5 %, positive for tube bundle A and negative for tube bundle B. Another correlation that is expected to be valid for case 1 from table 2.2 is given by [22]: $\overline{Nu} = 0.229\, Re^{0.632}$. This amounts to $\overline{Nu} = 167.7$ which is quite close to the measured value. It is probably reasonable to assume that the accuracy of (2.3) is not much better that 5 % and the variations from the measured values are therefore acceptable.

In figure 2.15, plots of the Nusselt number for all the measurements are shown together, and in figure 2.16 two of the measurements are compared with a similar measurement by Baughn *et al* [19]. The local Nusselt number has been normalized by $Re^{0.6}$ since equation (2.3) indicates that the mean Nusselt number depends on the Reynolds number with an exponent of 0.60. All the curves for measurements in tube bundle A are quite close to each other and the correlation with $Re^{0.6}$ is therefore reasonable. A small difference in the shape of Nu are seen; for the high Reynolds numbers the Nusselt number is slightly lower near the front stagnation point and somewhat higher and with a smaller variation for $\phi = 80°–130°$.

case	tube bundle	row	*Re*	$\overline{Nu}$, exp.	$\overline{Nu}$ eq. (2.3)	difference
1	A	4.	34 100	168.5	162.1	3.9 %
2	A	4.	41 500	190.7	182.3	4.6 %
3	A	4.	70 000	263.7	248.6	6.1 %
4	A	4.	91 200	310.0	292.4	6.0 %
5	B	6.	40 000	192.8	203.9	-5.4 %

Table 2.2: Measurements of local heat transfer in tube bundles A ($a \times b = 2.00 \times 2.00$) and and B ($a \times b = 2.07 \times 1.04$).

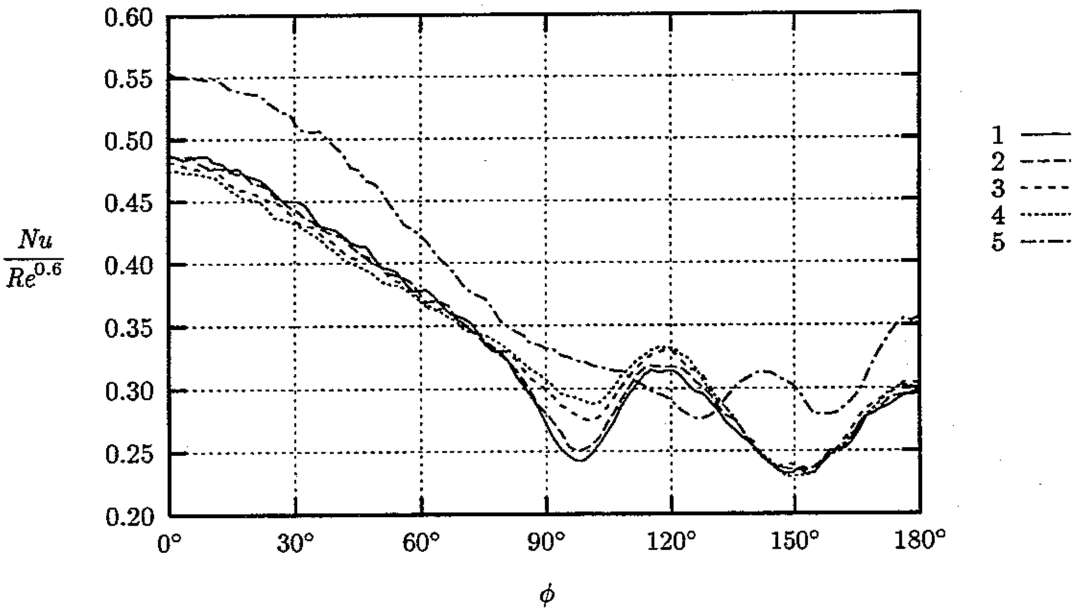

Figure 2.15: The measurements of the local Nusselt number. Refer to table 2.2 for key.

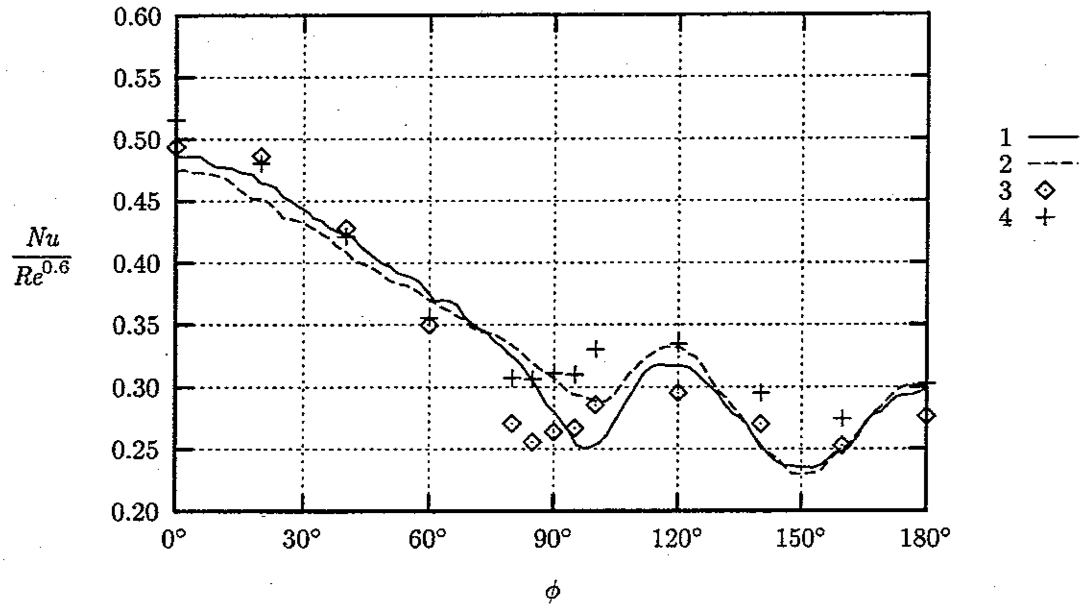

Figure 2.16: Local Nusselt number for case 1 (1) and case 4 (2) (see table 2.2) compared with measurements by [19] for *Re*=34 500 (3) and *Re*=84 600 (4).

The measurements of Baughn *et al* [19] are in fair agreement with the present measurements. The differences from the present measurements seem to be that the first minimum in *Nu* is located about 15° closer to the stagnation point and that *Nu* for ϕ greater that 90° has a higher level, but smaller variations. The measurements of Baughn *et al* were performed in the third row. The same difference between the local *Nu* in the third and the fourth row was found with measurements [5] using the same tube bundle and wind tunnel, but another measuring tube than in the present measurements. It is therefore plausible that this effect occurs because the flow and heat transfer is not fully developed at the third row even though the mean Nusselt numbers are quite close. It could therefore also be questioned whether the flow and heat transfer around the fourth row represents fully developed conditions. However, this can only be tested through measurements with more rows that the present. Unfortunately the LDA measurements in section 2.2 do not cover the first four tubes.

The measurements in tube bundle B (case 5) show that the level of *Nu* is higher than for tube bundle A. This is in agreement with the presence of the term $(a/b)^{0.2}$ in equation (2.3). Here the term is only valid for $\frac{1}{2} < (a/b) < 2$. As it is seen in table 2.2 the correlation (2.3) overpredicts $\overline{Nu}$ for tube bundle B while it underpredict $\overline{Nu}$ for tube bundle A. This might be because $(a/b) = 2$ for tube bundle B and the correlation might therefore be less reliable for this case. The local Nusselt number also has two minima, but these are located closer to the rear stagnation point and *Nu* here have a smaller variation than *Nu* has in tube bundle A. This corresponds well with the fact that the flow in tube bundle B has a smaller recirculating region than tube bundle A.

2.4.5 Conclusion

The local heat transfer from a tube in the middle of a tube bundle has been measured for two different bundle configurations. This is done for four different Reynolds numbers for the first tube bundle and for a single Reynolds number for the second one. The Reynolds numbers are chosen so that they are in the same range as typical industrial applications of tube bundles. The results have been shown to be in good agreement with experiments and correlations found in the literature.

Simple measurements with a single hot-wire indicates that the flow in the tube bundle used for LDA-measurements in section 2.2 and in the tube bundle used for heat transfer measurements are in good agreement with each other. Although many authors state that the heat transfer in a tube bundle is fully developed from the third or fourth row, it would be interesting, especially for tube bundle A, to verify this by measurements in the first four rows. The LDA-measurements indicate that there are enough tubes in each row to eliminate the significance of the side walls. This is, however, a subject that also could be interesting to investigate further. These problems are probably less important for the measurements in tube bundle B since the tubes here are more closely packed and since the measurements are performed in the sixth instead of the fourth row.

The most important source of uncertainty in the measurements of the local Nusselt number Nu probably comes from the determination of the wall temperature. It is estimated that the uncertainty of the Nu is about 3 % in most cases, but it might be a little higher at the extrema in Nu on the rear side of the tube. At these extrema, the internal heat conduction takes it largest values (typically 5 %) and this gives both larger uncertainties and a disturbance in the uniformity of the heat flux.

The design of the measuring tube could be further improved. Especially, it would be interesting to use a even more insulating material (e.g. some sort of foam) instead of acryl to support the gold coated plastic film. This would reduce internal conduction inside the tube and thereby improve both the uniformity of the convective heat flux and the accuracy of measurement of the heat transfer coefficient. A more accurate arrangement for the calibration of the thermocouples would also give some improvement of the overall accuracy.

2.5 Closure

The measurements reported in this chapter have been used to establish a database that is suited as a test case for validation of calculations of turbulent flows with heat transfer. Together with the LDA-measurements of Simonin and Bacouda [10] the present measurements form test cases for two quite different staggered tube bundles. These data can therefore be used to give a fair impression of how well calculations models are able to predict the flow and heat transfer in a staggered tube bundle.

There are several possibilities of improving the reliability and the accuracy of the measured data. However, it is judged that with the present state of the methods and models for predicting turbulent heat transfer in complex flow, the present set of data will be able to give a good impression of how well a calculation reproduces the actual flow and heat transfer in a tube bundle.

Chapter 3

Models for turbulent heat transfer

3.1 Introduction

With the rapid development of the performance of computers, numerical simulations of turbulent flow and heat transfer has the possibility of becoming more realistic. This chapter describes some of the most used turbulence models and boundary conditions with special attention to heat transfer. According to Launder [23] the local heat transfer coefficient, even for a gaseous flow where the molecular Prandtl number is close to unity, is determined to a very large extent by the variation of the effective diffusivity within the immediate vicinity of the wall. This indicates that the modelling of the near-wall turbulence is of special importance when considering heat transfer. The near-wall modelling will therefore be given special attension in this chapter. It will only consider incompressible flow.

3.2 Turbulence models

If the flow variables are assumed to be described by the Reynolds decomposition $f = F + f'$ where F is the mean value of f and f' is the fluctuation about the mean, one can obtain the time averaged continuity, momentum and scalar transport equations (for brevity fluctuating variables are from now on written without $'$):

$$\frac{\partial U_i}{\partial x_i} = 0, \tag{3.1}$$

$$\frac{\partial U_i}{\partial t} + U_j \frac{\partial U_i}{\partial x_j} = -\frac{1}{\rho}\frac{\partial P}{\partial x_i} + \frac{\partial}{\partial x_j}\left[\nu\left(\frac{\partial U_i}{\partial x_j} + \frac{\partial U_j}{\partial x_i}\right)\right] - \frac{\partial \overline{u_i u_j}}{\partial x_j} + F_i, \tag{3.2}$$

$$\frac{\partial \Theta}{\partial t} + U_i \frac{\partial \Theta}{\partial x_i} = \frac{\partial}{\partial x_j}\left[\Gamma \frac{\partial \Theta}{\partial x_j}\right] - \frac{\partial \overline{u_j \theta}}{\partial x_j} + S. \tag{3.3}$$

The equations are written in cartesian tensor notation. U_i and F_i are velocity and body force component along the coordinate direction i $(i = 1, 2, 3)$, P is the pressure, S a source term and Γ the molecular diffusivity of the transported scalar Θ. The equations contain the Reynolds stresses $\overline{u_i u_j}$ and the turbulent scalar flux $\overline{u_i\theta}$ as additional unknowns whose values have to be determined for the closure of system (3.1)-(3.3) to be possible. This requires a turbulence model.

There is a significant effort going on trying to improve and develop better turbulence models. Recently there has been several reviews concerning this topic. A few of these are [23-28]. This note will therefore only give a brief introduction to two common turbulence models: the k-ϵ model and the differential Reynolds Stress model (RSM).

3.2.1 The k-ϵ model

The k-ϵ model is based on the Boussinesq eddy viscosity concept. The main effect of turbulence is to increase transport of the conserved properties and dissipation effect with respect to the laminar state. In a laminar flow these processes are controlled by the viscosity of the fluid and one can therefore represent the effect of turbulence by introducing a turbulent viscosity ν_t. The Reynolds stresses can be rewritten as a function of the turbulent viscosity ν_t as:

$$\overline{u_i u_j} = -\nu_t\left(\frac{\partial U_i}{\partial x_j}+\frac{\partial U_j}{\partial x_i}\right)+\frac{2}{3}\delta_{ij}k \tag{3.4}$$

where

$$k=\frac{1}{2}\overline{u_i^2} \tag{3.5}$$

is the kinetic energy per unit mass associated with the turbulence. Similarly, an eddy diffusivity Γ_t must be defined for every transported scalar:

$$\overline{u_j\theta} = -\Gamma_t\left(\frac{\partial\Theta}{\partial x_j}\right). \tag{3.6}$$

Turbulent diffusivities of momentum and a scalar such as thermal energy can be related, by Reynolds analogy, using a turbulent Prandtl (or Schmidt) number:

$$\sigma_t=\frac{\nu_t}{\Gamma_t}. \tag{3.7}$$

In most models σ_t is assumed to be a constant, at least for fluids whose molecular Prandtl number is of the order of unity. Commonly used values in gases are 0.7 for free shear layers and 0.9 for wall bounded flows.

Introducing (3.4) and (3.6), the equations for the average transport of momentum and scalars become

$$\frac{\partial U_i}{\partial t}+U_j\frac{\partial U_i}{\partial x_j}=-\frac{1}{\rho}\frac{\partial P}{\partial x_i}+\frac{\partial}{\partial x_i}\left[(\nu+\nu_t)\left(\frac{\partial U_i}{\partial x_j}+\frac{\partial U_j}{\partial x_i}\right)\right]+F_i, \tag{3.8}$$

$$\frac{\partial\Theta}{\partial t}+U_i\frac{\partial\Theta}{\partial x_i}=\frac{\partial}{\partial x_j}\left[(\Gamma+\Gamma_t)\frac{\partial\Theta}{\partial x_j}\right]+S, \tag{3.9}$$

where the isotropic part of the Reynolds stress tensor $\frac{2}{3}\delta_{ij}k$ has been lumped together with the average pressure in the variable P. Eqs. (3.8) and (3.9) together with a relationship for ν_t form a closed system of equations which can be solved numerically. The k-ϵ model is one of the most popular and most tested models for this. It consists of two partial differential equations: one for the turbulent kinetic energy k and one for the kinetic energy dissipation ϵ. A transport equation for ϵ can be derived from the Navier-Stokes equations starting from the definition:

$$\epsilon = \nu \overline{\frac{\partial u_i}{\partial x_j}\frac{\partial u_i}{\partial x_j}}. \tag{3.10}$$

Due to the dominant role played by small scales, which have no characteristic length, but simply adjust themselves to the energy level of the larger eddies, the modelled form of ϵ heavily relies on "dimensional analysis and intuition" [24]. The standard form used in the k-ϵ model is:

$$\frac{\partial \epsilon}{\partial t}+U_i\frac{\partial \epsilon}{\partial x_i} = \nu_t c_1 \frac{\epsilon}{k}\left(\frac{\partial U_i}{\partial x_j}+\frac{\partial U_j}{\partial x_i}\right)\frac{\partial U_i}{\partial x_j}+\frac{\partial}{\partial x_k}\left(\frac{\nu_t}{\sigma_\epsilon}\frac{\partial \epsilon}{\partial x_k}\right)-c_2\frac{\epsilon^2}{k}+c_1\frac{\epsilon^2}{k}F_\epsilon, \tag{3.11}$$

$$\frac{\partial k}{\partial t}+U_i\frac{\partial k}{\partial x_i} = \nu_t\left(\frac{\partial U_i}{\partial x_j}+\frac{\partial U_j}{\partial x_i}\right)\frac{\partial U_i}{\partial x_j}+\frac{\partial}{\partial x_k}\left(\frac{\nu_t}{\sigma_k}\frac{\partial k}{\partial x_k}\right)-\epsilon+F_k. \tag{3.12}$$

F_k and F_ϵ are the body force, see Rodi [29] for further details. The turbulent viscosity is modelled as

$$\nu_t = c_\mu \frac{k^2}{\epsilon}. \tag{3.13}$$

The model contains five empirical constants which has to be adjusted through experimental data. For incompressible flows the commonly accepted values are [29]:

c_μ	c_1	c_2	σ_k	σ_ϵ
0.09	1.44	1.92	1.0	1.3

3.2.2 Reynolds Stress Model

Transport equations for $\overline{u_iu_j}$ and $\overline{u_i\theta}$ can be obtained from the instantaneous velocity and temperature by applying the Reynolds decomposition, taking the fluctuating part, multiplying by u_i and averaging. The resulting equation for $\overline{u_iu_j}$ is:

$$\begin{aligned}\frac{\partial \overline{u_iu_j}}{\partial t}+U_k\frac{\partial \overline{u_iu_j}}{\partial x_k} &= \\ &-\left[\overline{u_iu_k}\frac{\partial U_j}{\partial x_k}+\overline{u_ju_k}\frac{\partial U_i}{\partial x_k}\right]+\frac{1}{\rho}\left(\overline{u_i\frac{\partial p}{\partial x_j}}+\overline{u_j\frac{\partial p}{\partial x_i}}\right)+\nu\frac{\partial^2\overline{u_iu_j}}{\partial x_k^2} \\ &-\frac{\partial}{\partial x_k}\left(\overline{u_iu_ju_k}\right)-2\nu\overline{\frac{\partial u_i}{\partial x_k}\frac{\partial u_j}{\partial x_k}}+\left(\overline{f_iu_j}+\overline{f_ju_i}\right).\end{aligned} \tag{3.14}$$

The term in (3.14) involving the gradient of pressure fluctuations is usually decomposed into turbulent diffusion by pressure and the so-called pressure strain term:

$$\frac{1}{\rho}\left(\overline{u_i\frac{\partial p}{\partial x_j}}+\overline{u_j\frac{\partial p}{\partial x_i}}\right) = -\frac{\partial}{\partial x_k}\left(\frac{\overline{u_jp}}{\rho}\delta_{ik}+\frac{\overline{u_ip}}{\rho}\delta_{jk}\right)+\overline{\frac{p}{\rho}\left(\frac{\partial u_i}{\partial x_j}+\frac{\partial u_j}{\partial x_i}\right)}, \tag{3.15}$$

and (3.14) is then written as

$$
\begin{aligned}
&\frac{\partial \overline{u_i u_j}}{\partial t} + \underbrace{U_k \frac{\partial \overline{u_i u_j}}{\partial x_k}}_{C_{ij}} = \\
&\quad \underbrace{-\left[\overline{u_i u_k}\frac{\partial U_j}{\partial x_k} + \overline{u_j u_k}\frac{\partial U_i}{\partial x_k}\right]}_{-P_{ij}} + \underbrace{\overline{\frac{p}{\rho}\left(\frac{\partial u_i}{\partial x_j} + \frac{\partial u_j}{\partial x_i}\right)}}_{\phi_{ij}} + \underbrace{\nu \frac{\partial^2 \overline{u_i u_j}}{\partial x_k^2}}_{D^{\nu}_{ij}} \\
&\quad \underbrace{-\frac{\partial}{\partial x_k}\left[\overline{u_i u_j u_k} + \frac{\overline{u_j p}}{\rho}\delta_{ik} + \frac{\overline{u_i p}}{\rho}\delta_{jk}\right]}_{-D^t_{ij}} \underbrace{-2\nu \overline{\frac{\partial u_i}{\partial x_k}\frac{\partial u_j}{\partial x_k}}}_{-\epsilon_{ij}} + \underbrace{\left(\overline{f_i u_j} + \overline{f_j u_i}\right)}_{F_{ij}}
\end{aligned}
\tag{3.16}
$$

The resulting equation for $\overline{u_i\theta}$ can be found using a similar procedure:

$$
\begin{aligned}
&\frac{\partial \overline{u_i \theta}}{\partial t} + \underbrace{U_k \frac{\partial \overline{u_i \theta}}{\partial x_k}}_{C_{i\theta}} = \\
&\quad \underbrace{-\overline{u_i u_k}\frac{\partial \Theta}{\partial x_k}}_{-P_{i\theta 1}} \underbrace{-\overline{u_k \theta}\frac{\partial U_i}{\partial x_k}}_{-P_{i\theta 2}} + \underbrace{\overline{\frac{p}{\rho}\left(\frac{\partial \theta}{\partial x_i}\right)}}_{\phi_{i\theta}} + \underbrace{\frac{\partial}{\partial x_k}\left[\Gamma \overline{u_i \frac{\partial \theta}{\partial x_k}} + \nu \overline{\theta \frac{\partial u_i}{\partial x_k}}\right]}_{D^{\nu}_{i\theta}} \\
&\quad \underbrace{-\frac{\partial}{\partial x_k}\left[\overline{u_i u_k \theta} + \frac{\overline{p\theta}}{\rho}\delta_{ik}\right]}_{-D^t_{i\theta}} \underbrace{-2\left(\Gamma + \nu\right)\overline{\frac{\partial \theta}{\partial x_k}\frac{\partial u_i}{\partial x_k}}}_{-\epsilon_{i\theta}} + \underbrace{\overline{f_i \theta}}_{F_{i\theta}} .
\end{aligned}
\tag{3.17}
$$

The symbolic terms in (3.16) and (3.17) have the following physical interpretation: C_{ij} and $C_{i\theta}$ is the convective transport, P_{ij} and $P_{i\theta}$ is the production, ϕ_{ij} and $\phi_{i\theta}$ is the pressure strain, D^{ν}_{ij} and $D^{\nu}_{i\theta}$ is the viscous transport, D^t_{ij} and $D^t_{i\theta}$ is the turbulent transport, ϵ_{ij} and $\epsilon_{i\theta}$ is the dissipation and F_{ij} and $F_{i\theta}$ is body forces (e.g. buoyancy force). In e.g. buoyant situations an additional equation for the scalar fluctuation $\overline{\theta^2}$ is necessary to compute the body force $F_{i\theta}$. See Rodi [29] for further details.

The pressure-strain, the diffusion and the dissipation terms of (3.16) and (3.17) contain correlations for which model approximation must be introduced if the system is to be closed at the level of the stress-equation. This is called second-moment closure. The most used closure is called the Basic Closure. It is essentially the form developed by Launder, Reece and Rodi [30]. It assumes a high Reynolds number and therefore the viscous transport D^{ν}_{ij} and $D^{\nu}_{i\theta}$ is neglected. It consists of approximations for the unknown terms and an additional equation for ϵ.

The first unknown term is the turbulent diffusion D^t_{ij}. It contains an additional unknown namely the triple correlation $\overline{u_i u_j u_k}$. Hanjalic and Launder [31] has obtained an expression for this term by a severe simplification of the exact transport equation for $\overline{u_i u_j u_k}$:

$$-\overline{u_i u_j u_k} = c_s' \frac{k}{\epsilon}\left[\overline{u_i u_l}\frac{\partial \overline{u_j u_k}}{\partial x_l} + \overline{u_j u_l}\frac{\partial \overline{u_k u_i}}{\partial x_l} + \overline{u_k u_l}\frac{\partial \overline{u_i u_j}}{\partial x_l}\right], \tag{3.18}$$

where the constant is estimated to $c_s' = 0.11$. In the Basic Closure a simple gradient-diffusion hypothesis (3.19) proposed by Daly and Harlow [32] is often used instead of eq. (3.18) . The pressure-induced diffusion in D_{ij}^t is usually neglected although there seems no direct evidence to retain or neglect the assumption [30].

The form found by Gibson and Launder [33] is often referred to as the Basic Closure. Following [25] it can be summarized as:

Reynolds stress equations:

$$\begin{aligned} D_{ij}^t &= c_s \frac{\partial}{\partial x_k}\left[\overline{u_k u_l}\frac{k}{\epsilon}\frac{\partial \overline{u_i u_j}}{\partial x_l}\right], && (3.19)\\ \epsilon_{ij} &= -\frac{2}{3}\delta_{ij}\epsilon, && (3.20)\\ \phi_{ij} &= \phi_{ij1} + \phi_{ij2} + \phi_{ij3} + \phi_{ijw} && (3.21) \end{aligned}$$

where ϕ_{ijw} is used only in wall flows. The terms ϕ_{ij1}, ϕ_{ij2} and ϕ_{ijw} are called return-to-isotropi, rapid distortion and the wall reflection term. The terms in eq. (3.21) are modelled the following way:

$$\begin{aligned} \phi_{ij1} &= -c_1\frac{\epsilon}{k}(\overline{u_i u_j} - \frac{1}{3}\delta_{ij}\overline{u_k u_k}), && (3.22)\\ \phi_{ij2} &= -c_2\left[(P_{ij} - \frac{1}{3}\delta_{ij}P_{kk}) - (C_{ij} - \frac{1}{3}\delta_{ij}C_{kk})\right], && (3.23)\\ \phi_{ij3} &= -c_3(F_{ij} - \frac{1}{3}\delta_{ij}F_{kk}), && (3.24) \end{aligned}$$

$$\begin{aligned} \phi_{ijw} = \{ & c_1'\frac{\epsilon}{k}(\overline{u_k u_m} n_k n_m \delta_{ij} - \frac{3}{2}\overline{u_k u_i} n_k n_j - \frac{3}{2}\overline{u_k u_j} n_k n_i)\\ + \ & c_2'(\phi_{km2} n_k n_m \delta_{ij} - \frac{3}{2}\phi_{ik2} n_k n_j - \frac{3}{2}\phi_{kj2} n_k n_i)\\ - \ & c_3'(\phi_{km3} n_k n_m \delta_{ij} - \frac{3}{2}\phi_{ik3} n_k n_i - \frac{3}{2}\phi_{kj3} n_k n_i)\}\frac{k^{3/2}}{c_l \epsilon x_n}. && (3.25) \end{aligned}$$

where n_k is a unit vector normal to the wall and x_n is the distance from the wall. The term $(C_{ij} - \frac{1}{3}\delta_{ij}C_{kk})$ in eq. (3.23) is not always included. It is strictly essential to render the model independent of the observer, although it is of little practical consequence except in strongly swirling flows [34]. In the wall reflection term ϕ_{ijw} the factor $k^{3/2}/(c_l \epsilon x_n)$ acts to reduce the effect of ϕ_{ijw} with increasing distance from a wall. The constant c_l is equal to $\kappa / c_\mu^{3/4}$.

ϵ - equation:

$$\frac{\partial \epsilon}{\partial t} + U_i \frac{\partial \epsilon}{\partial x_i} = c_\epsilon \frac{\partial}{\partial x_k}\left(\overline{u_k u_l}\frac{k}{\epsilon}\frac{\partial \epsilon}{\partial x_l}\right) + \frac{1}{2}c_{\epsilon 1}\left(P_{kk} + F_{kk}\right)\frac{\epsilon}{k} - c_{\epsilon 2}\frac{\epsilon^2}{k}. \tag{3.26}$$

The coefficients in (3.19) to (3.26) are:

c_s	c_1	c_2	c_3	c_1'	c_2'	c_3'	c_l	c_ϵ	$c_{\epsilon 1}$	$c_{\epsilon 2}$
0.22	1.8	0.6	c_2	0.5	0.3	0	2.5	0.15	1.44	1.92

Scalar-Flux Equations:

$$\begin{aligned} D_{i\theta}^t &= c_\theta \frac{\partial}{\partial x_k}\left[\overline{u_k u_l}\frac{k}{\epsilon}\frac{\partial \overline{u_i\theta}}{\partial x_l}\right], && (3.27)\\ \epsilon_{i\theta} &= 0 && (3.28)\\ \phi_{i\theta} &= \phi_{i\theta 1} + \phi_{i\theta 2} + \phi_{i\theta 3} + \phi_{i\theta w}. && (3.29) \end{aligned}$$

The terms in (3.29) are modelled the following way ($\phi_{i\theta w}$ wall flows only):

$$\begin{aligned} \phi_{i\theta 1} &= -c_{\theta 1}\frac{\epsilon}{k}\overline{u_i\theta}, && (3.30)\\ \phi_{i\theta 2} &= -c_{\theta 2}P_{i\theta 2}, && (3.31)\\ \phi_{i\theta 3} &= -c_{\theta 3}F_{i\theta}, && (3.32) \end{aligned}$$

$$\phi_{i\theta w} = \{c_{\theta 1}'\frac{\epsilon}{k}\overline{u_k\theta}n_k n_i + c_{\theta 2}'\phi_{k\theta 2}n_k n_i + c_{\theta 3}'\phi_{k\theta 3}n_k n_i\}\frac{k^{3/2}}{c_l \epsilon x_n}. \qquad (3.33)$$

The coefficients in (3.27) to (3.33) are:

c_θ	$c_{\theta 1}$	$c_{\theta 2}$	$c_{\theta 3}$	$c_{\theta 1}'$	$c_{\theta 2}'$	$c_{\theta 3}'$
0.15	2.9	0.4	0.4	0.25	0	0

3.2.3 Algebraic Reynolds stress model

The Basic Closure in the previous section consists of 11 partial differential equations (or 15 if a scalar equation is included). Even with modern numerical schemes and computers the model is quite expensive. There has therefore been made attempts to simplify the model. It is possible to make a model based on the equations for k and ϵ where the Reynolds stresses $\overline{u_i u_j}$ are found by algebraic relations. These models are often referred to as the algebraic stress models (ASM).

An equation for k that is based on the Reynolds stresses $\overline{u_i u_j}$ instead of the eddy viscosity ν_t can be made by taking the trace of the $\overline{u_i u_j}$-equation (3.16) with its modelled terms for the three normal stresses ($\overline{u_i^2}$, $i = 1, 2, 3$):

$$\underbrace{\frac{\partial k}{\partial t} + U_i\frac{\partial k}{\partial x_i}}_{C_k} = \underbrace{c_s\frac{\partial}{\partial x_k}\left(\frac{k}{\epsilon}\overline{u_k u_l}\frac{\partial k}{\partial x_l}\right)}_{D_k} \underbrace{- \overline{u_k u_l}\frac{\partial U_k}{\partial x_l}}_{-P_k} - \epsilon + F_k, \qquad (3.34)$$

where C_k is the convective transport, D_k is the diffusion and P_k is the production of k. P_k is related to the corresponding term in the $\overline{u_i u_j}$-equation P_{ij}, by $P_k = \frac{1}{2}\, P_{ii}$.

Derivatives of $\overline{u_i u_j}$ appear only in four terms in the $\overline{u_i u_j}$-equation (3.16): the rate of change $\partial\overline{u_i u_j}/\partial t$, the convective transport C_{ij} and the diffusive transport terms D_{ij}^ν and D_{ij}^t. Rodi [35] has proposed an algebraic Reynolds stress model based on the assumption that the transport of $\overline{u_i u_j}$ is proportional to the transport of k (with the factor $\overline{u_iu_j}/k$). The four terms containing gradients of $\overline{u_iu_j}$ can then be modelled by eq. (3.34):

$$\frac{\partial \overline{u_iu_j}}{\partial t} + C_{ij} - D^{\nu}_{ij} - D^{t}_{ij} = \frac{\overline{u_iu_j}}{k}\left(\frac{\partial k}{\partial t} + C_k - D_k\right) = \frac{\overline{u_iu_j}}{k}\left(-P_k - \epsilon + F_k\right). \tag{3.35}$$

This is a good approximation when the temporal and spatial change of $\overline{u_iu_j}/k$ is small compared with the change of $\overline{u_iu_j}$ itself. By substituting eq. (3.35) into the $\overline{u_iu_j}$-equation with the modelled term for ϵ_{ij} and ϕ_{ij} (with $\phi_{ij2} = -c_2(P_{ij} - \frac{1}{3}\delta_{ij}P_{kk})$) the Reynolds stresses are found as

$$\frac{\overline{u_iu_j}}{k} = \frac{2}{3}\delta_{ij} + \frac{(1-c_2)(P_{ij} - \frac{2}{3}\delta_{ij}P_k) + (1-c_3)(F_{ij} - \frac{2}{3}\delta_{ij}F_k) + \phi_{ijw}}{P_k + F_k + (c_1 - 1)\epsilon}. \tag{3.36}$$

An algebraic relation for $\overline{u_i\theta}$ can made using the same procedure, see [29]:

$$\frac{\overline{u_i\theta}}{k} = \frac{2\left[\overline{u_iu_l}\frac{\partial \Theta}{\partial x_l} + (1 - c_{\theta 2})\left(\overline{u_l\theta}\frac{\partial U_i}{\partial x_l} + F_{i\theta}\right) + \phi_{i\theta w}\right]}{P_k + F_k + (2C_{1\theta} - 1)\epsilon}. \tag{3.37}$$

In e.g. buoyant situations, an additional equation for the scalar fluctuation $\overline{\theta^2}$ is necessary to compute the body force $F_{i\theta}$. See Rodi [29] for further details.

Eqs. (3.36) and (3.37) together with the equations for k (3.34) and ϵ (3.26) form the Algebraic Reynolds stress model. It makes it possible to take into account some of the anisotropy of the turbulence with a computational effort not much larger than for the standard k-ϵ model. It also offers a better treatment of buoyancy.

3.3 Wall laws

The wall boundary conditions have to be given special attention for the turbulence models presented in the previous section. There are two problems in the near-wall region:

1. Gradients are very steep in the near-wall region. A fine grid is therefore needed and this will make the computation more expensive.

2. The presented turbulence models are only valid for high Reynolds numbers. They are therefore not applicable in the near-wall region.

The common solution to these problems is to use the logarithmic wall laws described in this section.

It is assumed that the flow is approximately two-dimensional near the wall. The coordinate system used here has the first axis parallel to the wall pointing in the direction of the local velocity and the second axis normal to the wall. In general, the boundary condition will have to be transformed into the coordinate system used in the calculations. This is fairly simple for a vector like the velocity, but more complicated for a tensor like the Reynolds stresses $\overline{u_iu_j}$. The transformation for $\overline{u_iu_j}$ is shown in appendix A.1

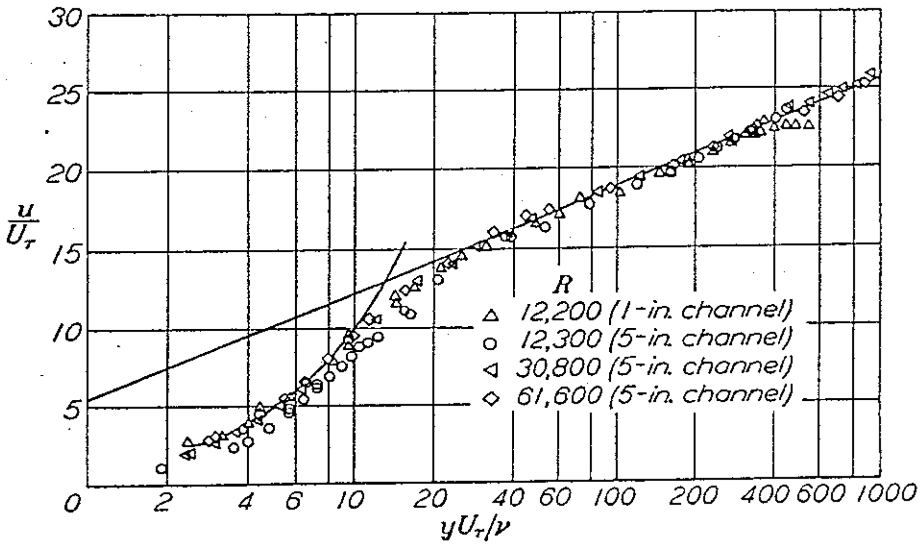

Figure 3.1: Measurements of velocity U^+ vs. distance from the wall y^+ in a 2-dimensional channel flow (after Laufer [36])

3.3.1 Standard logarithmic wall law

Experimental results (eg. a fully developed channel flow, see figure 3.1) show that the velocity near a wall can be described by the equation:

$$U^+ = \frac{1}{\kappa} \ln E y^+ \tag{3.38}$$

where $\kappa = 0.4187$ and $E = 9.8$. The equation is valid for $y^+ \geq 30$. The wall coordinates, U^+ and y^+, are defined using the wall friction velocity $U_\tau = \sqrt{\tau_w/\rho}$:

$$U^+ = \frac{U}{U_\tau} = \frac{U}{\sqrt{\tau_w/\rho}}, \tag{3.39}$$

$$y^+ = \frac{yU_\tau}{\nu} = \frac{y\sqrt{\tau_w/\rho}}{\nu}. \tag{3.40}$$

For scalars, a similar wall coordinate Θ^+ can be defined:

$$\Theta^+ = \frac{\rho c_p \sqrt{\tau_w/\rho}(\Theta_w - \Theta)}{q''_w}, \tag{3.41}$$

and Θ^+ can be expressed as a function of U^+

$$\Theta^+ = \sigma_\theta (U^+ + P) \tag{3.42}$$

where $\sigma_\theta = 0.91$ and P is an empirical function (the so-called "pee-function") found by Jayetilleke [37]

$$P = 9.24 \left[\left(\frac{\sigma}{\sigma_\theta} \right)^{3/4} - 1 \right] \left[1 + 0.28 \exp \left(-0.007 \frac{\sigma}{\sigma_\theta} \right) \right]. \tag{3.43}$$

In (3.43) σ is the Prandtl number for the general scalar Θ.

In general, the shear stress at the wall τ_w is not known. However it can be estimated by assuming that the near wall layer is a simple shear layer in local equilibrium, where the production of k is equal to the dissipation ϵ. A near parallel flow approximation of (3.12) then reduces to:

$$\nu_t \left(\frac{\partial U}{\partial y}\right)^2 = \epsilon. \tag{3.44}$$

Using (3.13) and approximating the wall shear stress by the shear stress near the wall ($\tau_w \simeq \tau_{xy} = \rho\nu_t \partial U/\partial y$), τ_w can be found as

$$\tau_w = {c_\mu}^{1/2} \rho k. \tag{3.45}$$

In some flows τ_w is known and eq. (3.45) can be used as a boundary condition for k. When τ_w is not known a boundary condition for k must be found by other means. Sections 3.3.3 will describe an alternative boundary condition for k.

Eq. (3.44) can also be used to estimate ϵ in the near wall region. By inserting eq. (3.13) in eq. (3.44), rearranging and using $(\partial U/\partial y)$ found from eq. (3.38), ϵ can be expressed as

$$\epsilon = \frac{{c_\mu}^{3/4} k^{3/2}}{\kappa y}. \tag{3.46}$$

The wall laws described in this section are sufficient in simple flows such as pipe flow. In more complex flows there will be problems. An example following from the definition of θ^+ in eq. (3.41) is that the Nusselt number falls to zero at separation and reattachment points, while experiments often show the maximum levels of heat transfer at reattachment. A remedy for this problem will be shown in the next section.

3.3.2 Modified Wall Coordinates

As clearly seen in figure 3.1 there is a region close to the wall ($y^+ < 11$) where eq. (3.38) is not valid. In this region viscous forces begin to dominate the flow and here another approximation can be used:

$$U^+ = y^+. \tag{3.47}$$

The influence of this region can be approximated by assuming that the flow changes abruptly from fully turbulent to viscous behaviour at a distance $y_v^+ = 11$. U^+ should then be found from (3.47) in the viscous region and from (3.38) in the turbulent region.

A set of modified wall coordinates that are more capable of handling complex flow can be defined following Chieng [38] and Launder [23]. The modified coordinates are based on the Prandtl-Kolmogorov formula from the one-equation turbulence model:

$$\nu_t = c_\mu k^{1/2} l. \tag{3.48}$$

Near the wall, the length scale l can be assumed to increase linearly with the distance from the wall, $l = c_l y$. Eq. (3.48) then takes the form $\nu_t = c_\mu c_l k^{1/2} y$. By approximating τ_w with the shear stress τ_{xy} in the turbulent region near the wall we get

$$\tau_w \simeq \tau_{xy} = \rho \kappa^* k^{1/2} y \frac{\partial U}{\partial y} \tag{3.49}$$

where $\kappa^* = c_\mu c_l$ is approximately 0.22 [23]. In a fully turbulent flow of constant stress, the turbulent kinetic energy is also essentially uniform so eq. (3.49) may be integrated to give a logarithmic law similar to (3.38), but in the new modified wall coordinates

$$U^* \equiv \frac{U k^{1/2}}{(\tau_w / \rho)} = \frac{1}{\kappa^*} \ln E^* y^*. \tag{3.50}$$

E^* and y^* are found by assuming that the transition from fully turbulent to laminar behaviour occurs abruptly at the distance y_v from the wall. The velocity–distance relation at y_v must therefore satisfy both eq. (3.50) and the viscous relation $U = (\tau_w / \mu) y$ and from this y^* and E^* can be found to be

$$y^* \equiv \frac{y k_v^{1/2}}{\nu}, \tag{3.51}$$

$$E^* \equiv \frac{\exp(\kappa^* y_v)}{y_v^*}. \tag{3.52}$$

In (3.51) k_p can be used as an approximation of k_v [23].

A similar expression in modified coordinates can be made for a scalar Θ. If the turbulent scalar diffusivity is assumed to be σ_θ^{-1} times the turbulent kinematic viscosity then in a layer with uniform scalar flux the flux can be found using eq. (3.49)

$$\frac{q''_w}{\rho c_p} = \frac{\kappa^*}{\sigma_\theta} k^{1/2} y \frac{\partial}{\partial y} (\Theta_w - \Theta), \tag{3.53}$$

and this can be integrated to

$$\Theta^* \equiv \frac{\rho c_p (\Theta_w - \Theta) k^{1/2}}{q''_w} = \frac{\sigma_\theta}{\kappa^*} \ln \tilde{E}^* y^*, \tag{3.54}$$

where $\tilde{E}^* \equiv \exp(\kappa^* y_c \sigma / \sigma_\theta) / y_c^*$. Eq. (3.54) can be rewritten using a modified "pee-function"

$$\Theta^* = \sigma_\theta (U^* + P^*). \tag{3.55}$$

Eqs. (3.50) and (3.55) are analogous to eqs. (3.38) and (3.42). In a equilibrium layer with constant stress they should give identical results and by using eq. (3.45) it follows that $U^* = c_\mu^{-1/4} U^+$, $y^* = c_\mu^{-1/4} y^+$, $\kappa^* = c_\mu^{-1/4} \kappa$ and $P^* = c_\mu^{-1/4} P^+$. From these relations the constants become $y_v^* = 20.4$ and $E^* = 5.4$.

The two formulations (U^+ and U^*) give identical behaviour in near-wall layer with constant stress. The rationale behind the U^* coordinates is that

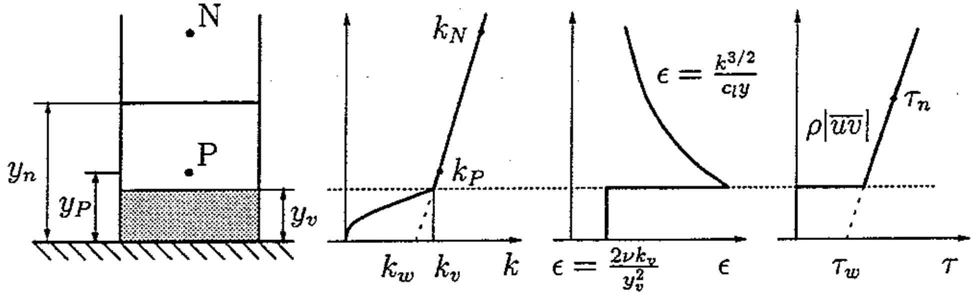

Figure 3.2: Assumed distribution of variables across near-wall control volume

they should give forms that better extrapolate to conditions far from equilibrium: where the stress varies rapidly with distance from the wall, and where generation and dissipation rates of turbulence energy are not in balance. An example is that the use of U^* gives, for a fixed y^*, a wall shear stress that is directly proportional to the near-wall velocity, and the wall shear stress will simply change sign if the velocity does. Another example is the use of Θ^* does not require the Nusselt number to vanish if the wall shear stress τ_w is zero provided k_v is not zero. In the examples there is a much more plausible behaviour near separation and reattachment than that implied by the traditional law of the wall.

3.3.3 Boundary conditions for k

If the wall shear stress τ_w is known and the near wall layer can be approximated by a shear layer in local equilibrium, k can be found by eq. (3.45) as $k = \tau_w/(\rho c_\mu^{1/2})$. However, in general τ_w is not known and k is usually found by solving the equation for k. Using the symbolic form presented in eq. (3.34) this equation takes the form (without source terms from body forces):

$$\frac{\partial k}{\partial t} + C_k = D_k + P_k - \epsilon. \tag{3.56}$$

To solve eq. (3.56) a boundary condition is needed. If the viscous sublayer can be assumed to be small a simple boundary condition is a zero gradient of k at the wall: $\partial k/\partial y = 0$. In flows where the viscous sublayer is a significant part of the near wall cell, a more thorough treatment of the terms in eq. (3.56) is required. This is illustrated in figure 3.2.

As with the velocity, the near-wall control volume is imagined to have a viscous sublayer up to the distance y_v from the wall where there is an abrupt change to a fully turbulent region. In the turbulent region the viscous transport can be ignored and in the viscous sublayer the turbulent stress is negligible. The kinetic energy k is not negligible in the viscous sublayer and experiments suggest a parabolic variation [23]:

$$k = k_v(y/y_v)^2. \tag{3.57}$$

To solve eq. (3.56) the mean contribution of the right hand terms has to be found. Following eq. (3.57) the diffusion of k is zero at the wall and therefore the net diffusive flow to the control volume is that entering the north face. To find the mean value of ϵ the two regions have to be integrated separately. In a sublayer it may be shown [39] that

$$\epsilon = 2\nu \left(\frac{\partial k^{1/2}}{\partial y} \right)^2 . \tag{3.58}$$

Substituting for k from eq. (3.57), ϵ takes the constant value in the viscous sublayer:

$$\epsilon = \frac{2\nu k_v}{y_v^2}. \tag{3.59}$$

In the turbulent region ϵ can be determined by eq. (3.46). Integrating over the control volume the mean value $\overline{\epsilon}$ is found as

$$\overline{\epsilon} \equiv \frac{1}{y_n} \int_0^{y_n} \epsilon dy = \frac{2\nu k_v}{y_v y_n} + \frac{c_\mu^{3/4} k^{3/2}}{\kappa y_n} \ln \left(\frac{y_n}{y_v} \right). \tag{3.60}$$

The mean turbulence energy generation $\overline{P}$ is also found by integrating over the control volume. The turbulent shear stress is assumed to be uniform and equal to τ_w in the turbulent region and zero in the viscous sublayer:

$$\overline{P} = \frac{1}{y_n} \int_{y_v}^{y_n} \frac{\tau_w}{\rho} \frac{\partial U}{\partial y} dy = \frac{\tau_w}{\rho} \frac{U_n - U_v}{y_n} \tag{3.61}$$

and substituting U found from eq. (3.50), $\overline{P}$ is found as

$$\overline{P} = \frac{(\tau_w/\rho)^2}{\kappa^* y_n k^{1/2}} \ln \left(\frac{y_n}{y_v} \right) \tag{3.62}$$

In the evaluation of (3.60) and (3.62) k and τ_w are assumed to be uniform over the turbulent region and the linear variation showed in figure 3.2 is thus not used. However, the sensitivity of the equations to moderate variations in k and $\overline{u_1 u_2}$ is not great and, moreover, k and $\overline{u_1 u_2}$ usually vary in the same sense. Chieng and Launder [38] evaluated eqs. (3.60) and (3.62) assuming a linear variation of energy and shear stress and this lead to a very cumbersome formula for $\overline{\epsilon}$.

It is easily seen that at local equilibrium (where $(\tau_w/\rho) = c_\mu^{1/2} k$) $\overline{P}$ equals $\overline{\epsilon}$ if the viscous sublayer is neglected. Near separation and reattachment τ_w falls to zero faster than k and in such regions $\overline{P}$ will be considerably less than $\overline{\epsilon}$. In complex flow eqs. (3.60) and (3.62) therefore give better results than wall laws based only on the local equilibrium assumption.

3.3.4 Boundary conditions for $\overline{u_i u_j}$ and $\overline{u_i \theta}$

As with the boundary condition for k, a simple boundary condition for $\overline{u_i u_j}$ and $\overline{u_i \theta}$ is a zero gradient at the wall, e.g. $\partial \overline{u_i u_j} / \partial y = 0$. This boundary condition is valid for any coordinate system and there is therefore no complication arising from coordinate transformations. The boundary condition assumes the viscous sublayer to be small. In flows where the viscous sublayer is a significant part of the near wall cell, an analysis like the one presented in the previous section could be made.

In a near-wall approximation the Reynolds stress $\overline{u_1u_2}$ can be approximated as $\overline{u_1u_2} \approx \tau_w/\rho$. This can be combined with the zero gradient condition for $\overline{u_1u_1}$, $\overline{u_2u_2}$, $\overline{u_3u_3}$ and $\overline{u_i\theta}$ and by setting $\overline{u_1u_3} = \overline{u_2u_3} = 0$. This boundary condition can, however, give difficulties in codes where a transformation of the boundary condition is needed, because the transformed boundary condition will be a combination of Dirichlet and Neumann conditions.

Another possibility that overcomes this problem is to obtain a Dirichlet boundary condition from the Algebraic Reynolds Stress model by assuming a local equilibrium layer. This calculation is shown in appendix A.2 for flows where body forces do not contribute to the $\overline{u_iu_j}$-equations. The result is

$$\begin{aligned} \overline{u_1u_1} &= 1.098k, \\ \overline{u_2u_2} &= 0.2476k, \\ \overline{u_3u_3} &= 2k - \overline{u_1u_1} - \overline{u_2u_2}. \end{aligned} \tag{3.63}$$

It is assumed that k has been found in the near wall cell by solving the equation for k (using terms from (3.60) and (3.62)). The conditions for the remaining Reynolds stresses are again $\overline{u_1u_2} = \tau_w/\rho$ and $\overline{u_1u_3} = \overline{u_2u_3} = 0$.

It is interesting to see, that when this boundary condition for $\overline{u_1u_2}$ is related to the Algebraic Reynolds model in a local equilibrium layer (see Appendix A.2) it turns out that the value of the constant c_μ should be $c_\mu = 0.065$ instead of the value $c_\mu = 0.09$ used in the k-ϵ model. The reason for this is that the k-ϵ model has been calibrated in a free flow. Some authors, e.g. [40], use the value $c_\mu = 0.065$ in the calculations near the wall. Both values will be tested in in chapter 5.

In Appendix A.3, a similar boundary condition for $\overline{u_i\theta}$ is derived from the Algebraic Reynolds model in a local equilibrium layer. This is more complicated that the condition for $\overline{u_iu_j}$, because it involves gradients of both velocity and temperature. This boundary condition has not been tested against the alternative zero gradient flux boundary condition.

3.4 Low Reynolds number turbulence models

In the previous section, the problems with wall boundaries were solved by using logarithmic wall laws. Another solution is to modify the turbulence models from section 3.2 so that they are also valid for the low Reynolds number flow near the walls. This solution is especially interesting in complex flows where the wall laws often perform poorly. However, the low Reynolds number models also have problems. They will need a solution of the boundary layer down to approximately $y^+ = 1$ and will therefore need significantly more grid nodes than the wall laws.

Another problem is that the low Reynolds number models are only little tested, especially in the case of complex geometries. They are also more difficult to develop and validate because there exist few good measurements of the turbulence very near the wall. In the recent years new progress has been reached through the use of data for near wall turbulence obtained by direct numerical simulations.

There has been made several proposals for models, but a "standard" has not yet been found. This section will neither present these models nor give a review of the present state of the models but only mention some references to important models and reviews. The models are based on the high Reynolds number models, which are modified to include viscous effects that dampen out turbulent effects as the turbulent Reynolds number goes to zero.

A review of two-equation models has been given by Patel *et al* [41]. They tested several k-ϵ models and compared the results with data from available measurements. The model of Launder and Sharma [42] was one of the few reasonably well performing models. This model is purhaps the most extensively tested two-equation model for low Reynolds numbers. One of the problems with these model is that there are no natural boundary conditions for ϵ. A solution is to use a derived boundary condition like (3.58).

An interesting trend is two-equations models where ϵ is replaced with another variable. An example is the kω-model, e.g. the model by Wilcox and Rubesin [43]. This model also performed reasonably well in the review of Patel *et al.* The new variable ω is defined as $\omega = \epsilon/k$. Another example is the kτ-model where τ is defined as $\tau = 1/\omega = k/\epsilon$. Speziale *et al* [44] suggest a version of this model. An advantages with these models is that the variation of both ω and τ are simple near walls. This makes the numerical modelling of the problem in the near wall region easier.

Lai and So [45] have used results from direct simulations to investigate how Reynolds stress models should be modified to acount for low Reynolds number effects. In their paper they propose a modification of the basic Reynolds stress model and in a later paper [46] also of the basic Reynolds flux model. In a review [47] their Reynolds stress model is compared with other models.

The low Reynolds number models still need considerable further development. This is due both to the known shortcomings in the high Reynolds number models and to the lack of reliable data for the flow and turbulence near walls. Concerning the recent direct simulations they have become a very valuable tool and are presently used extensively for development of new models.

3.5 Closure

This chapter has given a review of the 'standard' models for modelling turbulent heat transfer. This include the k-ϵ model, the Reynolds stress and flux models and the handling of wall boundary conditions with the use of wall laws. It should be mentioned that several weaknesses are known for the models and that an extensive research to improve the models is going on. However, it is beyond the scope of the chapter to give a full review of this research.

Chapter 4

Computational Method

4.1 Introduction

This chapter will give a brief review of the computational method used in the project. The method is a traditional finite volume method and the focus of the chapter will therefore be the implementation of curvilinear grids and turbulence models. The calculations are made with the commercial program FLOW3D from Harwell Laboratory, UK. A more detailed description of the program can be found in references [48-51]. However, several changes of the original implementation have been made during the project and these will be described in this chapter together with a review of the method used in FLOW3D based on the reference [48]. Due to the complex mathematical relations, general tensor notation will be used in this chapter instead of Cartesian tensor notation.

The finite volume method has been used for many year for the calculation of heat transfer and fluid flow. A thorough description of the method used on rectangular grids can be found in [52]. However most practical geometries are too complex for simple grids like a rectangular grid. A common solution is to use a body-fitted grid. In this project a general non-orthogonal grid will be used. The basic idea is to use a curvilinear transformation to map the complex flow domain in physical space to a simple rectangular flow domain in computational space, see figure 4.1. A Cartesian coordinate system $(x^i) = (x, y, z)$ in the physical space is therefore replaced by a curvilinear coordinate system $(\xi^i) = (\xi, \eta, \zeta)$ where the boundaries of the flow domain correspond to surfaces ξ^i = constant. The equations are then discretized with respect to the computational space coordinates. Boundary conditions are simple to implement in the rectangular computational domain, and it is also easier to control grid density in regions where high resolution is desired. The expense is that the partial differential equations become more complicated due to the non-linear coordinate transformation.

A traditional approach to ensure velocity-pressure coupling is to use an algorithm like e.g. SIMPLE and to store the velocities on a staggered grid to avoid the so-called "checker-board" oscillations. However, this is a quite complicated approach to implement with a curvilinear transformation. During the transformation one might also consider to treat velocities as vectors and Reynolds stresses as tensors, but this gives more complicated equations and

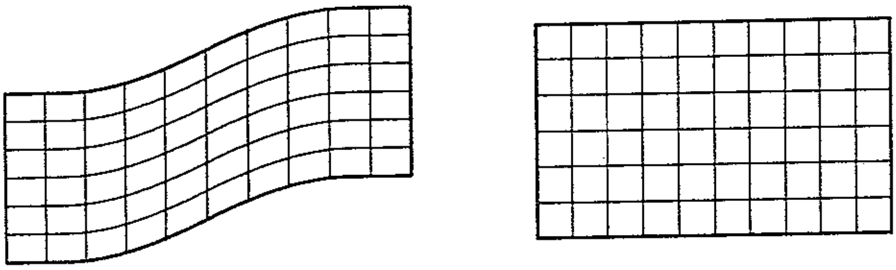

physical space x^i computational space ξ^i

Figure 4.1: Grid structure in physical space and computational space

furthermore also an undesirable sensitivity to the grid. The solution chosen here is the same as advocated by Peric [53], namely to store all variables at the cell centers and to treat them all as scalars when discretized. This method therefore uses a non-staggered grid. A method by Rhie and Chow [54] will be used to avoid the "checker-board" oscillations.

4.2 Equations in curvilinear coordinates

This section shows how the equations are handled in general curvilinear coordinates. First the coordinate transformation will be shown and then the general convection equation will be integrated over a finite volume in the physical space.

4.2.1 Coordinate Transformations

The analysis will be using the two coordinate systems, (x^i) and (ξ^i), shown in figure 4.1. The following notation is used (see [55] for further details about tensor notation):

$$\begin{aligned} J^i_j &= \frac{\partial x^i}{\partial \xi^j} = \text{Jacobian matrix} \\ \overline{J}^i_j &= \frac{\partial \xi^i}{\partial x^j} = (J^{-1})^i_j = \text{Inverse Jacobian matrix} \\ |J| &= det(J^i_j) = \text{Jacobian determinant} \\ A^i_j &= |J|\overline{J}^i_j = \text{Adjugate Jacobian matrix} \end{aligned}$$

It is assumed that the coordinate transformation is non-singular and therefore that the Jacobian determinant is non-vanishing. It is also assumed that the transformation is positively oriented, i.e. that a right handed frame of local base vectors in computational space is mapped to a right-handed frame in the physical space, and vice-verca. The Jacobian matrix and its inverse relates, by the chain rule, derivatives in the physical space to derivatives in

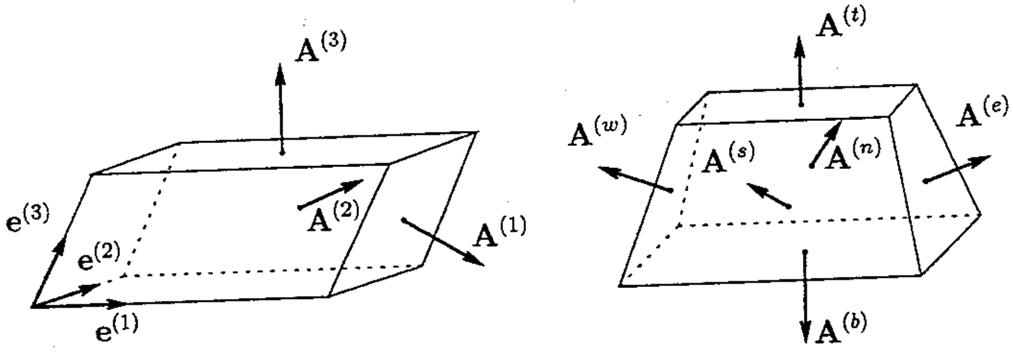

a) elementary parallelepiped

b) control volume Ω

Figure 4.2: Elementary parallelepiped and general cell Ω.

the computational space, and vice versa:

$$\frac{\partial \phi}{\partial \xi^i} = \frac{\partial x^j}{\partial \xi^i}\frac{\partial \phi}{\partial x^j} = J^j_i \frac{\partial \phi}{\partial x^j} \tag{4.1}$$

$$\frac{\partial \phi}{\partial x^i} = \frac{\partial \xi^j}{\partial x^i}\frac{\partial \phi}{\partial \xi^j} = \overline{J}^j_i \frac{\partial \phi}{\partial \xi^j}. \tag{4.2}$$

In the analysis, equation (4.2) is important because derivatives will be expressed relative to computational space. A numerical approximation to the inverse Jacobian matrix must therefore be found. A route to this is to evaluate the Jacobian matrix by simple numerical differentiation and then invert the matrix. However, another route will be used here.

In any curvilinear coordinate system (ξ^i), at any point, it is possible to associate two distinct frames of base vectors:

$$\mathbf{e}_{(i)} = e_{(i)k} = \frac{\partial x^k}{\partial \xi^i} = J^k_i \qquad \text{(tangent to coordinate curves)} \tag{4.3}$$

$$\mathbf{e}^{(i)} = e^{(i)}_k = \frac{\partial \xi^i}{\partial x^k} = \overline{J}^i_k \qquad \text{(normal to coordinate surfaces)} \tag{4.4}$$

They are called, respectively, the covariant and contravariant frames of base vectors. Any Cartesian vector $\mathbf{V} = (V_i)$ has two sets of distinct components with respect to the above frames of base vectors:

$$\mathbf{V} = V_i = V'^i \mathbf{e}_{(i)} = V'_i \mathbf{e}^{(i)} \tag{4.5}$$

where V'^i, V'_i are called the contravariant and covariant components of $\mathbf{V}$, respectively.

Now, since $J^i_k \overline{J}^k_j = \delta^i_j$, it follows that the triads $(\mathbf{e}_{(i)})$ and $(\mathbf{e}^{(i)})$ are dual to each other, i.e.

$$\mathbf{e}^{(i)} \cdot \mathbf{e}_{(i)} = \delta^i_j. \tag{4.6}$$

It is interesting to look at a parallelepiped generated by the covariant base vectors, see figure 4.2. Let $\mathbf{A}^{(i)}$, $(i = 1, 2, 3)$, denote the area vectors normal to the surface of the parallelepiped, i.e. vectors normal to the faces and with a magnitude equal to the areas of the faces. Then

$$\mathbf{A}^{(1)} = \mathbf{e}_{(2)} \times \mathbf{e}_{(3)}, \qquad \mathbf{A}^{(2)} = \mathbf{e}_{(3)} \times \mathbf{e}_{(1)}, \qquad \mathbf{A}^{(3)} = \mathbf{e}_{(1)} \times \mathbf{e}_{(2)}, \tag{4.7}$$

and

$$\mathbf{A}^{(i)} \cdot \mathbf{e}_{(j)} = \mathbf{e}_{(1)} \cdot [\mathbf{e}_{(2)} \times \mathbf{e}_{(3)}]\delta^i_j = vol\ \delta^i_j \tag{4.8}$$

where *vol* is the volume of the parallelepiped found as

$$vol = \mathbf{e}_{(1)} \cdot [\mathbf{e}_{(2)} \times \mathbf{e}_{(3)}] = |J|. \tag{4.9}$$

Comparing equation (4.8) with the relation (4.6) we have

$$\mathbf{A}^{(i)} = |J|\mathbf{e}^{(i)} \qquad \Rightarrow \qquad \mathbf{e}^{(i)} = \frac{\mathbf{A}^{(i)}}{|J|} \tag{4.10}$$

The contravariant base vectors $\mathbf{e}^{(i)}$ are therefore given from the area vectors of the elementary parallelepiped formed by $\mathbf{e}_{(i)}$ divided by its volume. Therefore, the adjugate Jacobian matrix A^i_k can be found from the area vectors $A^{(i)}_k$ as

$$A^i_k = |J|\overline{J}^i_k = A^{(i)}_k \tag{4.11}$$

An infinitesimal rectangular volume element $(\delta\xi, \delta\eta, \delta\zeta)$ in computational space is transformed to a parallelepiped generated by the vectors $\delta\xi\mathbf{e}_{(1)}$, $\delta\eta\mathbf{e}_{(2)}$, $\delta\zeta\mathbf{e}_{(3)}$ in physical space. Therefore the volume and the area vectors are just simple scalings of the volume and area vectors of the elementary parallelepiped in figure 4.2.

Instead of working with the contravariant components V'^i of a vector field $\mathbf{V}$, it is found to be more convenient to work with the normal flux components $\hat{V}^i$ defined by

$$\hat{V}^i = |J|V'^i = A^i_j V_j, \tag{4.12}$$

and it is easily shown that $\hat{V}^i$ is simply the scalar product of $\mathbf{V}$ with the area vectors

$$\hat{V}^i = |J|V'^i = V'^i\mathbf{e}_{(i)} \cdot |J|\mathbf{e}^{(i)} = \mathbf{V} \cdot \mathbf{A}^{(i)}. \tag{4.13}$$

In a general cell Ω in a grid in physical space, the area vectors of the faces can be found by splitting each face up in two triangles and computing the area vector of each triangle as a vector product of the vectors spanning two of its sides. Using Gauss' law, the volume of Ω is obtained by an integration of the faces of the cell.

The Jacobian determinant and adjugate Jacobian matrix may now be approximated from the volume and the area vectors. The present method should be compared with the alternative method, where the inverse Jacobian matrix is found simply inverting the Jacobian matrix. Although both methods are formally second order accurate, the present method has less emphasis on the presence of the coordinate transformation and more on the fact that the physical domain has been filled with an array of irregularly shaped volumes, where the discrete conservation laws will be imposed. The present method is therefore expected to approximate the geometric information more accurately on highly distorted grids.

During the analysis it will be necessary to make interpolation from variables at grid nodes at the center of the cells to the faces of the cells. Although it can be done formally second order accurate in computational space, in the analysis, liniar interpolation in physical space will be used, because this will be more accurate with a non-linear coordinate transformation.

4.2.2 Integration over control volume

All the equations that are to be solved in this analysis have the general form:

$$\frac{\partial \rho\phi}{\partial t} + \frac{\partial}{\partial x^i}\left(\rho U^i \phi\right) - \frac{\partial}{\partial x^i}\left(\Gamma \frac{\partial \phi}{\partial x^i}\right) = S. \tag{4.14}$$

Equation (4.14) is now integrated over the control volume Ω in figure 4.2 using Gauss' law where dA^i is a local area vector to a small part of the surface of Ω

$$\int_\Omega \frac{\partial \rho\phi}{\partial t} dV + \int_{\delta\Omega} \rho\phi U^i dA^i - \int_{\delta\Omega} \Gamma \frac{\partial \phi}{\partial x^i} dA^i = \int_\Omega S dV. \tag{4.15}$$

The first term in (4.15) is the time dependent term. It will later be shown that this term can be treated as a source term. At first we will therefore neglect this term and rewrite (4.15) using the total flux (convection + diffusion) $\hat{I}^i_{nn}$ through each of the surfaces of Ω on figure 4.2. The index nn runs through the six surfaces of Ω with a value of i that corresponds to the face, and we then have

$$\sum_{nn} \hat{I}^i_{nn} = vol \cdot S\,, \tag{4.16}$$

where

$$\hat{I}^i_{nn} = \left(\rho U^k A^{(nn)}_k \phi - \Gamma A^{(nn)}_k \frac{\partial \phi}{\partial x^k}\right)_{nn} \tag{4.17}$$

The term $\partial\phi/x^k$ can be expressed in terms of computational space derivatives as follows

$$\frac{\partial \phi}{\partial x^k} = \overline{J}^j{}_k \frac{\partial \phi}{\partial \xi^j} = \frac{A^j_k}{|J|}\frac{\partial \phi}{\partial \xi^j} \tag{4.18}$$

and we therefore have

$$A^{(i)}_k \frac{\partial \phi}{\partial x^k} = \frac{A^i_k A^j_k}{|J|}\frac{\partial \phi}{\partial \xi^j} \tag{4.19}$$

Equation (4.17) can now be written as

$$\hat{I}^i_{nn} = C^i_{nn}\phi_{nn} - D^{ij}_{nn}\left(\frac{\partial \phi}{\partial \xi^j}\right)_{nn} \tag{4.20}$$

where C^i_{nn} and D^{ij}_{nn} are the convective and the diffusive coefficients

$$C^i_{nn} = \left(\rho \hat{U}^i\right)_{nn} = \rho U^k A^{(nn)}_k \tag{4.21}$$

$$D^{ij}_{nn} = \Gamma^{ij} = \Gamma \frac{A^i_k A^j_k}{|J|} \tag{4.22}$$

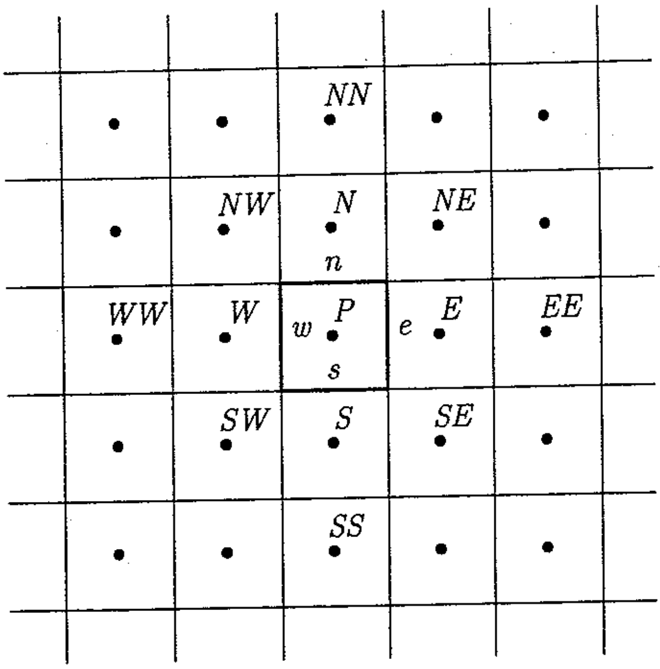

Figure 4.3: Control cell and discretization molecule in two dimensions

It can be shown [48] that if the diffusivity in (4.14) had been anisotropic, this would also result in an anisotropic diffusion coefficient in the transformed equation. The only difference between the transformed equation (4.16) and (4.20) and the original equation (4.14) is that the transformed equation has an anisotropic diffusion coefficient. The next steps in the discretization are therefore nearly the same as the ones taken in the traditional finite volume analysis.

4.3 Discretization

The general convective equation integrated over a control volume Ω can now be discretized. This will be done for each of the terms in (4.15). A general molecule for the discretization in two dimensions is shown in figure 4.3. Index *nb* will be used for nodes in the neighbouring cells. The examples of the discretization schemes will be for the west side of the control volume and will assume that the flow comes from west.

4.3.1 Time dependent term

Equation (4.14) can be written in the form

$$\frac{\partial \rho \phi}{\partial t} = F(\phi). \tag{4.23}$$

The left side of (4.23) can be discretized using several different schemes. Since only steady state flows are considered in the present study, the discretization will only be illustrated with an example, the backward difference,

$$\frac{(\rho\phi)^n - (\rho\phi)^{n-1}}{\delta t} = F(\phi^n), \tag{4.24}$$

where n is the index for the time step. For a more extensive discussion on time discretization, see e.g. [52]. The term on the left hand side of (4.24) can be absorbed into the source terms and the resulting equation will then look like the steady state equation. Other schemes can be implemented in similar ways.

4.3.2 Diffusion terms

In an orthogonal grid the cross derivatives in (4.20) vanish, i.e. $D^{ij}_{nn} = 0$ for $i \neq j$. The diffusion term can then be estimated using central differences, here with the west face as example,

$$\int_w \Gamma \frac{\partial \phi}{\partial x_j} dA^j = D^{ii}_w(\phi_P - \phi_W) \qquad \text{(no summation of i)}. \tag{4.25}$$

For a non-orthogonal grid the cross derivatives give extra terms that involve a larger difference molecule. In order to obtain a simple matrix structure it has been chosen to use a deferred correction approach, where the discretization first is performed using (4.25) and then the extra terms arising from cross derivatives will treated as explicit known terms by including them as a source term called S'

$$S' = \sum_{\substack{nn \\ i\neq j}} D^{ij}_{nn} \left(\frac{\partial \phi}{\partial \xi_j}\right)_{nn}. \tag{4.26}$$

The cross derivatives are approximated with central difference interpolated to the appropriate face of the control volume. This can be illustrated with an example for the west face (noting that the distances between cell nodes in computational space are all unity):

$$\left(\frac{\partial \phi}{\partial \eta}\right)_w = \tfrac{1}{4}\left(\phi_N - \phi_S + \phi_{NW} - \phi_{SW}\right) \tag{4.27}$$

4.3.3 Advection terms

The advection terms are the terms that cause the greatest difficulties. The advection term involves a value of ϕ at the faces of the control volume while the values of ϕ are actually saved at the cell centers. Therefore, some sort of interpolation is needed, and table 4.1 lists some common methods of doing this. The most natural solution is to use a central difference. This scheme is second order accurate, but unfortunately it is only robust for small mesh Peclet numbers ($\mathrm{Pe}_w = C_w/D_w < 2$). A simple and very robust differencing scheme is the upwind scheme, but the expense is that it is only first order accurate. It can therefore give errors referred to as numerical diffusion. The central difference and the upwind schemes are often combined to the hybrid

scheme	order	ϕ_w	ϕ_e
central	second	$\frac{1}{2}(\phi_P + \phi_W)$	$\frac{1}{2}(\phi_E + \phi_P)$
upwind	first	ϕ_W	ϕ_P
higher upwind	second	$\frac{3}{2}\phi_W - \frac{1}{2}\phi_{WW}$	$\frac{3}{2}\phi_P - \frac{1}{2}\phi_W$
quick	third	$\frac{3}{8}\phi_P + \frac{3}{4}\phi_W - \frac{1}{8}\phi_{WW}$	$\frac{3}{8}\phi_E + \frac{3}{4}\phi_P - \frac{1}{8}\phi_W$

Table 4.1: Difference schemes for advection term (west and east faces; flow from left)

scheme: Central differencing is used if Pe is less that 2 and upwind differencing is used if Pe is larger that 2.

The higher upwind and the quick schemes give better accuracy with the expense of being less compact since they use two upwind points. They also tend to be less robust. The extra upwind point ϕ_{WW} can be handled using deferred correction in the same way as was done with the cross derivatives that appear in the diffusion terms.

4.3.4 Matrix equation

The source term in (4.15) is simply integrated over the control volume assuming that the values in P are valid over the entire volume. To enhance the diagonal dominance, the source term is split into two terms

$$\int_\Omega S\,dV = S_u + S_p\,\phi_P \tag{4.28}$$

where S_p is non-positive [52].

The matrix equation to the solved then has the form

$$a_P\phi_P - \sum_{nb} a_{nb}\phi_{nb} = S_u + S' + S_d \tag{4.29}$$

where a_{nb} are the coefficients to the neighbouring nodes and S' and S_d are the deferred correction source term coming from the discretization of the diffusive and advection term, respectively. The coefficient a_P is found as

$$a_P = \sum_{nb} a_{nb} + S_m - S_p \tag{4.30}$$

where S_m is a mass source term found from the convection coefficients C_{nn}

$$S_m = \sum_{nn} C_{nn}. \tag{4.31}$$

Equation (4.29) can, after implementation of boundary condition, be solved using any suitable equation solvers. However, solvers will not be described in this review.

4.4 Implementation of physical equations

It is now straightforward to implement equations for scalars like the temperature. For turbulent scalars like the turbulent kinetic energy k and it dissipation ϵ, it is important to take measures to ensure that they never can take negative values. For the momentum equations and the equations for the Reynolds stresses and fluxes more detailed modelling will be described in the following. Also, the handling of the pressure and the continuity equation will be described.

4.4.1 Momentum equations

The incompressible steady state momentum equations with no additional body forces can be written in their Cartesian form as

$$\frac{\partial}{\partial x^k}(\rho U^k U^i) = -\frac{\partial P}{\partial x^i} - \rho\frac{\partial \overline{u_i u_j}}{\partial x^j} + \frac{\partial}{\partial x^k}\left(\mu\left(\frac{\partial U^k}{\partial x_i} + \frac{\partial U^i}{\partial x_k}\right)\right) \tag{4.32}$$

where P is the pressure and μ is the effective viscosity. This equation can now be rewritten using the total flux I_i^k of U^i

$$\frac{\partial}{\partial x_i} I_i^k = S_i \tag{4.33}$$

where

$$\begin{aligned} I_i^k &= \rho U^k U^i - \mu\frac{\partial U^i}{\partial x^k}, &(4.34)\\ S_i &= -\frac{\partial P}{\partial x_i} - \rho\frac{\partial \overline{u_i u_j}}{\partial x^j} + \frac{\partial}{\partial x^k}\left(\mu\frac{\partial U^k}{\partial x^i}\right). &(4.35)\end{aligned}$$

These equations can now be transformed to computational space

$$\frac{\partial}{\partial \xi^k}\hat{I}_i^k = |J|S_i, \qquad \hat{I}_i^k = \rho\hat{U}^k U^i - \Gamma^{kj}\frac{\partial U^i}{\partial \xi^k}, \tag{4.36}$$

where Γ^{kj} is found from (4.22) using μ as Γ.

The calculation of diffusion and advection coefficients are now straightforward. The source term S_i from (4.35) contains derivatives of both P and U^k. These terms will be evaluated by integrating over the control volume Ω

$$\begin{aligned}[|J|S_i]_\Omega &= -\int_\Omega \frac{\partial P}{\partial x^i} dV - \int_\Omega \frac{\partial \overline{u_i u_j}}{\partial x^j} dV + \int_{\delta\Omega} \mu\frac{\partial U^k}{\partial x^i} dA^k \\ &= A_i^k \frac{\partial P}{\partial \xi^k} + \frac{\partial A_j^k \overline{u_i u_j}}{\partial \xi^k} + \sum_{nn}\left(\mu A_i^j \frac{\partial U^k}{\partial \xi^j} A_k^{(nn)}\right)_{nn}. \end{aligned} \tag{4.37}$$

It is seen from (4.37) that, in general, each momentum equation contains all three computational space derivatives of the pressure.

4.4.2 Pressure correction equation

The pressure can be found by e.g. the SIMPLE algorithm, see [52]. This section will describe the implementation of this algorithm in the curvilinear coordinate system. Similar algorithms like the SIMPLEC and PISO can be implemented using the same technique.

Assuming that U^{i*} and P^* denote the most recent updated velocity and pressure fields, the discretised momentum equations can be written

$$U^{i*}{}_P = \sum_{nb} \frac{a^i_{nb} U^{i*}{}_{nb}}{a^i{}_P} + S^*_i - B^k_i \frac{\partial P^*}{\partial \xi^k} \tag{4.38}$$

where a^i_{nb} and $a^i{}_P$ are coefficients for node P and its neighbouring nodes and S^*_i are the source terms, except the pressure gradient source term, divided by $a^i{}_P$. B^k_i is defined as

$$B^k_i = \frac{A^k_i}{a^i{}_P}. \tag{4.39}$$

The velocity U^{i*} found from (4.38) does not in general satisfy the continuity equation, but has a residual mass source S_m which can be found as a summation over all faces of the control volume of the convection coefficient $C_{nn} = \rho \hat{U}^{i*}_{nn}$,

$$S_m = \sum_{nn} \rho \hat{U}^{i*}_{nn} = \sum_{nn} C_{nn} \tag{4.40}$$

The convection coefficient C_{nn} has to be interpolated from the velocities stored at the cell center in an appropriate way. This will be done using the Rhie-Chow algorithm that will be described in the next section.

The idea of the SIMPLE algorithm is to find corrections P' to the pressure so that when the corrected pressure $P^{**} = P^* + P'$ is inserted into the discretised momentum equation (4.38), corrected velocities U^{i**} will obey the continuity equation. The corrected velocities are found by the equation

$$U^{i**} = U^{i*} - D^k_i \frac{\partial P'}{\partial \xi^k} \tag{4.41}$$

where $D^k_i = B^k_i$ for the SIMPLE algorithm.

The discretised continuity equation can be written in terms of the corrected normal velocity flux component $\hat{U}^{i**}$ as

$$\sum_{nn} \rho \hat{U}^{i**}_{nn} = 0. \tag{4.42}$$

Equation (4.41) can now be transformed to normal flux components

$$\hat{U}^{i**} = \hat{U}^{i*} - \hat{D}^{ik} \frac{\partial P'}{\partial \xi^k}, \quad \text{where} \quad \hat{D}^{ik} = A^i_j D^k_j. \tag{4.43}$$

Following [54] the off-diagonal components of $\hat{D}^{ik}$ are small and will vanish for a converged solution; they can therefore be ignored in the calculations. An equation for the pressure corrections can now be found by substitution the appropriate equation (4.43) into the continuity equation (4.42) using central differences to approximate pressure correction gradients. This gives

$$b_P P'_P = \sum_{nb} b_{nb} P'_{nb} - S_m, \tag{4.44}$$

where

$$b_P = \sum_{nb} b_{nb}, \quad b_{nb} = \rho \hat{D}^{ii} \qquad \text{(i corresponds to nb).} \tag{4.45}$$

In cases where it is important to achieve good mass conservation during the iterations the off-diagonal components of $\hat{D}^{ik}$ can be taken in account using a deferred correction method similar to the one used for diffusivities, see [48] for further details.

The boundary conditions for (4.44) are implemented in the same way as it is done for the general scalar equation. However, it should be noted that for a Diriclet boundary (e.g. an inlet or a wall) either the velocity or the pressure should be specified. If the velocities are specified on a boundary, then no corrections will be needed for the velocity fluxes at the corresponding cell faces, i.e. $\hat{U}^{i**} = \hat{U}^{i*}$. From (4.43) it then follows that the gradient of P' projected into the area vector for the corresponding face should be zero. This can be done by setting the relevant coefficient b_{nb} to 0. If instead the pressure is specified on a boundary, the pressure correction P' should take the value 0 at the boundary and an appropriate boundary condition should be applied to the velocities, e.g. a Neumann condition

4.4.3 Rhie-Chow interpolation

It is essential for the evaluation of the continuity equation in the previous section that the interpolation of the velocities to the faces of the control volume are accurate. A simple interpolation scheme based on physical distances is not satisfactory since it can lead to the so-called "checkerboard" oscillations. Rhie and Chow [54] has developed an interpolation method that overcomes this problem. The method is based on the discretised momentum equations. However, the method has to be extended to include the Reynolds stresses in the interpolation. Equation (4.38) can be rewritten

$$U_P^{i*} + \left[B_i^k \frac{\partial R^{k*}}{\partial \xi^k}\right]_P = \left[\sum_{nb} \frac{a_{nb}^i U_{nb}^{*i}}{a_P^i}\right]_P + [S]_P, \tag{4.46}$$

where S is the remaining source terms and the term R^{k*} in the original method by Rhie and Chow is the pressure P^*. However, when the Reynolds stresses are present, they have to be included and R^{k*} then takes the form

$$R^{k*} = P^* + \frac{\rho A_i^k A_j^k \overline{u_i u_j}}{A_r^k A_r^k}. \tag{4.47}$$

The idea is now to interpolate equation (4.46) to the faces of the control volume. At e.g. face e this equation reads

$$U_e^{i*} + \left[B_i^k \frac{\partial R^{k*}}{\partial \xi^k}\right]_e = \left[\sum_{nb} \frac{a_{nb}^i U_{nb}^{*i}}{a_e^i}\right]_e + [S]_e. \tag{4.48}$$

This equation can also be written using a weighted interpolation from the corresponding terms for the equations at the nodes P and E (this interpolation is denoted by an $\overline{\text{overline}}$),

$$\overline{U^{i*}}_e + \overline{\left[B_i^k \frac{\partial R^{k*}}{\partial \xi^k}\right]}_e \cdot = \overline{\left[\sum_{nb} \frac{a_{nb}^i U_{nb}^{*i}}{a^i}\right]}_e + \overline{[S]}_e. \tag{4.49}$$

Rhie and Chow prescribes the following method to interpolate to (4.48). It is assumed that the terms on the right hand of (4.48) may be approximated by the corresponding terms in (4.49). It is also assumed that $[B_i^k]_e = \overline{[B_i^k]}_e$ and $\overline{[B_i^k \partial R^{k*}/\partial \xi^k]}_e = \overline{[B_i^k]}_e \overline{[\partial R^{k*}/\partial \xi^k]}_e$, and the Rhie-Chow interpolation formula then becomes

$$U_e^{i*} = \overline{U_e^{i*}} + \overline{\left[B_i^k\right]}_e \left(\overline{\left[\frac{\partial R^{k*}}{\partial \xi^k}\right]}_e - \left[\frac{\partial R^{k*}}{\partial \xi^k}\right]_e\right). \tag{4.50}$$

This can be expressed in normal velocity components as

$$\hat{U}_e^{i*} = \overline{\hat{U}_e^{i*}} + \left[\hat{B}^{ik}\right]_e \left(\overline{\left[\frac{\partial R^{k*}}{\partial \xi^k}\right]}_e - \left[\frac{\partial R^{k*}}{\partial \xi^k}\right]_e\right) \quad \text{where} \quad \left[\hat{B}^{ik}\right]_e = A_j^i \overline{B_j^k}. \tag{4.51}$$

Since all gradients of R^{k*} are computed using central differences, the cross-derivative terms in (4.51) cancel, and the formula reduces to

$$\hat{U}_e^{i*} = \overline{\hat{U}_e^{i*}} + \left[\hat{B}^{ii}\right]_e \left(\overline{\left[\frac{\partial R^{i*}}{\partial \xi^i}\right]}_e - \left[\frac{\partial R^{i*}}{\partial \xi^i}\right]_e\right) \qquad \text{(i not summed).} \tag{4.52}$$

The interpolation formula is therefore a simple interpolation of $\hat{U}^{i*}$ plus a correction term containing the difference between the gradients of R^{i*} evaluated respectively at the cell nodes and interpolated to the face and a simple gradient at the same face. It can be shown [48] that using this practice the continuity equation will contain a fourth order derivative of the pressure. This will give a third order error in continuity and will ensure that the pressure field is smooth.

4.4.4 Turbulent momentum and scalar equations

In the equations for turbulent momentum and scalar transport the molecular diffusive terms are often quite small compared to respectively Reynolds stresses and fluxes. The diffusive terms are therefore often neglected. The smallness of the diffusive terms has two effects: It makes the equation system less stable and with the lack of the smoothing effect of diffusion, checkerboard oscillation can occur for velocities and scalars. The present code takes two measures to repair these unfortunate effects; it adds a physical reasonable diffusion on both sides of the equations and uses an interpolation method similar to the Rhie-Chow method for gradients at the cell faces.

For the momentum equations the following turbulent diffusion terms are used

$$D^{jj} = \frac{\rho c_s k}{|J|\epsilon} A^j_{\,m} A^j_{\,n} \overline{u_m u_n} \qquad \text{(j not summed).} \tag{4.53}$$

Here, c_s is a constant from the turbulence model. These diffusion terms are divided by a turbulent Prandtl number for scalar equations.

The gradient of a variable ϕ is evaluated by relaxation as

$$\left(\frac{\partial \phi}{\partial \xi^j}\right)_{e,new} = \alpha \left(\frac{\partial \phi}{\partial \xi^j}\right)_e + (1-\alpha)\overline{\left(\frac{\partial \phi}{\partial \xi^j}\right)}_e . \tag{4.54}$$

The last term in (4.54) is the gradients of ϕ calculated at the cell nodes and then interpolated to the cell face. It can be shown [50] that this interpolation method introduces a fourth order error in the source term. This ensures a smooth scalar (or velocity) field. In [50] the authors found that $\alpha = 0.9$ gave the most satisfactory results.

It should be noted that other authors use a somewhat different method developed by Obi *et al* [40]. By rearranging the equations for $\overline{u_i u_j}$, $\overline{u_i u_j}$ can be split into a part containing gradients of the velocities and a part containing the other parts. When the gradients $\overline{u_i u_j}$ are inserted into the momentum equations the terms containing gradients of the velocities can be arranged as apparent diffusive terms. In this way these apparent-diffusive terms are not artificially added, but are simply a rearrangement of the equations. However, a disadvantage with this method is that it is dependent of the Reynolds Stress model used. A change of e.g. wall reflection terms will also involve changes of the apparent diffusive terms.

4.4.5 Equations for Reynolds stresses and fluxes

As mentioned earlier, in order to avoid the mathematically complex transformation of the equations for Reynolds stresses and fluxes, their elements will be treated as scalars during the discretisation. In three dimensions there will then be 6 separate equations for the Reynolds stresses and 3 separate equations for the Reynolds fluxes. The equations will have the same form as (4.14) with the exception that the diffusivity will be anisotropic.

The source terms in the equations are quite complicated to evaluate. The productions terms contain gradients of the velocities (and of the scalar for Reynolds fluxes). These should be computed in computational space and then transformed into physical space using (4.2). However, the largest difficulties come from the wall reflection terms because they are dependent on the geometry. For each face in the geometry, the wall reflection terms consist of complex terms involving a unit vector from the face and a distance from the face.

In FLOW3D the user has to implement the wall reflection terms. In the present study this has been done in a general way so that the same implementation could be used for all the presented calculations.

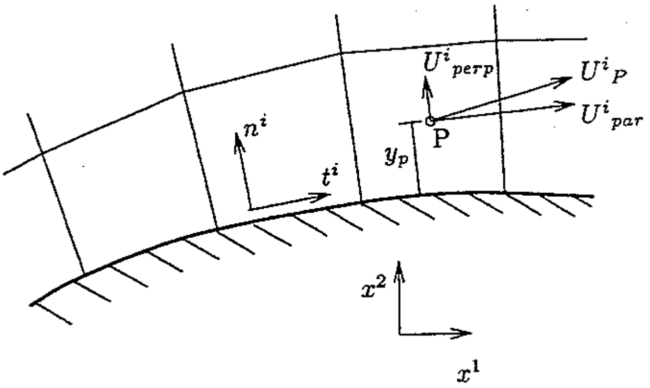

Figure 4.4: Coordinate system local to a wall

4.5 Boundary conditions

Boundary conditions can be implemented by several methods. Two different methods are

1. Modifying coefficients in the near wall cells,
2. Setting values in dummy cells, i.e. extra cells just outside the computational domain.

The first method offers greater flexibility while the second in many situations is the simplest to implement. In FLOW3D the first method is used for walls and the second method is used for other types of boundaries such as inlet and outlets.

In a curvilinear grid the boundary conditions are often specified in a local coordinate system (t^i, n^i) with one axis t^i tangential to the boundary and the other axis n^i perpendicular to the boundary, see figure 4.4. During the transformation in section 4.4 it was chosen to specify velocities and Reynolds stresses and fluxes in a global coordinate system (x^i) to obtain a simpler transformation. As a consequence of this, the resulting effect of the boundary will in some situations have to be transformed to the global coordinate system. The transformation of the Reynolds stresses is shown in appendix A.1.

4.5.1 Walls

A Neumann boundary condition, e.g. a specified heat flux, can be implemented in the near wall cells by putting the relevant coefficient a_{nb} to zero and instead adding the effect of the flux to the source terms. For a Dirichlet boundary condition, e.g. a specified wall temperature, a similar approach can be used. The flux on the wall must then be expressed as a function of the value in the near wall cells node. As an example it will be shown how a boundary condition for the velocity can be implemented. The physical velocity near the wall U_P^i

can be split into two components, a velocity perpendicular to the wall U^i_{perp} and a velocity parallel to the wall U^i_{par}, see figure 4.4,

$$U^i_{perp} = (U^j_P \cdot n^j)n^i, \qquad U^i_{par} = U^i_P - U^i{}_{perp}\,. \tag{4.55}$$

The vector t^i in figure 4.4 can now be found as $t^i = U^i_{par}/|U_{par}|$. Assuming that the velocity of the wall is U^i_{wall}, the momentum flux from the wall, i.e. the wall shear stress τ^i_{wall} can be written as

$$\tau^i_{wall} = T_m(U^i_{wall} - U^i_{par}). \tag{4.56}$$

In the laminar case the multiplier T_m is given by $T_m = \mu/y_{wall}$, where y_{wall} is the distance between the near wall node P and the wall. In the turbulent case T_m can be found from the modified wall law (3.50) to be

$$T_m = \frac{\rho\kappa^* k^{1/2}}{\ln(E^* y^*)}. \tag{4.57}$$

If A^i_{nn} is the area of the cell face coincident with the wall the integral across A^i_{nn} of the velocity flux vector I^i_k is

$$\int_{A_{nn}} I^i_k dA^i = |A^i_{nn}|\tau^i_{wall}. \tag{4.58}$$

This boundary condition can be incorporated in the discretized equation by setting the coefficient $a_{nn} = 0$ and

$$\begin{aligned} S_p &= S_p - |A_{nn}|T_m, &(4.59)\\ S_{u(i)} &= S_{u(i)} + |A_{nn}|(U^i_{perp} + U^i_{wall}). &(4.60) \end{aligned}$$

A similar technique is used for scalar equations. For the Reynolds stresses a more complex transformation is sometimes needed. This has been implemented in the code during this project and is discussed in section 3.3.4.

4.5.2 Periodic boundary condition

In FLOW3D, a simple periodic boundary condition is implemented. This uses a row of dummy cells just outside the boundary. The values just inside one of the boundaries are simply copied to the corresponding dummy cells for the other boundary. This is also done for e.g. gradients and the velocity flux at the boundary. The boundary is illustrated in figure 4.5.a. However, the illustrated flow is a flow in a repeated geometry (e.g. a channel containing periodic ribs) and here the pressure and e.g. the temperature differ by a constant value from "inlet" to "outlet". This can not be easily handled by the standard implementation in FLOW3D. An even more complicated situation is the "unit cell" in the staggered tube bundle shown in figure 4.5.b. Here, the periodic boundary for "inlet/outlet" is furthermore anti-symmetric, i.e. the bottom left correspond to the top right of the domain and vice versa.

A new periodic boundary condition has been implemented in FLOW3D during the project. The implementation assumes, that the grid is orthogonal

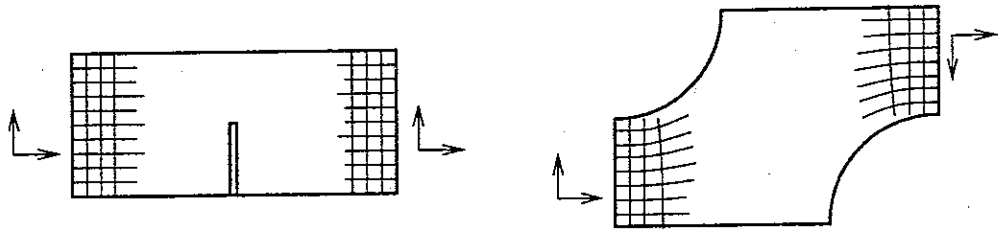

a) symmetric b) anti-symmetric

Figure 4.5: Periodic boundary conditions

at the boundary and furthermore that the axes in physical space here coincides with the axes in computational space. Besides copying to the dummy cells according to the symmetric or anti-symmetric condition, it takes the following circumstances in consideration:

1. Velocity corrections are added to the velocities that are copied to the "inlet" in order to obtain the specified mass flow through the domain.

2. There will be a difference between the corresponding values of e.g. pressure and temperature due to the effects of wall friction and heat transfer in the domain, respectively. This difference is estimated and taken into account each time values are copied into the dummy cells.

3. Elements of vectors and tensors that contain *one* element in the anti-symmetric direction must change sign when they are copied. If the anti-symmetric direction is the x^2-axis this must be done for $U_2, \overline{u_1u_2}, \overline{u_2u_3}$ and $\overline{u_2\theta}$.

It is not always simple to estimate the pressure difference used in the implementation of the boundary condition. Basically this is a kind of regulation problem. The imposed pressure difference affects the solution of the flow conditions, the flow conditions determine the wall shear stresses and the sum of the wall shear stresses determine the actual pressure difference. This implementation of the periodic boundary condition can therefore in some cases lead to unstable solutions that are either oscillating or diverging.

In some cases it is therefore a better solution to remove the pressure difference by the addition of a body force in the main flow direction. No correction of the velocities or pressure difference between inlet and outlet are then needed. There is still a regulation problem; now the body force that gives the desired mass flow through the domain must be found in an iterative process. This process is often more stable, but may at the same time need a large amount of iterations. Also, the solution with body terms can not be applied with the same ease to scalar variables like the temperature because their boundary conditions are more complicated.

4.5.3 Other boundary conditions

The other boundary conditions used in the study are an inlet, an outlet and a symmetry boundary condition. In their implementation it is assumed that the grid is orthogonal at the boundaries.

The inlet boundary is quite simple. It is a Direclet boundary condition where all variables except the pressure are specified and copied to the dummy cells at the inlet.

As outlet condition, a Neumann boundary condition is used, namely a zero gradient across the boundary for of all variables except the pressure. This condition therefore assumes that the flow is fully developed at the outflow boundary. For the velocity it is important to ensure global mass conservation during each iteration and this is done by adding corrections to the outflow velocities perpendicular to the boundary.

For a symmetry boundary condition there is no flux across the boundary. Therefore, this boundary also has a zero gradient for all variables across the boundary. However, in order to ensure a zero flux over the boundary it is also necessary that there are no vector or tensor components in the direction perpendicular to the boundary.

Both the outlet and the symmetry boundary condition is implemented by copying the values from the near boundary nodes to the nodes of the dummy cells. In this process the special consideration for vector and tensor components perpendicular to the boundary are taken into account.

4.6 Closure

The solution procedure for the steady case can now be outlined.

1. A set of reasonable values for all variables is used as initial guess.
2. The momentum equations are solved for velocities U^{i*}.
3. The convection coefficients C_{nn} are found using the Rhie-Chow interpolation based on the discretized momentum equations.
4. The equation for the pressure correction is solved and corrected values of the pressure P^{**} and velocities U^{i**} are found, in effect satisfying the conservation of mass.
5. Equations for turbulent variables are solved.
6. Scalar equations and any equations for Reynolds fluxes are solved.
7. Steps 2 to 6 are repeated until convergence.

The present review of the method used in FLOW3D has only described the parts of the code that are relevant for the study. It should be mentioned that the code also able is to make calculations with simple orthogonal grids using rectangular or polar grids coordinates. These parts of the code are straightforward simplifications of the general code and has therefore not been presented in this review. It should also be mentioned that the test cases presented in chapter 5 all are two-dimensional cases. FLOW3D takes measures to avoid unnecessary calculation, when it is specified, that the flow is two-dimensional.

Chapter 5

Results from numerical calculations

5.1 Introduction

This chapter will describe calculations made on three different test cases with turbulent flow and heat transfer. Since the flow in a tube bundle is quite complex some of the features of this flow will be examined with two more simple test cases. The abrupt pipe expansion is one of the classical test cases for recirculating flows and this has been chosen as the first test case. The second test case is an axisymmetric impinging jet and it is used to examine the capability of the turbulence models to handle the very complex features of in an impinging zone. The third test case is then the flow in the middle of a staggered tube bundle. The three test cases all represent typical turbulent flows found in industrial processes.

All the calculations are performed with the program FLOW3D version 2.4. The computational method for this program is described in chapter 4. Aside from the turbulence models and some of the wall boundary conditions, the calculations use the standard version of FLOW3D. To ensure the continuity the SIMPLE scheme described in section 4.4.2 is used. The higher upwind convection scheme (see table 4.1) has been used in the calculations unless otherwise stated. This second order accurate scheme has been chosen because it is significantly more accurate than first order accurate schemes like the upwind scheme. In some of the preliminary calculations it was found that the higher upwind scheme gave results close to even more accurate and costly schemes like the quick scheme, but at the same time the higher upwind scheme tended to be significantly more stable.

In each calculation, the iterations were continued until a constant (low) level of the residuals for the discretized equations was reached. For each calculation it has also been checked that the values at a selected monitor point were constant during the last iterations. The calculations were performed on a Hewlett-Packard workstation (HP 9000/720) and had calculation times from 5 to 48 hours. The typical usage of virtual memory was about 10 Megabytes.

The effect of the turbulence is modelled with the turbulence models described in chapter 3. Both the k-ϵ model and the basic Reynolds stress model have been used. For the latter the wall reflection terms have been implemented for each of the cases. A modified wall reflection term proposed by Craft and Launder [56] has also been implemented and used in some of the cases. This modified version is designed to be more able to handle flows that are not parallel to the wall and the modification only involves changes of the part of equation (3.25) that contains the c_2' constant. This term will be denoted ϕ^2_{ijw}, i.e.

$$\phi^2_{ijw} = c_2'(\phi_{km2} n_k n_m \delta_{ij} - \tfrac{3}{2}\phi_{ik2} n_k n_j - \tfrac{3}{2}\phi_{kj2} n_k n_i)\frac{k^{3/2}}{c_l \epsilon x_n}. \tag{5.1}$$

The modified term called the Craft-Launder term reads

$$\begin{aligned}
\phi^2_{ijw} &= \left\{ -0.08 \frac{\partial U_l}{\partial x_m} \overline{u_l u_m} \left(\delta_{ij} - 3 n_i n_j\right) \right. \\
&- 0.1k\, a_{lm} \left(\frac{\partial U_k}{\partial x_m} n_l n_k \delta_{ij} - \frac{3}{2} \frac{\partial U_i}{\partial x_m} n_l n_j - \frac{3}{2} \frac{\partial U_j}{\partial x_m} n_l n_i \right) \\
&+ \left. 0.4k \frac{\partial U_l}{\partial x_m} n_l n_m \left(n_i n_j - \frac{1}{3}\delta_{ij} \right) \right\} \frac{k^{3/2}}{c_l \epsilon x_n}
\end{aligned} \tag{5.2}$$

where

$$a_{ij} \equiv \frac{\overline{u_i u_j} - \frac{1}{3}\delta_{ij}\overline{u_k u_k}}{k}. \tag{5.3}$$

Both wall reflection terms use a weight function that depends on distances to the walls. Following the practice of e.g. [40] this weight function has been delimited so that it is never greater that unity, i.e. $(k^{3/2}/(c_l \epsilon x_n)) \leq 1$.

The boundary conditions used for the walls in the standard implementation of FLOW3D differ somewhat from the implementation shown in section 3.3.2. It does use the modified wall coordinates, but it does not take the effect of the viscous sublayer into account in the integration of the k-equation in the near wall cell. For the Reynolds stress equation a simple zero gradient condition is used for all Reynolds stresses and fluxes. The shear stress on the walls is found by extrapolation of the Reynolds stresses and not from the modified wall laws.

In some of the calculations with the Reynolds stress models the wall boundary conditions described in sections 3.3.2–3.3.4 has been implemented into the code. This will be referred to as the 'new' boundary condition. The k-equation is solved in cells immediately adjacent to walls and here the viscous sublayer is taken into account in the integration. The values of the Reynolds stresses are then in these cells found from algebraic relations. The zero gradient condition has been maintained as the boundary condition for the Reynolds fluxes.

5.2 Abrupt pipe expansion

The backward facing step and the abrupt pipe expansion are perhaps the most classical test cases for internal flows with recirculating regions. They can be implemented using a cartesian (or cylindrical) grids and are therefore easy to implement in most computer codes. Recirculating regions occur in many

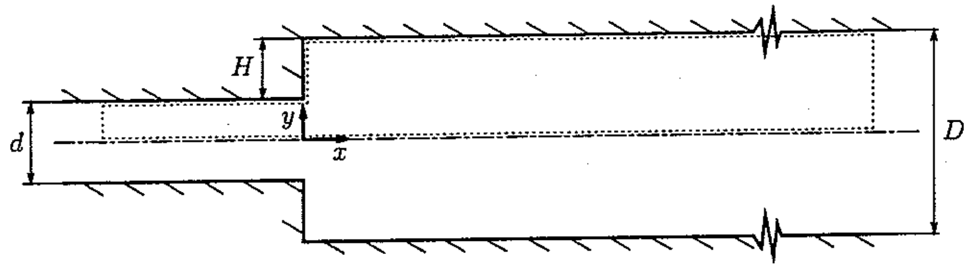

Figure 5.1: Sketch of the abrupt pipe expansion ($d = 0.4D$) – the dotted line shows the computational domain.

industrial applications and the purpose of many calculations on industrial geometries is to predict the position and size of these regions. In some cases heat transfer to the walls are also of interest.

The prediction of recirculating regions in turbulent flows is a challenge for turbulence modelling. Two-equation models like the k-ϵ model and simpler turbulence models usually have difficulties predicting recirculating regions correctly while the Reynolds models are more reliable here, at least for confined recirculating flows. Another problem is the boundary conditions for the walls. The approach with logarithmic wall functions is based on the assumption of a flow parallel with the wall. Especially at the separation and reattachment points one can therefore not expect the wall functions to give good results.

5.2.1 Description of the test case

The emphasis of this calculation is the local heat transfer. Good measurements of both the local heat transfer and the local velocities and turbulence have not been found. No detailed investigation of the prediction of the local velocity field will therefore be performed. The test case is based on measurements of the local heat transfer downstream of an abrupt pipe expansion made by Baughn *et al* [57]. In these measurements the downstream pipe was heated with a constant heat flux produced by a thin, gold coated plastic film. This technique gives a boundary condition that is well suited for calculations and it is believed that the measurements are of good quality. Among the different geometries and Reynolds numbers that were measured, it has been chosen to use an expansion ratio of $(1:2.5)$ and a Reynolds number of $Re = 40\,750$ for the calculations.

The geometry of the test case is shown in figure 5.1. The Reynolds number $Re = U_m D/\nu$ is based on the downstream mean velocity U_m and the downstream diameter D. The kinematic viscosity ν and the thermal conductivity λ of the fluid are both evaluated at the upstream temperature. The diameter of the upstream pipe is $d = 0.4\,D$ and the height of the step is $H = 0.3\,D$. The origin of the coordinate system is located at the expansion with the x-axis coinciding with the center line.

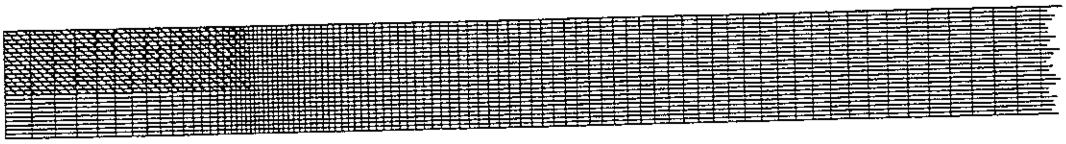

Figure 5.2: Part of the grid used for abrupt pipe expansion. The hatched area show cells that are treated as solids.

The local heat transfer coefficient $h(x)$ is defined as

$$h(x) = \frac{q''}{T_w(x) - T_B(x)}, \tag{5.4}$$

where q'' is the local heat flux (in this test case q'' is constant), $T_w(x)$ is the local wall temperature and $T_B(x)$ is the local mean bulk temperature found by integral control volume analysis,

$$T_B(x) = \frac{\pi D}{\dot{m} c_p} \int_0^x q'' dx + T_{in} = \frac{\pi D x q''}{\dot{m} c_p} + T_{in}. \tag{5.5}$$

Here $\dot{m}$ is the mass flow, c_p the constant specific heat and T_{in} is the upstream temperature. The local Nusselt number is calculated as $Nu = h(x)D/\lambda$ and it will be normalized with the Nusselt number for the fully developed pipe flow downstream of the expansion, which is given by the Dittus-Boelter formula as

$$Nu_{DB} = 0.023\, Re^{0.8} Pr^{0.4}. \tag{5.6}$$

The computational domain is shown with a dotted line on figure 5.1. The calculation is performed in cylindrical coordinates and the center axis is therefore a symmetry line in the domain. Since FLOW3D is a three-dimensional code a symmetric boundary condition has been applied to the tangential direction. The downstream boundary is a traditional outlet with zero gradient as boundary condition for variables and an adjustment of the global continuity. The wall boundary conditions are different kinds of wall laws.

The upstream boundary condition has been found by a calculation of a straight pipe. This calculation has been performed with the standard Reynolds stress model in FLOW3D including wall reflection terms and using standard wall laws. It used the same grid distribution in the y-direction as the inlet to the abrupt pipe expansion and in the x-direction 100 grid nodes were used. The length of the inlet pipe was 100 upstream diameters and it was verified that a fully developed flow was reached at the end of the pipe.

5.2.2 Numerical results

The grid used for most of the calculations is shown on figure 5.2. In the y-direction the grid is uniform with 25 cells. In the x-direction the grid is stretched both up- and downstream of the expansion and is starting with the same cell length as in the y-direction. The expansion ratio are 1.1 and 1.025 and the number of cells are 20 and 110 for the up- and downstream

Case	wall law	wall reflection term	special conditions
1	standard	standard	–
2	standard	standard	upwind/hybrid
3	standard	standard	coarse grid
4	standard	standard with $c_\mu = 0.065$	–
5	standard	not included	–
6	standard	–	k-ϵ model
7	new	standard	–
8	new	Craft-Launder term	–

Table 5.1: The abrupt pipe expansion test cases.

sections, respectively. The length of the upstream section is therefore about 1.1 D and the downstream section is about 12 D. The expansion was modelled by specifying that the cells in the hatched area in figure 5.2 should be treated as solids.

An overview of the performed calculations is shown as a list of cases in table 5.1. The results are shown as streamline plots of selected cases in figure 5.3 and as plots of local heat transfer downstream of the expansion on figures 5.4–5.6.

To investigate the solutions sensitivity to the grid, case 3 represent a calculation made with a coarser grid. This grid was uniform in both directions and had 110×25 cells as compared to 130×25 cells used otherwize. The cells in the recirculating region were therefore significantly larger than in the grid shown in figure 5.2. Test case 2 represents a calculation made with the grid in figure 5.2 but instead of the more accurate higher upwind convection difference scheme the upwind scheme was used for momentum equations and the hybrid scheme was used for the other equations. If the solution is grid dependent this change of differencing scheme is likely to cause a change in the solution.

Streamline plots of case 1–3 (not shown here) showed only small differences in the flow. The difference was largest for case 3 just after the expansion where there is a very large difference in the grid density for the two grids used. The local heat transfer for the three cases are shown in figure 5.4. There is only a quite small difference between the cases. It is therefore assumed that the grid in figure 5.2 is fine enough for the present calculations.

The streamline plots in figure 5.3 show that solutions for all models are close to each other. Streamline plots of case 1, 4 and 7 are almost identical and only the plot of case 1 is therefore shown. The fact that streamlines stop just before the walls is due to the plotting program. Compared with the Reynolds stress model, the k-ϵ model only finds a very small secondary recirculation area in the corner of the expansion. A closer examination of the velocity fields show that the k-ϵ model predicts a shorter reattachment length than the other models. This is a feature of the k-ϵ model that is found by most authors.

In case 5 no wall reflection term was included in the calculation. The

Case 6 – k-ϵ model

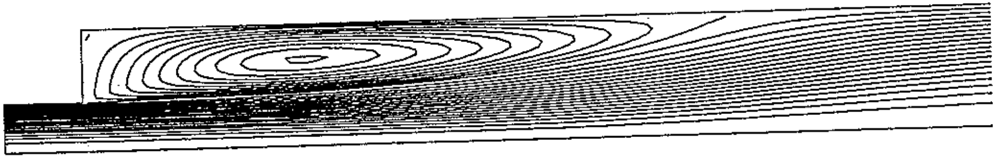

Case 1 – Standard Reynolds stress model

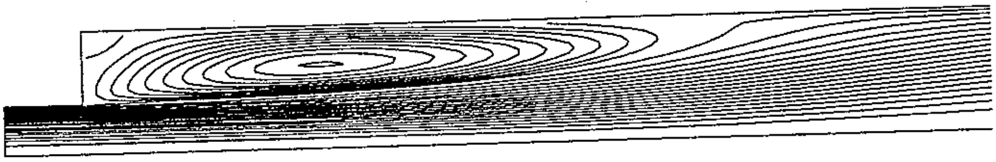

Case 5 – No wall reflection term

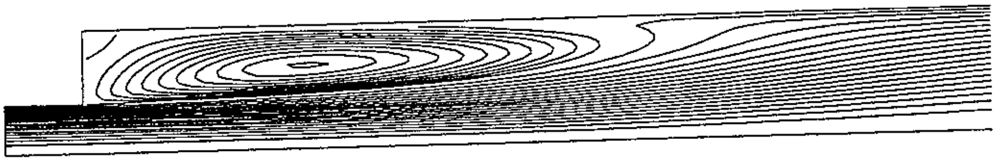

Case 8 – Craft-Launder wall reflection term

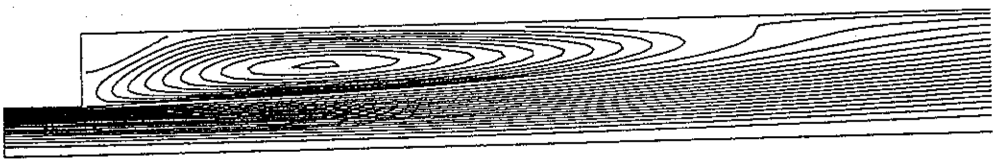

Figure 5.3: Streamline plots for the abrupt pipe expansion

streamline plot here shows a 'kinked' streamline in the reattachment zone. While approaching the wall from the centerline, the x-composant of the mean velocity changes from positive to negative and then again to positive very near the wall. This is an unrealistic behaviour. A closer examination shows that all calculations with the Reynolds stress model have this behaviour in the reattachment zone. Other authors have found the same problem in similar flows. Lasher and Taulbee [58] used the basic Reynolds stress model together with a low Reynolds number model at the wall on a backward facing step flow. Their conclusion was that the problem lay within the wall reflection term and they were able to remove the problem with a change of the c_1' constant in this term. The present calculations also make it probable that the problem comes from the wall reflection term. However, a consistent modification of the Reynolds stress model is a rather large task and this is therefore not within the scope of the present study.

The new wall reflection term by Craft and Launder [56] (case 8) only involves changes in the other part of the wall reflection term – the part preceded with the c_2' constant. This might explain why the problem in the reattachment zone is also found with this model. Compared with case 1 this model finds a

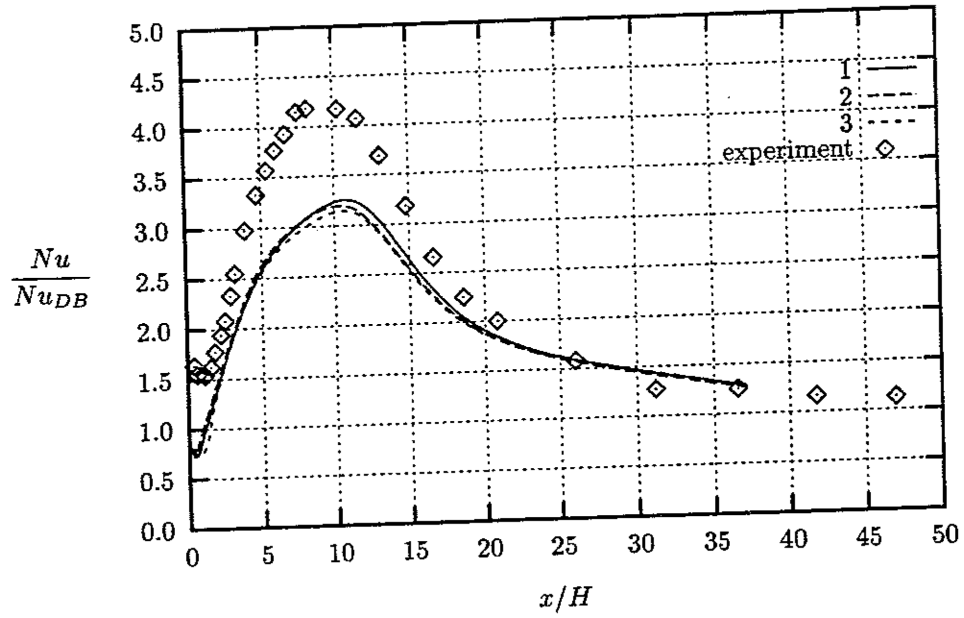

Figure 5.4: Local heat transfer – test of grid dependency. Legend numbers are explained in table 5.1.

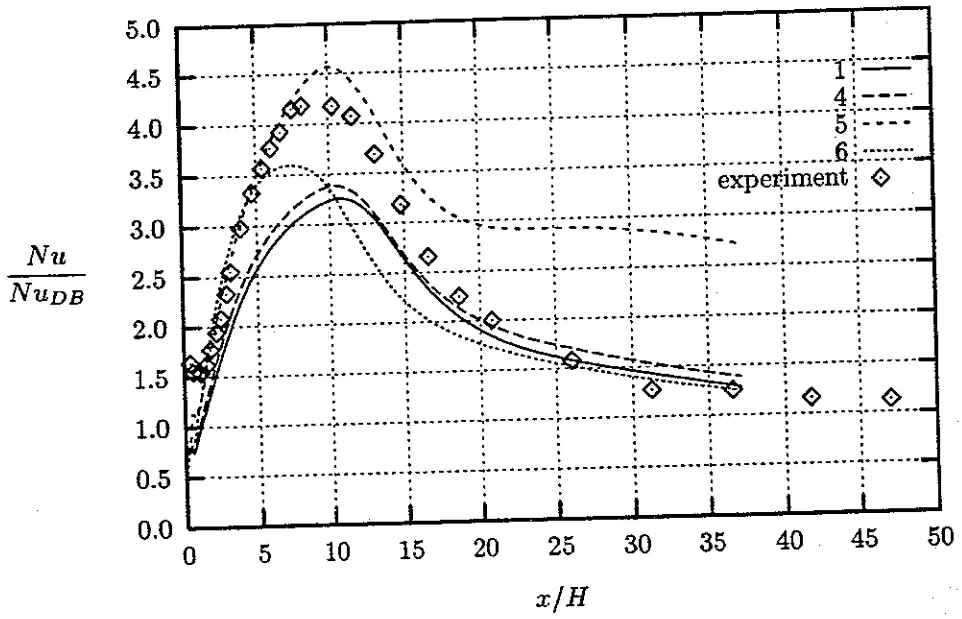

Figure 5.5: Local heat transfer – test of standard wall reflection term and of k-ϵ model. Legend numbers are explained in table 5.1.

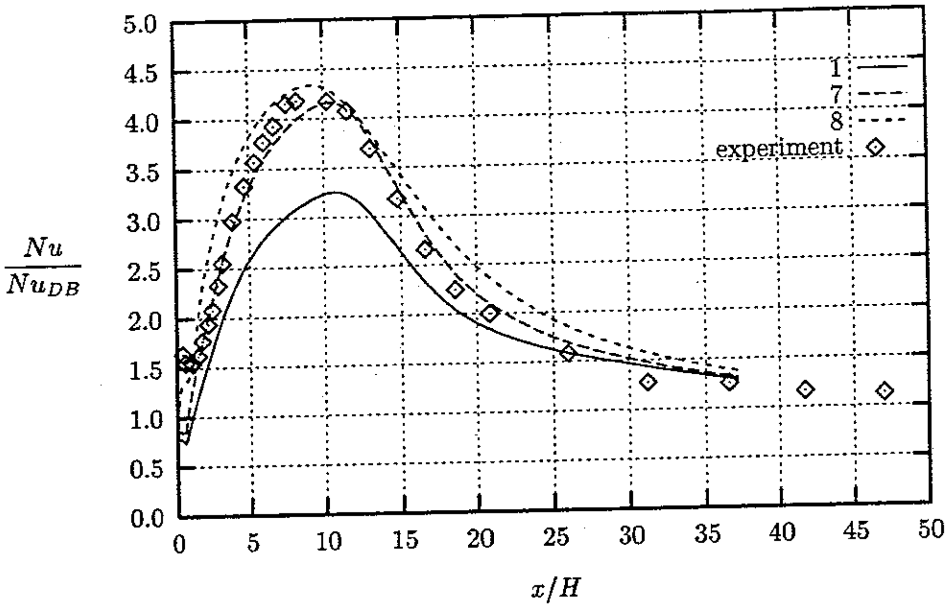

Figure 5.6: Local heat transfer – test of new wall law and of the Craft-Launder wall reflection term. Legend numbers are explained in table 5.1.

larger secondary recirculating region.

In figure 5.5 the k-ϵ model (case 6) has a maximum of the heat transfer at $x/H \approx 7$ instead of $x/H \approx 10$ found by the experiment. This corresponds to the difference in the prediction of the reattachment point. All the calculations done with the Reynolds stress model find a position of the maximum heat transfer that is close to that of the experimental result.

All calculations with the standard wall law predict a too low level of heat transfer in the proximity of the reattachment point. The only exception is the calculation without any wall reflection term where the heat transfer is predicted to be too high. This effect is particular evident further downstream where the calculated heat transfer is about twice that measured. The wall reflection term therefore seems to be important for the heat transfer.

Most of the calculations predict the local heat transfer just after the expansion to be significantly lower than the experimental heat transfer. This region has low velocities and turbulence and the turbulence models therefore have difficulties in predicting the flow correctly. The grid has generally been chosen so that $y^+ > 11$ for the near wall nodes, but in some of the calculations y^+ is less than 11 very near the expansion. This might lead to wrong predictions of the flow and heat transfer. However, this is also the region where the largest errors in the experiment is found due to conduction in the pipe wall. It is therefore difficult to say whether the experiment or the calculation are closest to the correct value of the heat transfer.

As mentioned in section 3.3.4, some authors use $c_\mu = 0.065$ instead of $c_\mu = 0.09$ in calculations near a wall. Since the constant c_l in the wall reflection term is equal to $\kappa/c_\mu^{3/4}$ this constant will then be different from the standard value, $c_l = 2.5$, that corresponds to $c_\mu = 0.09$. To test the effect of this change, a calculation has been performed with the value of c_l corresponding to $c_\mu = 0.065$ (case 4). In streamline plots no difference could be seen and only a small improvement on the local heat transfer is seen in figure 5.5. It has therefore been decided to use the standard value $c_\mu = 0.09$ for the further calculations.

The effect of the new wall boundary condition is illustrated on figure 5.6, case 7 and 8. Here the local heat transfer is predicted quite well and the new boundary condition therefore seems to be more capable of handling heat transfer than the standard wall law. However, before any final conclusion can be drawn, the new boundary condition should be tested at different Reynolds numbers. A calculation with the Craft-Launder wall reflection term and the new wall law is shown as case 8. The local heat transfer is found to be quite close to the result made with the standard wall reflection term.

5.2.3 Conclusion

Different models for turbulent flow and heat transfer have been tested for the abrupt pipe expansion which is a 'classical' test case. It was found that the k-ϵ model tended to have a too short recirculation zone while the basic Reynolds stress model gave results close to that of the experiment. This is a tendency that is also found for many other types of flow with recirculation zones. For the Reynolds stress model some strange behaviour of the velocities was found near the reattachment point. This behaviour has also been reported by other authors and is probably caused by a deficiency in the wall reflection terms of the Reynolds stress model.

Some changes to the wall reflection terms in the Reynolds stress model was tested: another value of the constant c_l and a replacement proposed by Craft and Launder [56] for one of the terms in the wall reflection term. None of these changes gave significant changes in the results of the calculations. Also, a new implementation of the wall boundary condition was tested. This consisted of a more accurate integration in the near-wall cell and a new boundary condition for the Reynolds stresses. This change gave a significant improvement of the prediction of the level of heat transfer in the recirculation zone. With this improvement the Reynolds stress model was able to predict the local heat transfer quite accurately.

5.3 Impinging jet

Like the abrupt pipe expansion, the axisymmetric impinging jet is a flow with a relatively simple geometry that it is easy to implement in most computer codes. Impinging jets are important for many industrial applications, especially for cooling purposes where it can establish very high local heat transfer. However, it is also a flow that is radically different from the flows parallel to walls that most turbulence models are developed for.

In parallel flows the turbulence is generated by shear, length scales are usually determined by the distance from the wall and convective transport

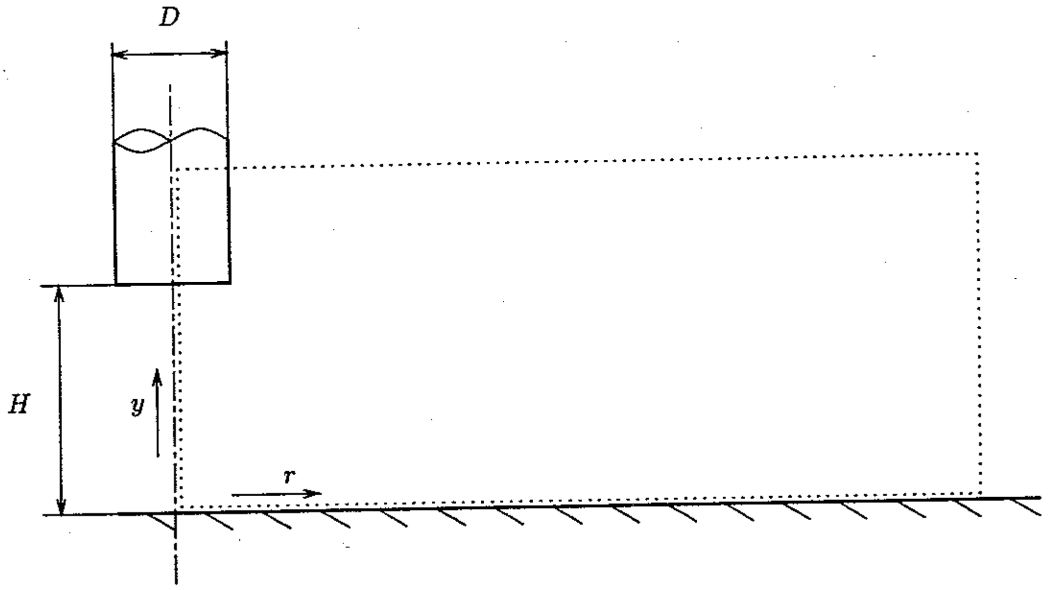

Figure 5.7: Sketch of the impinging jet – the dotted line shows the computational domain

of turbulence is usually small because of the approximate balance between generation and dissipation. The turbulent processes for the impinging jet are more complicated. In the vicinity of the axis of symmetry, the turbulence is generated by normal straining, length scales are strongly affected by the length scales of the jet turbulence and the convective transport of turbulence energy is important. Just beyond the impinging region the flow structure is significantly affected by the strong curvature of the streamlines and while the flow further downstream reverts to a thin shear flow, it is not a simple one because the maximum shear stress occurs outside the wall region.

The impinging jet is therefore a very challenging test for turbulence models. The purpose of the present calculation will therefore be to demonstrate how well the models used in the study are able to handle a more complicated flow. The results have been presented at the *'2nd ERCOFTAC-IAHR Workshop on Refined Flow Modelling'* [59] where this case was used as one of the test cases.

5.3.1 Description of the test case

The jet for this test case is produced by a fully developed pipe flow and it is released perpendicular to an flat plate. A sketch of this axisymmetric impinging jet is shown in figure 5.7. The Reynolds number for the test case is the Reynolds number of the pipe producing the jet, i.e. found as $Re = U_m D/\nu$ where U_m is the mean velocity in the pipe, D its diameter and ν is the kinematic viscosity. The local heat transfer coefficient h is based on the local heat flux and the temperature difference between the local wall temperature and the inlet temperature. The local Nusselt number is found as $Nu = h\,D/\lambda$ where λ is the thermal conductivity of the fluid. Both ν and λ are evaluated at the isothermal temperature of the jet. The coordinate system consists of the r-axis following the wall and the y-axis following the symmetry line of the pipe. The origo is located in the jet stagnation point on the wall.

Four different cases have been calculated. These are obtained using two different Reynolds numbers, $Re = 23\,000$ and $Re = 70\,000$, and two different jet release heights, $H/D = 2.0$ and $H/D = 6.0$. For these cases measurements of both the local velocity and turbulence fields have been performed by [60] using hot-wires. Data for local heat transfer with a constant heat flux are available for the low Reynolds number from [61] and for the high Reynolds number from [62]. All the measurements have been performed with special concern to turbulence modelling.

The computational domain is shown with a dotted line on figure 5.7. The calculation is performed in cylindrical coordinates where the left boundary is a symmetry line. The inlet conditions are found with a separate calculation of a pipe flow in the same way as described in section 5.2.2. The inlet data are prescribed one diameter upstream of the pipe exit. The rest of the upper boundary is an entrainment boundary specified by constant pressure, zero turbulence for entering fluid and zero gradient on velocities. On the right boundary, zero gradients are applied to outflowing fluid. The lower boundary is modelled by wall laws. The part of the pipe that is inside the domain is modelled by treating some cells as solids. The boundary condition on these solids is also modelled with wall laws.

5.3.2 Numerical results

The grid used for the calculation of the cases with $H/D = 2.0$ is shown in figure 5.8. The grid has 98×71 cells (r- and y-directions, respectively) and the grid is uniform for grid lines covering the inlet pipe. Outside this uniform region the grid is stretched with a factor 1.03 in the r-direction starting from the pipe and stretched with a factor 1.01 in the y-direction starting from the wall. The size of the near wall cells has been chosen so that the center in all cases was at a position where $y^+ > 11$. The solution's dependency of the grid has been tested with several grids using from 53 to 98 r-cells, 57 to 120 y-cells and different degrees of stretching. These tests indicated that the chosen grid gave grid independent solutions. For the $H/D = 6.0$ case the grid was simply extended by adding extra rows of cells to the grid in the y-direction. This grid has 98×121 cells (r- and y-directions, respectively).

Three different models have been used in the calculations and they are listed in table 5.2. Model 1 is the standard implementation of FLOW3D together with an implementation of the standard wall reflection terms. Model 2 uses as the only difference from model 1 the new implementation of wall laws made in this study. Model 3 represents data from the literature compiled by Craft *et al* [63]. Their calculations also use the basic Reynolds stress model, but the near wall layer is modelled using a well tested low-Re k-ϵ model [42]. It is believed that these calculations give a significantly better representation of the near-wall conditions and they will therefore be used as a kind of reference to the calculations made with model 1 and 2. Finally model 4 uses both the

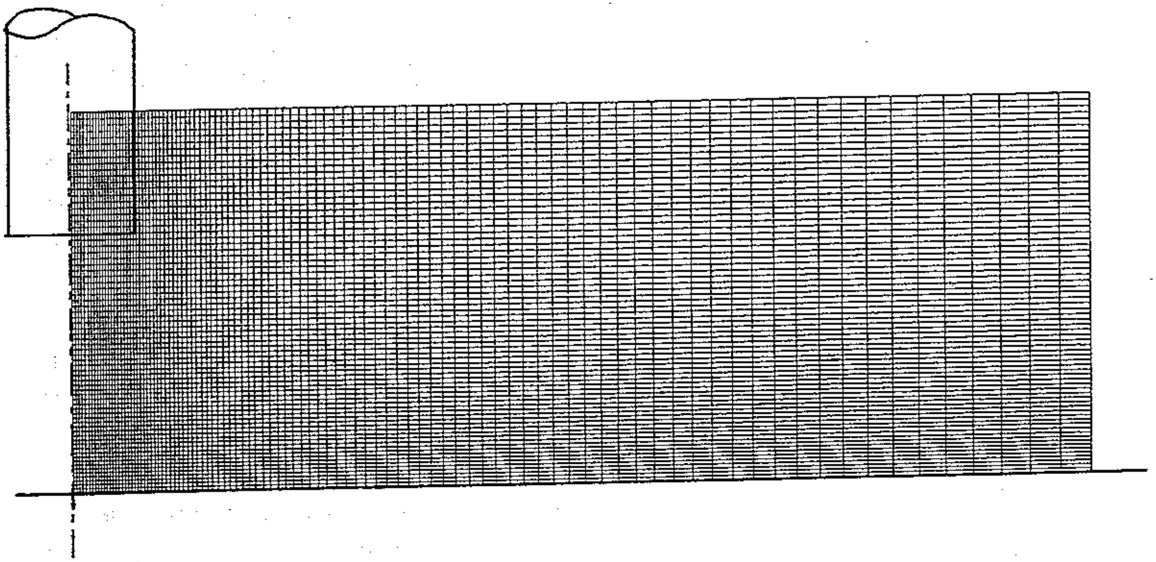

Figure 5.8: Grid used for impinging jet ($H/D = 2.0$).

Model	wall law	wall reflection term	key
1	standard	standard	——
2	new	standard	----
3	low-*Re* k-ϵ model	standard	-----
4	new	Craft-Launder term	....
Experimental data from [60]			◇

Table 5.2: The Reynolds stress models used for the impinging jet cases. Model 3 is data produced by Craft *et al* [63].

new wall laws and the new wall reflection term by Craft and Launder [56].

Plots of the local bulk velocity $U_{bulk} = \sqrt{U^2 + V^2}$ and of the local Reynolds stresses are shown in appendix D.1 for two of the cases: a) $Re = 23\,000$, $D/H = 2.0$ and b) $Re = 70\,000$, $D/H = 6.0$. Here it is seen that the results of model 1, 2 and 3 are quite close to each other. The largest differences occur not unexpectedly at the first near wall cells for wall law boundaries. The prediction of the mean flow and the turbulence seems not to be affected by the simplifications used in the wall laws. The deviations from the experimental data are most likely due to deficiencies in the standard Reynolds stress model.

This is quite evident in the plot of the Reynolds stress component normal to the wall on the stagnation line. The basic Reynolds stress model predicts a too high level of this component. The reason for this can be found in the part of the wall reflection term that is preceded by the c_2' constant. In a parallel flow this term redistributes energy from the Reynolds stress component normal to the wall to the other components. However, when the flow direction is normal to the wall the term has the opposite effect leading to too high levels of the component normal to the wall. The Craft-Launder term used in model 4 has been constructed to remove this weakness. The prediction of model 4 is closer to the experimental results, but especially for the high Reynolds number, the level of component normal to the wall is still too high.

For model 1–3, too high levels of the Reynolds stresses are found. For $r/D \leq 1.0$, the profiles of the bulk velocity match the experimental velocity quite well. For higher values of r/D the Reynolds stresses tend to have their maximum too far away from the wall. Combined with the generally too high levels of turbulence this is probably the reason why the predicted bulk velocities are too low close to the wall. For both geometries, the calculations with model 4 has a region downstream of the stagnation point where very low levels of the $\overline{uv}$ component are found. This problem was not found in the similar calculation by Craft *et al* [63] using the same wall treatment as model 3. The very low levels of the $\overline{uv}$ component in the present calculations with model 4 might be caused by numerical problems, purhaps in combination with usage of wall laws.

Plots of the local heat transfer are shown on figures 5.9–5.12. All the models predict the same heat transfer as the experiments far downstream of the stagnation point. Close to the stagnation point large differences are found. The highest Nusselt number found by the experiments is not unexpectedly found at the stagnation point. Because of the too high levels of the Reynolds stresses at the stagnation point it is expected that the Nusselt number will also be too high here. The result found by model 3 is in agreement with this while the other models that all use wall laws happen to find a Nusselt number quite close to that of the experiments. They do, however, predict the maximum Nusselt number to be located at some distance from the stagnation point. The flow condition near the stagnation point are far from those of the assumptions used in the wall laws. It is therefore believed that the predicted Nusselt number is a combination of the wall laws predicting too low heat transfer and the turbulence model predicting too high heat transfer.

For the $H/D = 2.0$ case a characteristic variation of the local Nusselt

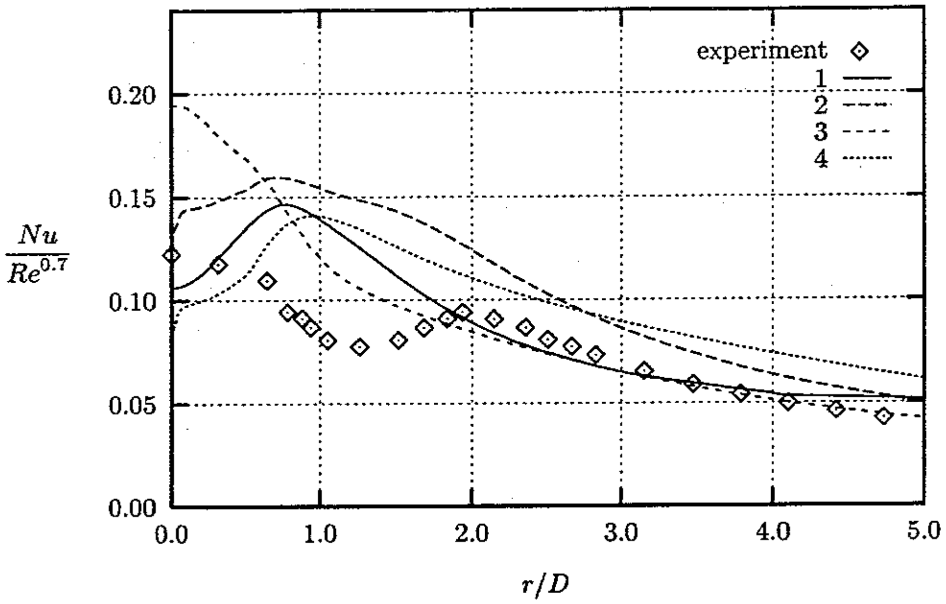

Figure 5.9: Local Heat transfer for $H/D = 2.0$ and $Re = 23\,000$. See key in table 5.2

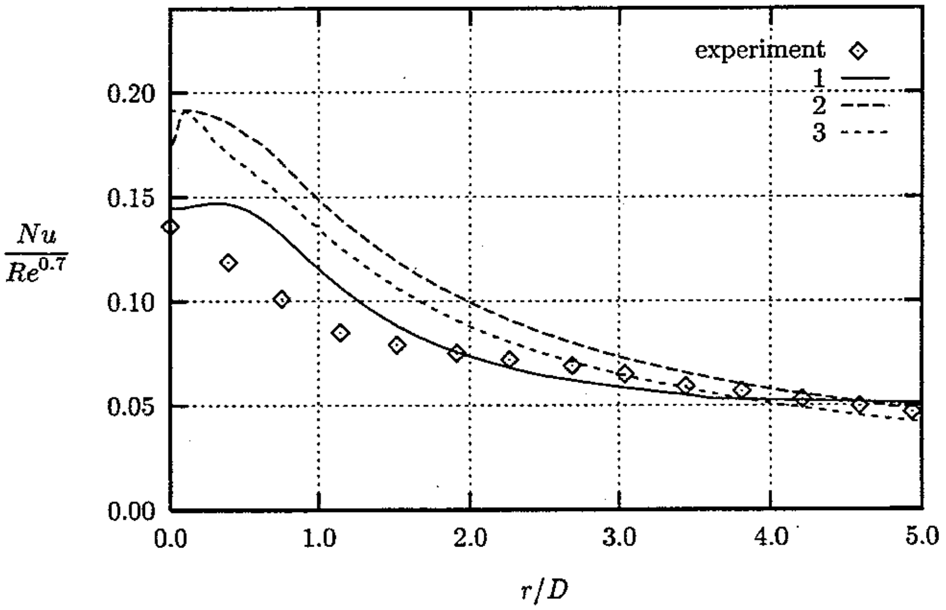

Figure 5.10: Local Heat transfer for $H/D = 6.0$ and $Re = 23\,000$. See key in table 5.2

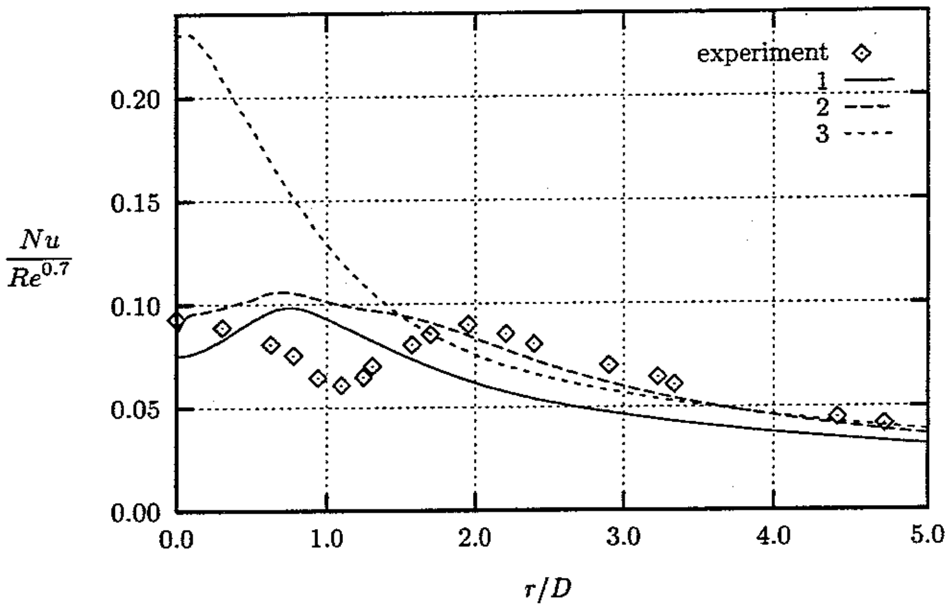

Figure 5.11: Local Heat transfer for $H/D = 2.0$ and $Re = 70\,000$. See key in table 5.2

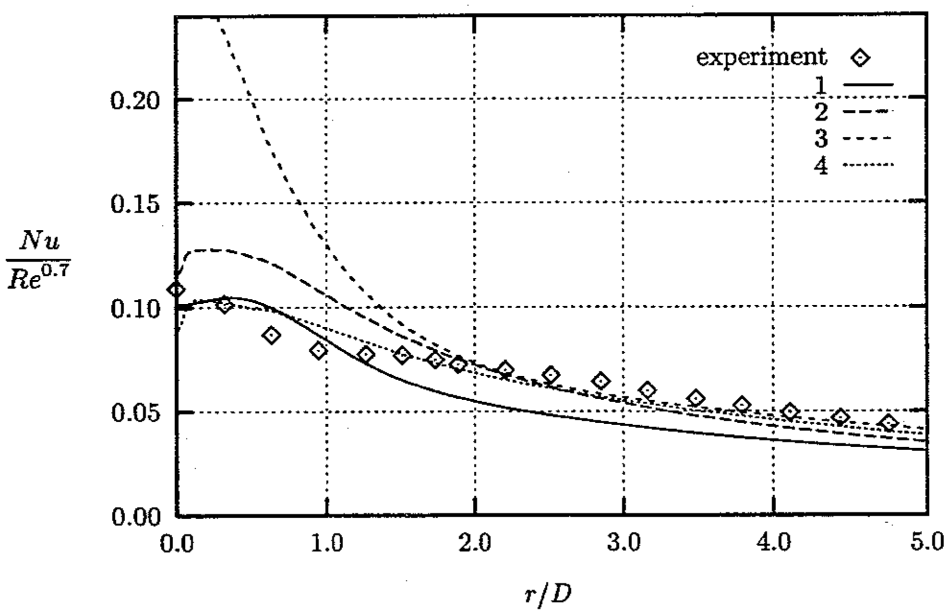

Figure 5.12: Local Heat transfer for $H/D = 6.0$ and $Re = 70\,000$. See key in table 5.2

number is found by the experiments near the stagnation point. None of the models are able to reproduce this variation. In calculations of Craft *et al* [63] this variation *is* reproduced with the Craft-Launder term. In spite of the quite wrong levels of the Reynolds stresses found by model 4, the Nusselt number found by this model is close to the Nusselt numbers found by the other models using wall laws. This indicates that the Nusselt number found by models 1, 2 and 4 is mainly a result of the wall law.

5.3.3 Conclusion

Calculations have been performed with the Reynolds stress model for an impinging jet for two different geometries and two different Reynolds numbers. The predicted velocities, Reynolds stresses and local heat transfer are compared with experimental results.

The most important result for the velocity and Reynolds stresses was that too high levels of the Reynolds stresses were found. This is caused by a well know deficiency in the wall reflection terms. The Craft-Launder term which tries to overcome this deficiency, was also tested in a calculation. An improvement was observed in the impingement zone while the results in the rest of the flow were poor with this model. This problem in the rest of the flow might be caused by a numerical problem.

The standard and the new implementation of the wall boundary condition were both tested with the basic Reynolds stress model and the only important difference in the performance of these two wall boundary conditions was found to be the level of the heat transfer. Here the standard implementation tended to be closest to the experimental data. However, since the Reynolds stresses are overpredicted it is not possible to judge which of the wall boundary conditions that gives the best performance.

The results from the basic Reynolds stress model were compared to those of Craft *et al* [63] that used a low Reynolds number k-ϵ model as boundary condition instead of wall laws. Quite good agreement was found between the predictions of the Reynolds stresses while the prediction of the local heat transfer was significantly better for the model of Craft *et al*. The good agreement between the predictions of the Reynolds stresses might seem surprising because the flow conditions are quite far away from the assumptions that the wall laws are based on. The good agreement therefore indicates that for this case the wall boundary condition is not very important for the prediction of the flow parameters, but only for the prediction of the local heat transfer.

5.4 Staggered tube bundle

Tube bundles are used in many industrial applications, especially as heat exchangers. The tube bundle also represents a typical test case for industrial flows because it has both a complex geometry and a complex turbulent flow. As a test case, the calculation is performed in a unit cell with periodic boundary conditions. This give the important advantage that no inlet boundary condi-

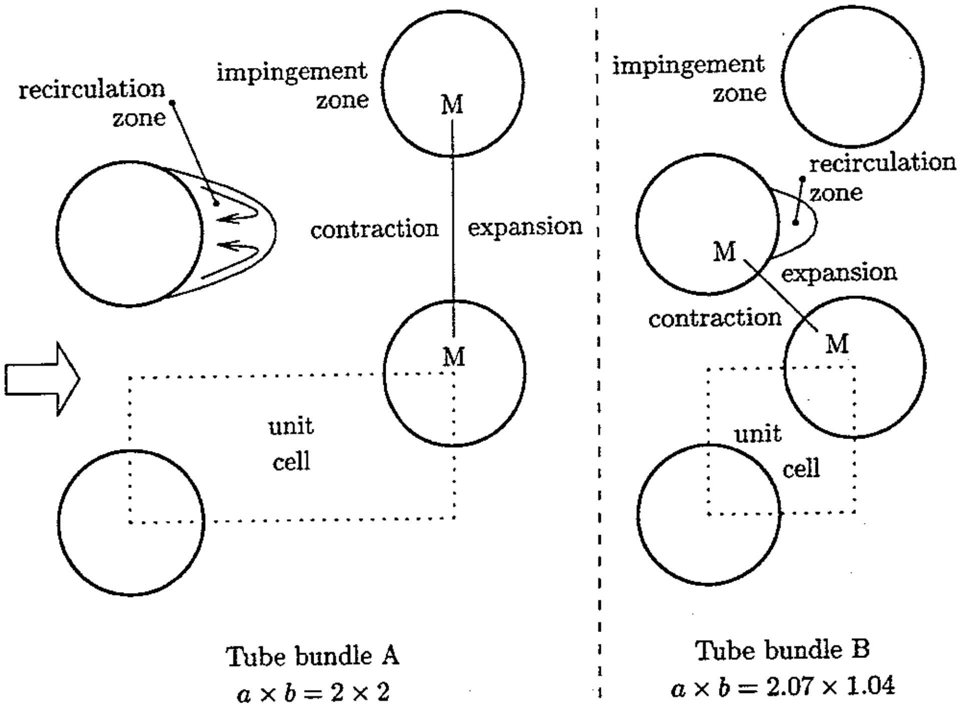

Figure 5.13: The two tube bundles used as test cases. The dotted line show the computational domains and the lines M—M show the minimum flow sections.

tion needs to be specified. Because of the complex geometry the calculations must be performed in curvilinear coordinates on a body fitted mesh.

As it is illustrated in figure 5.13 the flow contains features from the two previous test cases: It has both an impinging zone and a zone with recirculating flow. Furthermore, the test case has a contracting region where the flow is accelerated and an expanding region where the flow is decelerated. The turbulence levels are quite high because the tubes act as a sort of a grid. A more detailed discussion of the physics of the flow in a tube bundle is found in section 2.1.2.

Some numerical results on turbulent flow in tube bundles have been reported. The tube bundle has been used as an examples to test a curvilinear code, [53, 64]. Numerical results have also been compared to data for the mean heat transfer for a tube bundle [65]. However, it is not until very recently that calculations have been compared to detailed measurements of the flow and turbulence. The only example known to the author is the numerical results in [66, 59] that are compared to the LDA-measurements of Simonin and Barcouda [10].

5.4.1 Description of the test cases

The definitions related to the geometry, the Reynolds number and the Nusselt number are found in section 2.1.1. Two geometries will be used in the calculations, see figure 5.13. The longitudinal and transversal pitches are

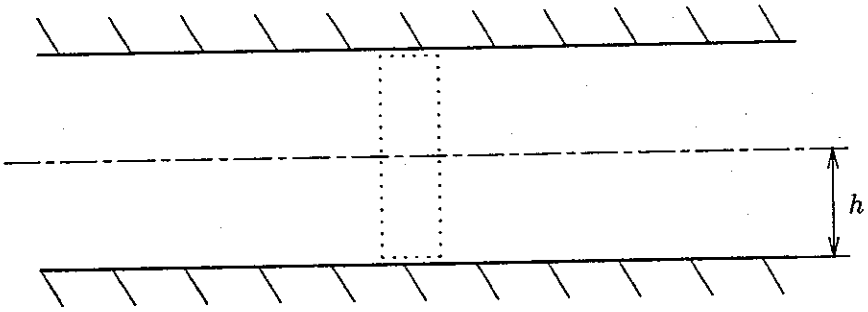

Figure 5.14: Straight channel with two-dimensional flow – the dotted line shows the computational domain.

for tube bundle A: $a \times b = 2 \times 2$ and LDA-measurements are available from section 2.2.3. Simonin and Barcouda [10] have performed LDA-measurements for tube bundle B. In their experiments, the diameter was 21.7 mm and the longitudinal and transversal pitches were respectively 45 mm and 22.5 mm corresponding to $a \times b = 2.07 \times 1.04$.

Measurements of the local heat transfer for both geometries are found in section 2.4.4. Here only one tube in the tube bundle was heated and the temperature difference used in the calculation of the local heat transfer coefficient is the difference between the local wall temperature and the upstream fluid temperature. In the calculations, all tubes are heated and it is therefore not so obvious what the fluid temperature is. In tube bundle A there is a significant distance between the rows. Since the effective thermal diffusion is high in the middle of a turbulent flow, the temperature differences in a cross section of the flow between two rows are quite small compared to the temperature difference between the fluid and the wall. It has therefore been found reasonable to use the mean temperature in a cross section of the flow just upstream of the tube as the fluid temperature. In tube bundle B the distance between two rows is very small and the choice of the fluid temperature is therefore less obvious. It has been chosen to use the mean temperature in a cross section between two tubes in the row just upstream of the tube considered, i.e. at the inlet to the unit cell. This choice of fluid temperature might give a minor difference in the level of the Nusselt number from the measurements and the calculations.

The LDA experiment reported in section 2.2 supports the commonly used assumption that the flow in the middle of a tube bundle can be calculated using a 'unit'-cell with parts of two tubes. This unit-cell is shown for the two tube bundles in figure 5.13. Aside from the wall boundaries, the boundary conditions are a symmetry condition on the sides aligned with the main flow direction and a special periodic boundary condition for the up- and downstream sides. Since the flow is two-dimensional a symmetry condition is used in the planes that are perpendicular to the tube axis.

In the present study special attention has been given to the periodic boundary condition. Section 4.5.2 describes a new implementation of the periodic boundary condition. The implementation of this boundary condition has been tested for a simple two-dimensional turbulent flow in a straight channel with a height $2h$, see figure 5.14. This flow can be considered one-dimensional and therefore also periodic in the flow direction. Furthermore it is symmetric around a line in the middle of the channel aligned with the flow direction and therefore both the anti-symmetric and the standard periodic boundary condition can be used for this flow.

The straight channel is one of the most simple flows that can be used as test case for the periodic boundary condition, but the simplicity of the case gives some problems in the calculations. Since the momentum equations for the flow reduce to a balance between the pressure drop in the channel and the shear forces generated by the walls, the calculation with a periodic boundary condition becomes very sensitive to the estimated pressure drop. This problem is discussed further in section 4.5.2. It turned out during the calculations that it was very difficult to get a stable solution with the approach that used corrections of inlet velocities. Instead the approach where the pressure drop is replaced with a body force is used for both the periodic boundary conditions. The convergence of these calculations were quite slow and they therefore had calculation times in the same order of magnitude as the calculation of the $200\,h$ long channel.

The results of several calculations are shown for the velocity U and for one of the Reynolds stresses, $\overline{u_1u_1}$, in figure 5.15. Both U and $\overline{u_1u_1}$ has been normalized with the maximum velocity U_0 in the channel and they are plotted against the distance from the wall y. Here the solid line represents a calculation with normal inlet and outlet conditions for a $200\,h$ long channel with 100×40 grid cells, the short-dashed line represents a calculation for a $0.5\,h$ long channel with 10×40 grid cells and with the standard periodic boundary condition in FLOW3D and, finally, the long-dashed line represents a calculation for the same channel and grid, but with the new anti-symmetric boundary condition. All calculations use the standard wall boundary condition for turbulent flows in FLOW3D.

The results from the three calculations are all in reasonable agreement with the experimental data. The results from the calculations with periodic boundary conditions are closest to the experimental data. The reason for this is probably that the flow at the end of the $200\,h$ long channel is not fully developed. The deviations from the experimental data are seen most clearly near the wall because U and $\overline{u_1u_1}$ are normalized by the maximum velocity U_0 and not the mean velocity of the channel. However, the deviations of $\overline{u_1u_1}$ from the experimental data near the wall might also be caused by weaknesses in the wall boundary conditions. In general, the calculations indicate that the implementation of the anti-symmetric periodic boundary condition gives the correct results.

5.4.2 Numerical results for tube bundle A

The grid used in the calculations on tube bundle A has 80×40 cells and is shown in figure 5.16. It is a compromise between the desire to have a grid

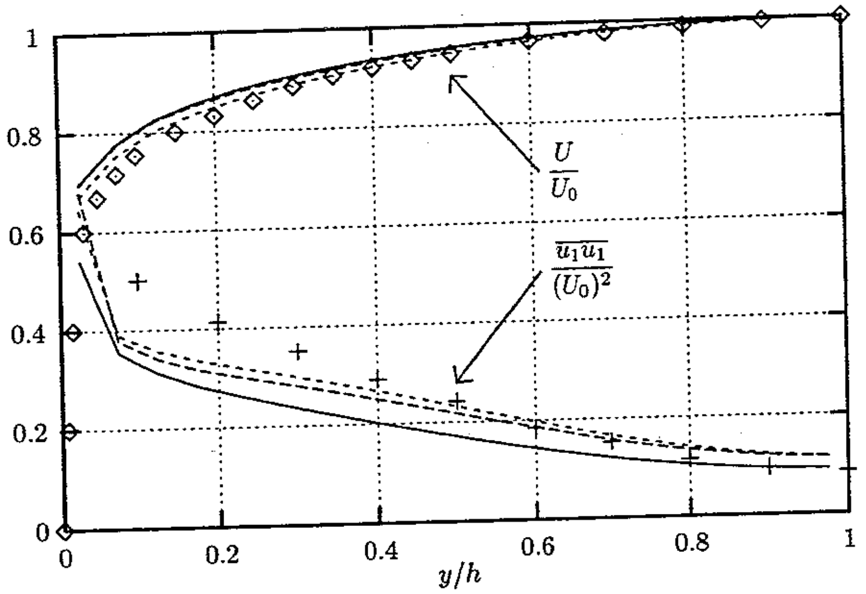

Figure 5.15: Fully developed flow in a plane channel with $Re = U_0 h/\nu = 30\,800$. Symbols show experimental data from [36] and the lines show computational results using different boundary conditions (see text).

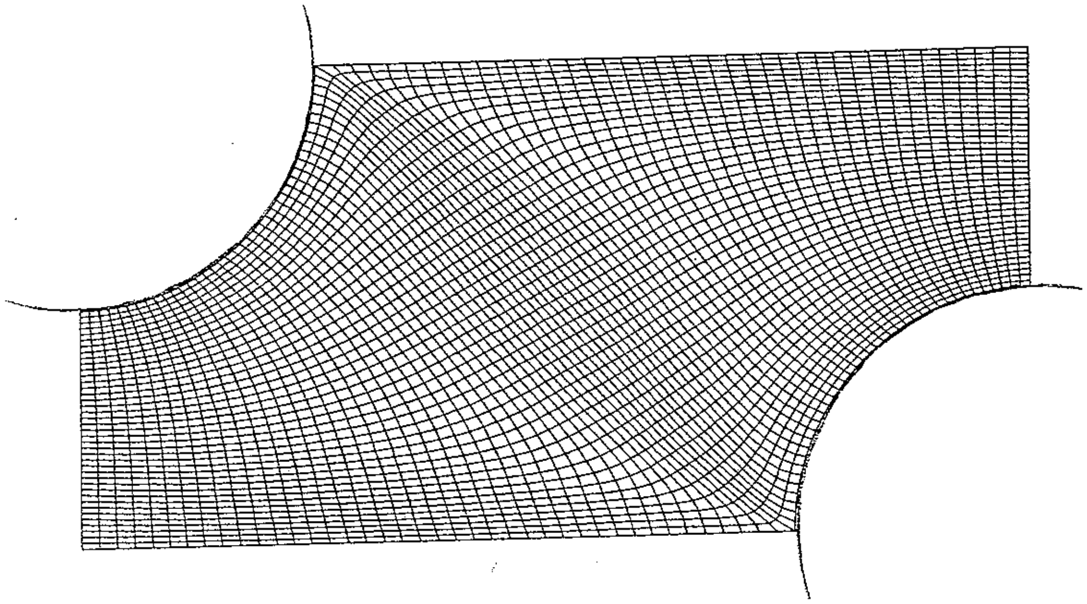

Figure 5.16: Grid used for tube bundle A.

that is fine enough to give grid independent results and the demand for the near-wall cell nodes to have a distance where $y^+ > 11$. The latter is a problem in the tube bundle cases used in the present study. In the grid in figure 5.16 some of the near-wall cell nodes at the rear of the first tube have distances from the wall where y^+ is smaller than 11. The computer code takes measures to handle this in a physically reasonable way, but of course the result can not be completely correct.

On the other hand, calculations have been performed with several different grids, both more and less fine that the grid on figure 5.16. For the more fine grid the row of cells that were nearest to the walls were removed. In this way the height of the near-wall cells were twice the size of the height of their neighbouring cells and the near wall nodes were thereby located at a distance from the wall so that $y^+ > 11$ for most of the nodes. The price of this arrangement is that there is a jump in the cell size from the near-wall cells to the rest of the cells and this gives a greater discretization error in this region.

A general problem with the grid generation for a tube bundle unit cell is that the unit cell has 6 corners while there is only 4 corners in computational space. Two of the corners of the unit cell therefore have to be located in the middle of a boundary in computational space. On figure 5.16 these corners are located at the front and rear stagnation points on the tubes. As it can be seen these corners will inevitable have severly distorted cells. This problem could be solved by using a multi block approach, i.e. several domains in computational space that are linked together in the physical space. Unfortunately this option was not present in the version of FLOW3D that was available at the time where the problem was implemented.

In could be argued that it would be better to locate the corners with distorted cells in those of the corners of the unit cells that are not located at the walls (the lower-left and the upper-right corners on figure 5.16). Such a grid with the same number of cells as the grid in figure 5.16 has been generated and used in a single calculation. This calculation gave more smooth results at the stagnation points, but no significant change in the results in the rest of the flow. However, since FLOW3D does not support the use of both a symmetric and a periodic boundary condition along the same boundary, it is more complicated to implement the tube bundle problem with this grid. It has also turned out to be quite difficult to give the near wall nodes a uniform distance from the wall with this type of grid. It has therefore not been used for further calculations.

The calculations with these different grids all gave similar results, but they had minor differences in the prediction of actual values. The grid in figure 5.16 seems to be a fair compromise, but it can not be claimed that this grid gives grid independent results.

The final calculations consist of a calculation with the k-ϵ model and a series of calculations with the Reynolds stress and flux models. During the first preliminary calculations, both the standard implementation and the implementation made of the wall laws in the present study were tested. It was found that the difference between the two implementations was small compared to other problems found in the calculations. The final calculations have therefore only been performed for the standard implementation of the wall laws.

It was attempted also to use the higher upwind convection scheme. It turned out to be quite difficult to get a converged solution with this scheme. Since the importance of the convection scheme probably is small compared to some of the other problems in the calculations, it was decided to used the hybrid convection scheme in final calculations. Since no 'effective' viscosity or diffusivity appears in the momentum and the temperature equations for the Reynolds stress and flux model, it is not possible to use the hybrid scheme here and therefore the upwind scheme has been used instead for these equations.

The wall reflection terms has been implemented so that they take the walls of the tubes inside the unit cell into account. It could be argued that the contributions from some of the tubes outside the unit cell also should be taken into account. However, the wall reflection term is most important in the immediate vicinity of the reflecting wall and it is probably questionable whether it really represents effects from other walls in the quite complex flow in a tube bundle. Furthermore, it would be quite complicated to implement the term for all possible walls and therefore it has been chosen only to use the walls of the tubes inside the unit cell.

A first impression of the difference between the results from the k-ϵ model and the Reynolds stress model is given by the streamline plots in figure 5.17. It is evident that the k-ϵ model predicts a much smaller recirculation zone than the Reynolds stress model. The streamline plots should be compared with the visualization shown on e.g. figure 2.8. The velocity field predicted using the Reynolds stress model seems to be in the best agreement with the experimental results. This is a tendency that is also found for other flows with recirculation zones, e.g. the abrupt pipe expansion.

In appendix D.2 the numerical result for both tube bundles are compared with the results from LDA measurements. This is done with plots of profiles of the velocities and the Reynolds stresses along the five lines shown in figure 5.18. These lines are the sides of a unit-cell, a line through the recirculation zone and a line downstream of the recirculation zone. The five profiles together therefore give an impression of the most important features in the flow. The coordinate systems used for the plots are also shown in figure 5.18.

The numerical results for tube bundle A with a Reynolds number of $Re = 32\,000$ are compared in appendix D.2.1 with the results from the LDA results presented in section 2.2. The pattern observed from the streamline plots is also seen here. The length of the recirculation zone can be judged from the plots of U_1 in the wake region ($x_2 = 0$). The plot of the measured data indicate that the recirculation zone extends to $x_1 = 0.99\,D$ while the plots of the numerical results predict that the recirculation zone extends to $x_1 = 0.70\,D$ and $x_1 = 1.07\,D$ for the k-ϵ and the Reynolds stress models, respectively. The k-ϵ model therefore predicts a too small recirculation zone, while the predictions of the Reynolds stress model is closer to the experiments; the recirculation zone is here a little too long and, according to the plot of U_1 for $x_1 = 0.8\,D$, a little too narrow compared with the experiment. At the inlet to the unit cell the velocity profile predicted by the Reynolds stress model is

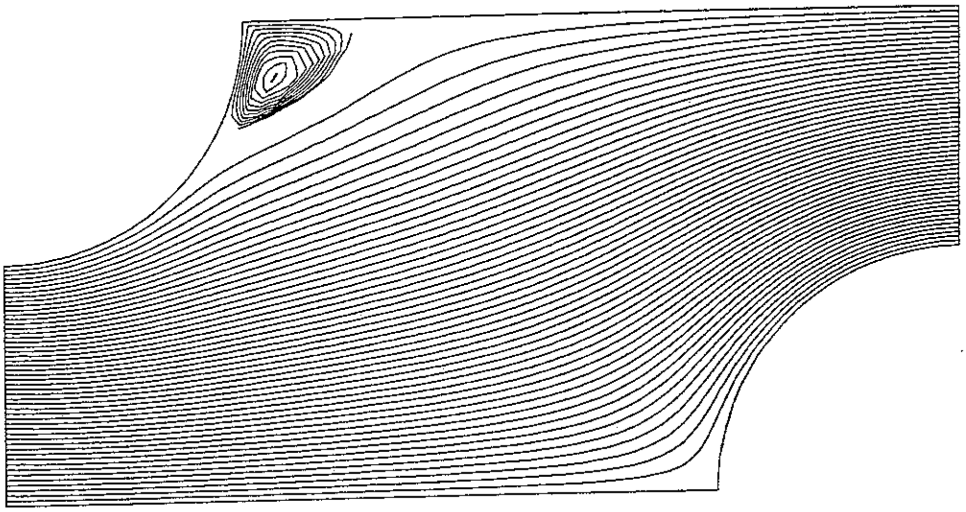

a) k-ϵ model

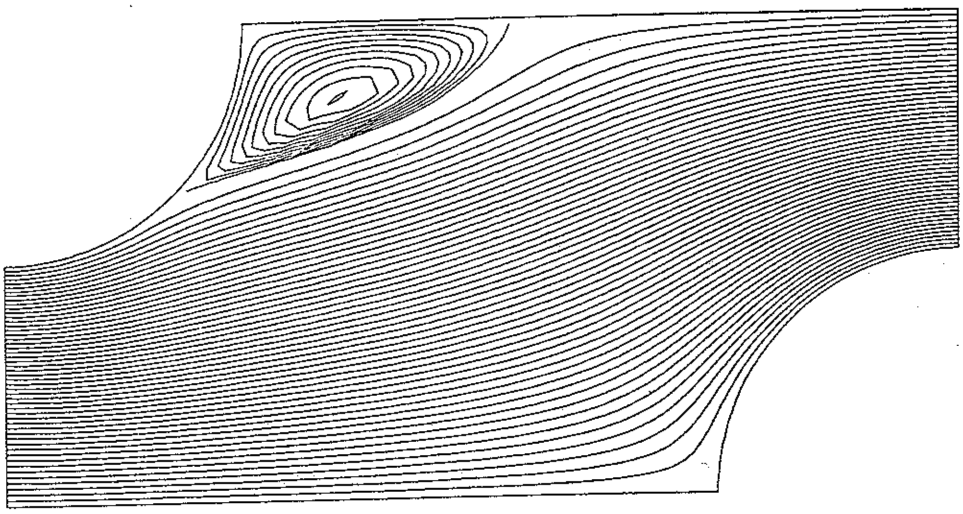

b) Reynolds stress model

Figure 5.17: Streamline plots for $Re = 32\,000$ in tube bundle A.

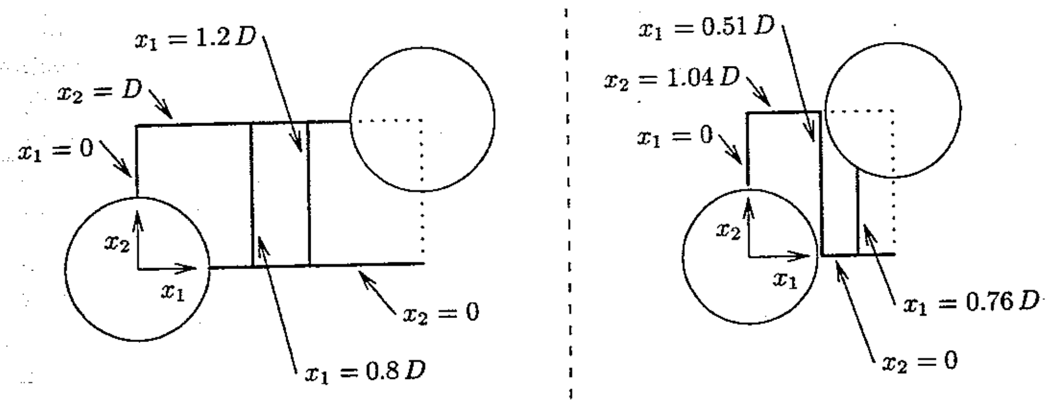

Tube bundle A

Tube bundle B

Figure 5.18: Lines in the tube bundle unit cells where profiles have been plotted.

quite close to the experiment while the k-ϵ model finds a more flat velocity profile, probably because of the too small recirculation zone. In the impact region the U_1 velocity predicted by the k-ϵ model is in good agreement with the experiment while the Reynolds stress model predicts a U_1-profile with the right shape, but with a level about 20 % too low. This problem is probably connected to the narrowness of the recirculation zone.

The turbulent kinetic energy $k = \frac{1}{2}\overline{u_i u_i}$ can not be found from the LDA-experiments because $\overline{u_3 u_3}$ was not measured. Since $\overline{u_1 u_1}$ and $\overline{u_2 u_2}$ are quite different in many parts of the flow an estimate value like $k = \frac{3}{4}(\overline{u_1 u_1} + \overline{u_2 u_2})$ will probably be quite inaccurate in many positions. It can be said that the k-ϵ model assumes that the Reynolds stresses are isotropic. It has therefore been found reasonable to compare the results from the calculations with the k-ϵ model with the experiments using an isotropic estimate of the Reynolds stresses: $\overline{u_1 u_1} = \overline{u_2 u_2} = \frac{2}{3}k$. This is an estimate and it can only be used to give an impression of the level of k compared to the experimental data.

The plots in appendix D.2.1 show that in the wake of the tube the level of k predicted by the k-ϵ model is clearly too low while it at the inlet to the unit cell and in the impact region it tends to be too high. While the general levels of k outside the wake therefore has the same order of magnitude as the measurements, the general levels of the Reynolds stresses predicted with the Reynolds stress model are much too low at all positions. In contrast to the k-ϵ model, the Reynolds stress model does predict a peak for the Reynolds stresses in the recirculation zone although the peak is closer to the symmetry line than the peak found experimentally. Both models finds a peak in $\overline{u_1 u_1}$ just upstream of the front stagnation point. The experimental data show no indication of such a peak although the measurements do not cover this position very well.

The performance of the k-ϵ model is reasonable when the well known weaknesses of this model are taken into account. But it is surprising that the performance of the Reynolds stress model is significantly poorer than the k-ϵ model. The reason for this is not clear. To test whether the periodic boundary condition could cause problems a calculation on a 'full' tube bundle was performed. This bundle contained five unit cells, a rather coarse grid with 200×20 cells and used traditional inlet and outlet instead of the periodic boundary condition. The Reynolds stresses in the fourth unit cell were compared with the results of the calculations shown in appendix D.2.1. The calculation on the 'full' tube bundle gave essentially the same results as the calculations with the periodic boundary condition. This indicates that it is not the periodic boundary condition that causes the low levels of the Reynolds stresses.

In the figures 5.19 and 5.20 the local heat transfer from the surface of a tube is plotted against the angle ϕ from the front stagnation point. The local Nusselt number Nu has been normalized by $Re^{0.6}$, since both the correlation (2.3) and the figure 2.15 indicates that this should take account of the effect for the Reynolds number.

In figure 5.19, the local heat transfer for the k-ϵ and Reynolds stress models at $Re = 32\,000$ is compared with experimental data at $Re = 34\,100$. Both models find a general level of the heat transfer that is somewhat smaller than that of the experiment. The major difference between the k-ϵ model and the Reynolds stress model is that the k-ϵ model has a higher level of the local Nusselt number, particularly on the front side of the tube.

The calculated Nusselt numbers have small peaks at the front and rear stagnation points. These peaks are probably caused by the distorted cells at the stagnation points. This is supported by the fact that a calculation with the grid having distorted cells located at another position (mentioned on page 84) did not find these peaks in the local Nusselt number.

Increasing the angle ϕ the calculated local Nusselt number is increasing on the front side of the tube, takes its highest value at $\phi \approx 90°$ and is then decreasing again until the recirculation zone where the Nusselt number with minor variations takes a constant level. In contrast to this, the local Nusselt number found experimentally takes its largest value at the front stagnation point and is decreasing on the front side of the tube. On the rear of the tube it has a generally lower level and a characteristic variation with minima at 100° and 150° and maxima at 120° and 180°.

Figure 5.20 shows a series of calculations with the Reynolds stress model using different Reynolds numbers. The local Nusselt numbers normalized by $Re^{0.6}$ are generally close to each other. With increasing Reynolds number the level is increasing slightly outside the recirculation zone while it is decreasing slightly inside the recirculation zone. Although the variation is somewhat larger than the quite small variations seen for the experimental data on figure 2.15 using the same Reynolds numbers, the plots on figure 5.20 show that the calculated Nusselt number also scales reasonable well with $Re^{0.6}$.

5.4.3 Numerical results for tube bundle B

Using the same type of grid and calculation procedure as the one used in the previous section for tube bundle A, the calculations on tube bundle B gave

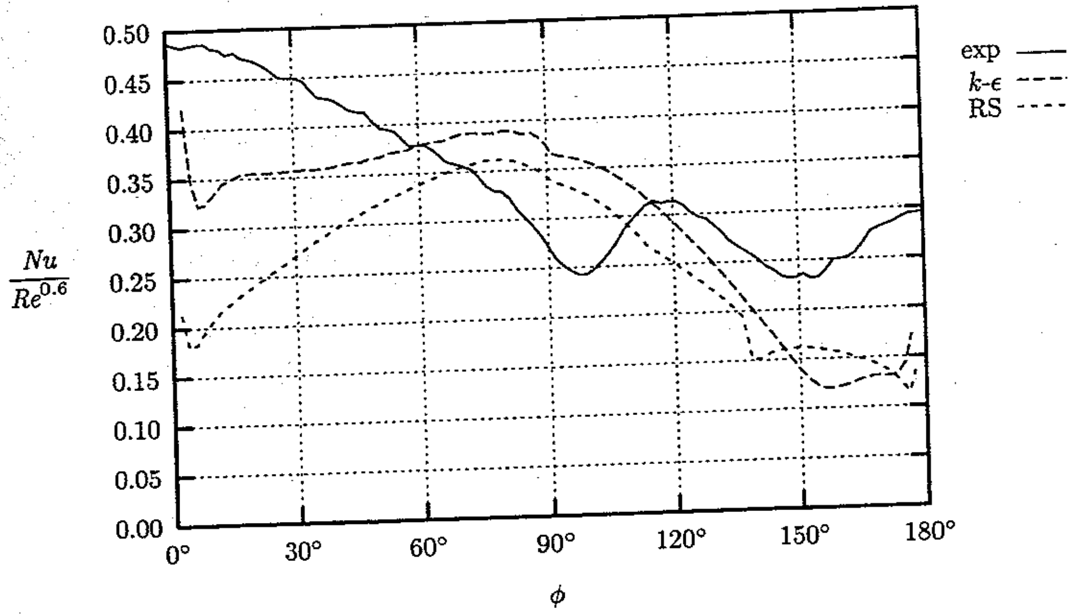

Figure 5.19: Local heat transfer for k-ϵ and Reynolds stress (RS) models at $Re = 32\,000$ compared with experimental data at $Re = 34\,100$.

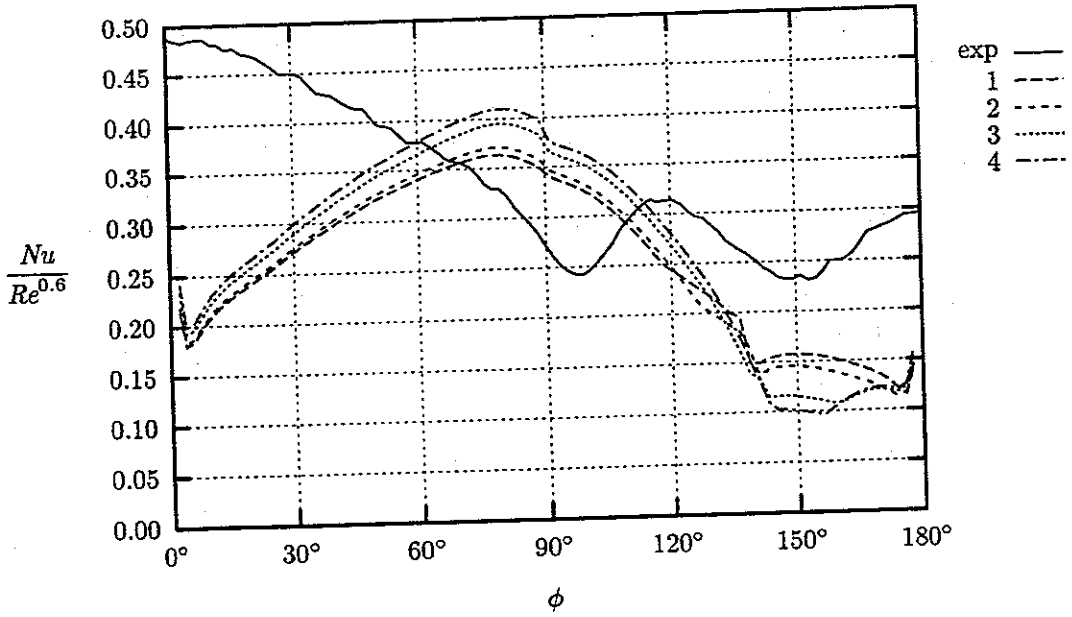

Figure 5.20: Local heat transfer for Reynolds stress models at 1) $Re = 34\,100$, 2) $Re = 41\,500$, 3) $Re = 70\,000$ and 4) $Re = 91\,200$ compared with experimental data at $Re = 34\,100$.

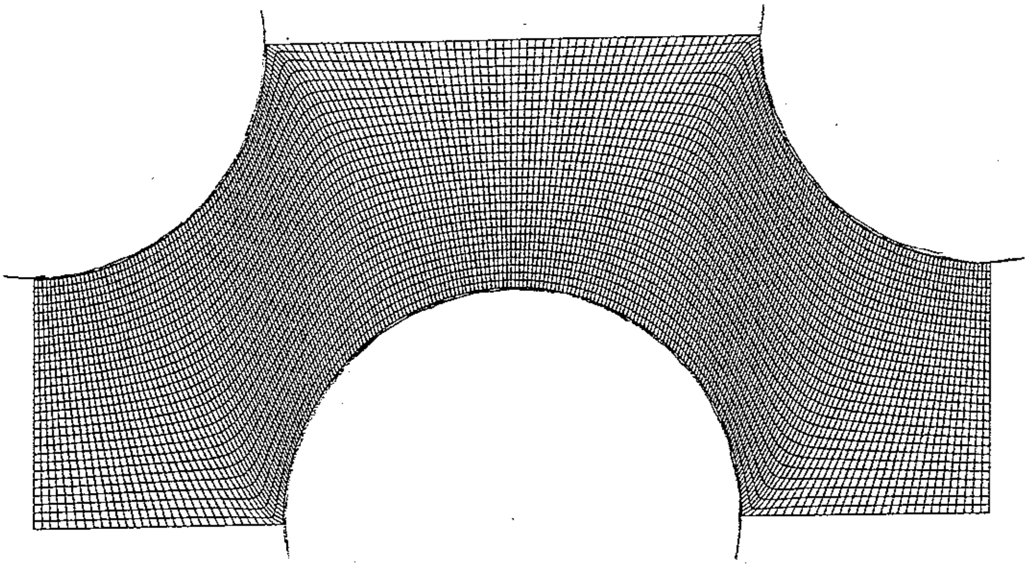

Figure 5.21: Grid used for tube bundle B.

either unstable or oscillating solutions. Several different procedures to solve this problem were attempted. It was found that with a computational domain consisting of two unit cells combined with the use of low underrelaxation factors for the equations it was possible to obtain a solution where the oscillations were dampened so that a steady solution could be reached.

Two grids with 160×20 and 240×30 cells, respectively, where tested. There was found some differences in the level of the Reynolds stresses for the two grids and none of the grids can therefore be claimed to give grid independent solutions. However, values of y^+ less than 11 on parts of the tube walls are found for the calculations made with both grids and it was estimated that it therefore was not reasonable to refine the grid further. The grid with 240×30 cells is shown in figure 5.21 and was chosen for the final calculations.

The results in terms of the velocity and Reynolds stresses for this calculation has been presented at the *'2nd ERCOFTAC-IAHR Workshop on Refined Flow Modelling'* [59], where the flow in tube bundle B was one of the test cases. Earlier calculations have also been reported by Sebag *et al* [66, 67].

Most of the problems with the calculation procedures that were discussed for tube bundle A also apply for tube bundle B and will therefore not be repeated. The final calculations on tube bundle B used nearly the same approach as tube bundle A: hybrid and upwind convection schemes, the wall functions implemented in the present study and the wall reflection terms from tube walls in the units cell. The calculations are only performed for a single Reynolds number: $Re = 40\,000$.

Figure 5.22 shows streamline plots for the performed calculations. The results from the k-ϵ model show no recirculation zone while the result from the Reynolds stress model show a small area with recirculation. The streamlines are here rather kinked because the grid is coarse compared to the dimensions of the recirculation area.

In appendix D.2.2 the profiles of the velocities and the Reynolds stresses

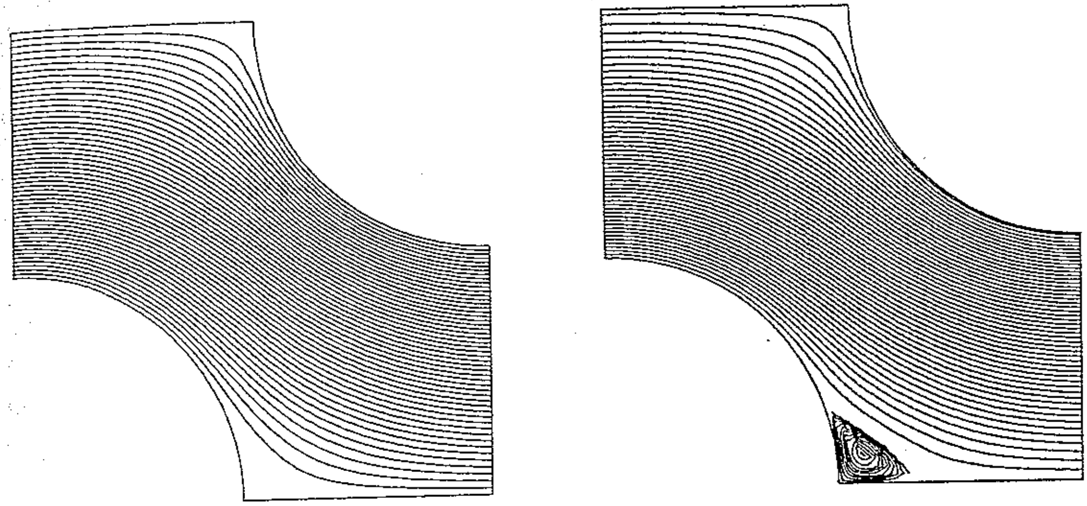

a) k-ϵ model

b) Reynolds stress model

Figure 5.22: Streamline plots for $Re = 40\,000$ in tube bundle B.

are plotted along the five lines shown on figure 5.18. These plots confirm the observations from the streamline plots about the recirculation zones. The recirculation zone found experimentally seems to be a little larger than the one found in the calculation with the Reynolds stress model. At the inlet, the velocities found by the calculation have a higher level than the velocities found experimentally. The reason for this must be that the velocities found experimentally do not correspond to the stated velocity U_0 upstream of the tube bundle. When this difference is taken into account it can be seen that in the impact region the Reynolds stress model tends to predict too low velocities while the k-ϵ model predicts velocities closer to the experimental data. This tendency was also found for tube bundle A.

In the plots of the Reynolds stresses the k-ϵ model again uses an isotropic estimate: $\overline{u_1u_1} = \overline{u_2u_2} = \frac{2}{3}k$. Here its is found that the k-ϵ model predicts too high levels of turbulent kinetic energy, except for the wake region where the levels are somewhat too low. In contrast to this, the Reynolds stress model predicts much too low levels of the Reynolds stresses at all locations. These results are very similar to the result of the calculations for tube bundle A. Like it was found for tube bundle A, both models also predict a peak in $\overline{u_1u_1}$ just upstream of the front stagnation point. Some measurements are available for tube bundle B in this region and they show no sign of a peak in $\overline{u_1u_1}$.

At the *'2nd ERCOFTAC-IAHR Workshop on Refined Flow Modelling'* [59] the flow in tube bundle B without heat transfer was used as one of the test cases. There was large scattering in the level of the Reynolds stresses for presented results with the Reynolds stress model, but in most of the cases the predicted levels were closer to the experimental data than those of the present study. This indicates that the difference between experiment and prediction to a large extent is cause by other factors than deficiencies in the basic Reynolds stress model.

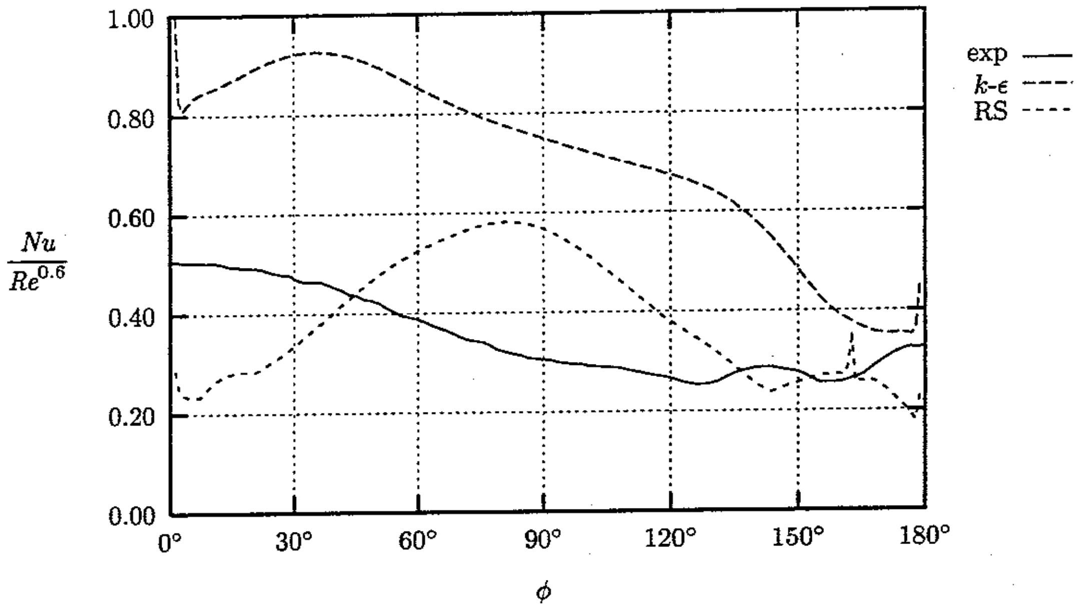

Figure 5.23: Local heat transfer at $Re = 40\,000$ for k-ϵ and Reynolds stress (RS) models compared with experimental data (see text).

The local heat transfer found in the calculations and the experiment is shown in figure 5.23. Like in the calculations on tube bundle A, the peaks in the Nusselt number that are found at the stagnation points are probably caused by the distorted cells in these regions. The mean Nusselt number is significantly too high for the k-ϵ model while it for the Reynolds stress model happens to be close the experimental Nusselt number. The k-ϵ model does not the find the maximum heat transfer at the front stagnation point as in the experiment, but instead at $\phi \approx 30°$. It also does not reproduce the small variations found in the recirculation zone.

The Reynolds stress model predicts minima in the front and rear stagnation points which is in contrast to the experimental data that have maxima at these locations. As for tube bundle A the Reynolds stress model again finds a maximum at $\phi = 90°$. It also finds some variations and a minor peak in the recirculation zone, but the variations do not correspond to the variations found experimentally. The peak is probably caused by a very low value of y^+ at this location.

5.4.4 Conclusion

It is not unexpected that the performance of the k-ϵ model is not very good for the quite complex flow in a tube bundle. However, it is surprising that the Reynolds stress model gives a significantly poorer prediction of the level of turbulence than the k-ϵ model. There are several possible reasons for this of which some will be discussed in the following:

There could be some sort of deficiency in the Reynolds stress model that caused e.g. to low generation or too high dissipation of the turbulent kinetic energy for this particular flow. An example could be that the turbulence model was incapable of modelling irregular vortex shedding from the rear side of the tubes. However, since the k-ϵ model seems to be able predict a level of the turbulent kinetic energy that is in the same order of magnitude as the experiment, it is not likely that the modelling of e.g. vortex shedding is the problem for the Reynolds stress model. The fact that other authors [66, 59] have made calculations with the Reynolds stress model that find a level of the turbulent kinetic energy significantly closer to the experimental data, makes it likely that the low levels found in the present study is caused by other factors as well as possible deficiencies in the Reynolds stress model.

One of the possible factors is that the wall boundary conditions cause problems in connection with the Reynolds stress model. Since two different boundary conditions for the Reynolds stresses has been tested, it is not likely that the reason should be found in the boundary condition of the Reynolds stresses. However, as it is seen in equation (4.56) and (4.57) the term that is used to find the wall shear stress used in the momentum equations contains a factor that is roughly proportional to $k^{1/2}$. A low level of k will therefore result in a low wall shear stress. This might decrease the velocity gradients near the wall and a decrease in the velocity gradients might result in a lower generation of k. If the productions terms in the Reynolds stress equations are more sensitive to such a reduction of the velocity gradients than the production term in the k-equation, this could explain the large difference in the levels of k.

In FLOW3D the value of y^+ is calculated as $y^+ = (c_\mu)^{1/4} y^*$ where y^* is the modified wall coordinate defined in equation (3.51). This value of y^+ therefore also contains $k^{1/2}$ as a factor. While $y^+ > 11$ for nearly all near wall cells in the calculations with the k-ϵ model, the calculations with the Reynolds stress model generally have lower levels of y^+ due to low values of k and there are large areas where $y^+ < 11$. Even if the wall laws are not the most important reason for the low levels of k the assumptions, that the wall laws are based on, are not fulfilled. The wall laws will therefore probably cause some kind of errors in the results.

Because of the problems with low levels of k it is difficult to make any further conclusion regarding the performance of the Reynolds stress and flux models in a tube bundle. Further investigations should probably use an improved treatment of the walls, e.g. use a low Reynolds number turbulence model near the walls.

5.5 Closure

This chapter reports numerical results for three different test cases that have turbulent flow and heat transfer. 'Standard' models were use to model the turbulence: the k-ϵ model and the Reynolds stress and flux models. The wall boundary conditions were handled by wall laws.

The abrupt pipe expansion is the most simple of the cases and here it was possible to obtain satisfactory results for the local heat transfer coefficient. The calculations with the impinging jet demonstrated some well known deficiencies in the Reynolds stress model. Quite good agreement with numerical results by other authors was found for the Reynolds stresses. The wall boundary condition is probably not very important for the calculation of the Reynolds stresses. However, this calculations also demonstrated that the wall laws are unable to give good predictions of the local heat transfer for a flow with quite complex structures.

For these two test cases the inlet was found from a calculation of a fully developed pipe flow. The level of the turbulent kinetic energy is here to a large extent determined by the level at the inlet. The staggered tube bundle cases uses a periodic boundary condition instead of a traditional inlet and the level of the turbulent kinetic energy is therefore entirely determined in the calculation domain. The modelling of the wall boundary conditions therefore become important not only for the prediction of the heat transfer but also for the prediction of the flow and turbulence.

The calculation with the Reynolds stress model for the staggered tube bundles gives a much too low level of the Reynolds stresses. No final explanation for this has been established, but there is reason to believe that the use of wall laws is an important factor in this problem.

The calculations in this chapter has demonstrated that the use of walls laws in many simple flows, even flows with a recirculation zone, can give satisfactory results. However, for more complex flows it is probably essential to use a more refined way of handling the walls, e.g. a low Reynolds number turbulence model.

Chapter 6

Summary and conclusions

The most important of the tasks that have been performed in the present study are listed below:

- A water test channel with flow system has been designed to be used for LDA-measurements in a tube bundle. LDA-measurements have been performed in the middle of the tube bundle.
- Visualizations of the flow in the water channel designed for LDA-measurements was performed.
- A special constant heat flux tube has been designed to measure the local heat transfer in a tube bundle in an existing wind tunnel facility. This tube was used to measure the local heat transfer in the middle of two different tube bundles.
- Several changes have been made in the commercial finite volume computer code FLOW3D:
  - A new periodic boundary condition which enables both an asymmetric periodicity and a usual periodicity where variables such as pressure and temperature have a net change of level from "inlet" to "outlet".
  - A general form of the wall reflection terms for the Reynolds stress and flux equations. In the present version it can be used for two-dimensional geometries (but three-dimensional flows). It is straightforward to extend the implementation to three-dimensional geometries.
  - A new version of the Reynolds stress model proposed by Craft and Launder [56]. The implementation is valid for two-dimensional flows.
  - A new wall boundary condition has been implemented. This boundary condition uses a more accurate integration at the wall based on [23] and a new boundary condition for the Reynolds stresses based on [66].

- Calculations with the k-ϵ model and the Reynolds stress and flux models have been performed, of both flow and local heat transfer, for three different test cases. The results in terms of the velocities, Reynolds stresses and the local heat transfer have been compared with experimental data from the literature and from the present study.

The present experiments have been designed to produce data that are suitable for verification of calculations with turbulence models. The measurements have produced data for both local velocities and turbulence and for the local heat transfer in one staggered tube bundle. Data for the local heat transfer have also been produced for a tube bundle with another geometry. Data for local velocities and turbulence for this other geometry are available from [10]. All these data form two test cases for staggered tube bundles with quite different geometries.

The accuracy of the experimental data (typically ±3 %) are found to be satisfactory for the verification of calculations with turbulence models. However, there are several ways that the measurements could be improved and extended. The most important extention would probably be measurements of the velocities and turbulence close to the tube walls. Although there are reasons to believe that the flow can be considered to be fully developed at the positions where the measurements have been performed, it would be interesting with an investigation of the development of the flow and heat transfer in the inlet section to a tube bundle. An investigation of the importance of the number and the length of the tubes in each row would also be interesting. Several possible improvements of the accuracy of the measurements have been discussed in the thesis.

The calculations with the k-ϵ model have demonstrated that this model tends to predict too small recirculation zones. This is a well known problem with the k-ϵ model and this model is not very good for most complex flows. The Reynolds stress model has a significantly better performance although the test case with an impinging jet demonstrates that the basic Reynolds stress model also has deficiencies. Both models can be designed to give better improvements although the Reynolds stress model probably has the largest potential. However, the work with improvements of turbulence models is a laborious task and has not been covered in the present study.

Wall laws are based on assumptions that are not very well fulfilled in complex flows. Nevertheless, wall laws are used in lack of a better boundary condition. In the present study, a version of the wall laws that should be more robust to the conditions in a complex flow have been implemented. The flow conditions in the first two test cases seem to a large extent to be determined by the inlet conditions and not so much by the wall laws. The flow is therefore probably mostly determined by the turbulence model. However, the local heat transfer is very dependent of the conditions near the wall and is therefore mostly determined by the wall laws. For the abrupt pipe expansion, the new implementation of the wall laws seems to give important improvements and a result quite close to the experiment.

It is not surprising that the k-ϵ model gives a rather poor prediction of the flow and heat transfer in a tube bundle. It is, however, surprising that the Reynolds stress models, in constrast to the k-ϵ model, find much too low levels of the turbulent kinetic energy. The tube bundle calculations use a periodic boundary condition as the 'inlet'. The flow is therefore much more determined by the wall laws. There is therefore reason to believe that the problem with the low levels of the turbulent kinetic energy might be connected to the weaknesses in the wall laws and/or to numerical problems that come from the combination of the Reynolds stress model and the use of wall laws.

The most important way to improve the results of the calculations is probably to use a low Reynolds number turbulence model at the wall instead of wall laws. This requires a grid that is able to resolve the sublayer at the wall down to about $y^+ = 1$ and therefore a larger computational effort. Unfortunately, there was no direct possibilities of performing such calculations in the used version of FLOW3D.

Since the present study has used the commercial code FLOW3D a short evaluation will be given of this program. It has been found that the program is relatively easy to use in most cases. However, it is quite difficult and laborious to make changes, like the periodic boundary condition and the new implementation of the wall functions that have been made in the present study. Unfortunately, there seems to be a tendency that commercial programs for computational fluid mechanics give very limited possibilities for changes in the calculation procedures. There is therefore still a great need for programs that might be less easy to use, but that instead makes it easy to implement new models and methods.

Nomenclature

Below follows a list of the most important symbols used in the present study. Note that general tensor notation is used in chapter 4 while Cartesian tensor notation is used in other parts of the study.

Italic symbols:

$A, \mathbf{A}$	Area.
$A^i_{\;j}$	Adjugate Jacobian matrix.
a	Transverse pitch between tubes; matrix coefficient.
B^k_i	Coefficient used in equation (4.39).
b	Longitudinal pitch between tubes; matrix coefficent.
C	Convective term or coefficient.
c	Various constants – indices are defined in the text.
c_p	Specific heat.
D^k_i	Coefficient used in equation (4.41).
D	Diffusive term or coefficient.
D, d	Diameter.
E	Logarithmic wall law constant.
$e, \mathbf{e}$	Basis vector.
F	Time averaged body force or body force term.
f	Fluctuating part of body force; frequency.
Fr	Frössling number.
H, h	height.
h	Heat transfer coefficient.
$\hat{I}^i$	Total flux.
$J^i_{\;j}$	Jacobian matrix.
$\|J\|$	Jacobian determinant.
k	Turbulent kinetic energy.

k_q	Blokage factor.
L, l	Length.
$\dot{m}$	Mass flow rate.
n_i	Unit vector.
Nu	Nusselt number.
Nu_{DB}	Nusselt number given by Dittus-Boelter equation (5.6).
P	Time averaged pressure; Production term; "Pee-function" from equation (3.43).
p	Fluctuating part of pressure.
Pe	Peclet number.
Pr	Prandtl number.
q''	Heat flux.
R^{k*}	Rhie-Chow term, see equation (4.47).
R''	Surface resistance.
r	Coordinate in radial direction.
Re	Reynolds number.
S	Source term.
s_1, s_2	Transverse and longitudinal distance between tubes.
Sr	Strouhal number.
T	Temperature.
ΔT	Temperature difference.
t	Time.
t_i	Unit vector.
Tu	Turbulence intensity.
U	Time averaged velocity.
U_{bulk}	Bulk velocity ($U_{bulk} = \sqrt{U_1^2 + U_2^2 + U_3^2}$).
U_τ	Wall friction velocity.
u	Fluctuating part of velocity.
$\overline{u_i u_j}$	Reynolds stress.
$\overline{u_i \theta}$	Reynolds flux.
V	Voltage; volume; velocity in y-direction.
$V, \mathbf{V}$	Vector.
v	Fluctuating velocity in y-direction.

vol	Volume of control volume.
x	Coordinate in physical space.
y	Coordinate in physical space.
z	Coordinate in physical space.

Greek symbols

α	Underrelaxation factor.
β	Temperature coefficient.
Γ	Diffusivity for general scalar.
γ	Isentrop exponent.
δ_{ij}, δ^i_j	Kronecker delta.
ϵ	Dissipation of turbulent kinetic energy.
ϵ_g	Emissivity.
Θ	Time averaged general scalar.
θ	Fluctuating part of general scalar.
κ	von Karman constant.
λ	Thermal conductivity.
μ	Dynamic viscosity.
ν	Kinematic viscosity.
ρ	Density.
σ	Prandtl number for general scalar; Stefan Bolzmann's constant.
τ	Shear stress.
ϕ	Angle; pressure strain term; general scalar.
ξ	Coordinate in computational space.
η	Coordinate in computational space.
ζ	Coordinate in computational space.
Ω	Control volume.

Subscripts

i, j, k, l, m	Vector and tensor indices.
E, N, P, S, W	Cell nodes, see figure 4.3.
e, n, s, w	Cell faces, see figure 4.3.
nb	Index running through neighbouring cell nodes.

nn	Index running through faces of control volume.
$cond$	Conduction.
$conv$	Convection.
eff	Effective.
el	Electric.
in	Inlet.
rad	Radiation.
k	For k-equation.
m	Mean value; mass.
t	Turbulent.
w	At the wall.
0	Reference condition.
∞	Condition far away from wall.

Superscripts

$\overline{}$	Time average; average between nodes; mean value; inverse.
$\hat{}$	Normal flux component.
$+$	Wall coordinates.
$*$	Modified wall coordinates; most recent updated value.
$**$	Corrected value.
i, j, k	Vector and tensor indices.
n	Time step index.

Bibliography

[1] A. Žukauskas and R. Ulinskas. *Heat Transfer in Tube Banks in Crossflow.* Hemisphere Publishing Corporation, 1988.

[2] A. Žukauskas. Heat transfer from tubes in crossflow. *Anvances in Heat Transfer*, 18:87–157, 1987.

[3] A. Žukauskas and J. Žiugžda. *Heat Transfer of a Cylinder in Crossflow.* Hemisphere Publishing Corporation, 1985.

[4] S. Ziada and A. Oengören. Vorticity shedding and acoustic resonance in an in-line tube bundle part 1: Vorticity shedding. *Journal of Fluids and Structures*, 6(3):271–292, 1992.

[5] K. E. Meyer, F. Christensen, and H. S. Kristensen. Measurement of flow and heat transfer in staggered tube bundle. Report AFM 92–04, Department of Fluid Mechanics, Technical University of Denmark, 1992.

[6] S. B. H. C. Neal and J. A. Hitchcock. Heat transfer and gas flow processes within a bank of close pitched plain tubes in cross-flow. Note RD/L/N 9/67, CERL, 1967.

[7] R. J. Simoneau and G. J. VanFossen. Effect of location in an array on heat transfer to a short cylinder in crossflow. *Journal of Heat Transfer*, 106:42–48, 1984.

[8] A. Dybbs and R. V. Edwards. Refractive index matching for difficult situations. In *Second International Conference on Laser Anemometry – Advances and Applications*, Strathclyde, Scotland, Sept. 1987.

[9] M. S. Halim and J. T. Turner. Measurements off cross flow development in a staggered tube bundle. In *Proceedings of the 3rd International Symposium on Applications of LDA to Fluid Mechanics*, Lisbon, Portugal, July 1986.

[10] O. Simonin and M. Barcouda. Measurements and prediction of turbulent flow entering a staggered tube bundle. In *Proceedings of the 4th International Symposium on Applications of LDA to Fluid Mechanics*, Lisbon, Portugal, 1988.

[11] Durchflußmessung mit genormten düsen, blenden und venturidüsen. DIN 1952, Deutsche Normen, Aug. 1971.

[12] O. A. Jørgensen and U. Marxen. Turbulent strømning over ribber. Report AFM EP 93-06 C, Department of Fluid Mechanics, Technical University of Denmark, Aug. 1993. Documentation of program for LDA-measurements (in danish).

[13] P. Buchhave, W. K. George, Jr., and J. L. Lumley. The measurement of turbulence with the laser-Doppler anemometer. *Annual Reviews of Fluid Mechanics*, 11:443–503, 1979.

[14] C. C. Winding and A. J. Cheney. Mass and heat transfer in tube banks. *Industrial and Engineering Chemistry*, 40(6):1087–1093, 1948.

[15] R. A. DeBortoli, R. E. Grimble, and J. E. Zerbe. Average and local heat transfer for cross flow through a tube bank. *Nuclear Science and Engineering*, 1:239–251, 1956.

[16] F. Mayinger and O. Schad. Örtliche wärmeübergangszahlen in querangeströmten stabbündeln. *Wärme- und Stoffübertragung*, 1:43–51, 1968.

[17] A. A. Žukauskas, R. V. Ulinskas, and K. F. Martsinauskas. Influence of the geometry of the tube bundle on the local heat transfer rate in the critical region of streamline flow. *International Chemical Engineering*, 17(4):744–751, 1977.

[18] A. A. Žukauskas, R. V. Ulinskas, and P. I. Daunoras. Local coefficients of heat transfer from staggered bundles of rough tubes in crossflow. *Heat Transfer - Soviet Research*, 18(1):108–117, 1986.

[19] J. W. Baughn, M. J. Elderkin, and A. A. McKillop. Heat transfer from a single cylinder, cylinders in tandem, and cylinders in the entrance region of a tube bank with a uniform heat flux. *Journal of Heat Transfer*, 108:386–391, 1986.

[20] J. W. Baughn, R. K. Takahashi, M. A. Hoffman, and A. A. McKillop. Local heat transfer measurments using an electrically heated thin gold-coated plastic sheet. *Journal of Heat Transfer*, 107:953–959, 1985.

[21] Courtaulds Performance Films, 21034 Osborne Street, Canoga Park, CA 91304, USA. *Gold coated plastic film.*

[22] F. P. Incropera and D. P. DeWitt. *Fundamentals of Heat and Mass Transfer.* John Wiley & Sons, second edition, 1985.

[23] B. E. Launder. On the computation of convective heat transfer in complex turbulent flows. *Journal of Heat Transfer*, 110:1112–1128, 1988.

[24] C. Benocci. Modelling of turbulent heat transport – a-state-of-the-art. Technical Memorandum 47, VKI, 1991.

[25] B. E. Launder. Second-moment closure: present ... and future? *International Journal of Heat and Fluid Flow*, 10(4):282–300, 1989.

[26] M. A. Leschziner. Modeling turbulent recirculating flows by finite-volume methods - current status and future directions. *International Journal of Heat and Fluid Flow*, 10(3):186–202, 1989.

[27] M. Nallasamy. Turbulence models and their applications to the prediction of internal flows: a review. *Computers and Fluids*, 15(2):151–194, 1987.

[28] C. G. Speziale. Analytical methods for the development of Reynolds-stress closures in turbulence. *Annual Reviews of Fluid Mechanics*, 23:107–157, 1991.

[29] W. Rodi. Turbulence models and their application in hydralics. State-of-the-art paper, IAHR, Delft, 1980.

[30] B. E. Launder, G. J. Reece, and W. Rodi. Progress in the development of a Reynolds-stress turbulence closure. *Journal of Fluid Mechanics*, 68(3):537–566, 1975.

[31] K. Hanjalic and B. E. Launder. A Reynolds stress model of turbulence and its application to thin shear flows. *Journal of Fluid Mechanics*, 52(4):609–638, 1972.

[32] B. J. Daly and F. H. Harlow. Transport equations in turbulence. *Physics of Fluids*, 13:2634–2649, 1970.

[33] M. M. Gibson and B. E. Launder. Ground effects on pressure fluxtuations in the atmospheric boundary layer. *Journal of Fluid Mechanics*, 86(3):491–511, 1978.

[34] UMIST. *4th Biennial Colloquium on Computational Fluid Dynamics*, 24–25 Apr. 1990.

[35] W. Rodi. A new algebraic relation for calculating the Reynolds stresses. *Zeitschrift für angewandte mathematik und mechanik*, 56:T219–T221, 1976.

[36] J. Laufer. Investigation of turbulent flow in a two-dimensional channel. Report 1053, Naca, 1952.

[37] C. L. V. Jayatilleke. The influence of prandtl number and surface roughness on the resistance of the laminar sub-layer to momentum and heat transfer. *Progress in Heat and Mass Transfer*, 1:193–329, 1969.

[38] C. C. Chieng and B. E. Launder. On the calculation of turbulent heat transport downstream from an abrupt pipe expansion. *Numerical Heat Transfer*, 3:189–207, 1980.

[39] W. P. Jones and B. E. Launder. The prediction of laminarization with a two-equation model of turbulence. *International Journal of Heat and Mass Transfer*, 15:301–314, 1972.

[40] S. Obi, M. Peric, and G. Scheuerer. Second-moment calculation procedure for turbulent flows with collocated variable arrangement. *AIAA Journal*, 29(4):585–590, 1991.

[41] V. C. Patel, W. Rodi, and G. Scheuerer. Turbulence models for near-wall and low Reynolds number flows: A review. *AIAA Journal*, 23(9):1305–1319, 1985.

[42] B. E. Launder and B. I. Sharma. Application of the energy-dissipation model of turbulence to the calculation of flow near a spinning disc. *Letters in Heat and Mass Transfer*, 1:131–138, 1974.

[43] D. C. Wilcox and W. M. Rubesin. Progress in turbulence modeling for complex flow fields including effects of compressibility. Technical Paper 1517, NASA, 1980.

[44] C. G. Speziale, R. Abid, and E. C. Anderson. A critical evaluation of two-equation models for near wall turbulence. Paper 90–1481, AIAA, 1990.

[45] Y. G. Lai and R. M. C. So. On near-wall turbulent flow modelling. *Journal of Fluid Mechanics*, 221:641–673, 1990.

[46] Y. G. Lai and R. M. C. So. Near-wall modelling of turbulent heat fluxes. *International Journal of Heat and Mass Transfer*, 33(7):1429–1440, 1990.

[47] R. M. C. So, Y. G. Lai, H. S. Zhang, and B. C. Hwang. Second-order near-wall turbulence closures: A review. *AIAA Journal*, 29(11):1819–1835, 1991.

[48] A. D. Burns and N. S. Wilkes. A finite differece method for the computation of fluid flows in complex three dimensional geometries. Technical Report AERE-R 12342, Harwell Laboratory, UK, 1987.

[49] CFDS, AEA Industrial Technology, Harwell Laboratory, UK. *FLOW3D Release 2.4 - Users Manual*, Aug. 1991.

[50] D. S. Clarke and N. S. Wilkes. The calculation of turbulent flows in complex geometries using a differential stress model. Technical Report AERE-R 13428, Harwell Laboratory, UK, 1989.

[51] D. S. Clarke and N. S. Wilkes. The calculation of turbulent flows in complex geometries using a differential flux model. Technical Report AEA-InTec-0216, Harwell Laboratory, UK, 1991.

[52] S. V. Patankar. *Numerical Heat Transfer and Fluid Flow.* Hemisphere Publishing Corporation, 1980.

[53] M. Peric. *A Finite Volume Method for the Prediction of Three-Dimensional Fluid Flow in Complex Ducts.* PhD thesis, University of London, Imperial College, Aug. 1985.

[54] C. M. Rhie and W. L. Chow. Numerical study of the turbulent flow past an airfoil with trailing edge separation. *AIAA Journal*, 21(11):1525–1532, 1983.

[55] G. A. Hawkins. *Multilinear Analysis for Students in Engineering and Science.* John Wiley and Sons, Inc., 1967.

[56] T. J. Craft and B. E. Launder. New wall-reflection model applied to the turbulent impinging jet. *AIAA Journal*, 30(12):2970–2972, 1992.

[57] J. W. Baughn, M. A. Hoffman, R. K. Takahashi, and B. E. Launder. Local heat transfer downstream of an abrupt expansion in a circular channel with constant wall heat flux. *Journal of Heat Transfer*, 106:789–796, 1984.

[58] W. C. Lasher and D. B. Taulbee. On the computation of turbulent backstep flow. *International Journal of Heat and Fluid Flow*, 13(1):30–40, 1992.

[59] M. A. Leschziner and B. E. Launder, editors. *2nd ERCOFTAC-IAHR Workshop on Refined Flow Modelling*, UMIST, Manchester, UK, 15–16 June 1993.

[60] D. Cooper, D. C. Jackson, B. E. Launder, and G. X. Liao. Impinging jet studies for turbulence model assessment – I. flow-field experiments. *International Journal of Heat and Mass Transfer*, 10:2675–2684, 1993.

[61] J. W. Baughn and S. Shimizu. Heat transfer measurements from a surface with uniform heat flux and an impinging jet. *Journal of Heat Transfer*, 111:1096–1098, 1989.

[62] J. W. Baughn, X. J. Yan, and M. Mesbah. The effect of Reynolds number on the heat transfer from a plate to a turbulent impinging jet. In *Winter Annual Meeting*. ASME, Nov. 1992.

[63] T. J. Craft, L. J. W. Graham, and B. E. Launder. Impinging jet studies for turbulence model assessment – II. an examination of the performance of four turbulence models. *International Journal of Heat and Mass Transfer*, 10:2685–2697, 1992.

[64] I. Demirdzic, A. D. Gosman, R. I. Issa, and M. Peric. A calculation procedure for turbulent flow in complex geometries. *Computers and Fluids*, 15(3):251–273, 1987.

[65] K. A. Antonopoulos. Heat transfer in tube banks under conditions of turbulent inclined flow. *International Journal of Heat and Mass Transfer*, 28(9):1645–1656, 1985.

[66] S. Sebag, V. Maupu, and D. Laurence. Non-orthogonal calculation procedures using second moment closure. In *Eighth Symposium on Turbulent Shear Flows*, Technical University of Munich, 9–11 Sept. 1991.

[67] S. Sebag. *Modele aux Tensions de Reynolds sur Maillages Structures Non-Orthogonaux Application a un Ecoulement dans un Faisceau de Tube en Quinconce.* PhD thesis, Electricite de France, Département Laboratoire National d'Hydraulique, 1991.

[68] H. S. Kristensen. *Formler til varmetransmission.* Polyteknisk forlag, Lyngby, Denmark, 5 edition, 1985. (in danish).

[69] H. S. Kristensen. Hot-wire målinger i turbulente strømninger. Report AFM 73-15, Department of Fluid Mechanics, Technical University of Denmark, Dec. 1973. (in danish).

[70] G. Ekström, editor. *Perstorpsboken.* Maskinaktiebolaget Karlebo, Stockholm, 3. edition, 1980.

[71] W. H. Press, B. P. Flannery, S. A. Teukolsky, and W. T. Vetterling. *Numerical Recipes – The Art of Scientific Computing.* Cambridge University Press, 1986.

Appendix A

Boundary conditions for $\overline{u_i u_j}$ and $\overline{u_i \theta}$

This appendix will show a possible implementation of a boundary condition for the Reynolds stresses and fluxes. First it will be shown how values of Reynolds stresses found in a coordinate system local to a wall can be transformed into a global coordinate system. Then it will be shown how values of the Reynolds stresses and fluxes can be approximated using the algebraic Reynolds stress and flux models. Although this section will only consider the two-dimensional case, the results can easily be extended to the many three-dimensional cases, where the flow near the wall can be approximated with a local two-dimensional flow.

A.1 Coordinate transformation of Reynolds stresses

A local coordinate system can be defined, as shown on figure A.1, with one axis $\mathbf{n}$ normal to the wall and the other axis $\mathbf{t}$ parallel to the wall and in the same direction as the velocity U near the wall. The global coordinate system is denoted $x^i = (x^1, x^2)$ and the vectors defining the local coordinate system have the components $\mathbf{t} = (t_1, t_2)$ and $\mathbf{n} = (n_1, n_2)$ in the global coordinate system. Let $x^{i'} = (x^{1'}, x^{2'})$ denote the local coordinate system and $\overline{u_k u_l}'$ denote the Reynolds stresses in the local coordinate system. If the Reynolds stresses are considered a contravariant tensor it can be transformed as [55]

$$\overline{u_i u_j} = \left(\frac{\partial x^i}{\partial x^{k'}} \frac{\partial x^j}{\partial x^{l'}} \right) \overline{u_k u_l}'. \tag{A.1}$$

Here, $\partial x^i / \partial x^{k'}$ can be expressed using $\mathbf{t}$ and $\mathbf{n}$ as

$$\frac{\partial x^i}{\partial x^{k'}} = \begin{pmatrix} \dfrac{\partial x^1}{\partial x^{1'}} & \dfrac{\partial x^1}{\partial x^{2'}} \\ \dfrac{\partial x^2}{\partial x^{1'}} & \dfrac{\partial x^2}{\partial x^{2'}} \end{pmatrix} = \begin{pmatrix} t_1 & n_1 \\ t_2 & n_2 \end{pmatrix}. \tag{A.2}$$

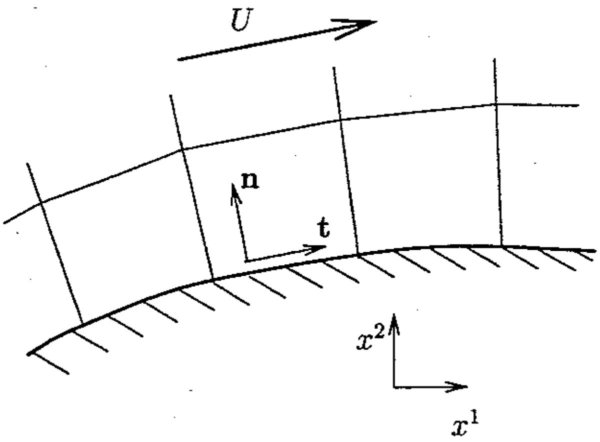

Figure A.1: Coordinate system local to a wall

Combining (A.1) and (A.2) the Reynolds stresses transformed to the global coordinate system can be expressed as

$$\begin{aligned}
\overline{u_1u_1} &= \overline{u_1u_1}'(t_1)^2 + \overline{u_2u_2}'(n_1)^2 + 2\overline{u_1u_2}'t_1n_1 \\
\overline{u_2u_2} &= \overline{u_1u_1}'(t_2)^2 + \overline{u_2u_2}'(n_2)^2 + 2\overline{u_1u_2}'t_2n_2 \\
\overline{u_1u_2} &= \overline{u_1u_1}'t_1t_2 + \overline{u_2u_2}'n_1n_2 + \overline{u_1u_2}'(t_1n_2 + t_2n_1).
\end{aligned} \tag{A.3}$$

A.2 Wall approximation for $\overline{u_iu_j}$

Values of the Reynolds stresses near a wall can be estimated by applying a local Couette flow assumption to the algebraic Reynolds stress model [66], see figure A.2. It is assumed that k and ϵ are found using the technique described in section 3.3.1 and 3.3.3.

The algebraic Reynolds stress model is described in section 3.2.3 and can be written without body forces as

$$\frac{\overline{u_iu_j}}{k} = \tfrac{2}{3}\sigma_{ij} + \frac{(1-c_2)(P_{ij}/\epsilon - \frac{2}{3}\sigma_{ij}P/\epsilon) + \phi_{ijw}/\epsilon}{P/\epsilon + c_1 - 1}, \tag{A.4}$$

where

$$\begin{aligned}
\phi_{ijw} &= \{c_1'\frac{\epsilon}{k}(\overline{u_ku_m}n_kn_m\sigma_{ij} - \tfrac{3}{2}\overline{u_ku_i}n_kn_j - \tfrac{3}{2}\overline{u_ku_j}n_kn_i) \\
&\quad + c_2'(\phi_{km2}n_kn_m\sigma_{ij} - \tfrac{3}{2}\phi_{ik2}n_kn_j - \tfrac{3}{2}\phi_{kj2}n_kn_i)\}\frac{k^{3/2}}{c_l\epsilon|x_n|},
\end{aligned} \tag{A.5}$$

where P_{ij} and ϕ_{ij2} are defined in equations (3.16) and (3.23).

Using the local Couette flow assumption and forcing $\epsilon_{nearwall} = -\overline{u_1u_2}(\partial U_1/\partial x_2)$, the production terms can be written

$$P_{11} = -2(\overline{u_1u_1}\frac{\partial U_1}{\partial x_1} + \overline{u_1u_2}\frac{\partial U_1}{\partial x_2}) = 2\epsilon, \tag{A.6}$$

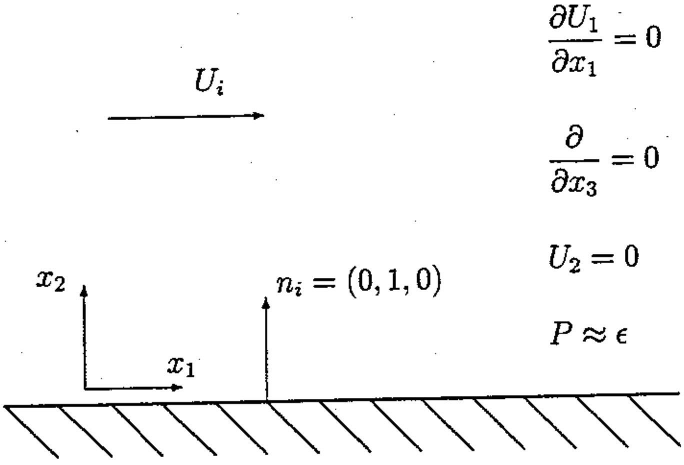

Figure A.2: Local Couette Flow

$$P_{22} = -2(\overline{u_1u_2}\frac{\partial U_2}{\partial x_1} + \overline{u_2u_2}\frac{\partial U_2}{\partial x_2}) = 0, \tag{A.7}$$

$$P_{12} = -(\overline{u_1u_1}\frac{\partial U_2}{\partial x_1} + \overline{u_1u_2}\frac{\partial U_2}{\partial x_2} + \overline{u_2u_1}\frac{\partial U_1}{\partial x_1} + \overline{u_2u_2}\frac{\partial U_1}{\partial x_2}) = -\overline{u_2u_2}\frac{\partial U_1}{\partial x_2} \tag{A.8}$$

From the usual definition of the dissipation length scale the weight function $k^{3/2}/(c_l\epsilon|x_n|)$ can be assumed to take the value of unity in the near wall cell and the wall reflection terms can then be found in the local Couette flow as

$$\phi_{11w} = c_1'\frac{\epsilon}{k}(\overline{u_2u_2} - 0) + c_2'(\phi_{222} - 0) = c_1'\frac{\epsilon}{k}\overline{u_2u_2} + c_2'\phi_{222}, \tag{A.9}$$

$$\begin{aligned}\phi_{22w} &= c_1'\frac{\epsilon}{k}(\overline{u_2u_2} - 3\overline{u_2u_2}) + c_2'(\phi_{222} - 3\phi_{222}) \\ &= -2c_1'\frac{\epsilon}{k}\overline{u_2u_2} - 2c_2'\phi_{222},\end{aligned} \tag{A.10}$$

$$\phi_{12w} = -\tfrac{3}{2}c_1'\frac{\epsilon}{k}\overline{u_1u_2} - \tfrac{3}{2}c_2'\phi_{222}. \tag{A.11}$$

Expressions for the Reynolds stresses can now be found using the assumption $P = \epsilon$ and the constants in the model as

$$\frac{\overline{u_1u_1}}{k} = \frac{\frac{2}{3}(c_1 + 2 - 2c_2 + c_2c_2') + c_1\frac{\overline{u_2u_2}}{k}}{c_1} = 1.098, \tag{A.12}$$

$$\frac{\overline{u_2u_2}}{k} = \frac{\frac{2}{3}(c_1 + c_2 - 1 - 2c_2c_2')}{c_1 + 2c_1'} = 0.2476, \tag{A.13}$$

$$\left(\frac{\overline{u_1u_2}}{k}\right)^2 = \frac{1 - c_2 + \frac{3}{2}c_2c_2'}{c_1 + \frac{3}{2}c_1'} \cdot \frac{\overline{u_2u_2}}{k} = 0.065 = c_\mu. \tag{A.14}$$

A.3 Wall approximation for $\overline{u_i\theta}$

A similar analysis can be performed with the algebraic Reynolds flux model from section 3.2.3. This model can be written, without body forces, as

$$\frac{\overline{u_i\theta}}{k} = \frac{2(\overline{u_iu_k}\frac{\partial \Theta}{\partial x_k} + (1 - c_{\theta 2})(\overline{u_l\theta}\frac{\partial U_i}{\partial x_l}) + \phi_{i\theta w})}{(P - \epsilon) + 2c_{1\theta}\epsilon}, \tag{A.15}$$

where

$$\phi_{i\theta w} = (c'_{\theta 1}\frac{\epsilon}{k}\overline{u_l\theta}n_l n_i)\frac{k^{3/2}}{c_l\epsilon|x_n|}. \tag{A.16}$$

With $n_i = (0,1,0)$ the wall reflection term can be reduces to

$$\phi_{1\theta w} = \phi_{3\theta w} = 0, \tag{A.17}$$

$$\phi_{2\theta w} = c'_{\theta 1}\frac{\epsilon}{k}\overline{u_2\theta}. \tag{A.18}$$

Using the same assumption as used for the Reynolds stresses, the Reynolds fluxes can be found as

$$\frac{\overline{u_1\theta}}{k} = \frac{\overline{u_1u_1}\frac{\partial\Theta}{\partial x_1} + \overline{u_1u_2}\frac{\partial\Theta}{\partial x_2} + (1-c_{\theta 2})\overline{u_2\theta}\frac{\partial U_1}{\partial x_2}}{c_{\theta 1}\epsilon}, \tag{A.19}$$

$$\frac{\overline{u_2\theta}}{k} = \frac{\overline{u_1u_2}\frac{\partial\Theta}{\partial x_1} + \overline{u_2u_2}\frac{\partial\Theta}{\partial x_2}}{(c_{\theta 1} - c'_{\theta 1})\epsilon}, \tag{A.20}$$

$$\frac{\overline{u_3\theta}}{k} = 0 \tag{A.21}$$

Appendix B

Plots of LDA measurements

B.1 Test of number of samples in a point

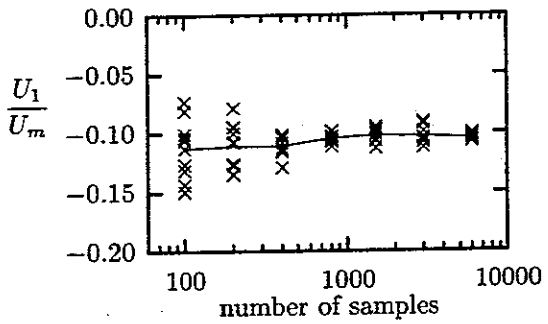

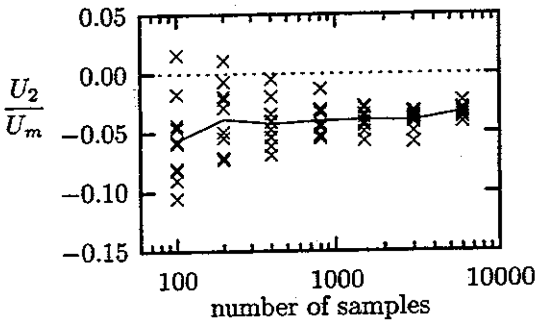

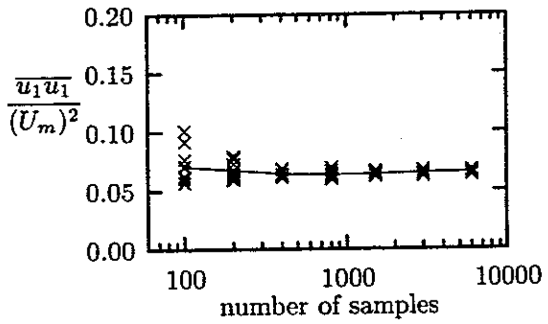

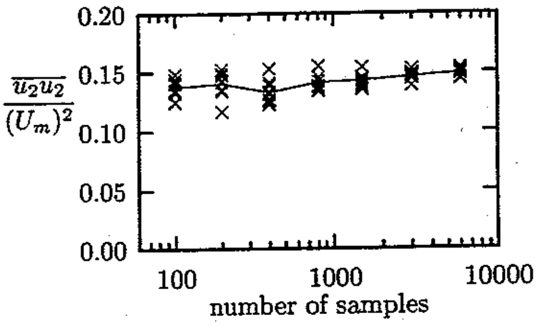

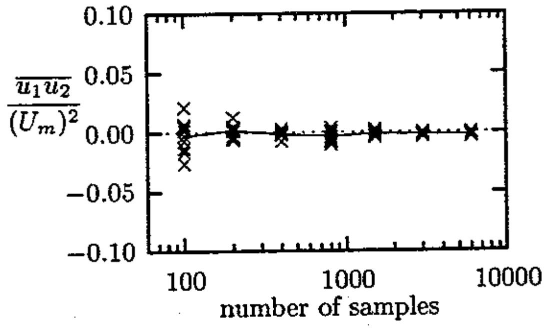

The above 5 plots show measurements that all are taken in the same physical point. The coordinates for this point is approximately $(x_1, x_2) = (0.85\,D, 0)$. The number of samples in each measurement has been changed in step from 100 to 6000 samples. For each number of samples 10 measurements were performed. The result from a single measurement is shown with the symbol × and the average of all measurements with the same number of samples are

	$\frac{U_1}{U_m}$	$\frac{U_2}{U_m}$	$\frac{\overline{u_1u_1}}{(U_m)^2}$	$\frac{\overline{u_2u_2}}{(U_m)^2}$	$\frac{\overline{u_1u_2}}{(U_m)^2}$
mean value	−0.10423	−0.03244	0.06554	0.14900	−0.00229
standard deviation	0.00228	0.00502	0.00148	0.00314	0.00122

Table B.1: Mean value and standard deviation for 10 measurements, each with 6000 samples.

shown with a solid line. The measurements have been normalized using the mean velocity between two tubes in a row: $U_m = 2.85\,\mathrm{m/s}$.

In table B.1 the mean value and the standard deviation are shown for each of the mean velocities and each of the Reynolds stresses in the measuring series that had 6000 samples in each measurement. For the mean velocities the standard deviation is less than 1 % of U_m. The standard deviations for $\overline{u_1u_1}$ and $\overline{u_2u_2}$ are about 2 % of their mean values. The point used in the measurements is located close to a line of symmetry and the mean value of $\overline{u_1u_2}$ is therefore close to zero. However, the standard deviation of $\overline{u_1u_2}$ is about 3 % of the general level of the mean value of $\overline{u_1u_2}$ in the surroundings of the measuring point.

B.2 Measurements in measuring section

The following 100 plots show all measurements taken in the measuring section. The plots are organized in 5 groups containing plots of respectively U_1, U_2, $\overline{u_1u_1}$, $\overline{u_2u_2}$ and $\overline{u_1u_2}$. Each single measurement is marked with a symbol and four different symbol are used to denote which of the unit cells in the measuring section a measurements has been taken in. The symbols are explained below this paragraph. Solid line denote average of all measurements in a point. On the plots, all the measurements have been transformed to the upper right unit cell where both x_1 and x_2 are positive). This transformation involves changing the sign on U_2 and $\overline{u_1u_2}$ for measurements in the unit cells with symbols + and ×.

Symbols used on plots:

	$x_1 < 0$	$x_1 > 0$
$x_2 < 0$	□	×
$x_2 > 0$	+	◇

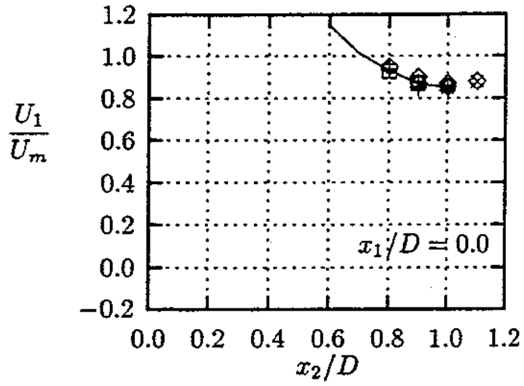
$\frac{U_1}{U_m}$
1.2
1.0
0.8
0.6
0.4
0.2
0.0
−0.2
$x_1/D = 0.0$
0.0 0.2 0.4 0.6 0.8 1.0 1.2
x_2/D

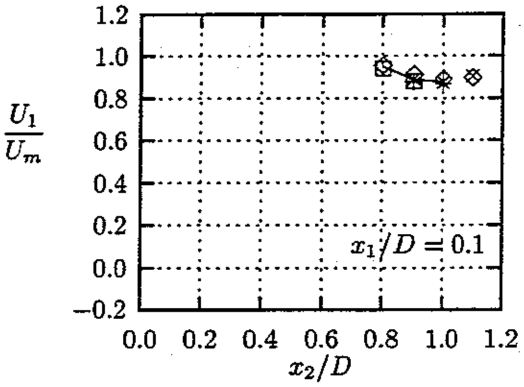
$\frac{U_1}{U_m}$
1.2
1.0
0.8
0.6
0.4
0.2
0.0
−0.2
$x_1/D = 0.1$
0.0 0.2 0.4 0.6 0.8 1.0 1.2
x_2/D

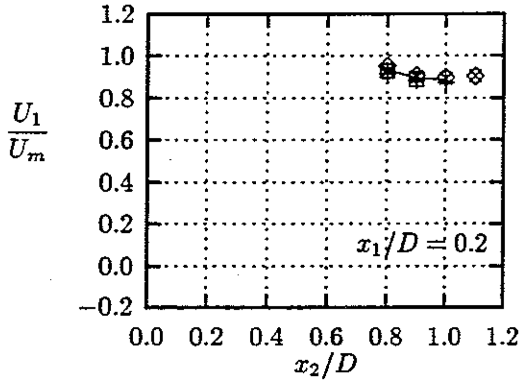
$\frac{U_1}{U_m}$
1.2
1.0
0.8
0.6
0.4
0.2
0.0
−0.2
$x_1/D = 0.2$
0.0 0.2 0.4 0.6 0.8 1.0 1.2
x_2/D

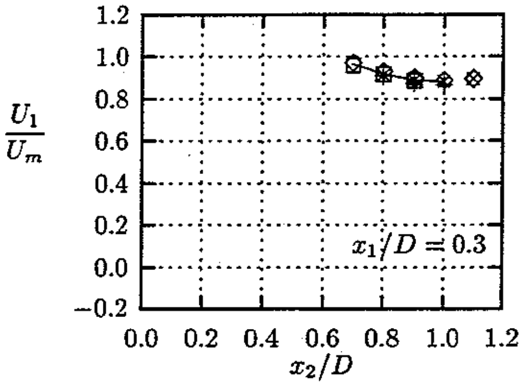
$\frac{U_1}{U_m}$
1.2
1.0
0.8
0.6
0.4
0.2
0.0
−0.2
$x_1/D = 0.3$
0.0 0.2 0.4 0.6 0.8 1.0 1.2
x_2/D

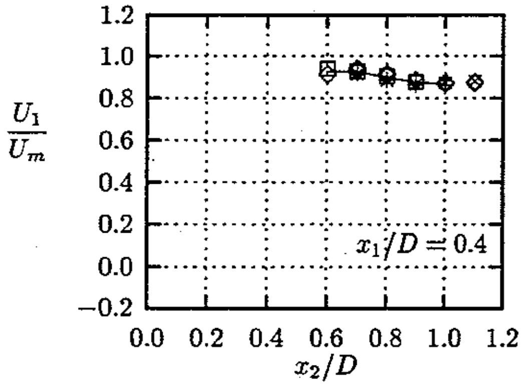
$\frac{U_1}{U_m}$
1.2
1.0
0.8
0.6
0.4
0.2
0.0
−0.2
$x_1/D = 0.4$
0.0 0.2 0.4 0.6 0.8 1.0 1.2
x_2/D

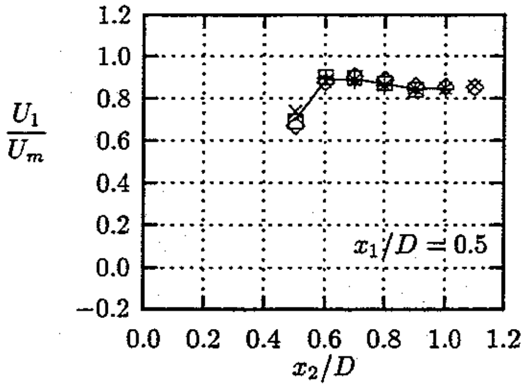
$\frac{U_1}{U_m}$
1.2
1.0
0.8
0.6
0.4
0.2
0.0
−0.2
$x_1/D = 0.5$
0.0 0.2 0.4 0.6 0.8 1.0 1.2
x_2/D

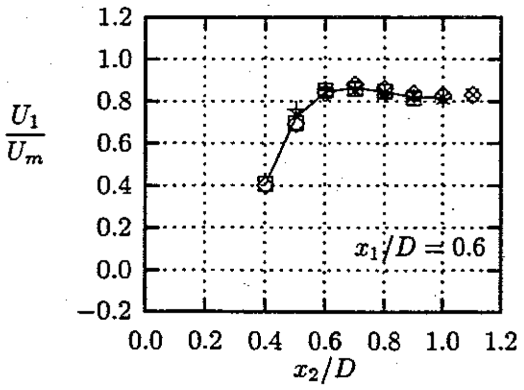
$\frac{U_1}{U_m}$
1.2
1.0
0.8
0.6
0.4
0.2
0.0
−0.2
$x_1/D = 0.6$
0.0 0.2 0.4 0.6 0.8 1.0 1.2
x_2/D

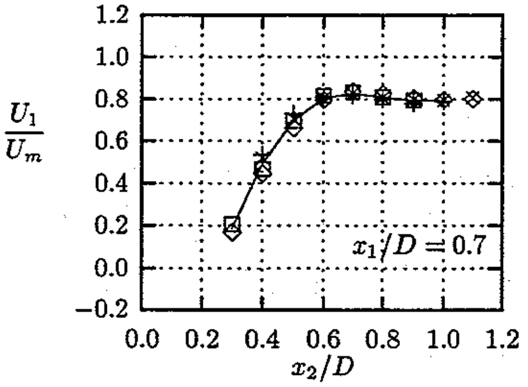
$\frac{U_1}{U_m}$
1.2
1.0
0.8
0.6
0.4
0.2
0.0
−0.2
$x_1/D = 0.7$
0.0 0.2 0.4 0.6 0.8 1.0 1.2
x_2/D

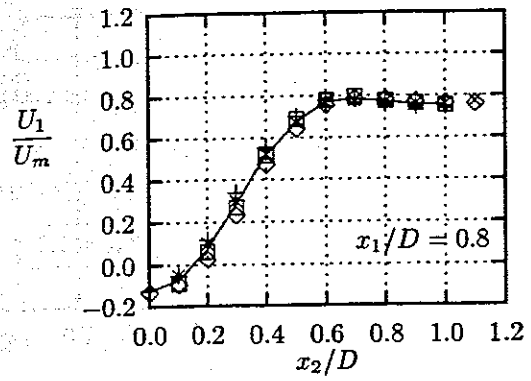
$\frac{U_1}{U_m}$
1.2
1.0
0.8
0.6
0.4
0.2
0.0
−0.2
$x_1/D = 0.8$
0.0 0.2 0.4 0.6 0.8 1.0 1.2
x_2/D

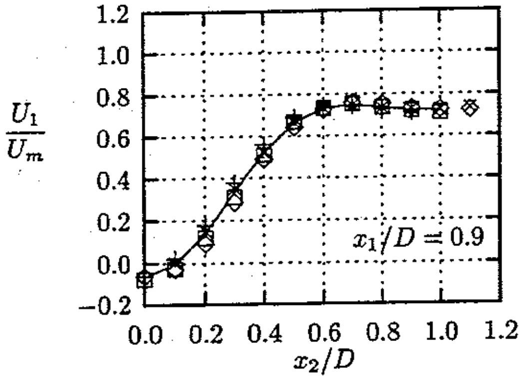
$\frac{U_1}{U_m}$
1.2
1.0
0.8
0.6
0.4
0.2
0.0
−0.2
$x_1/D = 0.9$
0.0 0.2 0.4 0.6 0.8 1.0 1.2
x_2/D

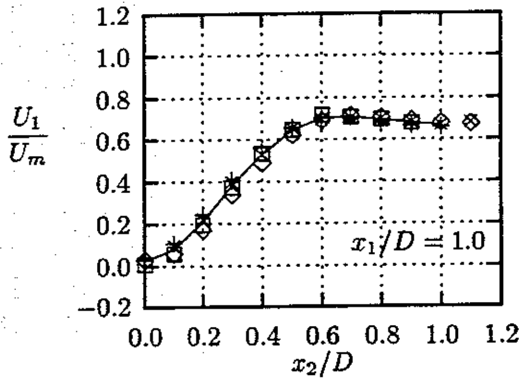
$\frac{U_1}{U_m}$
1.2
1.0
0.8
0.6
0.4
0.2
0.0
−0.2
$x_1/D = 1.0$
0.0 0.2 0.4 0.6 0.8 1.0 1.2
x_2/D

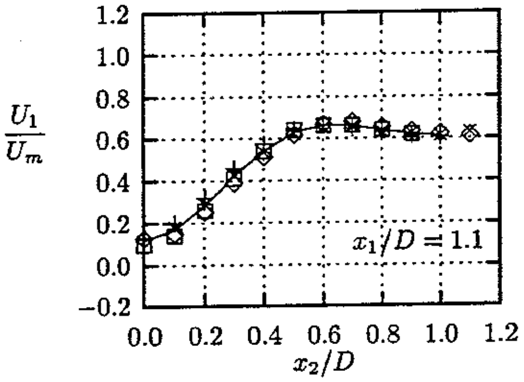
$\frac{U_1}{U_m}$
1.2
1.0
0.8
0.6
0.4
0.2
0.0
−0.2
$x_1/D = 1.1$
0.0 0.2 0.4 0.6 0.8 1.0 1.2
x_2/D

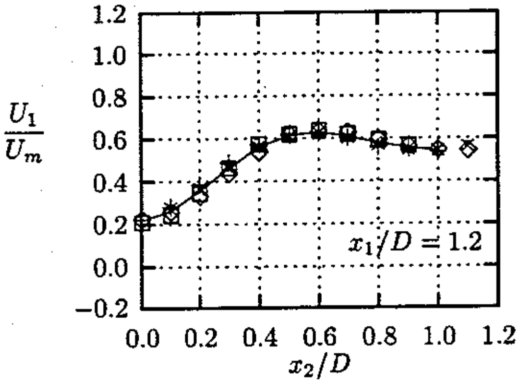
$\frac{U_1}{U_m}$
1.2
1.0
0.8
0.6
0.4
0.2
0.0
−0.2
$x_1/D = 1.2$
0.0 0.2 0.4 0.6 0.8 1.0 1.2
x_2/D

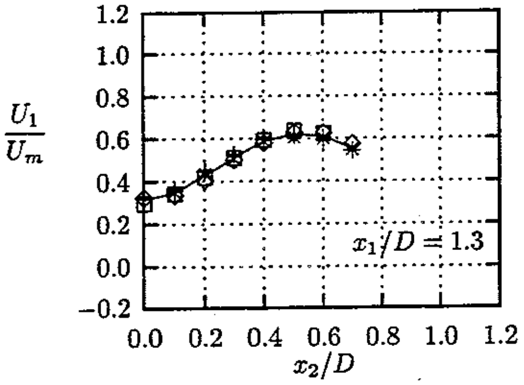
$\frac{U_1}{U_m}$
1.2
1.0
0.8
0.6
0.4
0.2
0.0
−0.2
$x_1/D = 1.3$
0.0 0.2 0.4 0.6 0.8 1.0 1.2
x_2/D

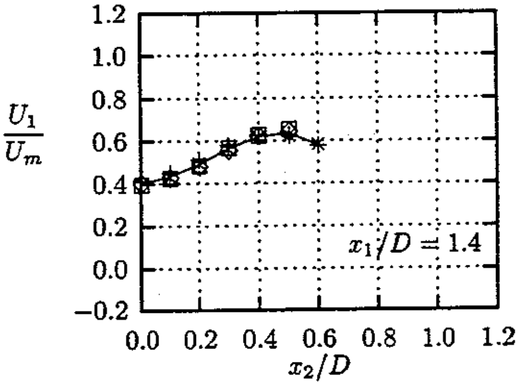
$\frac{U_1}{U_m}$
1.2
1.0
0.8
0.6
0.4
0.2
0.0
−0.2
$x_1/D = 1.4$
0.0 0.2 0.4 0.6 0.8 1.0 1.2
x_2/D

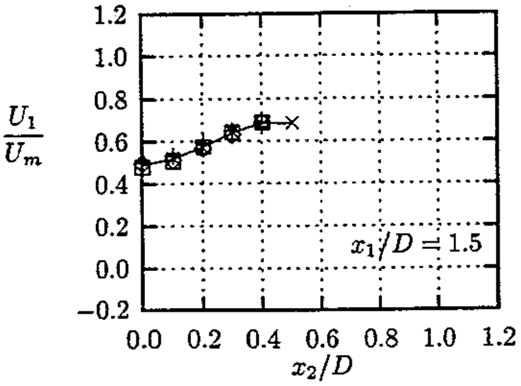
$\frac{U_1}{U_m}$
1.2
1.0
0.8
0.6
0.4
0.2
0.0
−0.2
$x_1/D = 1.5$
0.0 0.2 0.4 0.6 0.8 1.0 1.2
x_2/D

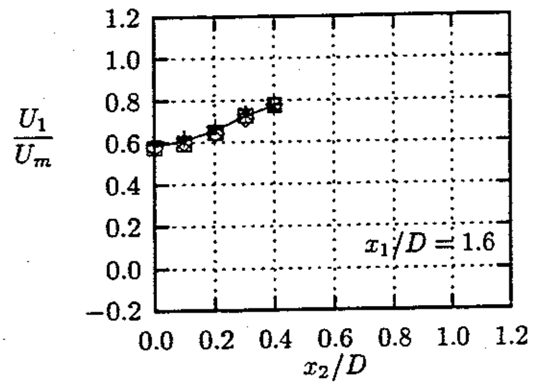
$\frac{U_1}{U_m}$
1.2
1.0
0.8
0.6
0.4
0.2
0.0
−0.2
0.0 0.2 0.4 0.6 0.8 1.0 1.2
x_2/D
$x_1/D = 1.6$

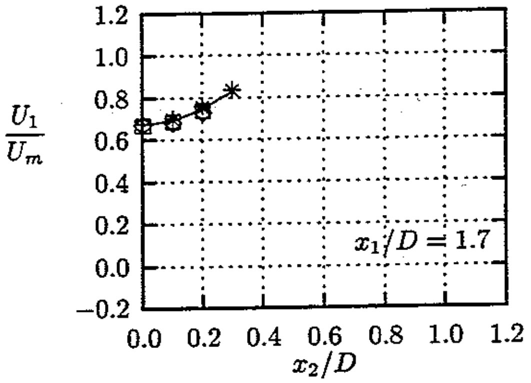
$\frac{U_1}{U_m}$
1.2
1.0
0.8
0.6
0.4
0.2
0.0
−0.2
0.0 0.2 0.4 0.6 0.8 1.0 1.2
x_2/D
$x_1/D = 1.7$

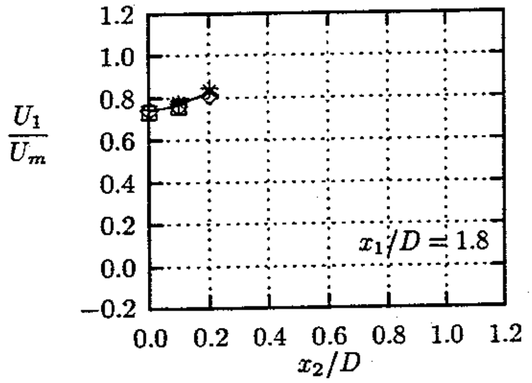
$\frac{U_1}{U_m}$
1.2
1.0
0.8
0.6
0.4
0.2
0.0
−0.2
0.0 0.2 0.4 0.6 0.8 1.0 1.2
x_2/D
$x_1/D = 1.8$

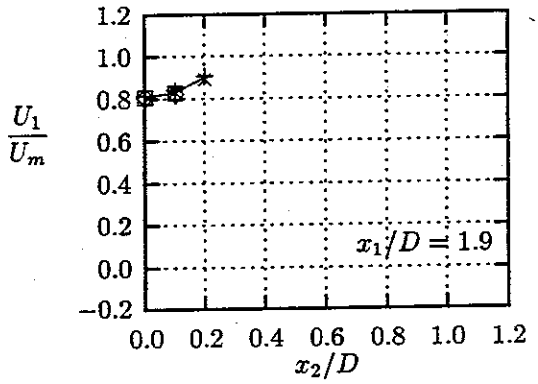
$\frac{U_1}{U_m}$
1.2
1.0
0.8
0.6
0.4
0.2
0.0
−0.2
0.0 0.2 0.4 0.6 0.8 1.0 1.2
x_2/D
$x_1/D = 1.9$

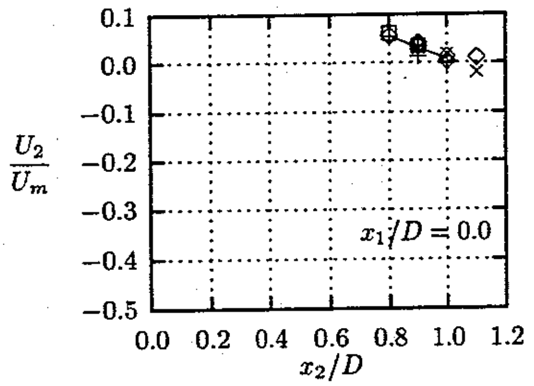
$\frac{U_2}{U_m}$
0.1
0.0
−0.1
−0.2
−0.3
−0.4
−0.5
0.0 0.2 0.4 0.6 0.8 1.0 1.2
x_2/D
$x_1/D = 0.0$

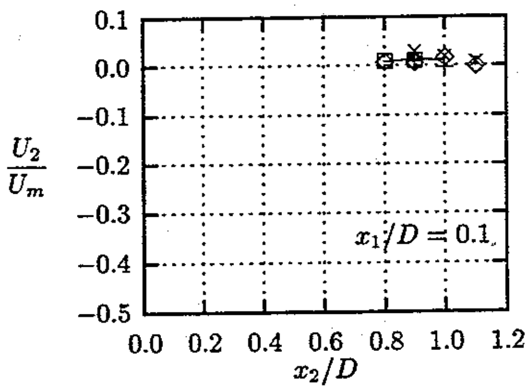
$\frac{U_2}{U_m}$
0.1
0.0
−0.1
−0.2
−0.3
−0.4
−0.5
0.0 0.2 0.4 0.6 0.8 1.0 1.2
x_2/D
$x_1/D = 0.1$

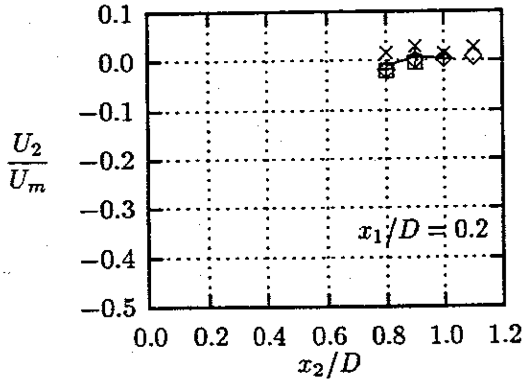
$\frac{U_2}{U_m}$
0.1
0.0
−0.1
−0.2
−0.3
−0.4
−0.5
0.0 0.2 0.4 0.6 0.8 1.0 1.2
x_2/D
$x_1/D = 0.2$

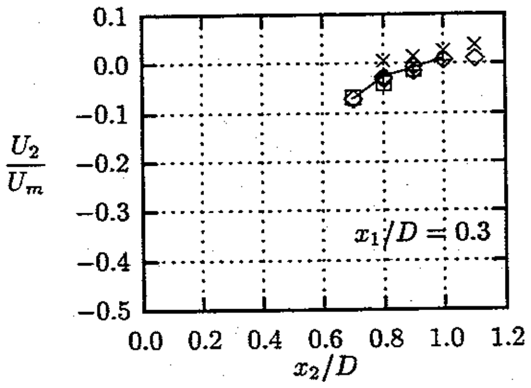
$\frac{U_2}{U_m}$
0.1
0.0
−0.1
−0.2
−0.3
−0.4
−0.5
0.0 0.2 0.4 0.6 0.8 1.0 1.2
x_2/D
$x_1/D = 0.3$

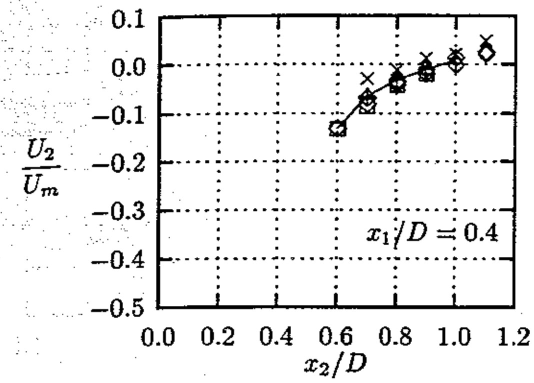
$\frac{U_2}{U_m}$
0.1
0.0
−0.1
−0.2
−0.3
−0.4
−0.5
$x_1/D = 0.4$
0.0 0.2 0.4 0.6 0.8 1.0 1.2
x_2/D

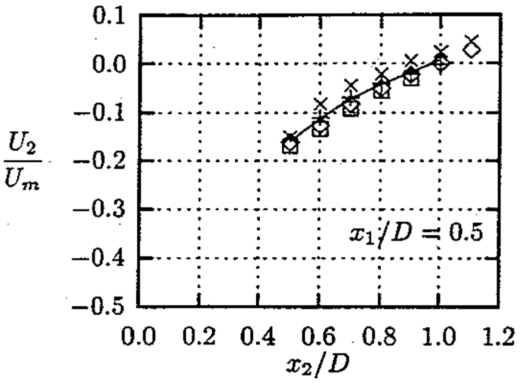
$\frac{U_2}{U_m}$
0.1
0.0
−0.1
−0.2
−0.3
−0.4
−0.5
$x_1/D = 0.5$
0.0 0.2 0.4 0.6 0.8 1.0 1.2
x_2/D

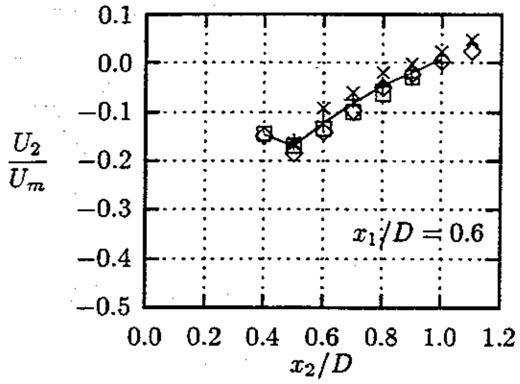
$\frac{U_2}{U_m}$
0.1
0.0
−0.1
−0.2
−0.3
−0.4
−0.5
$x_1/D = 0.6$
0.0 0.2 0.4 0.6 0.8 1.0 1.2
x_2/D

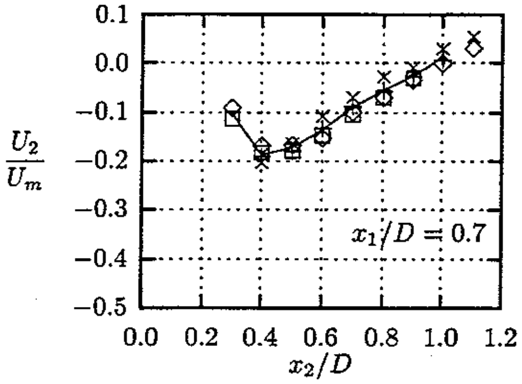
$\frac{U_2}{U_m}$
0.1
0.0
−0.1
−0.2
−0.3
−0.4
−0.5
$x_1/D = 0.7$
0.0 0.2 0.4 0.6 0.8 1.0 1.2
x_2/D

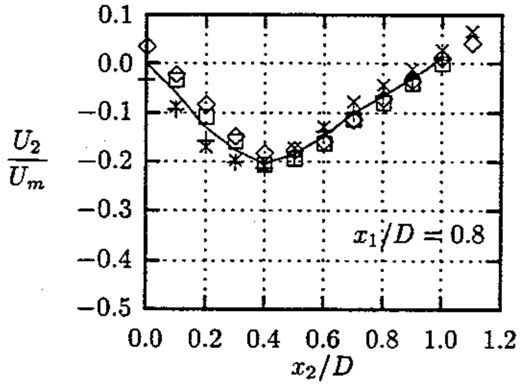
$\frac{U_2}{U_m}$
0.1
0.0
−0.1
−0.2
−0.3
−0.4
−0.5
$x_1/D = 0.8$
0.0 0.2 0.4 0.6 0.8 1.0 1.2
x_2/D

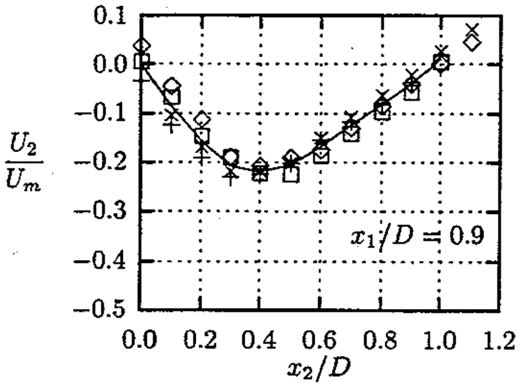
$\frac{U_2}{U_m}$
0.1
0.0
−0.1
−0.2
−0.3
−0.4
−0.5
$x_1/D = 0.9$
0.0 0.2 0.4 0.6 0.8 1.0 1.2
x_2/D

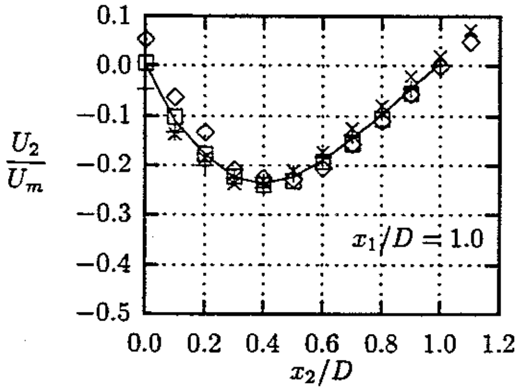
$\frac{U_2}{U_m}$
0.1
0.0
−0.1
−0.2
−0.3
−0.4
−0.5
$x_1/D = 1.0$
0.0 0.2 0.4 0.6 0.8 1.0 1.2
x_2/D

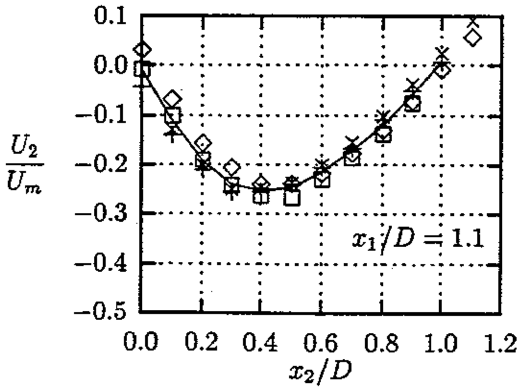
$\frac{U_2}{U_m}$
0.1
0.0
−0.1
−0.2
−0.3
−0.4
−0.5
$x_1/D = 1.1$
0.0 0.2 0.4 0.6 0.8 1.0 1.2
x_2/D

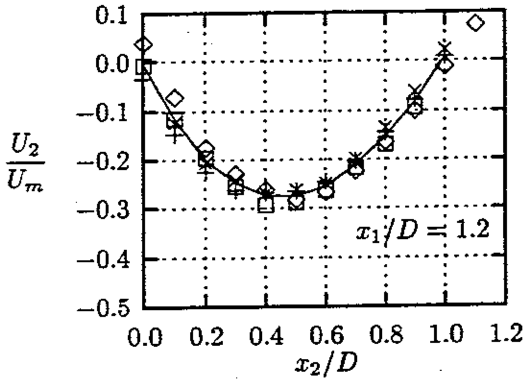
$\frac{U_2}{U_m}$
0.1
0.0
−0.1
−0.2
−0.3
−0.4
−0.5
0.0 0.2 0.4 0.6 0.8 1.0 1.2
x_2/D
$x_1/D = 1.2$

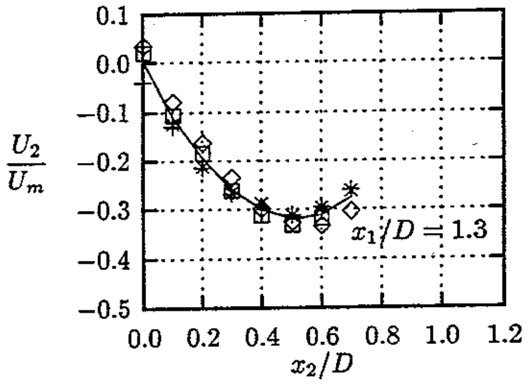
$\frac{U_2}{U_m}$
0.1
0.0
−0.1
−0.2
−0.3
−0.4
−0.5
0.0 0.2 0.4 0.6 0.8 1.0 1.2
x_2/D
$x_1/D = 1.3$

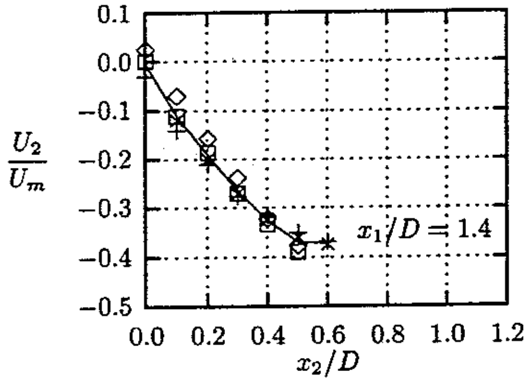
$\frac{U_2}{U_m}$
0.1
0.0
−0.1
−0.2
−0.3
−0.4
−0.5
0.0 0.2 0.4 0.6 0.8 1.0 1.2
x_2/D
$x_1/D = 1.4$

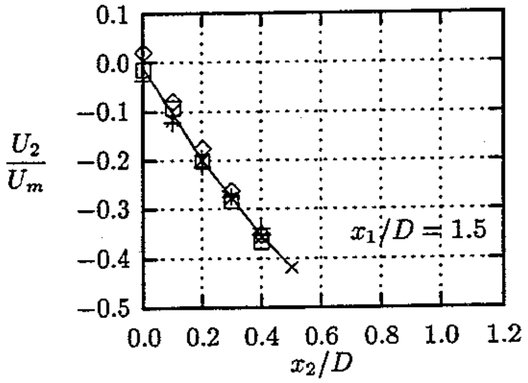
$\frac{U_2}{U_m}$
0.1
0.0
−0.1
−0.2
−0.3
−0.4
−0.5
0.0 0.2 0.4 0.6 0.8 1.0 1.2
x_2/D
$x_1/D = 1.5$

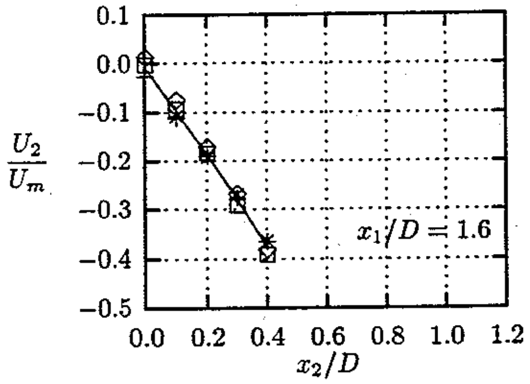
$\frac{U_2}{U_m}$
0.1
0.0
−0.1
−0.2
−0.3
−0.4
−0.5
0.0 0.2 0.4 0.6 0.8 1.0 1.2
x_2/D
$x_1/D = 1.6$

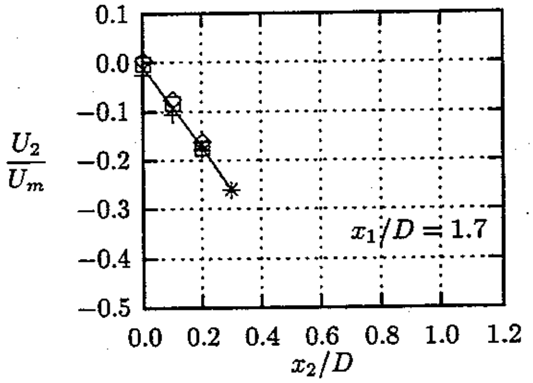
$\frac{U_2}{U_m}$
0.1
0.0
−0.1
−0.2
−0.3
−0.4
−0.5
0.0 0.2 0.4 0.6 0.8 1.0 1.2
x_2/D
$x_1/D = 1.7$

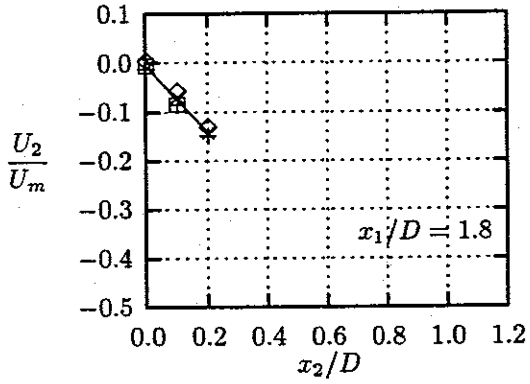
$\frac{U_2}{U_m}$
0.1
0.0
−0.1
−0.2
−0.3
−0.4
−0.5
0.0 0.2 0.4 0.6 0.8 1.0 1.2
x_2/D
$x_1/D = 1.8$

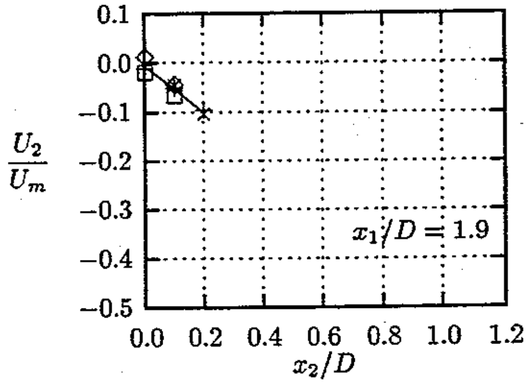
$\frac{U_2}{U_m}$
0.1
0.0
−0.1
−0.2
−0.3
−0.4
−0.5
0.0 0.2 0.4 0.6 0.8 1.0 1.2
x_2/D
$x_1/D = 1.9$

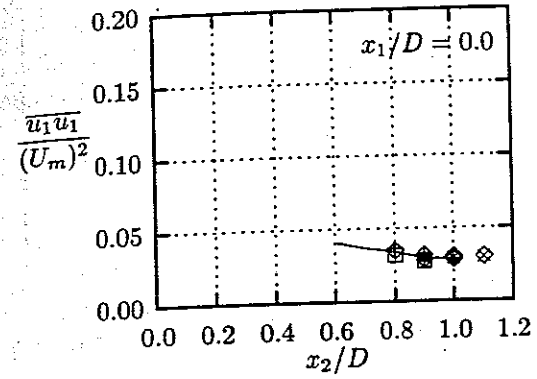
$x_1/D = 0.0$
$\frac{\overline{u_1 u_1}}{(U_m)^2}$
0.20
0.15
0.10
0.05
0.00
0.0
0.2
0.4
0.6
0.8
1.0
1.2
x_2/D

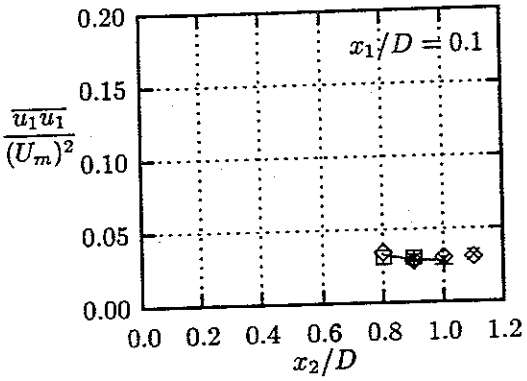
$x_1/D = 0.1$
$\frac{\overline{u_1 u_1}}{(U_m)^2}$
0.20
0.15
0.10
0.05
0.00
0.0
0.2
0.4
0.6
0.8
1.0
1.2
x_2/D

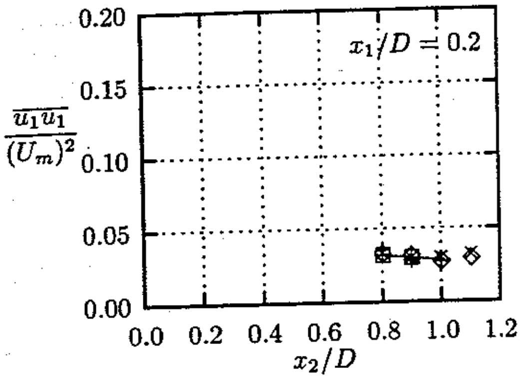
$x_1/D = 0.2$
$\frac{\overline{u_1 u_1}}{(U_m)^2}$
0.20
0.15
0.10
0.05
0.00
0.0
0.2
0.4
0.6
0.8
1.0
1.2
x_2/D

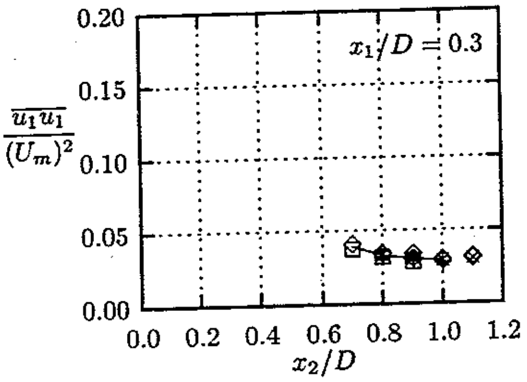
$x_1/D = 0.3$
$\frac{\overline{u_1 u_1}}{(U_m)^2}$
0.20
0.15
0.10
0.05
0.00
0.0
0.2
0.4
0.6
0.8
1.0
1.2
x_2/D

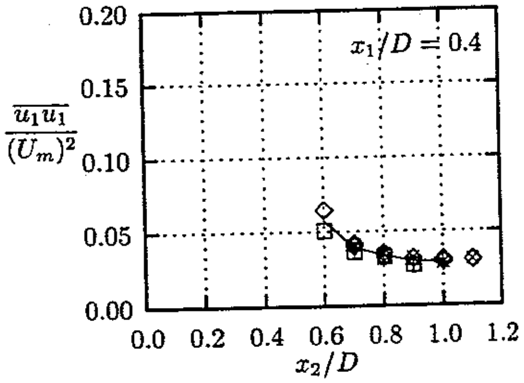
$x_1/D = 0.4$
$\frac{\overline{u_1 u_1}}{(U_m)^2}$
0.20
0.15
0.10
0.05
0.00
0.0
0.2
0.4
0.6
0.8
1.0
1.2
x_2/D

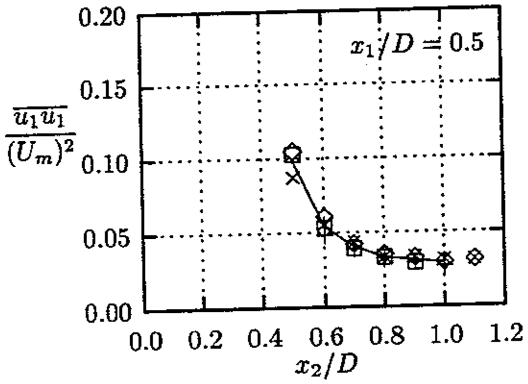
$x_1/D = 0.5$
$\frac{\overline{u_1 u_1}}{(U_m)^2}$
0.20
0.15
0.10
0.05
0.00
0.0
0.2
0.4
0.6
0.8
1.0
1.2
x_2/D

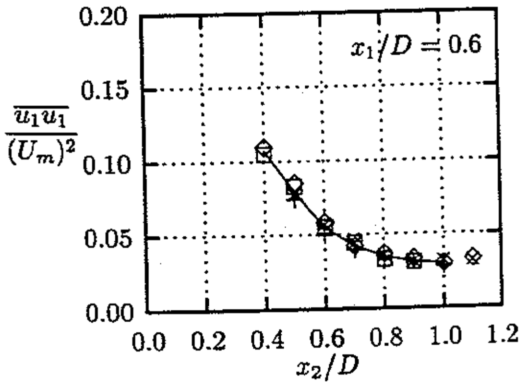
$x_1/D = 0.6$
$\frac{\overline{u_1 u_1}}{(U_m)^2}$
0.20
0.15
0.10
0.05
0.00
0.0
0.2
0.4
0.6
0.8
1.0
1.2
x_2/D

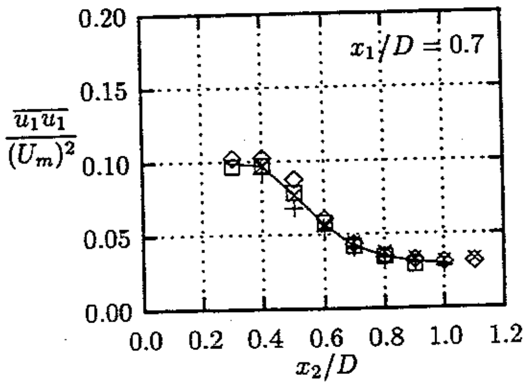
$x_1/D = 0.7$
$\frac{\overline{u_1 u_1}}{(U_m)^2}$
0.20
0.15
0.10
0.05
0.00
0.0
0.2
0.4
0.6
0.8
1.0
1.2
x_2/D

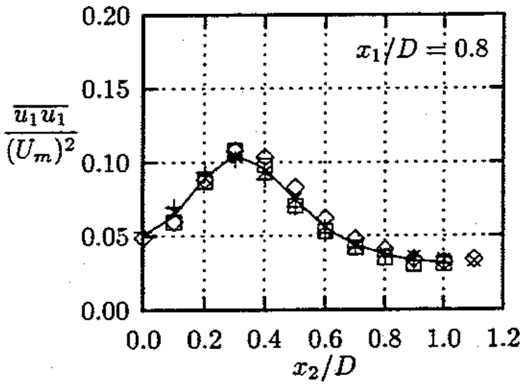
$\frac{\overline{u_1u_1}}{(U_m)^2}$
0.20
0.15
0.10
0.05
0.00
$x_1/D = 0.8$
0.0 0.2 0.4 0.6 0.8 1.0 1.2
x_2/D

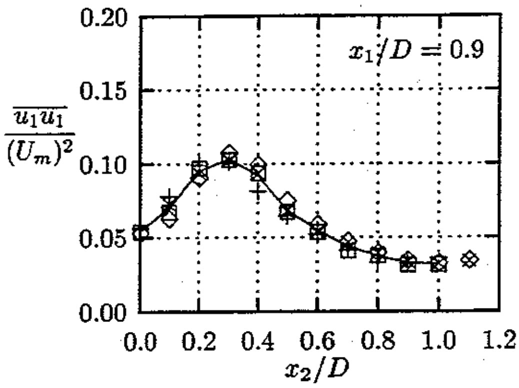
$\frac{\overline{u_1u_1}}{(U_m)^2}$
0.20
0.15
0.10
0.05
0.00
$x_1/D = 0.9$
0.0 0.2 0.4 0.6 0.8 1.0 1.2
x_2/D

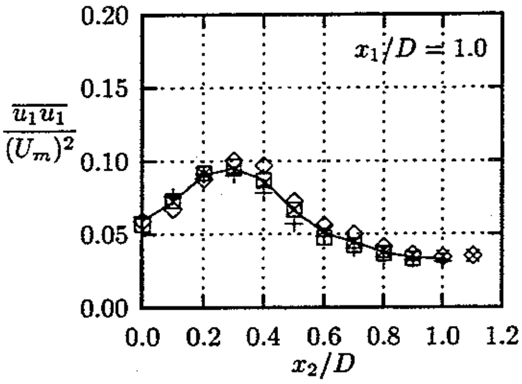
$\frac{\overline{u_1u_1}}{(U_m)^2}$
0.20
0.15
0.10
0.05
0.00
$x_1/D = 1.0$
0.0 0.2 0.4 0.6 0.8 1.0 1.2
x_2/D

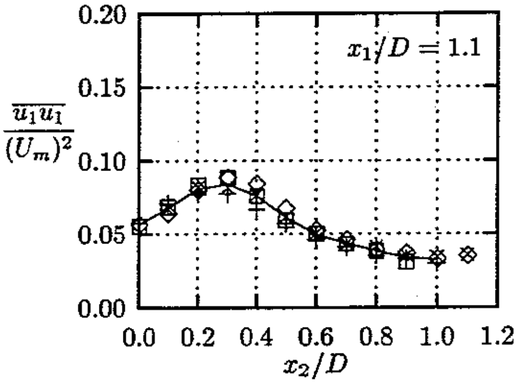
$\frac{\overline{u_1u_1}}{(U_m)^2}$
0.20
0.15
0.10
0.05
0.00
$x_1/D = 1.1$
0.0 0.2 0.4 0.6 0.8 1.0 1.2
x_2/D

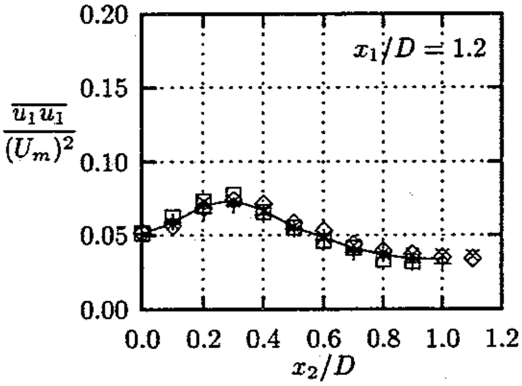
$\frac{\overline{u_1u_1}}{(U_m)^2}$
0.20
0.15
0.10
0.05
0.00
$x_1/D = 1.2$
0.0 0.2 0.4 0.6 0.8 1.0 1.2
x_2/D

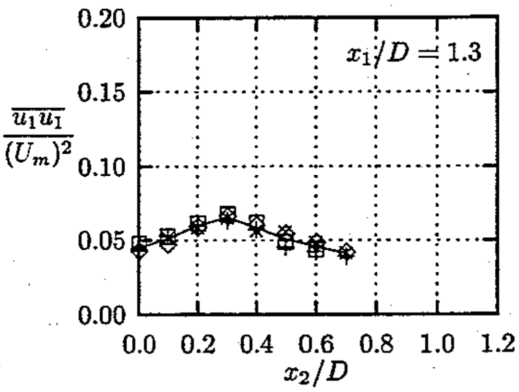
$\frac{\overline{u_1u_1}}{(U_m)^2}$
0.20
0.15
0.10
0.05
0.00
$x_1/D = 1.3$
0.0 0.2 0.4 0.6 0.8 1.0 1.2
x_2/D

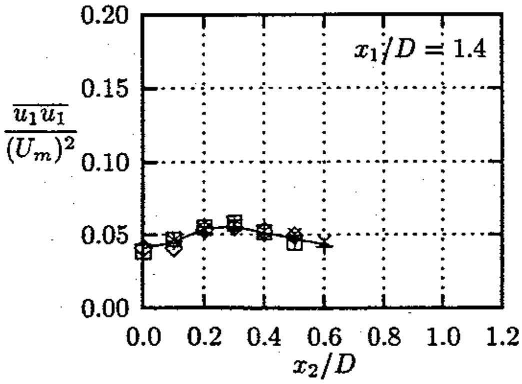
$\frac{\overline{u_1u_1}}{(U_m)^2}$
0.20
0.15
0.10
0.05
0.00
$x_1/D = 1.4$
0.0 0.2 0.4 0.6 0.8 1.0 1.2
x_2/D

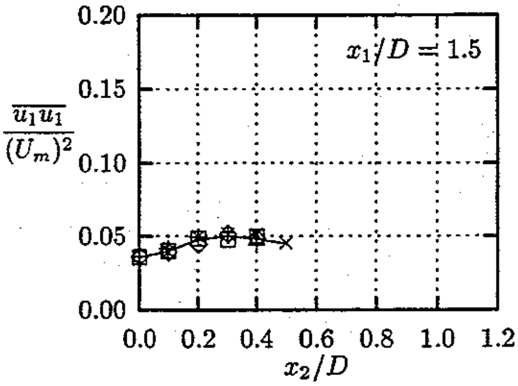
$\frac{\overline{u_1u_1}}{(U_m)^2}$
0.20
0.15
0.10
0.05
0.00
$x_1/D = 1.5$
0.0 0.2 0.4 0.6 0.8 1.0 1.2
x_2/D

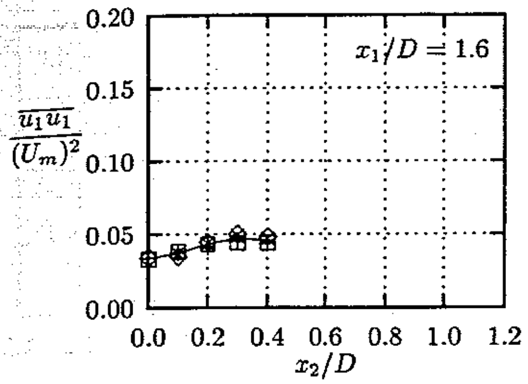
$x_1/D = 1.6$
$\frac{\overline{u_1u_1}}{(U_m)^2}$
0.20
0.15
0.10
0.05
0.00
0.0 0.2 0.4 0.6 0.8 1.0 1.2
x_2/D

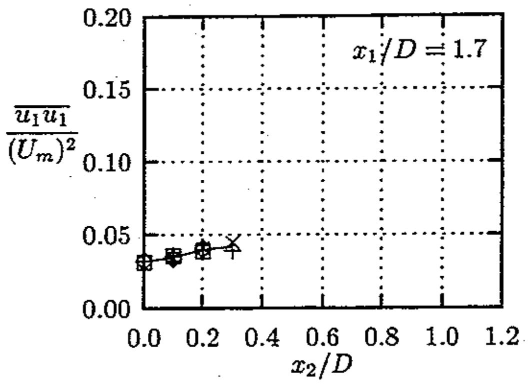
$x_1/D = 1.7$
$\frac{\overline{u_1u_1}}{(U_m)^2}$
0.20
0.15
0.10
0.05
0.00
0.0 0.2 0.4 0.6 0.8 1.0 1.2
x_2/D

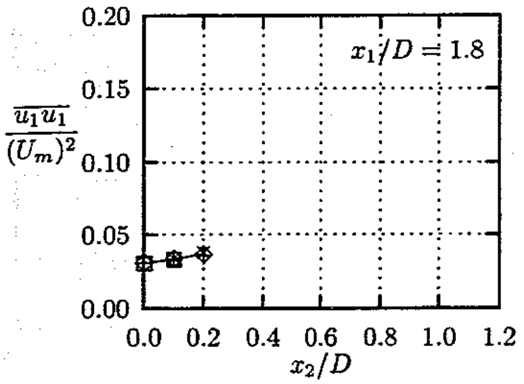
$x_1/D = 1.8$
$\frac{\overline{u_1u_1}}{(U_m)^2}$
0.20
0.15
0.10
0.05
0.00
0.0 0.2 0.4 0.6 0.8 1.0 1.2
x_2/D

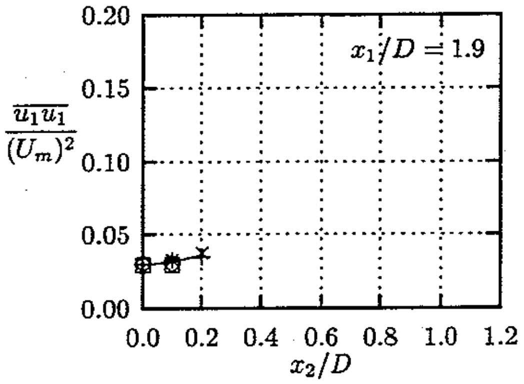
$x_1/D = 1.9$
$\frac{\overline{u_1u_1}}{(U_m)^2}$
0.20
0.15
0.10
0.05
0.00
0.0 0.2 0.4 0.6 0.8 1.0 1.2
x_2/D

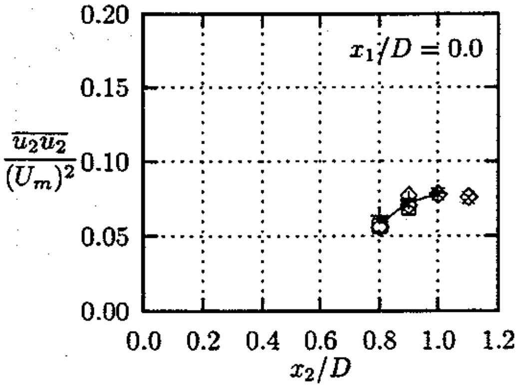
$x_1/D = 0.0$
$\frac{\overline{u_2u_2}}{(U_m)^2}$
0.20
0.15
0.10
0.05
0.00
0.0 0.2 0.4 0.6 0.8 1.0 1.2
x_2/D

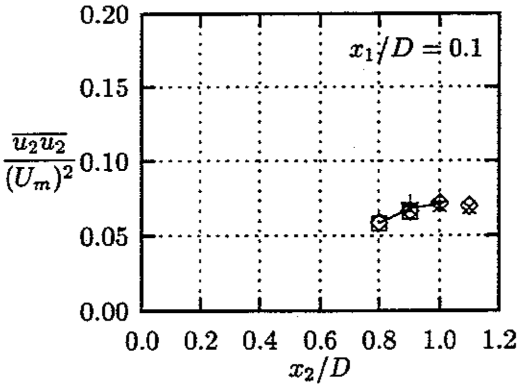
$x_1/D = 0.1$
$\frac{\overline{u_2u_2}}{(U_m)^2}$
0.20
0.15
0.10
0.05
0.00
0.0 0.2 0.4 0.6 0.8 1.0 1.2
x_2/D

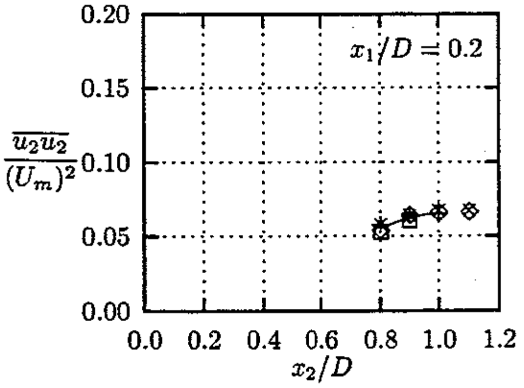
$x_1/D = 0.2$
$\frac{\overline{u_2u_2}}{(U_m)^2}$
0.20
0.15
0.10
0.05
0.00
0.0 0.2 0.4 0.6 0.8 1.0 1.2
x_2/D

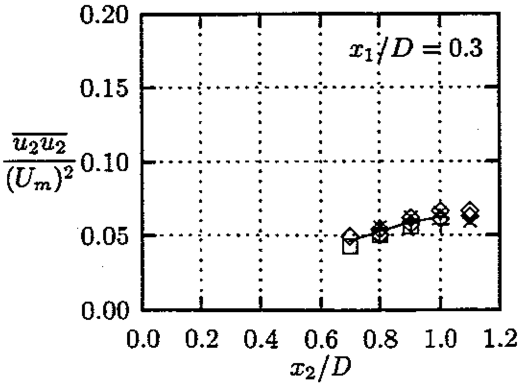
$x_1/D = 0.3$
$\frac{\overline{u_2u_2}}{(U_m)^2}$
0.20
0.15
0.10
0.05
0.00
0.0 0.2 0.4 0.6 0.8 1.0 1.2
x_2/D

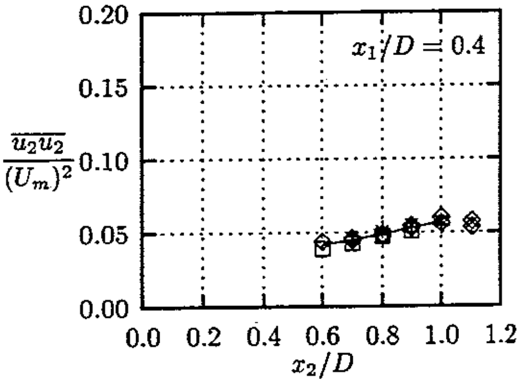
$x_1/D = 0.4$
$\frac{\overline{u_2u_2}}{(U_m)^2}$
0.20
0.15
0.10
0.05
0.00
0.0 0.2 0.4 0.6 0.8 1.0 1.2
x_2/D

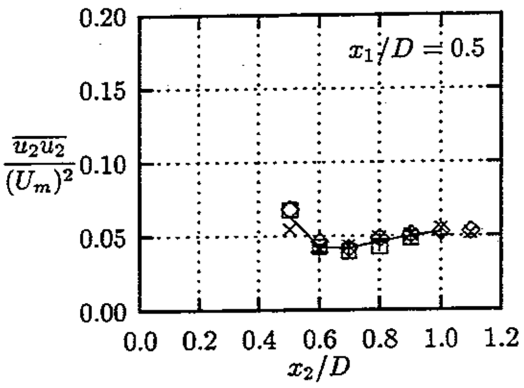
$x_1/D = 0.5$
$\frac{\overline{u_2u_2}}{(U_m)^2}$
0.20
0.15
0.10
0.05
0.00
0.0 0.2 0.4 0.6 0.8 1.0 1.2
x_2/D

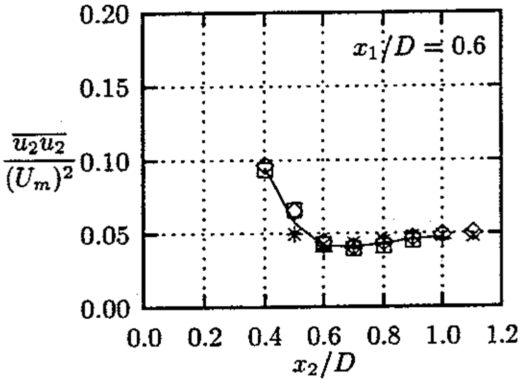
$x_1/D = 0.6$
$\frac{\overline{u_2u_2}}{(U_m)^2}$
0.20
0.15
0.10
0.05
0.00
0.0 0.2 0.4 0.6 0.8 1.0 1.2
x_2/D

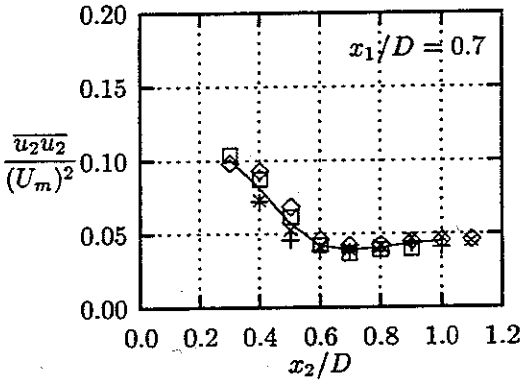
$x_1/D = 0.7$
$\frac{\overline{u_2u_2}}{(U_m)^2}$
0.20
0.15
0.10
0.05
0.00
0.0 0.2 0.4 0.6 0.8 1.0 1.2
x_2/D

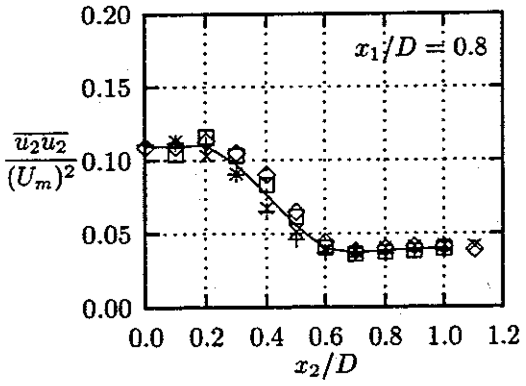
$x_1/D = 0.8$
$\frac{\overline{u_2u_2}}{(U_m)^2}$
0.20
0.15
0.10
0.05
0.00
0.0 0.2 0.4 0.6 0.8 1.0 1.2
x_2/D

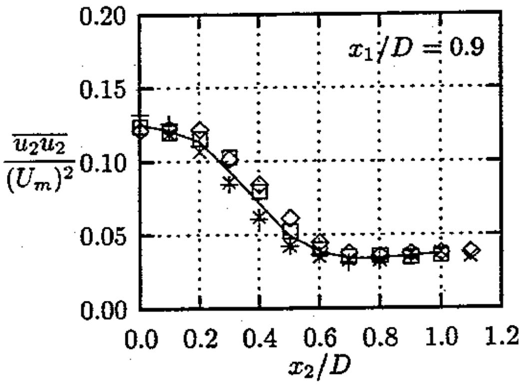
$x_1/D = 0.9$
$\frac{\overline{u_2u_2}}{(U_m)^2}$
0.20
0.15
0.10
0.05
0.00
0.0 0.2 0.4 0.6 0.8 1.0 1.2
x_2/D

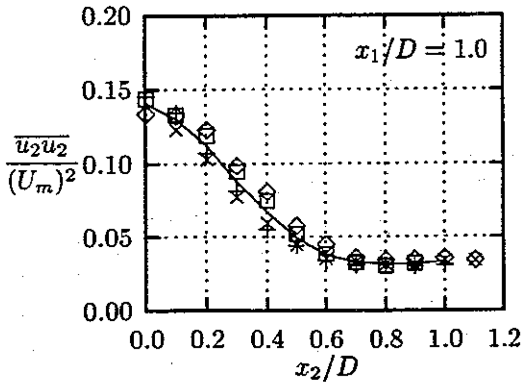
$x_1/D = 1.0$
$\frac{\overline{u_2u_2}}{(U_m)^2}$
0.20
0.15
0.10
0.05
0.00
0.0 0.2 0.4 0.6 0.8 1.0 1.2
x_2/D

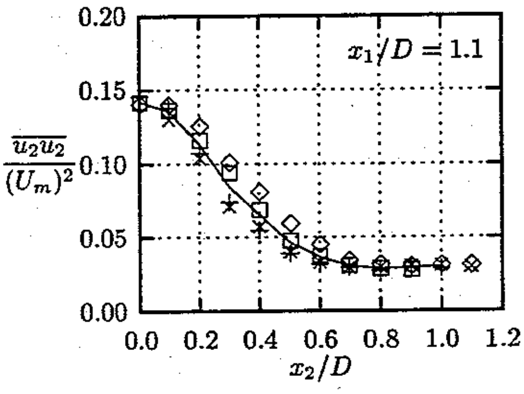
$x_1/D = 1.1$
$\frac{\overline{u_2u_2}}{(U_m)^2}$
0.20
0.15
0.10
0.05
0.00
0.0 0.2 0.4 0.6 0.8 1.0 1.2
x_2/D

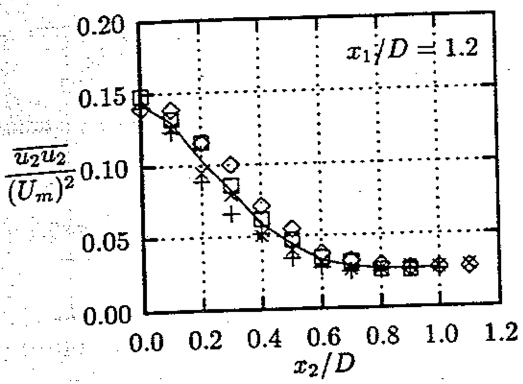
$x_1/D = 1.2$
$\frac{\overline{u_2u_2}}{(U_m)^2}$
0.00
0.05
0.10
0.15
0.20
0.0
0.2
0.4
0.6
0.8
1.0
1.2
x_2/D

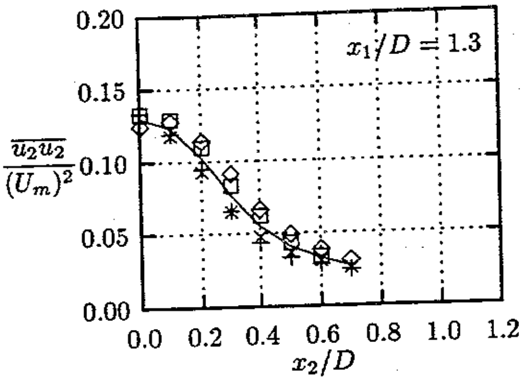
$x_1/D = 1.3$
$\frac{\overline{u_2u_2}}{(U_m)^2}$
0.00
0.05
0.10
0.15
0.20
0.0
0.2
0.4
0.6
0.8
1.0
1.2
x_2/D

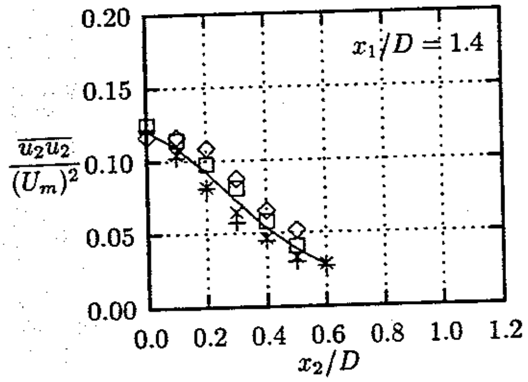
$x_1/D = 1.4$
$\frac{\overline{u_2u_2}}{(U_m)^2}$
0.00
0.05
0.10
0.15
0.20
0.0
0.2
0.4
0.6
0.8
1.0
1.2
x_2/D

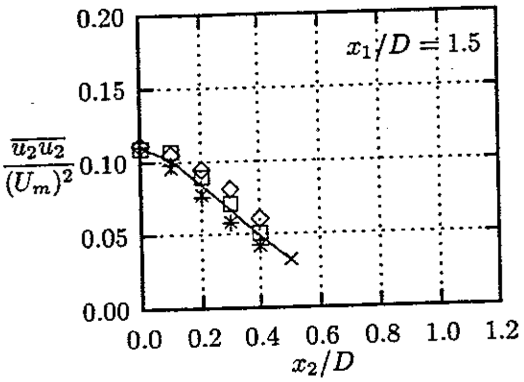
$x_1/D = 1.5$
$\frac{\overline{u_2u_2}}{(U_m)^2}$
0.00
0.05
0.10
0.15
0.20
0.0
0.2
0.4
0.6
0.8
1.0
1.2
x_2/D

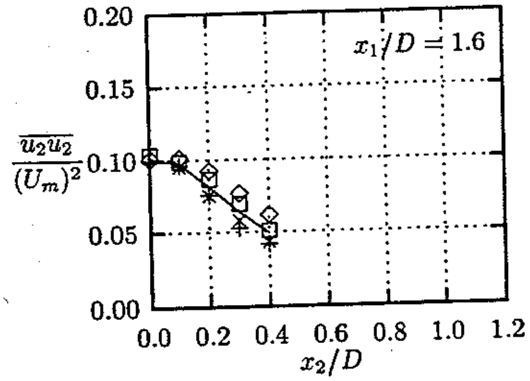
$x_1/D = 1.6$
$\frac{\overline{u_2u_2}}{(U_m)^2}$
0.00
0.05
0.10
0.15
0.20
0.0
0.2
0.4
0.6
0.8
1.0
1.2
x_2/D

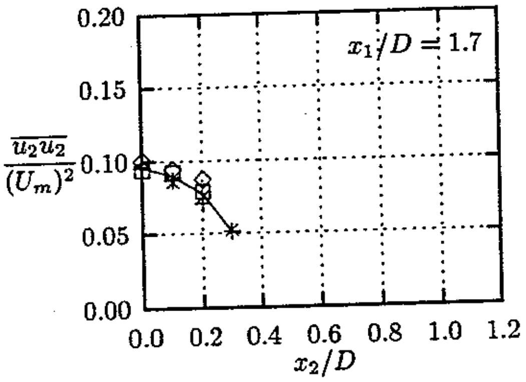
$x_1/D = 1.7$
$\frac{\overline{u_2u_2}}{(U_m)^2}$
0.00
0.05
0.10
0.15
0.20
0.0
0.2
0.4
0.6
0.8
1.0
1.2
x_2/D

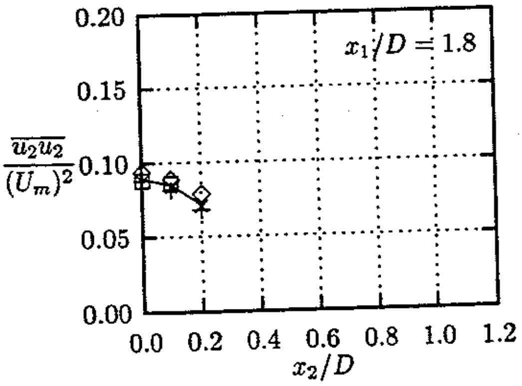
$x_1/D = 1.8$
$\frac{\overline{u_2u_2}}{(U_m)^2}$
0.00
0.05
0.10
0.15
0.20
0.0
0.2
0.4
0.6
0.8
1.0
1.2
x_2/D

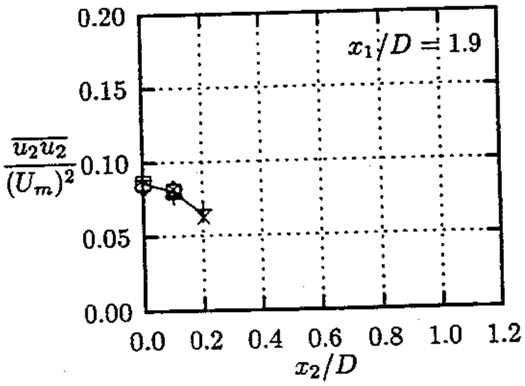
$x_1/D = 1.9$
$\frac{\overline{u_2u_2}}{(U_m)^2}$
0.00
0.05
0.10
0.15
0.20
0.0
0.2
0.4
0.6
0.8
1.0
1.2
x_2/D

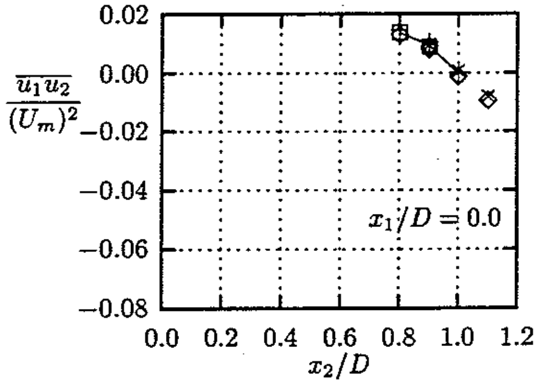
$\frac{\overline{u_1 u_2}}{(U_m)^2}$
0.02
0.00
−0.02
−0.04
−0.06
−0.08
0.0 0.2 0.4 0.6 0.8 1.0 1.2
x_2/D
$x_1/D = 0.0$

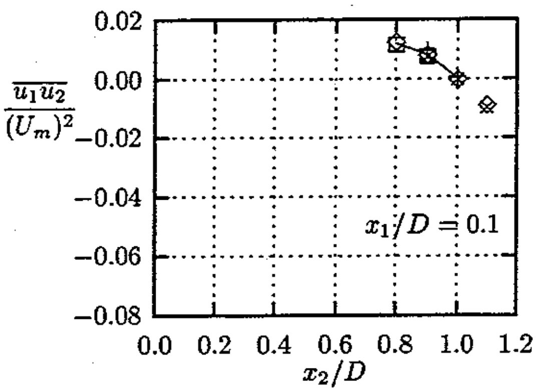
$\frac{\overline{u_1 u_2}}{(U_m)^2}$
0.02
0.00
−0.02
−0.04
−0.06
−0.08
0.0 0.2 0.4 0.6 0.8 1.0 1.2
x_2/D
$x_1/D = 0.1$

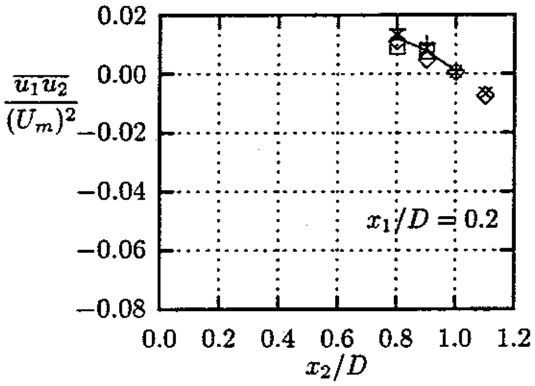
$\frac{\overline{u_1 u_2}}{(U_m)^2}$
0.02
0.00
−0.02
−0.04
−0.06
−0.08
0.0 0.2 0.4 0.6 0.8 1.0 1.2
x_2/D
$x_1/D = 0.2$

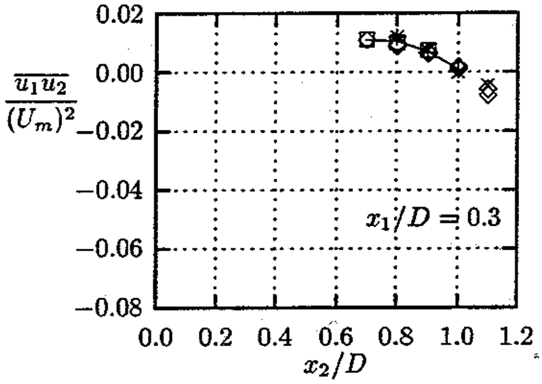
$\frac{\overline{u_1 u_2}}{(U_m)^2}$
0.02
0.00
−0.02
−0.04
−0.06
−0.08
0.0 0.2 0.4 0.6 0.8 1.0 1.2
x_2/D
$x_1/D = 0.3$

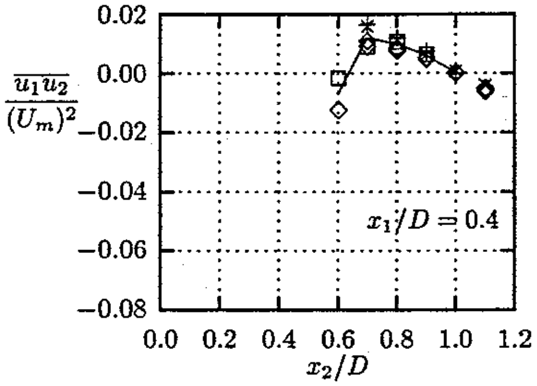
$\frac{\overline{u_1 u_2}}{(U_m)^2}$
0.02
0.00
−0.02
−0.04
−0.06
−0.08
0.0 0.2 0.4 0.6 0.8 1.0 1.2
x_2/D
$x_1/D = 0.4$

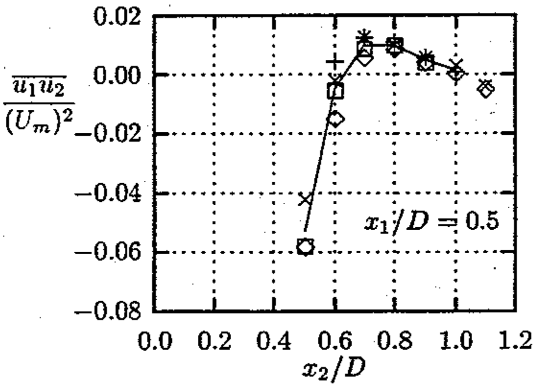
$\frac{\overline{u_1 u_2}}{(U_m)^2}$
0.02
0.00
−0.02
−0.04
−0.06
−0.08
0.0 0.2 0.4 0.6 0.8 1.0 1.2
x_2/D
$x_1/D = 0.5$

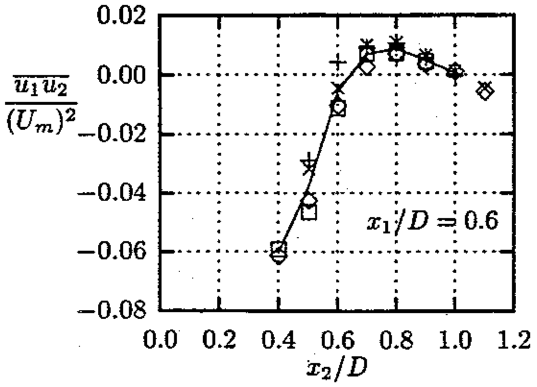
$\frac{\overline{u_1 u_2}}{(U_m)^2}$
0.02
0.00
−0.02
−0.04
−0.06
−0.08
0.0 0.2 0.4 0.6 0.8 1.0 1.2
x_2/D
$x_1/D = 0.6$

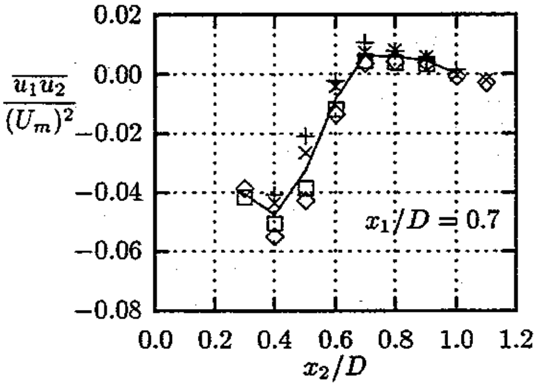
$\frac{\overline{u_1 u_2}}{(U_m)^2}$
0.02
0.00
−0.02
−0.04
−0.06
−0.08
0.0 0.2 0.4 0.6 0.8 1.0 1.2
x_2/D
$x_1/D = 0.7$

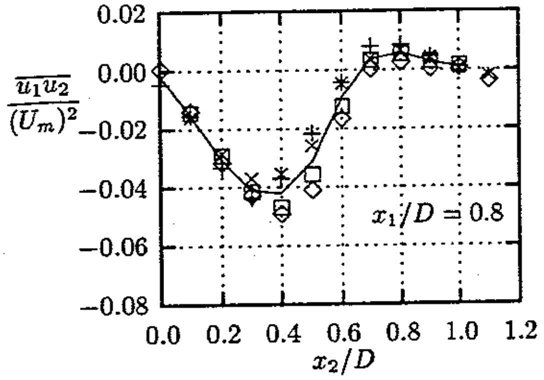
0.02
0.00
−0.02
−0.04
−0.06
−0.08
$\frac{\overline{u_1u_2}}{(U_m)^2}$
$x_1/D = 0.8$
0.0 0.2 0.4 0.6 0.8 1.0 1.2
x_2/D

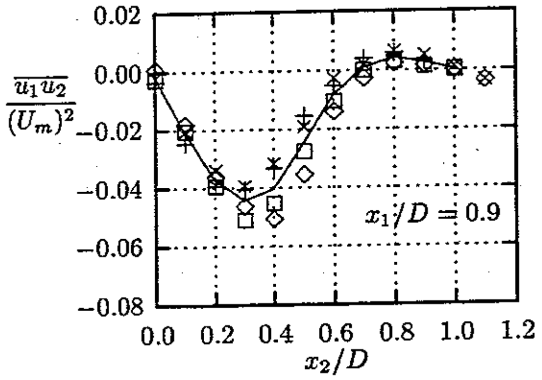
0.02
0.00
−0.02
−0.04
−0.06
−0.08
$\frac{\overline{u_1u_2}}{(U_m)^2}$
$x_1/D = 0.9$
0.0 0.2 0.4 0.6 0.8 1.0 1.2
x_2/D

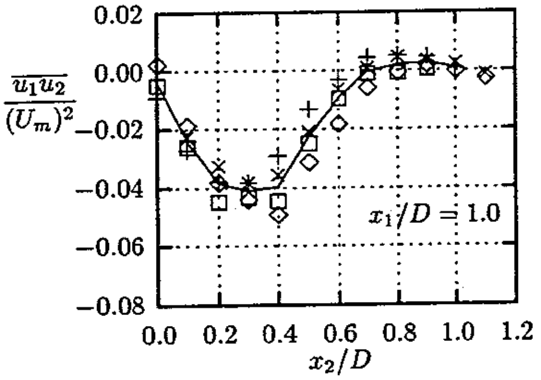
0.02
0.00
−0.02
−0.04
−0.06
−0.08
$\frac{\overline{u_1u_2}}{(U_m)^2}$
$x_1/D = 1.0$
0.0 0.2 0.4 0.6 0.8 1.0 1.2
x_2/D

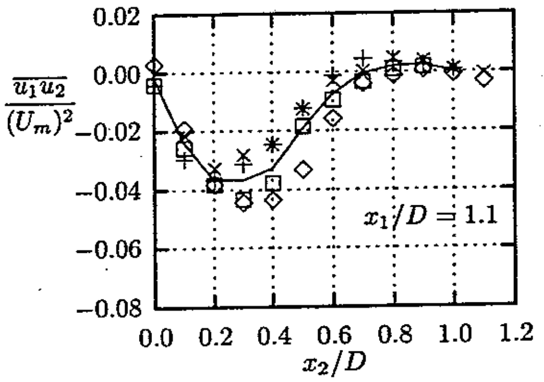
0.02
0.00
−0.02
−0.04
−0.06
−0.08
$\frac{\overline{u_1u_2}}{(U_m)^2}$
$x_1/D = 1.1$
0.0 0.2 0.4 0.6 0.8 1.0 1.2
x_2/D

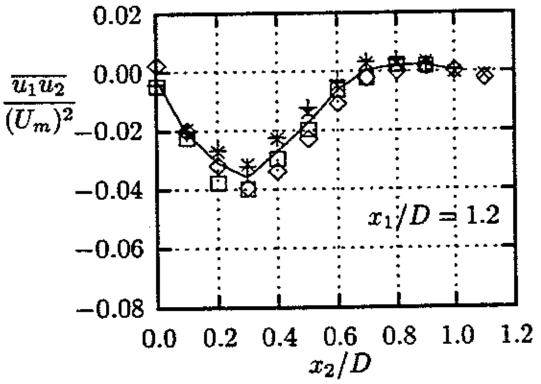
0.02
0.00
−0.02
−0.04
−0.06
−0.08
$\frac{\overline{u_1u_2}}{(U_m)^2}$
$x_1/D = 1.2$
0.0 0.2 0.4 0.6 0.8 1.0 1.2
x_2/D

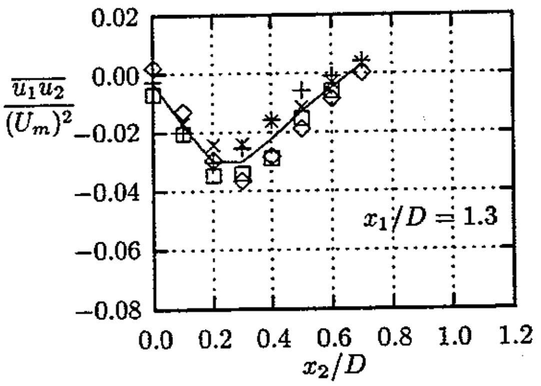
0.02
0.00
−0.02
−0.04
−0.06
−0.08
$\frac{\overline{u_1u_2}}{(U_m)^2}$
$x_1/D = 1.3$
0.0 0.2 0.4 0.6 0.8 1.0 1.2
x_2/D

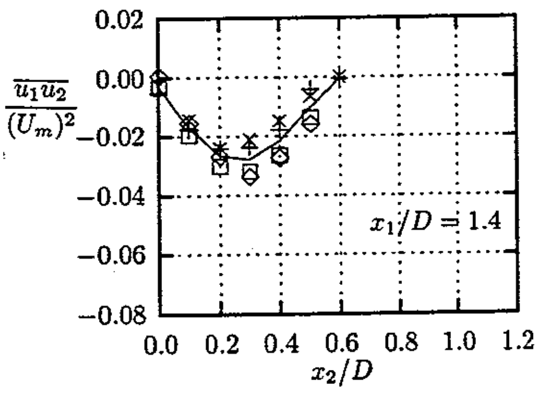
0.02
0.00
−0.02
−0.04
−0.06
−0.08
$\frac{\overline{u_1u_2}}{(U_m)^2}$
$x_1/D = 1.4$
0.0 0.2 0.4 0.6 0.8 1.0 1.2
x_2/D

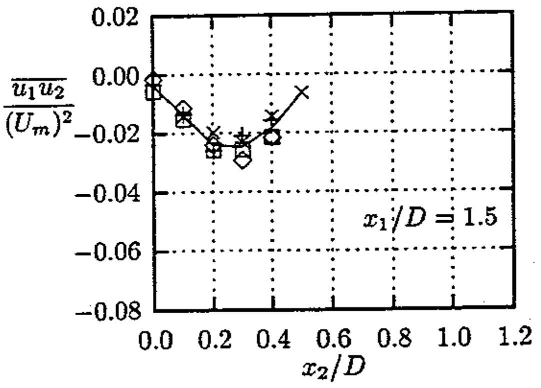
0.02
0.00
−0.02
−0.04
−0.06
−0.08
$\frac{\overline{u_1u_2}}{(U_m)^2}$
$x_1/D = 1.5$
0.0 0.2 0.4 0.6 0.8 1.0 1.2
x_2/D

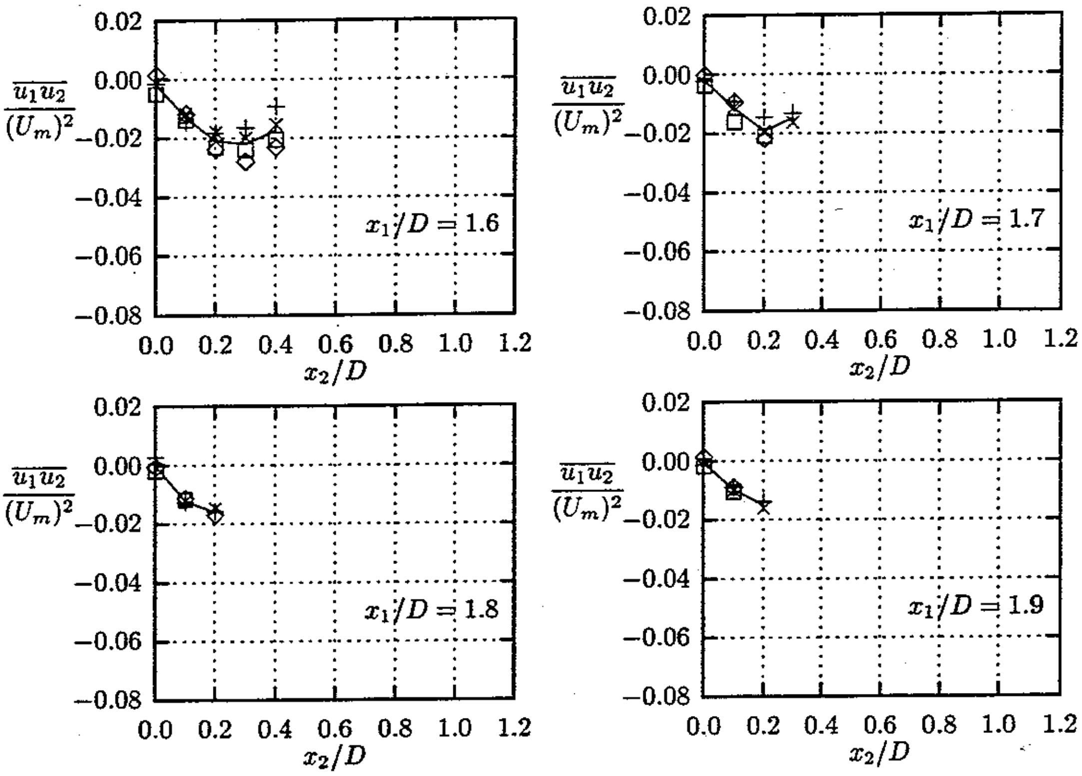
$\frac{\overline{u_1u_2}}{(U_m)^2}$
0.02
0.00
−0.02
−0.04
−0.06
−0.08
0.0
0.2
0.4
0.6
0.8
1.0
1.2
x_2/D
$x_1/D = 1.6$
$x_1/D = 1.7$
$x_1/D = 1.8$
$x_1/D = 1.9$

Appendix C

Wind tunnel experiments

This appendix will describe different problems and experiments related to experiments with tube bundles carried out in the wind tunnel.

C.1 General relations and properties

The mean velocity U_2 at the inlet to the wind tunnel test section is determined from the pressure before and after the contraction shown in figure C.1. It will be assumed that the flow in the contraction is steady and isentropic with a uniform velocity distribution. From conservation of mass and energy

$$\rho_1 A_1 U_1 = \rho_2 A_2 U_2, \tag{C.1}$$

$$P_1 + \tfrac{1}{2}\rho_1 U_1^2 = P_2 + \tfrac{1}{2}\rho_2 U_2^2, \tag{C.2}$$

the velocity U_2 is found as

$$U_2 = \sqrt{\frac{2(P_1 - P_2)}{\rho_2(1 - (\rho_2/\rho_1)(A_2/A_1)^2)}}. \tag{C.3}$$

The ratio of the densities can be found from the relation for an isentropic process

$$\frac{\rho_2}{\rho_1} = \left(\frac{P_2}{P_1}\right)^{1/\gamma}. \tag{C.4}$$

where γ is the isentrop exponent for air.

The properties for air used in this study are listed in table C.1. Except for the density ρ, all properties are assumed to be constant with the pressure P. The density is found from the ideal gas relation as $\rho(P) = \rho_0(P/P_0)$ where index 0 refers to conditions at $p_0 = 1\,\text{bar}$.

The Schiltknecht water micro manometer measures a pressure difference as a water height difference Δh. This is related to a pressure difference as $\Delta P = \rho_w g \Delta h$. The density of water at room temperature 21°C is $\rho_w = 998.0\,\text{kg/m}^3$ and the local gravity acceleration is $g = 9.8159\,\text{m/s}$.

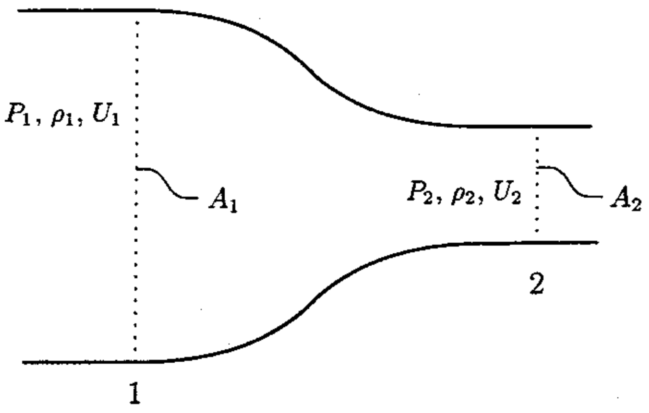

Figure C.1: Contraction at the inlet to the wind tunnel.

property	symbol	value	unit
density	ρ	1.189	kg/m^3
heat conductivity	λ	0.0258	$W/(K\,m)$
dynamic viscosity	μ	$1.82 \cdot 10^{-5}$	$kg/(m\,s)$
Prandtl number	Pr	0.708	–
isentropic exponent	γ	1.4	–

Table C.1: Properties for air at 20°C and 1 bar. Adopted from [68].

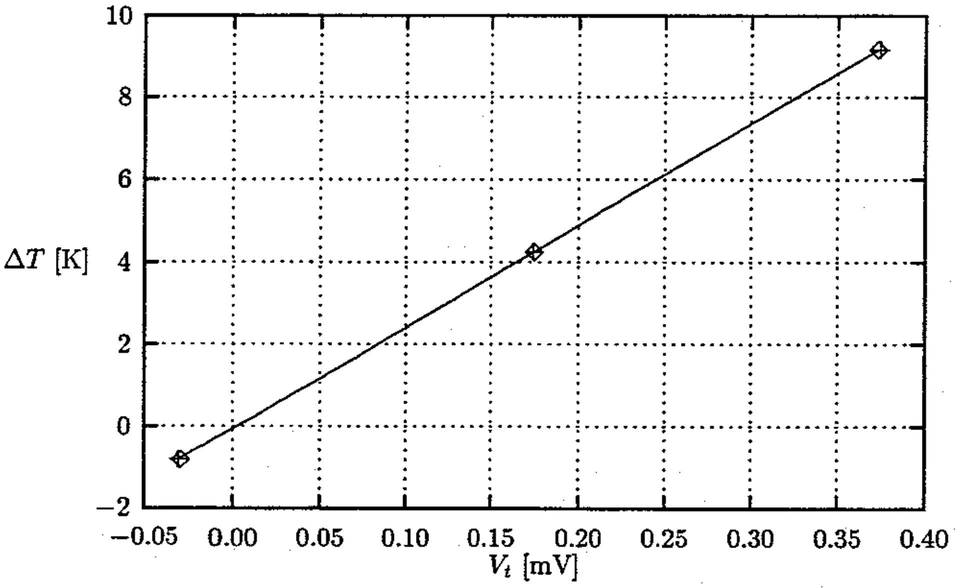

Figure C.2: Calibration of the thermocouple: Temperature difference ΔT vs. voltage over thermocouple V_t.

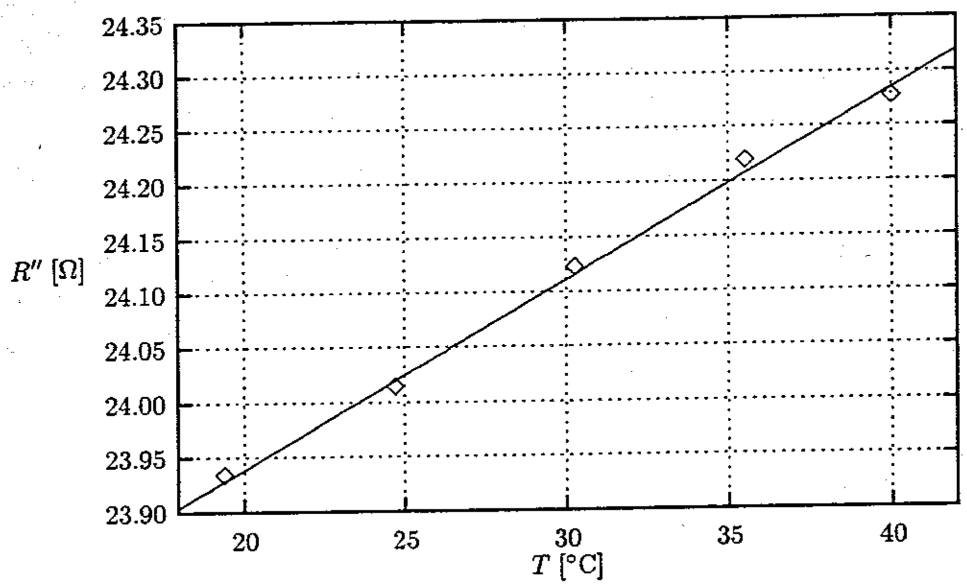

Figure C.3: Calibration of temperature coefficient of resistance, β, for the gold coating.

C.2 Calibration

In the first part of the calibration, the temperature of the air in the wind tunnel was varied in the interval 20°C–40°C. However, due to limitations in the cooling system it was only possible to keep the temperature constant over a longer period with temperatures up to 30° C and the termocouples in the measuring tube could therefore only be calibrated in this interval. The calibration for the thermocouple used in the measurements is shown in figure C.2 and two symbols used represents measurements at two different positions ($\phi = 0°$ and $\phi = 180°$). In both cases the difference between the wall and the upstream air temperatures $\Delta T = T_w - T_0$ has been corrected for the temperature difference found at adiabatic flow conditions. During these measurements, the cold junction was placed in an insulated jug with water at room temperature. Another thermometer was used to register the temperature here. It was checked that the two thermometers used showed the same temperature in the jug. Figure C.2 show a line that is fitted to the data with the least squares method and all the measurements are close to this line. The slope of the line is 24.718 K/mV and this is quite close to the table value of 25.0 K/mV. During the final measurements the calibrated slope has been used and the temperature difference measured at adiabatic flow conditions has been used as the zero value for ΔT. It is believed that the uncertainty of the temperature is less than 2%. This corresponds to 0.1 K at ΔT=5 K.

The calibration of the temperature coefficient of resistance β for the gold coating is shown on figure C.3. From the slope of the line showed on this figure, it is found that $\beta = 0.00072\,\mathrm{K}^{-1}$. It should be noted that this value is somewhat different from the value for solid gold.

The value of the surface resistance at the thermocouple is found by measurements of the heat transfer at the front stagnation point of a single cylinder in the wind tunnel. For the turbulence intensity $Tu \leq 1\,\%$ the Nusselt number at the front stagnation point can be expressed [3]

$$Nu = 1.11\, Re^{0.5}\, Pr^{0.35}\, (Pr_{\infty}/Pr_{w})^{0.25}. \tag{C.5}$$

The blockage factor is assumed to have only little effect and the Reynolds number used in (C.5) will therefore be based on the upstream velocity. Assuming that the Prandtl number is constant, $Pr = 0.708$, equation (C.5) can be written using the Frössling number as

$$Fr = \frac{Nu}{\sqrt{Re}} = 0.9836. \tag{C.6}$$

The heat balance from equation (2.1) can be written

$$\frac{(V_{el}/L)^2}{R''_{\beta}(1+\beta(T-T_{\beta}))} = h\,\Delta T + c_{cond}\,\Delta T + \epsilon_g \sigma((T_0+\Delta T)^4 - T_0^4) \tag{C.7}$$

where it is assumed that the conduction inside the tube q''_{cond} is proportional with ΔT with a factor c_{cond}, i.e. that it only depends little on the Reynolds number. The calibration has been performed as measurements with different Reynolds number but constant temperatures upstream T_0 and on the wall $T_w = T_{\beta}$. The heat transfer coefficent h found from (C.6) can then be combined with (C.7) to give

$$\left(\frac{V_{el}}{L}\right)^2 = R''_{\beta}\, c_1 \sqrt{Re} + c_2 \tag{C.8}$$

with the constants $c_1 = 0.9836\,(\lambda/D)\,\Delta T$ and $c_2 = R''_{\beta}\,(q''_{cond} + q''_{rad})$.

Measurements for $\Delta T = 4.67\,\mathrm{K}$ and for Reynolds numbers in the interval 25 000–54 000 is shown on figure C.4. All measurements are very close to the same straight line and from this it is estimated that $R''_{\beta} = 24.17\,\Omega$ and that $(c_2/R''_{\beta}) = -1.238\mathrm{W/m^2}$. A finite difference analysis of the heat conduction based on measurements of a single cylinder indicates that $c_{cond} = -0.5\,\mathrm{W/(K\,m^2)}$ and from this it can be estimated that the emissivity of the gold coating ϵ_g is less than 0.05. At the used temperatures, q''_{rad} is therefore small and it will be ignored in the final measurements.

C.3 Hot-wire measurements

The purpose of the measurements with hot-wire is to estimate whether the flow in tube bundles in the windtunnel corresponds reasonable to the LDA-measurements. The flow is highly turbulent. This limits the value of the hot-wire measurements considerably and the results can only be used as an indication. In each of the two tube bundles the measurements are performed between the two tubes upstream of the measuring tube. The measurements use the same coordinate system as the LDA-measurements, see figure 2.5.

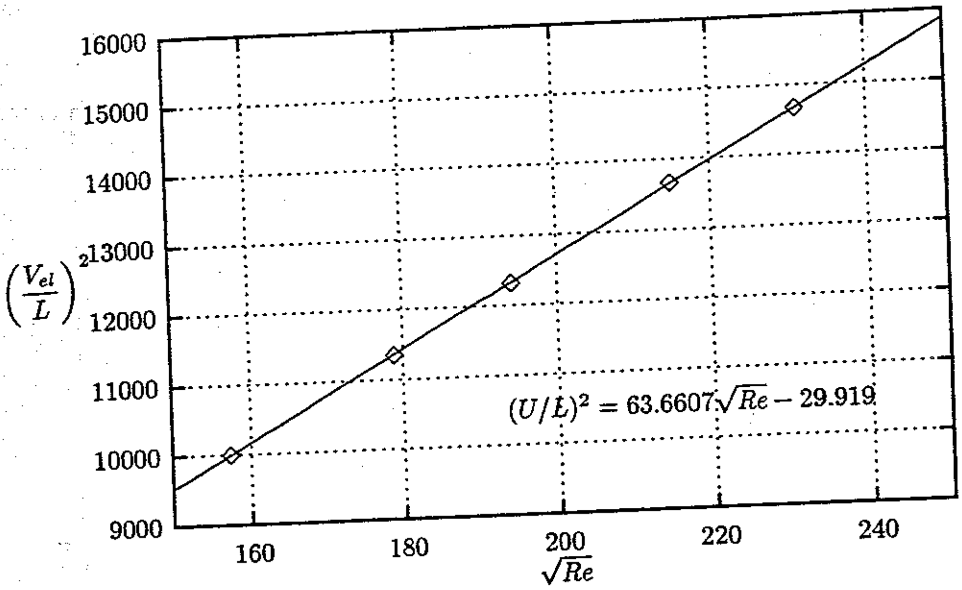

Figure C.4: Measurements at the stagnation point for a single cylinder and constant temperatures, $\Delta T = 4.67\,\mathrm{K}$.

The measurements are performed using a Dantec 55P11 single hot-wire and a Dantec CTA bridge 56C17 connected to an analog-to-digital conversion card (Metrabyte DAS-16) in a personal computer. The data were processed with the hot-wire anemometer software 'acqWIRE' from Dantec. The hot-wire was transversed manually with a precision of ±0.1 mm.

The hot-wire was located so that the main velocity was perpendicular to both the hot-wire and the prongs holding the hot-wire. The hot-wire was aligned in the same way during the calibrations in the empty windtunnel. About 10 single measurements with velocities in the range 0–20 m/s was used to fit a fourth order polynomial as a calibration curve. These measurements varied less that 1 % from the calibration curve. After the measurements the calibration curve was checked at several velocities. During these measurements the turbulence intensity in the empty wind tunnel was measured to be $Tu = 0.4\,\%$.

In each position four batches with 16 000 samples were taken with a frequency of 8000 kHz. In each batch the mean velocity and the RMS value was calculated by the program and the final values were found as the mean values of the four batches.

Due to the high levels of the turbulence in the tube bundle the mean velocity registered by the hot-wire U_{eff} is not the actual mean velocity. If it is assumed that the actual mean velocity U_1 is perpendicular to both the hot-wire and the prongs holding the hot-wire then the effective velocity registered by the hot-wire can be approximated as [69]

$$U_{eff} = U_1\left(1 + \frac{\overline{u_2u_2}}{2U_1^2} - \frac{\overline{u_1u_2u_2}}{3U_1^3} - \frac{\overline{u_1u_3u_3}}{U_1^3} - \ldots\right). \tag{C.9}$$

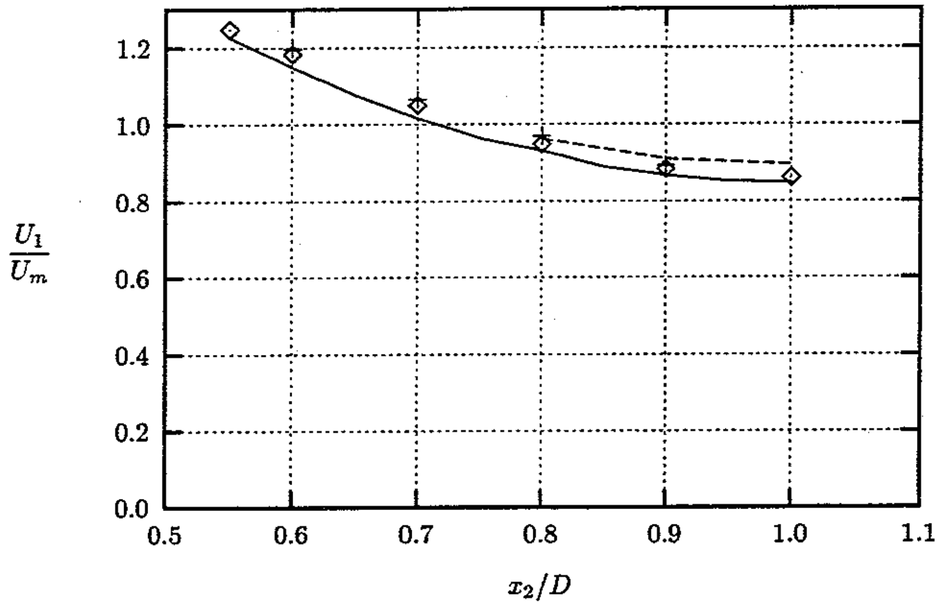

Figure C.5: Mean velocity in tube bundle A. Symbols are hot-wire measurements, solid line is U_1 and dashed line is U_{eff}, both from LDA measurements.

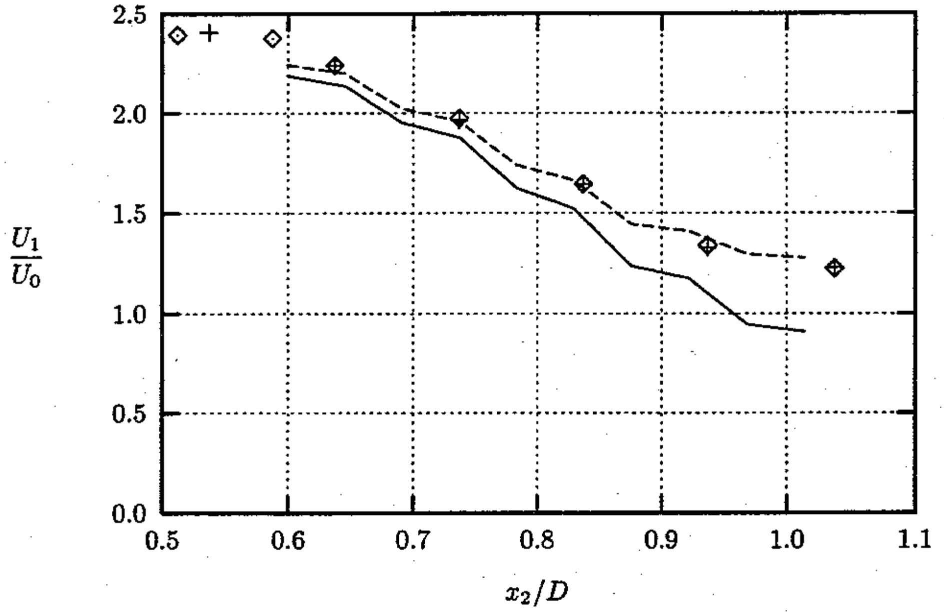

Figure C.6: Mean velocity in tube bundle B. Symbols are hot-wire measurements, solid line is U_1 and dashed line is U_{eff}, both from LDA measurements.

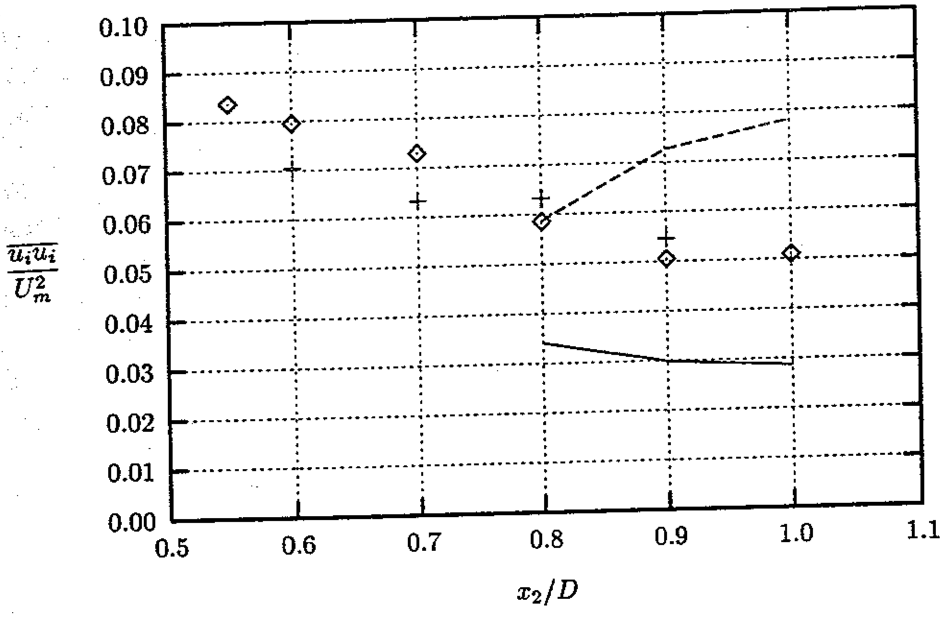

Figure C.7: Mean square of velocity fluctuations in tube bundle A. Symbols are hot-wire measurements, solid line is $\overline{u_1 u_1}$ and dashed line is $\overline{u_2 u_2}$, both from LDA measurements.

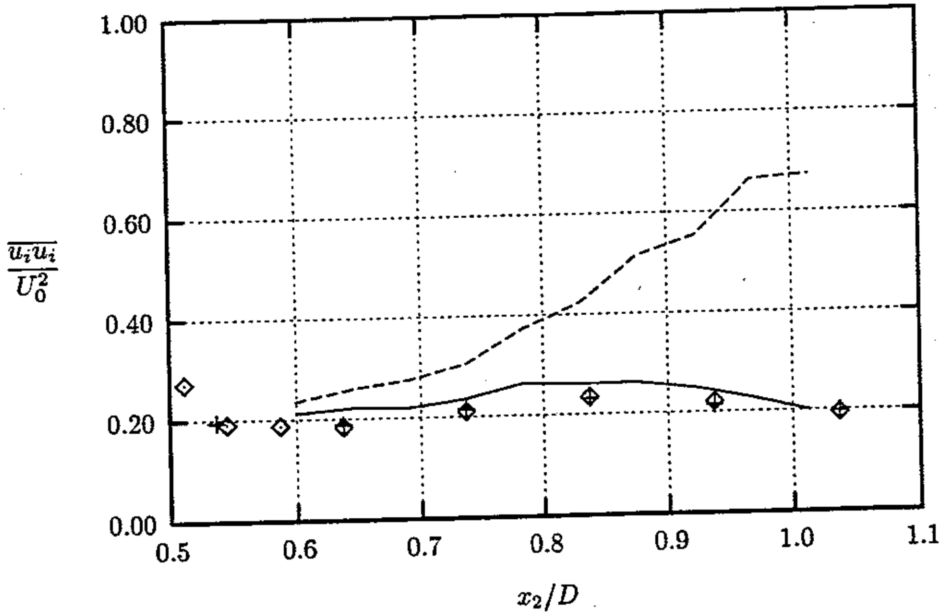

Figure C.8: Mean square of velocity fluctuations in tube bundle B. Symbols are hot-wire measurements, solid line is $\overline{u_1 u_1}$ and dashed line is $\overline{u_2 u_2}$, both from LDA measurements.

The measurements of the mean velocities by hot-wire will therefore be compared with U_{eff} calculated from (C.9) using only the first two terms: $U_{eff} = U_1(1 + \overline{u_2u_2}/(2U_1^2))$. The measurements are shown in figure C.5–C.8. The x-axis shows distance from the center between the two tubes. For tube bundle A the velocities have been made non-dimensional with the mean velocity U_m between the two tubes and for tube bundle B with the corresponding upstream (before tube bundle) velocity U_0. The symbol $\diamond$ represents positions moving away and symbol + represents positions moving towards the hot-wire support.

For tube bundle A the calculated effective mean velocity U_{eff} in figure C.5 is a little higher than U_1 with the measured hot-wire data laying between these two velocities. For tube bundle B the mean velocities from the LDA data shown in figure C.6 seem to have systematic fluctuations and are, in the middle between two tubes, somewhat lower that U_{eff}. The calculated effective mean velocity is quite close to the measured hot-wire measurements. For both tube bundles, the hotwire measurements therefore indicate that the mean velocities in the wind tunnel agree well with the LDA measurements.

The mean square of the velocity fluctuations from the hot-wire measurements in tube bundle A are shown in figure C.7. They are located somewhere between $\overline{u_1u_1}$ and $\overline{u_2u_2}$ measured by LDA. For tube bundle B figure C.8 shows that the velocity fluctuations are close to $\overline{u_1u_1}$ but significantly lower that $\overline{u_2u_2}$ measured by LDA. Because of the high level of turbulence it is difficult to draw any conclusion regarding the agreement between the measurements of the turbulence by hot-wire and by LDA measurements.

C.4 Calculation of heat conduction

The internal heat conduction inside the measuring tube has been calculated using a finite difference analysis, see e.g. [22]. The tube is considered to consist of two parts: The acrylic tube with a wall thickness of $t_1 = 5\,\text{mm}$ and the PET film with a thickness of $t_2 = 0.17\,\text{mm}$. The manufacturer states a heat conductivity for acryl of $\lambda_1 = 0.19\,\text{W}/(\text{K}\,\text{m})$. The manufacturer of the PET film was not able to state a heat conductivity and instead the value $\lambda_2 = 0.29\,\text{W}/(\text{K}\,\text{m})$ stated in [70] for PET is used. The heat conduction is assumed to be one dimensional in the PET film and two-dimensional in the acrylic tube. The grid used for the latter is shown on figure C.9. The equation for the heat conduction in a polar coordinate system can be written [22]

$$\frac{\partial^2 T}{\partial r^2} + \frac{1}{r}\frac{\partial T}{\partial r} + \frac{1}{r^2}\frac{\partial^2 T}{\partial \phi^2} = 0. \tag{C.10}$$

This equation can be discretized

$$\frac{T_{i+1,j} - 2T_{i,j} + T_{i-1,j}}{(\delta r)^2} + \frac{1}{r(i)}\frac{T_{i+1,j} - T_{i-1,j}}{2\delta r} + \frac{1}{(r(i))^2}\frac{T_{i,j+1} - 2T_{i,j} + T_{i,j-1}}{(\delta\phi)^2} = 0, \tag{C.11}$$

and rearranged on the form

$$a_i T_{i,j-1} + b_i T_{i,j} + c_i T_{i,j+1} = d_i T_{i-1,j} + e_i T_{i+1,j} \tag{C.12}$$

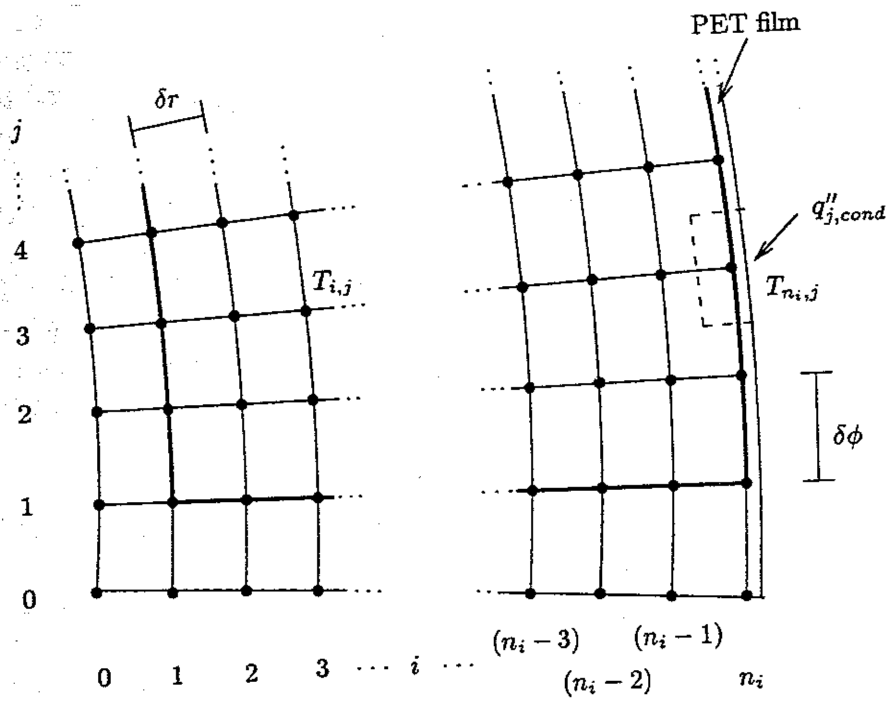

Figure C.9: Grid used in finite difference calculation. The boundaries of the acrylic tube is shown with thick lines.

where

$$a_i = c_i = \frac{1}{(r(i)\delta\phi)^2} \tag{C.13}$$

$$b_i = \frac{-2}{(\delta r)^2} + \frac{-2}{(r(i)\delta\phi)^2} \tag{C.14}$$

$$d_i = \frac{-1}{(\delta r)^2} + \frac{1}{2r(i)\delta r} \tag{C.15}$$

$$e_i = \frac{-1}{(\delta r)^2} + \frac{-1}{2r(i)\delta r} \tag{C.16}$$

The calculation is performed for a half tube. On the outer wall the measured temperature is used as the boundary condition. In order to reduce errors due to small local fluctuations in the measured temperature, this temperature is smoothed before it is used as boundary condition. The smoothing is done by fitting a second order polynomia with the least squares method to five adjacent point and then adjusting the point in the middle to the polynomia. This procedure is done for all points twice. The smoothed temperatures are only used in the finite difference calculation. A zero gradient condition is used on the other boundaries corresponding to an adiabatic inner wall and to symmetry at the ends. The zero gradient is implemented by extra rows of points just outside the boundary. During each iteration these 'dummy' points are given the same value as the corresponding points just inside the tube.

The temperatures are initialized with the corresponding outer wall temperatures. In the radial direction $n_i = 20$ points were used and in the tangential direction the grid was determined by the positions of the measured wall temperatures. A traditional tridiagonal line solver [71] is then used to solve lines with constant value of i, for i going from n_i to 1. This is repeated until the maximum change of temperature at any point during an iteration is less than 10^{-8} K.

The control volume shown with a dashed line in figure C.9 is used to find the heat flux removed by conduction from gold coating, $q''_{cond} = -q''_r - q''_t - q''_f$, where the three contributors to q''_{cond} are: The radial heat flux q''_r and the resulting heat flux from the balances of tangential heat conduction in the tube q''_t and in the PET film q''_f. These can be written

$$q''_{r,j} = -\lambda_1 \frac{\partial T}{\partial r} \tag{C.17}$$

$$q''_{t,j} = -\lambda_1 \frac{\delta r}{2r^2 \delta\phi} \left(\left[\frac{\partial T}{\partial \phi}\right]_{j-1/2} - \left[\frac{\partial T}{\partial \phi}\right]_{j+1/2} \right) \tag{C.18}$$

$$q''_{f,j} = -\lambda_2 \frac{t_2}{r^2 \delta\phi} \left(\left[\frac{\partial T}{\partial \phi}\right]_{j-1/2} - \left[\frac{\partial T}{\partial \phi}\right]_{j+1/2} \right) \tag{C.19}$$

where the temperature gradients at the sides of the control volume are found as

$$\frac{\partial T}{\partial r} = \frac{T_{n_i,j} - T_{n_i-1,j}}{\delta r}, \tag{C.20}$$

$$\left(\left[\frac{\partial T}{\partial \phi}\right]_{j-1/2} - \left[\frac{\partial T}{\partial \phi}\right]_{j+1/2} \right) = -\frac{T_{n_i,j+1} - 2T_{n_i,j} + T_{n_i,j-1}}{\delta\phi}. \tag{C.21}$$

The geometry around the thermocouple is shown in figure 2.12. The thermocouple is not in direct contact with the acrylic tube as it is assumed in the finite difference analysis. A small part of the material is removed and a coating of silicon rubber is used instead to keep the thermocouple in the correct position. The manufacture states that the silicon rubber has a thermal conductivity of $\lambda_3 = 0.12\,\mathrm{W/(K\,m)}$. The error introduced by this design can be roughly estimated by assuming that the design corresponds to a small area near the thermocouple with only half the heat conductivity of the acrylic tube. If tangential heat conduction is neglected and if the change of radial heat conduction due to the design is assumed to be small, the difference ΔT_λ between the temperature drop over the silicon rubber and over $\ell = 0.5\,\mathrm{mm}$ of massive acryl is

$$\Delta T_\lambda = \frac{q''_r\,\ell}{0.5\,\lambda_1}. \tag{C.22}$$

Equation (C.22) has been calculated for all the measurements; it was found that ΔT_λ at all positions was less that 1 % of ΔT except at a few points at the extrema of *Nu* where values up to 3 % were found. This indicates that the error introduced by the design with the silicon rubber is small and it has therefore been neglected in the calculation of the heat transfer coefficient. Also, as a

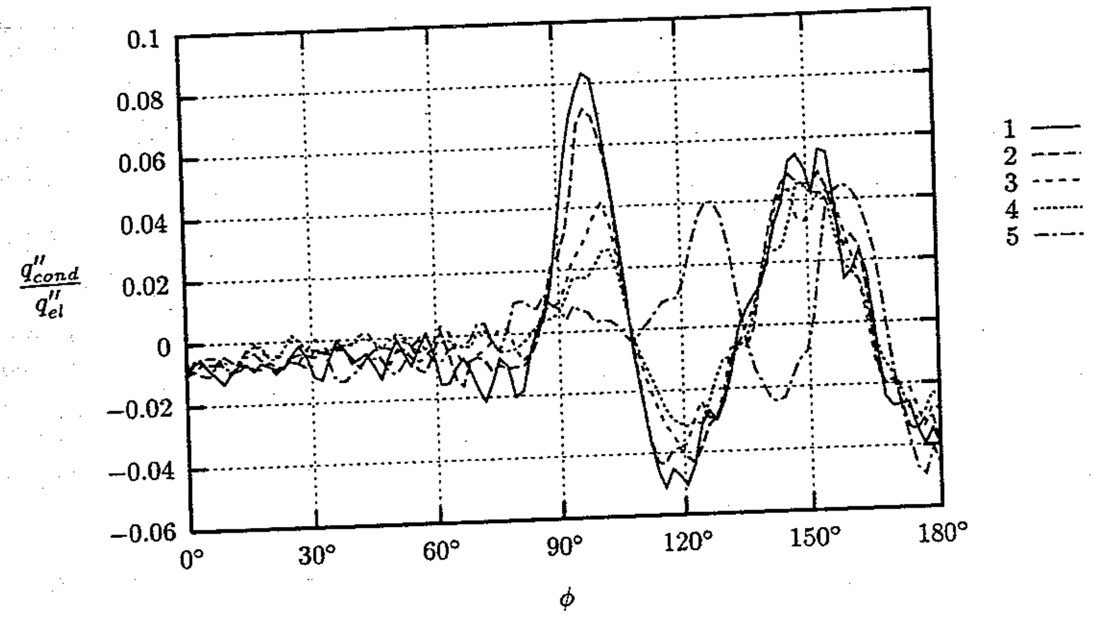

Figure C.10: Calculated heat conduction relative to the generate heat flux. Key as table 2.2.

partial correction the tangential heat conduction in the acrylic tube q''_t which is the smallest contributor to the heat flux has been neglected. The total heat flux is then found at the jth position as $q''_{cond,j} = q''_{r,j} + q''_{f,j}$.

The order of magnitude of the calculated heat conduction is illustrated in figure C.10. Here the ratio between q''_{cond} and q''_{el} is plotted as a function of the angle ϕ for each of the measurements listed in table 2.2. On the front side of the tube q''_{cond} is small, less than 2 % of q''_{el}. However on the rear side of the tube at the peaks in the local Nusselt number, values of q''_{cond} up to 8 % of q''_{el} are seen for the low Reynolds numbers. Here the assumption of a constant heat flux is not very good. The radial heat conduction q''_r is the main contributor to q''_{cond}. The best way to reduce q''_{cond} would therefore be to use an even more insulating material than acryl.

Appendix D

Plots from numerical calculations

D.1 Impinging jet

The figures in this section show plots of profiles in the y-direction of local bulk velocity U_{bulk} and the local Reynolds stresses. The Reynolds stresses are composed from the fluctuating velocity u in the r-direction and the fluctuating velocity v in the y-direction. The key to the figures is found in table 5.2.

Reynolds stress component normal to wall on stagnation line.

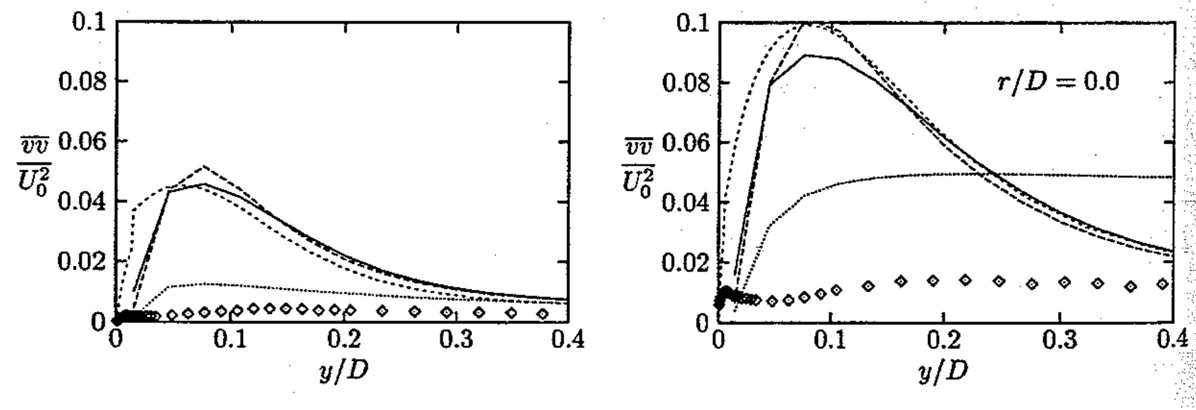

a) $Re = 23\,000$, $H/D = 2.0$

b) $Re = 70\,000$, $H/D = 6.0$

Velocity and Reynolds stresses for $Re = 23\,000$ and $H/D = 2.0$.

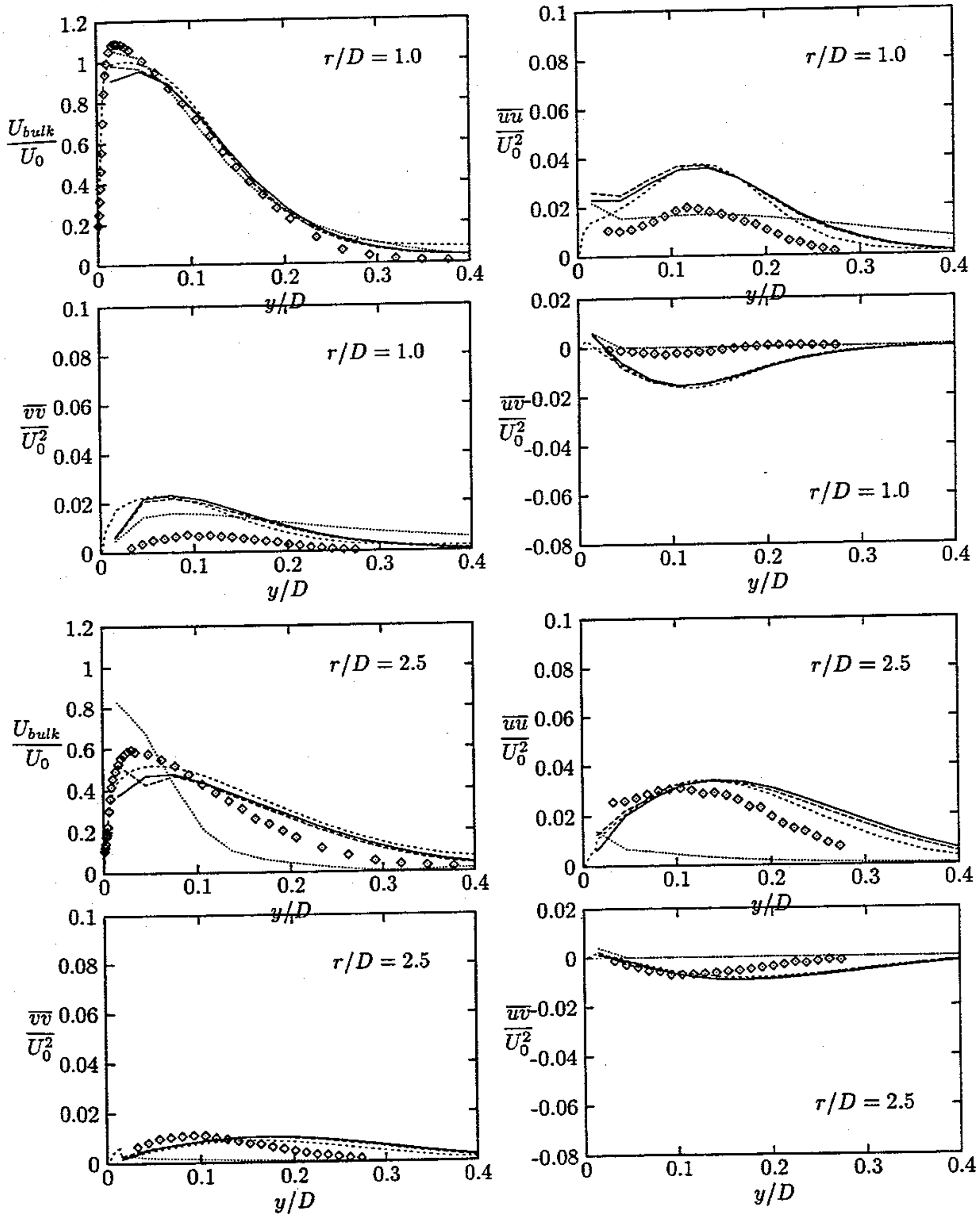

Velocity and Reynolds stresses for $Re = 70\,000$ and $H/D = 6.0$.

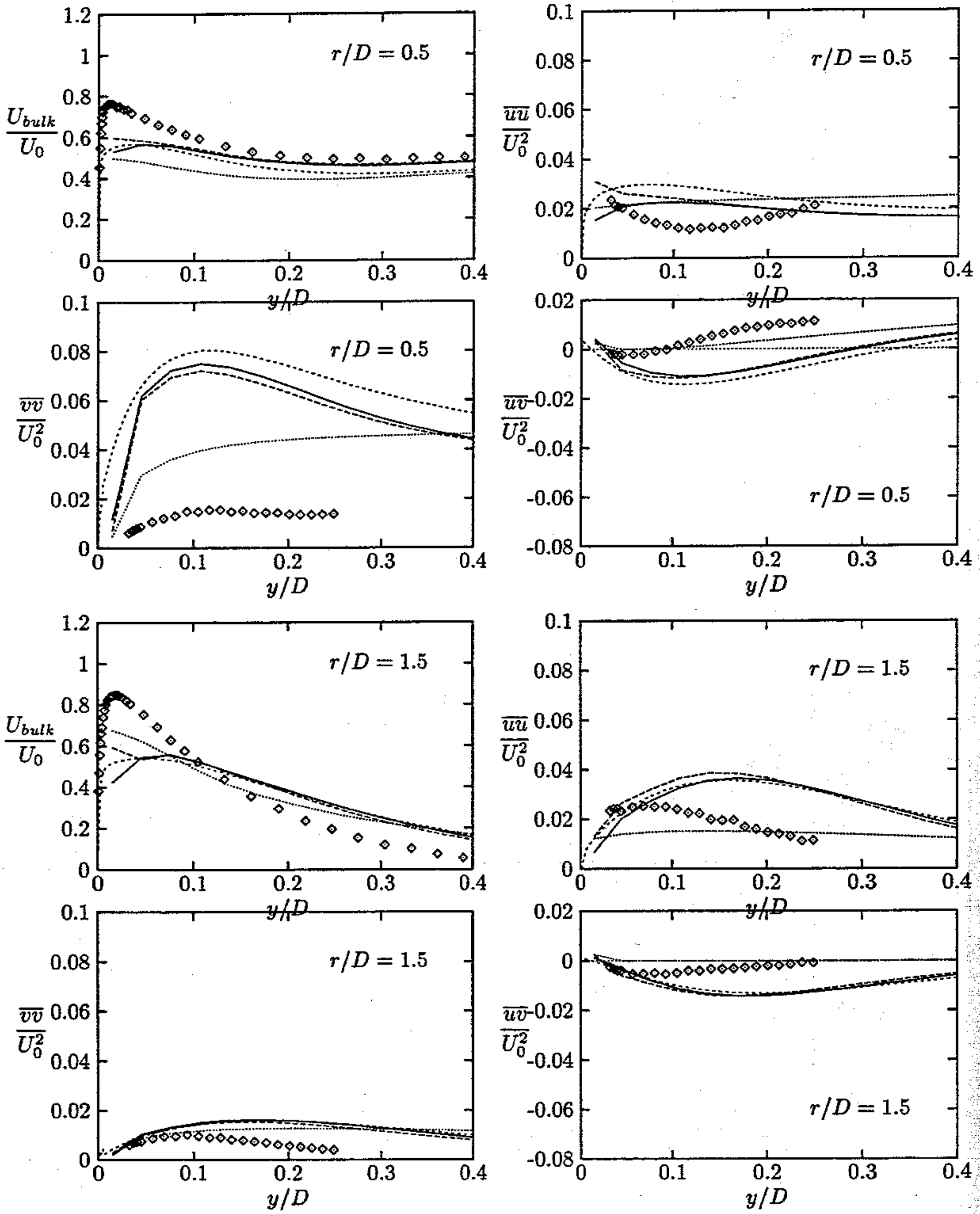

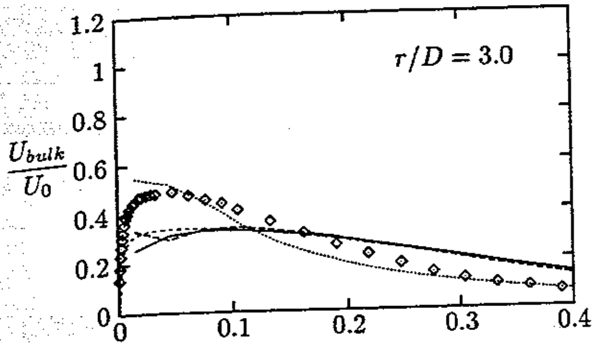

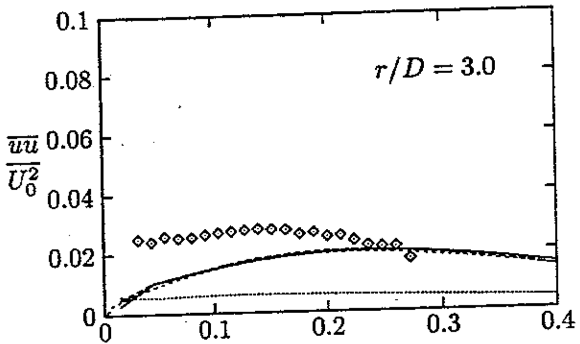

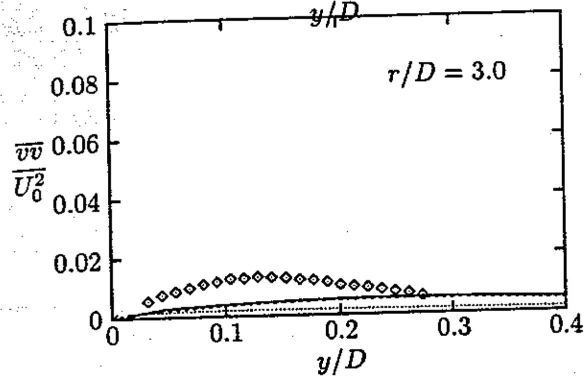

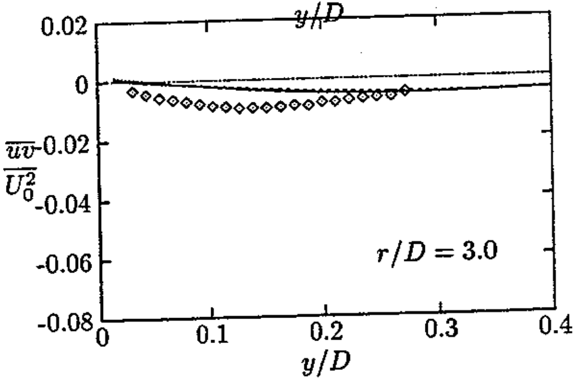

D.2 Tube bundles

The following two sections show plots of local velocities and Reynolds stresses along the lines shown in figure 5.18 using the coordinate system shown on the same figure. Experimental data obtained by LDA-measurements are shown with the symbol $\diamond$, the results from calculations with the Reynolds stress model are shown with solid lines and the results from calculation with the k-ϵ model are shown with dashed lines. For the k-ϵ model the Reynolds stresses on the plots have been estimated as $\overline{u_1u_1} = \overline{u_2u_2} = \frac{2}{3}k$.

D.2.1 Tube bundle A

The coordinates are normalized by the tube diameter D and the velocities and Reynolds stresses are normalized by the measured mean velocity in the minimum flow section U_m.

Profile at inlet to unit-cell, $x_1 = 0.0$.

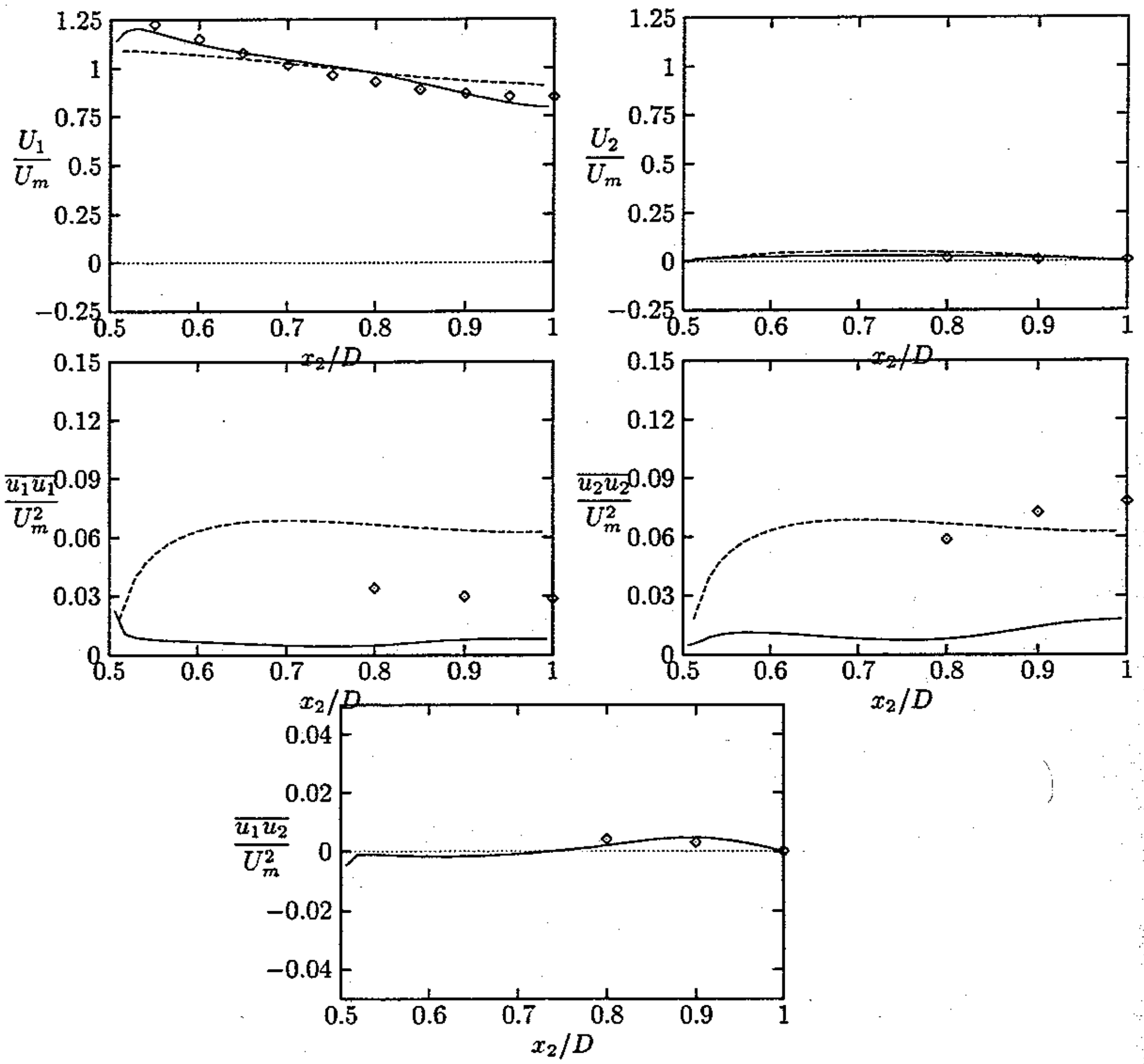

Profile at $x_1 = 0.8\,D$.

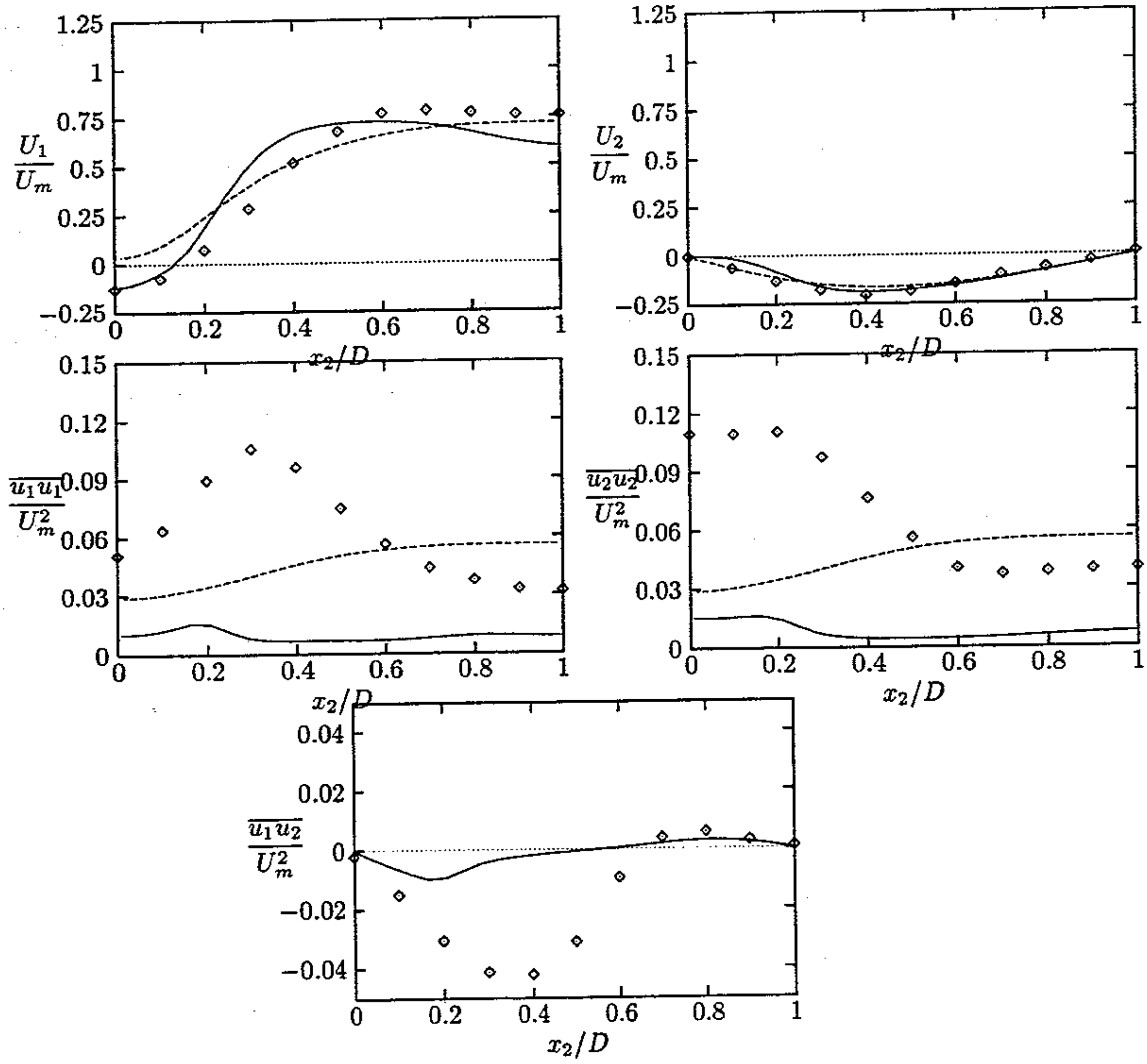

Profile at $x_1 = 1.2\,D$.

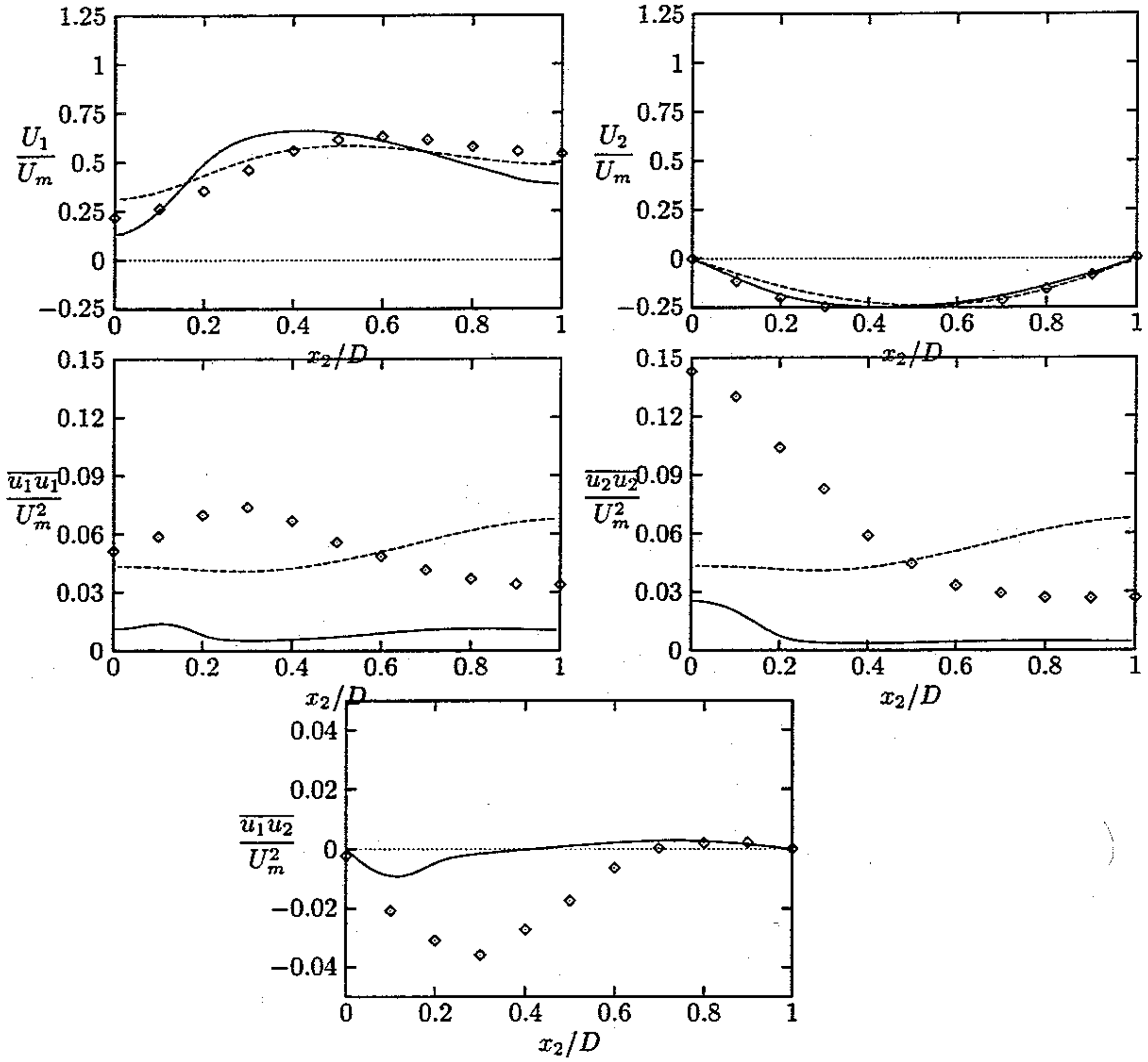

Profile in the impact region, $x_2 = 1.0\,D$.

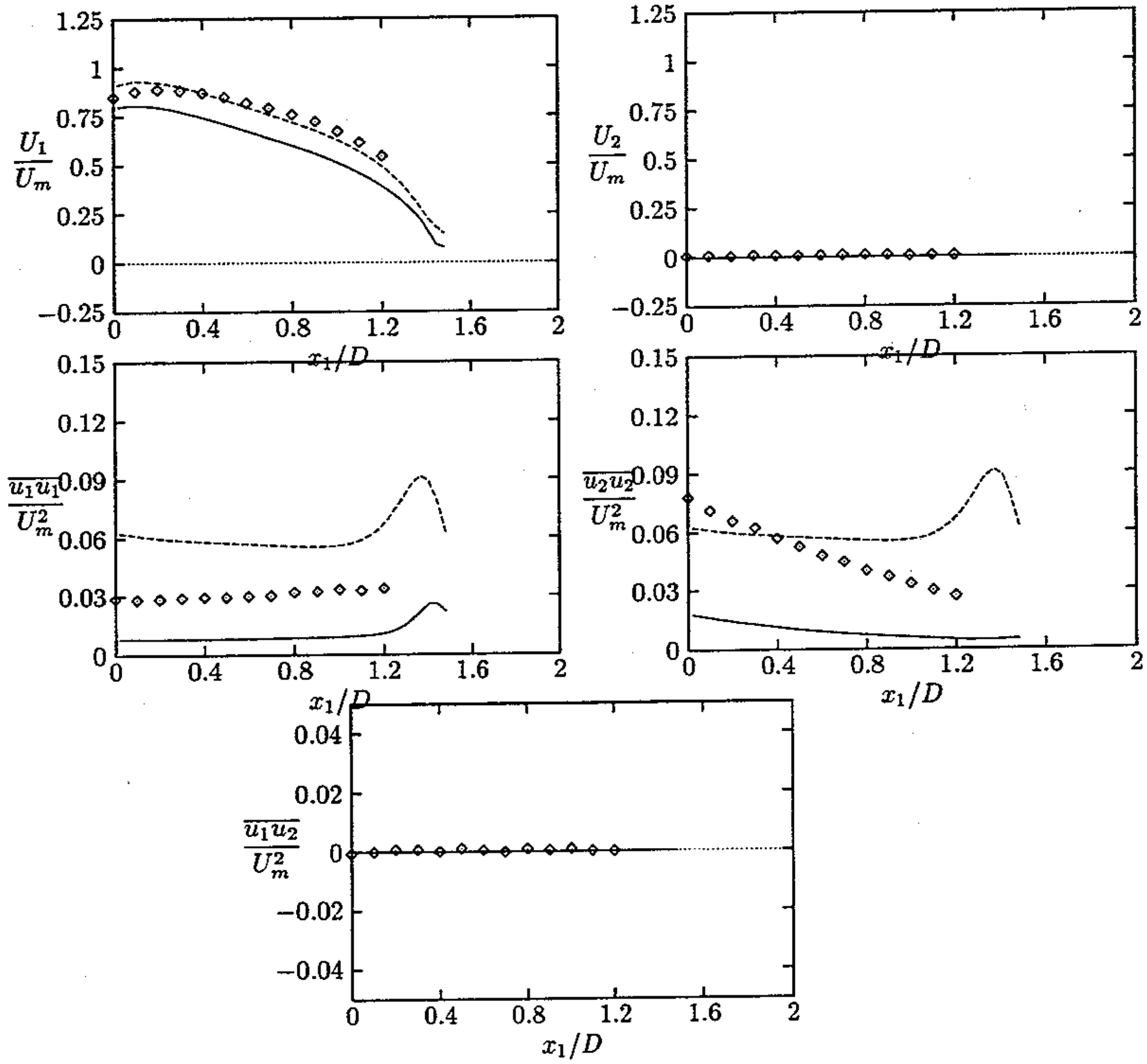

Profile in the wake region, $x_2 = 0.0$.

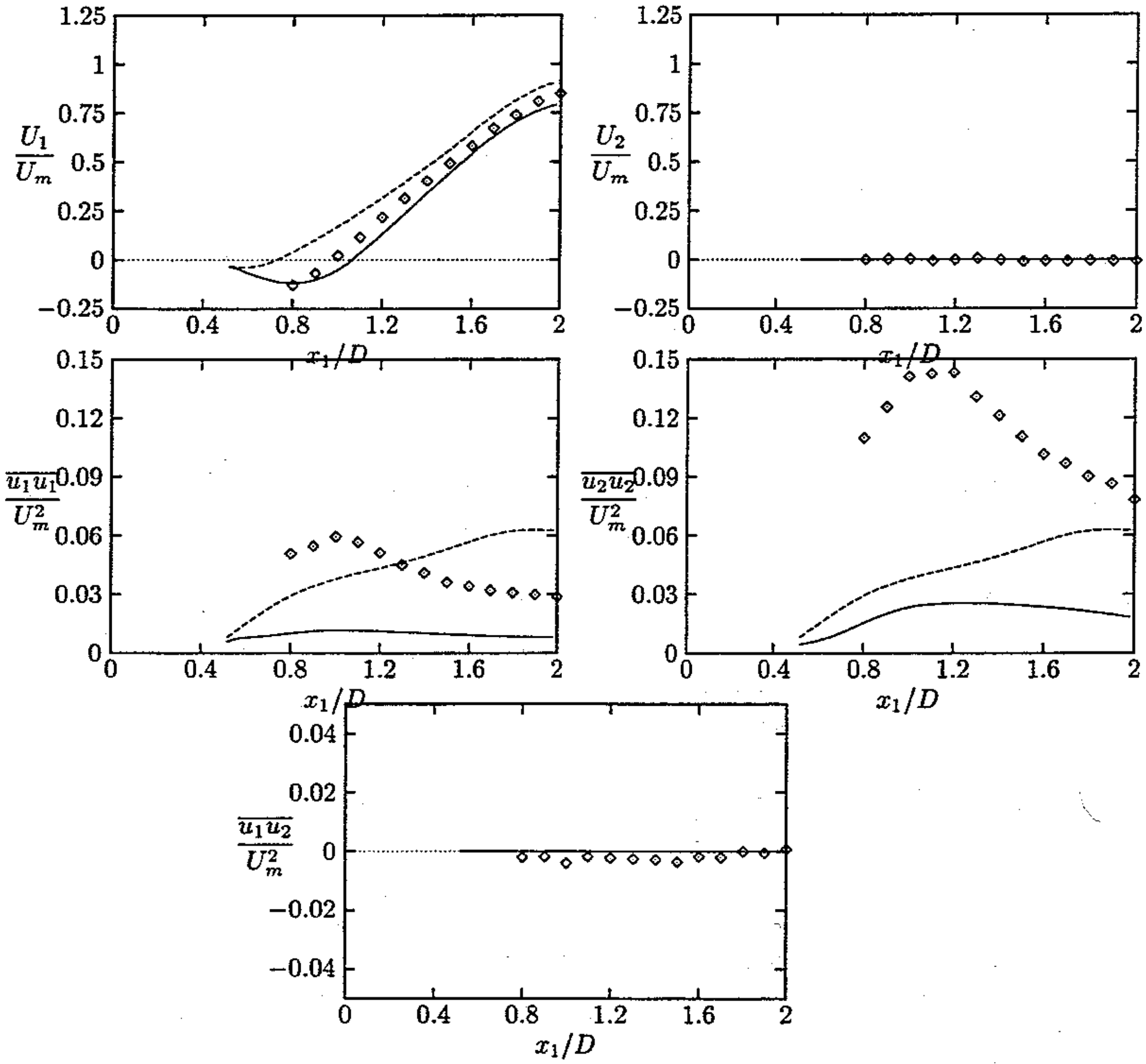

D.2.2 Tube bundle B

The coordinates are given in actual distances from the LDA-experiment [10] and the velocities and Reynolds stresses are normalized by the mean velocity upstream of the tube bundle section U_0.

Profile at inlet to unit-cell, $x_1 = 0.0$.

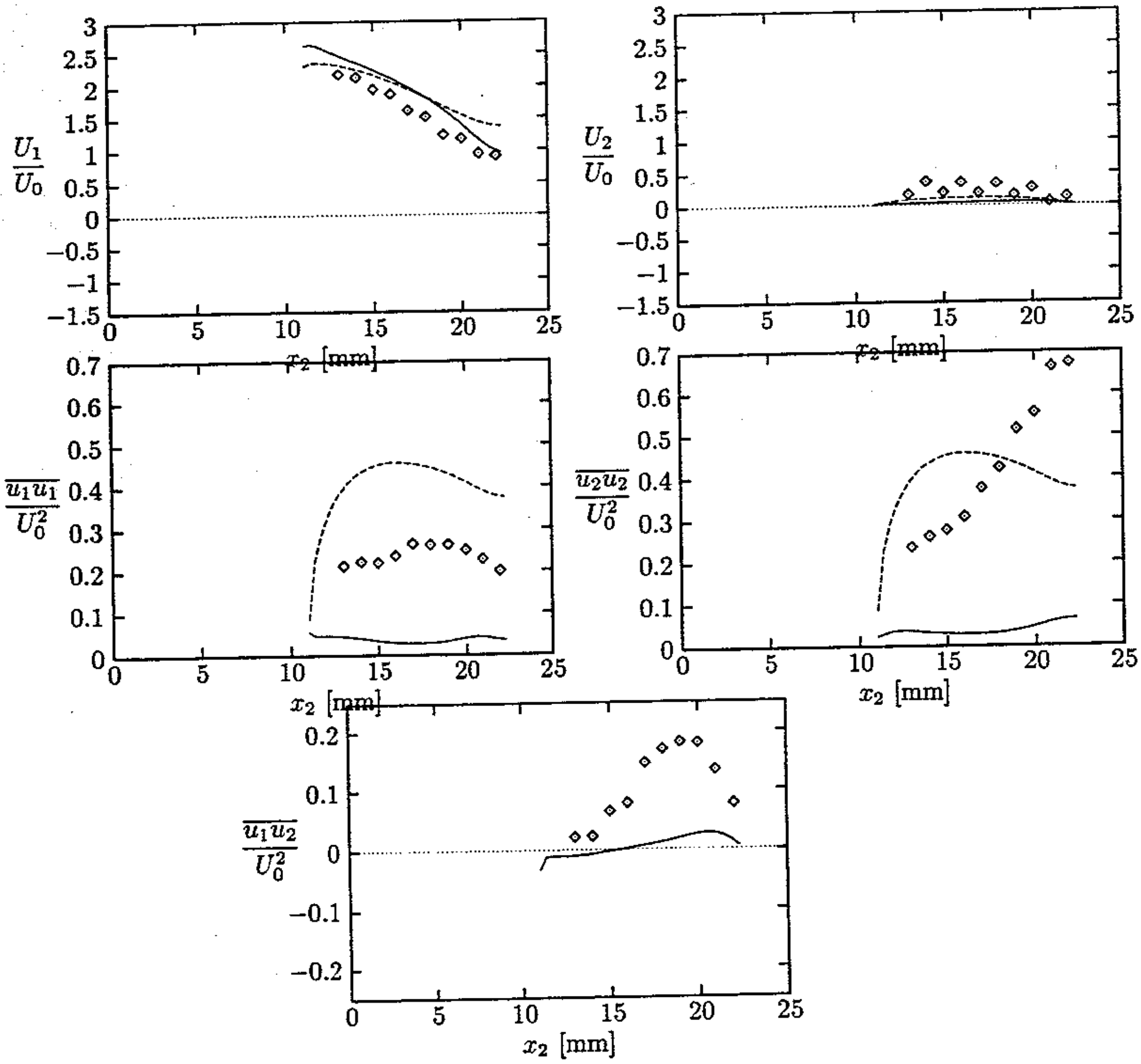

Profile at $x_1 = 0.51\,D$ ($x_1 = 11\,\mathrm{mm}$).

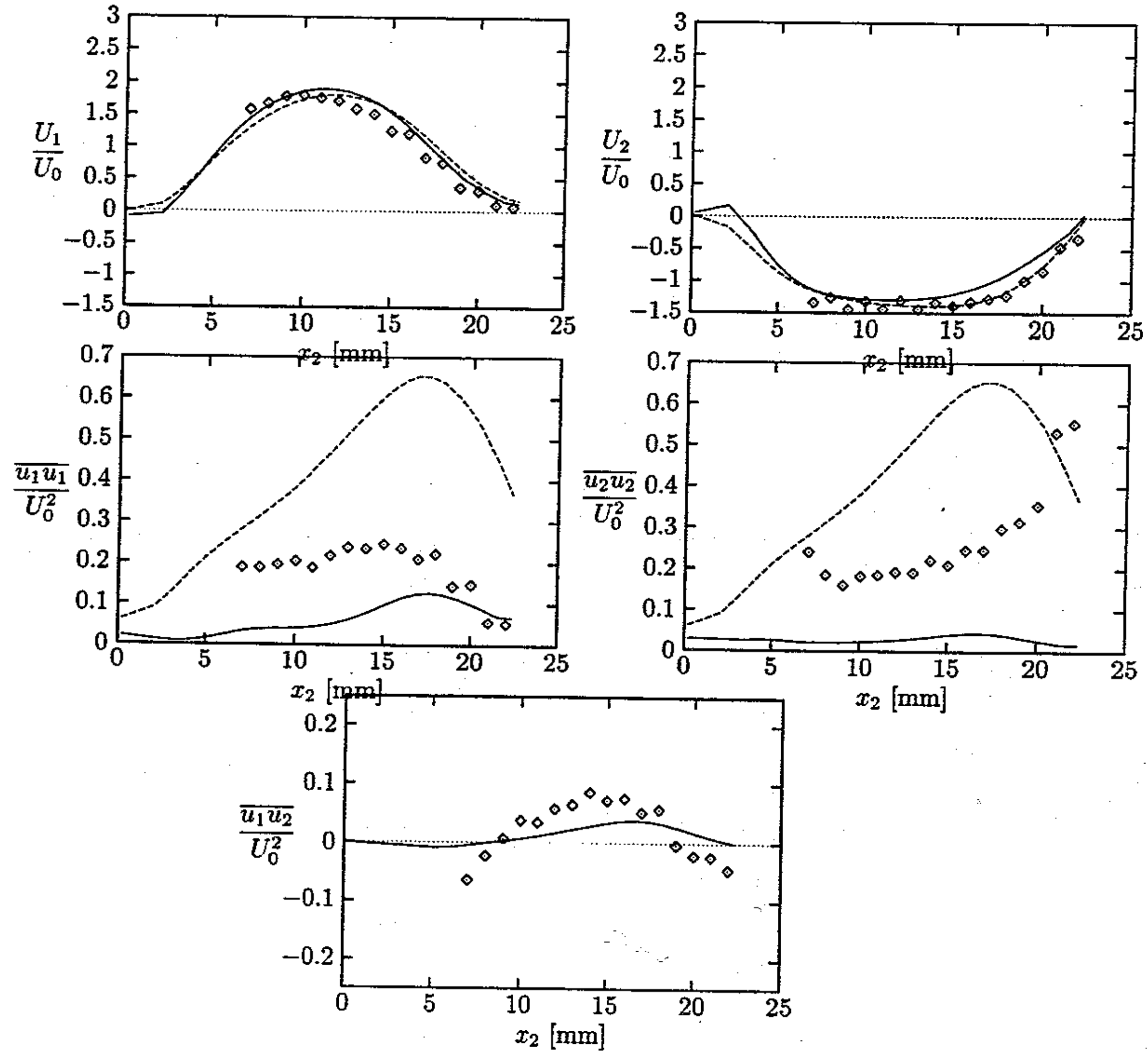

Profile at $x_1 = 0.76\,D$ ($x_1 = 16.5\,\mathrm{mm}$).

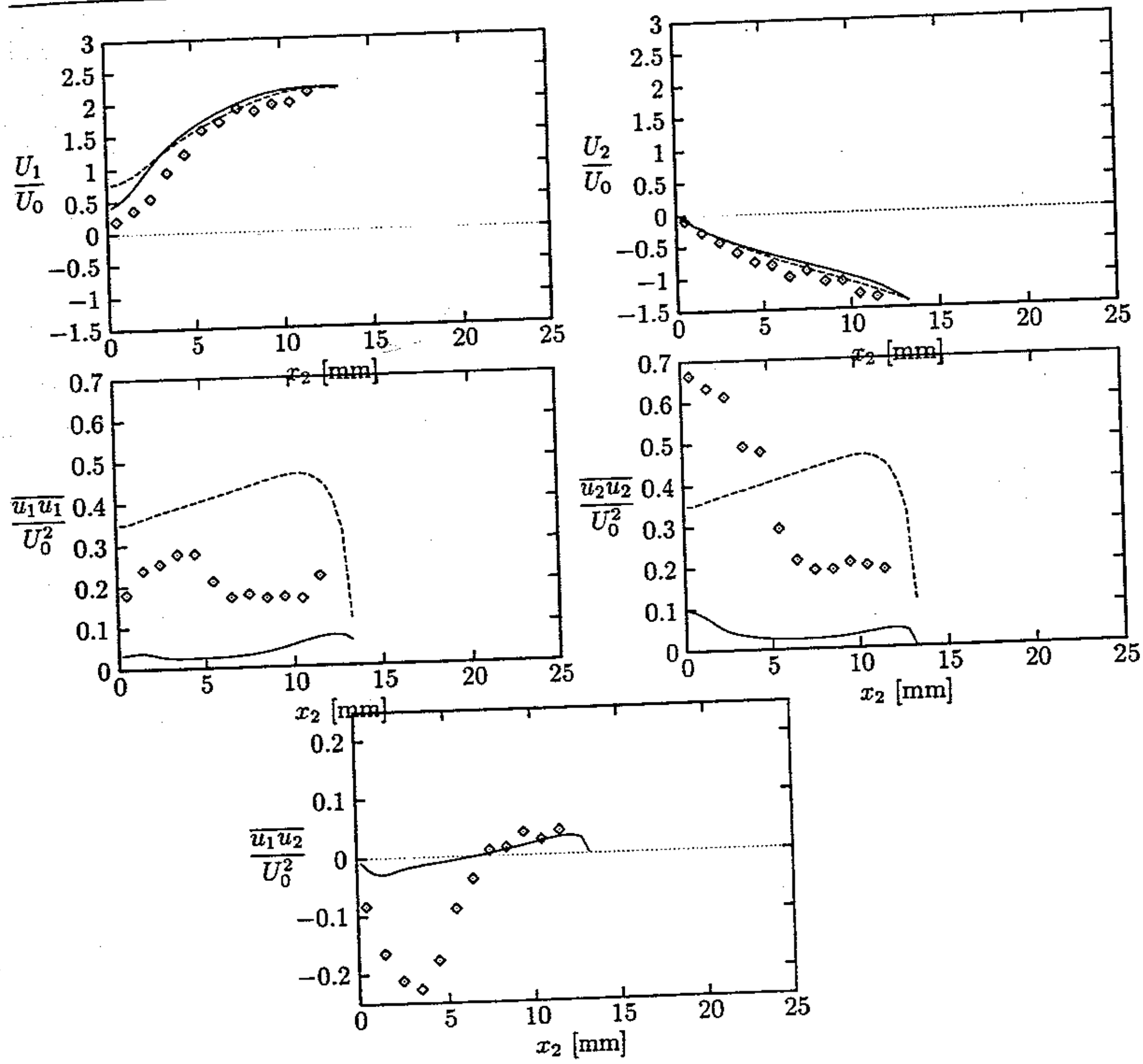

Profile in the impact region, $x_2 = 1.04\,D$.

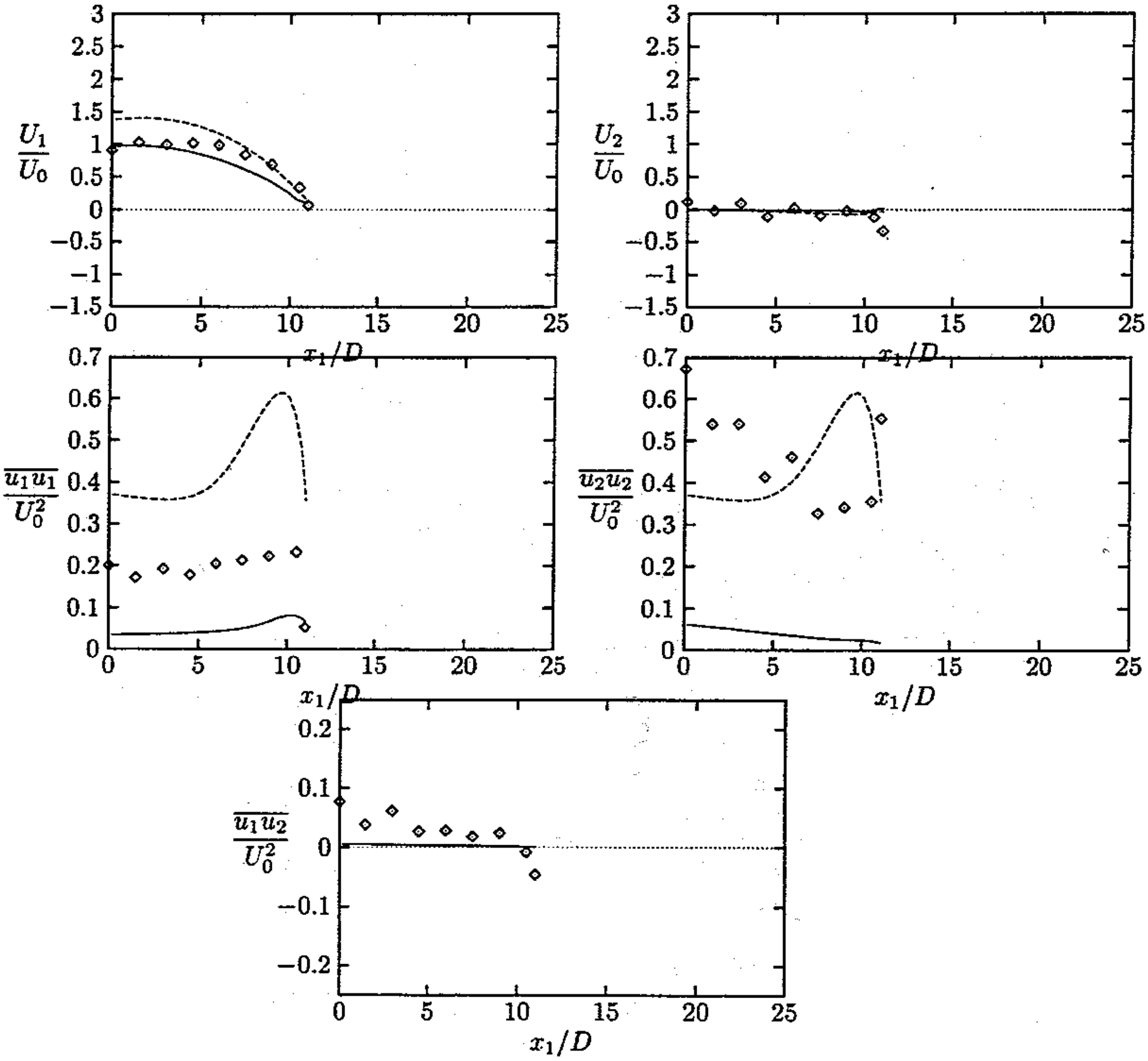

Profile in the wake region, $x_2 = 1.04\,D$.